SIMULTANEOUS MEASUREMENT OF VELOCITY AND TEMPERATURE USING LIQUID CRYSTAL PARTICLES

XIANGYANG JU

A thesis submitted in partial fulfilment of the
requirements of The Nottingham Trent University
for the degree of Doctor of Philosophy.

This research programme was carried out in the
Department of Mechanical and Manufacturing Engineering,
Faculty of Engineering and Computing,
The Nottingham Trent University,
Nottingham NG1 4BU, UK

October 1996

Contents

Simultaneous measurement of velocity and temperature using liquid crystal particles

by
Xiangyang Ju

Abstract

Particle Image Velocimetry (PIV) is a well established, non-intrusive technique, for full field flow measurements. It combines qualitative flow visualization with quantitative measurements, thus providing fluid mechanics with a most powerful tool. The display of colour distribution from Thermochromic Liquid Crystals (TLC) due to changes in temperature have been frequently exploited in the measurement of surface temperature. Thermochromic liquid crystals in encapsulated form can also act as particles for suspension in liquids, and due to their responsiveness to temperature, enable velocity and temperature to be measured simultaneously.

Velocity and temperature are two essential parameters for a basic understanding of heat transfer and heat convection phenomena. Traditional techniques for measuring velocity and temperature such as Laser Doppler Anemometry, Hot Wire Anemometry and Thermocoupling are generally point-wise. The technique of combining PIV with thermochromic liquid crystals will provide full field information on velocity and temperature simultaneously and can therefore be more advantageous. For the purpose of simultaneous measurement of velocity and temperature, video based PIV, instead of photographic PIV, is proposed using encapsulated liquid crystals as suspended particles in the liquid. Direct digital colour images are used for temperature measurement instead of colour photographs. This simplifies the procedure of the colour and temperature calibration and also provides fast full field temperature from a single colour image. However, direct usage of digital images for video based PIV leads to limitations caused by low resolution and low frame rate which is inherent to digital image facilities.

Low resolution of the video based PIV images, invalidates the assumption that the local velocity distribution in the interrogation region is uniform. The effects of local non-uniformity in the region are investigated. Evidence is provided that the accuracy of video based PIV is largely affected by local non-uniformity. Optimal parameters such as particle image density, the interrogation spot size and the particle image size are selected for video based PIV. An improved cross-correlation method is proposed to deduce the effects of local non-uniformity, which significantly improves the results when compared with the conventional PIV.

Several colour spaces are investigated for temperature measurement, especially the hue representations in HSI (Hue, Saturation and Intensity) colour space. The hue representation is selected since this gives a monotonic relationship with temperature and provides the largest temperature measurement range. The effects of saturation, intensity and viewing angle are investigated.

Finally, simultaneous velocity and temperature distributions are presented for natural convection flows. Uncertainties in the measurements are discussed.

ACKNOWLEDGEMENTS

I am grateful for all the support that I have received during the course of this work. In particular, I would like to thank the following persons: Dr Nath Jambunathan, my Director of Studies; Dr Shirley Ashforth-Frost, Professor Xiaoping Wu, my supervisors; Mr Brian Dobbins, my advisor; for their enthusiasm and tireless encouragement throughout this project and for many useful and stimulating discussions; Mr Eddie Edmonds, Principal Technician; Mr Rob Potter, Mr Ralph James and Mr Ron Clayton, Technicians; and other staff, for manufacturing components, and providing help and support in the development of the experimental rigs.

Thanks are also due to Mrs Doreen Corlett for her help in obtaining much of the information used for this work. Special thanks are due to my colleagues, Dr Chris Whitney, Dr Valentine Fontama, Mr Steve Ball for their friendship and worthwhile discussions. Many thanks are due to Mr Stephen Ball and Mr Roger Scholars for reading the early manuscript of my thesis with patience in their spare time.

I take great pleasure in dedicating this work to those who are closest to me and have endured these recent years with me; my wife, parents and professor Xiaoping Wu. I would like to express my deep gratitude to my father, mother and professor Xiaoping Wu who have offered overwhelming support all the time. I am indebted to my wife, Haiyan, for support and understanding during this busy period of our lives, which was mostly during her own demanding postgraduate education. The thanks I offer here hardly seems enough.

I would like to acknowledge The Nottingham Trent University and the Higher Education Funding Council (HEFCE) for the financial support provided, and to Hallcrest Ltd. (Poole, UK) for providing the liquid crystal materials.

List of publications

1. Ashforth-Frost S, Dobbins B N, Jambunathan K, Wu X P and Ju X Y. 1993 A comparison of interrogation methods for particle Image Velocimetry. SPIE Vol. **2005** 478-489.

2. Jambunathan K, Ju X Y, Dobbins B N and Ashforth-Frost S 1995 An improved cross correlation technique for particle image velocimetry. Meas. Sci. Technol. 6 507-514.

3. Ashforth-Frost S, Ju X Y, Jambunathan K and Wu X 1996 Application of liquid crystals to particle image velocimetry. Proceeding of Optical Methods And Data Processing in Heat And Fluid Flow. 81-89. 1996.

4. Ju X Y, Jambunathan K and Ashforth-Frost S 1996 Effects of flow movements on video based PIV. To be submitted.

List of figures and tables

Nomenclature

Symbol	Meaning
A	area of an interrogation spot / the area of interest in the first image
A_0	outside of A
B	the area of interest in the second image
B_0	outside of B
C	number of tracer particles per unit volume
d	diameter of a particle
d_i	distance of image to lens
d_0	distance of object to lens
d_τ	diameter of a image particle
$d(t\text{-}\boldsymbol{X})$	displacement function
$E(x, y)$	local light amplitude
f	focus length of lens
$f(x, y)$, $g(x, y)$	interrogation spot in A and B
F, G	Fourier transformations of f and g
$F_w(\boldsymbol{s})$	in-plane loss-of-pairs function
$F_z(\Delta z)$	out-of-plane loss-of-pairs function
$F_\tau(\boldsymbol{s})$	normalized correlation of particle intensity
$g(\boldsymbol{x}, t)$	location of particle at time t
$G(\boldsymbol{s})$	Fourier transformation of $I(\boldsymbol{x})$
I_0	intensity of light sheet

I_k	discrete intensity of image
$I(x)$	intensity of image/pattern
M	magnification of the camera
N	interrogation spot size
N_I	image particle density
N_i	bi-linear interpolation coefficients
N_s	source particle density
N_{pair}	number of particle pairs contribute to the correlation peak
n	refractive index of liquid crystals
n_e	refractive index parallel to the direction of plane
n_0	refractive index right to the direction of plane
Pr	Prandtl number
p	pitch length of liquid crystals
$p(k)$	probability of finding k particle pairs
$p(x)$	sampling function
r_i	location of particle
Ra	Rayleigh number
Re	Reynolds number
$R(s)$	correlation coefficient
s	shift of image/pattern/function
St	Stokes number
t, Δt	time, time interval
T_0	temperature of liquid crystal particles
T_s	temperature of ambient fluid

$u(\boldsymbol{x}, t)$	local velocity at time t
U_p, U_F	Fourier transform of u_p, u_F
u_p, u_F	velocity of particle, fluid
$w(\boldsymbol{x})$	window function
$\boldsymbol{x}$, $\Delta\boldsymbol{x}$	location, displacement
x, y, z	Cartesian coordinates
Z, ΔZ	distance from light sheet to camera lens, thickness of the light sheet
$\delta(x)$	Dirac function
δ_i, δ_j	sub-pixel displacements
ε_i, ε_j	sub-pixel displacements
ζ	shear strain
η	amplitude function
θ	rotation angle / viewing angle
λ	wavelength of light
ρ_p ρ_F	densities of particle, fluid
$\tau(\boldsymbol{x})$	transmissivity of the photographic recording
$\tau_0(\boldsymbol{X})$	individual particle intensity
χ	added mass coefficient
ψ_d	ratio of displacement to interrogation spot size
ω	frequency of periodic motion
φ	reflection angle
α	phase angle
PIV	particle image velocimetry

PTV	particle tracking velocimetry
TLC	thermochromic liquid crystals
LC	liquid crystals
HSI	hue, saturation and intensity
RGB	red, green and blue

Subscripts:

1, 2	first and second exposure
i	individual particles in the image

Chapter 1 Introduction

The main aim of the work described in this thesis is to develop a technique of simultaneous measurement of velocity and temperature of a thermally induced flow using liquid crystal particles. This is achieved by applying the cross-correlation method of Particle Image Velocimetry (PIV) combined with liquid crystal thermography. Liquid crystals in encapsulated form can act as particles enabling velocity measurement using the Particle Image Velocimetry technique, and, due to their responsiveness to temperature, enable temperature to be quantitatively visualised at the same time. The technique provides a full-field and non-intrusive velocity and temperature measurement tool for further investigation of natural convection flows.

1.1 Background

Knowledge of instantaneous temperature and velocity fields in steady and transient heat transfer processes is often required for a basic understanding of heat transfer or convection phenomena. A situation is often encountered in which knowledge of instantaneous temperature and velocity fields in convective heat transfer processes is essential in human daily life, industry and engineering. The two fundamental parameters of velocity and temperature play an important part in the basic understanding of the processes.

Most techniques used for temperature measurement are point-wise techniques and become less effective in thermal fluid flows, especially in transient situations. Thermocouples have been used conventionally for temperature measurements. However, to obtain full field information, extensive thermocoupling is necessary, which is expensive, and the test fields are invariably intruded. Data collection can also be cumbersome, especially in transient applications. Researchers thus resort to techniques such as Schlieren, Mach-Zehnder and holographic interferometry, to visualise temperature fields. However, these cannot be used for direct temperature measurement of aqueous solutions, because the refractive index distributions to be measured vary with both temperature and concentration. Micro-encapsulated liquid crystal particles have been adopted to indicate temperature variations in various systems, particularly involving thermal convection. Liquid crystals change colour according to the environmental temperature, the change being reversible and repeatable as long as the crystals are not physically damaged (Cooper et al., 1975). During the past 20 years, liquid crystals have emerged as reliable temperature sensors, and have been applied in a number of situations to visualize the temperature distribution inside complex flow fields. During the same period, advancements in imaging techniques have provided a powerful new approach, where digital processing of liquid crystal images, yield full-field measurement of temperature distributions. The development of liquid crystal techniques for temperature measurement, coupled with image processing, has opened up some new avenues for heat convection and transfer research, and is leading to important changes in the way research is conducted and continued during the next decade (Moffat, 1990).

For velocity measurements, Laser Doppler Anemometry (LDA), as well as Hot-Wire Anemometry (HWA), have been used in the past to study detailed flow dynamic characteristics. When a single probe is used in HWA, only magnitudes of velocities are measured. LDA enables components of velocity to be measured non-intrusively with high accuracy and resolution at a single point. Because LDA and HWA are point-wise measurement techniques, spatial velocity information therefore requires scanning a single probe throughout the region of interest which, in an unsteady flow, temporally smooths out the instantaneous nature. Multiple point measurements must therefore be made to derive a velocity profile or field. If these measurements are not performed simultaneously, any information on coherent structures in the flow cannot be easily determined. The most advanced and widely used full field technique is particle image velocimetry (PIV) which utilises a light sheet to illuminate a plane within the flow of interest which is seeded with fine particles. The light scattered from neutrally buoyant particles within the flow, recorded onto a high resolution recording medium, gives randomly distributed particle images. Extraction of particle displacement data from PIV pictures is routine and most commonly achieved by local interrogation (Adrian, 1991).

1.2 Simultaneous measurement of velocity and temperature

Thermochromic liquid crystals selectively reflect different colours according to temperature when the temperature is within the event temperature range of the liquid crystal formulation and they are illuminated by a white light source. The relationship of temperature and colour can be calibrated by identifying the temperatures which corresponding to colours. If a thermal flow is seeded with suitable liquid crystal particles and illuminated with a white light sheet, the flow will display a colour pattern when viewed perpendicularly to the white light sheet. The velocity distribution within the light plane can be measured by extracting the movement of particles within the white light sheet.

The research described in the thesis is divided into two major parts: a) identification of the colour reflected from the liquid crystals, and, b) extraction of velocity from the particle images. The two parts are interrelated for the purpose of simultaneous measurement of velocity and temperature. Firstly, very fine liquid crystal particles are used to obtain the continuous colour distribution necessary for convenient temperature measurement, whilst for particle tracking, or statistical analysis for velocity extraction, significant individual particles, or characteristic patterns uniquely related to the particle groups, are required. Secondly, the traditional light source for PIV is a laser, because of the good light scattering property of the coherent light, but a white light source is required for colour display of the liquid crystal. Thirdly, high resolution photographic PIV gives a highly accurate velocity measurement, but colour and temperature calibration based on film could be cumbersome (Wilcox et al., 1985). The true colour image system is convenient for temperature measurement (Moffat, 1990), but provides low resolution images (usually 512 by 512 pixel per frame) for PIV. In this thesis, a colour image system has been developed built up for simultaneous measurement of velocity and temperature. The intensity distribution of particle images of the flow is used to extract velocity data, while the hue distribution of the image is used for temperature measurement. The hue value is related to the wavelengths of light reflected from the liquid crystals which can be converted to temperature data, using a calibrated relationship of temperature and colour. A white light source is required for illumination.

For quantitative temperature measurement using thermochromic liquid crystals, interpretation of colours displayed by the liquid crystals becomes a key issue. Three major methods were used by researchers - human observations, image processing based on intensity and true colour image processing. Image processing based on intensity avoids the inconsistency of human observation and provides a temperature contour corresponding to a particular colour, usually a yellow-green colour. True colour image processing provides full field temperature information, and is especially advantageous for transient cases. Colour identification depends on different colour spaces and the properties of liquid crystals, may reveal different colour and temperature relationships. For accurate temperature measurement, accurate colour-temperature calibration is essential.

Statistical methods are used for velocity extraction in particle image velocimetry. Young's fringes and auto-correlation methods have the advantage of measuring high speed flows but suffer from directional ambiguity. The cross-correlation method does not have this problem of directional ambiguity. Video based particle image velocimetry using cross-correlation algorithms can be used for velocity extraction. Because of the low resolution and low frame rate of the image facilities used, the non-uniform velocity distribution within the interrogation spot of PIV causes large errors of velocity measurement. The errors must be eliminated for accurate velocity measurement.

1.3 Aims

1). To develop techniques which allow simultaneous measurement of velocity and temperature of the flow field using thermo-sensitive liquid crystal particles.

2). To validate the simultaneous measurement technique.

3). To apply the technique to natural convection flows to provide accurate velocity and temperature data, increasing the understanding of the convection flow phenomena.

1.4 Objectives

In order to achieve the specified aims in this thesis, the following objectives are identified:

1). Develop a colour image processing system incorporating a CCD camera, an image frame grabber and a personal computer in order to acquire the colour particle images for further measurements of velocity and temperature.

2). Theoretically investigate the side effects caused by low resolution due to using direct digital images for PIV, particularly investigate the errors caused by the non-uniform movements of fluid flow which are ignored by most researchers.

3). Carry out computer simulations of flow movements to investigate the effects of the image particle density, the interrogation spot size and the image particle size on the accuracy of video based PIV, at the same time investigate the errors caused by the non-uniform velocity movements.

4). Investigate a new method to improve the conventional cross-correlation method for video based particle image velocimetry, to provide more accurate velocity data.

5). To investigate the relationship between the surrounding temperature and the corresponding colour reflected by the liquid crystals. Find a reliable and accurate method of identifying colour, then convert the identified colour to corresponding temperature.

6). Resolve the problems of combination of the PIV technique with the liquid crystal technique to measure the velocity and temperature simultaneously. Apply the simultaneous measurement technique on natural convection flows. Estimate the experimental uncertainties of velocity and temperature measurements.

7). A menu driving package will be completed for the purpose of simultaneous measurement using particle image velocimetry combined with liquid crystals.

1.5 Outline of this thesis

In this chapter the general background of the velocity and temperature measurement is introduced. The aims and objectives of the research work described in this thesis have been specified in previous sections.

The relevant literature review is provided in Chapter 2. In this chapter a survey of the major aspects of temperature measurement using the thermochromic liquid crystals is presented. The special helical molecular structure of thermochromic liquid crystals enables their application to temperature measurement. Attention is paid to temperature measurement in fluids using liquid crystals and the techniques of identifying colours. A review of PIV is provided in the same chapter. Different techniques of extraction of velocity from the particle images are surveyed. Optimal analysis is introduced. The video based PIV is focused upon since this approach is easier to combining with the liquid crystal temperature measurement than other techniques.

In Chapter 3, the theory of PIV is presented and the major sources which cause the bias of the correlation peak are investigated. The theory provides a guideline for PIV investigations.

The side effects of low resolution due to direct use of image frame (512 x 512 pixel) are discussed in Chapter 4. Simulations are carried out to investigate the effects of image particle density, interrogation spot size and image particle size. Evidence is provided that the accuracy of video based PIV is largely affected by local non-uniformities.

In chapter 5, an improved cross-correlation method is proposed to deduce the effects of local non-uniformity. Details of the implementation of the method are presented. Results prove that the improved method provides more accurate velocity data than the conventional cross-correlation method.

To enable temperature measurement, colour identification becomes a key issue and is discussed in Chapter 6. The colour theories are studied and different colour spaces are presented. The relationship between temperature and the corresponding colour displayed by the liquid crystal particles are studied. Finally, suitable colour representation is chosen. The effect of viewing angle is investigated.

Combination of PIV with the liquid crystal temperature measurement is achieved in Chapter 7. Two natural convection flows are investigated, using the techniques developed, to provide the velocity and temperature simultaneously. Experimental uncertainties are estimated and presented.

Finally in chapter 8, the summary of outcomes are concluded and recommendations for further research works are proposed.

Chapter 2 Literature review

A review of literature on liquid crystals is given in the first part of the chapter. The unique helical structure of the Thermochromic Liquid Crystals (TLC) enables their application to temperature measurement. The colour displayed by liquid crystals in encapsulated form is determined mainly by their environmental temperature. The techniques of measuring temperature from colour patterns displayed by liquid crystals are surveyed. A literature review of particle image velocimetry is provided in the second part. The techniques of extraction of velocity data from particle images are focused upon. Finally, the combined technique of PIV with liquid crystal thermography is introduced.

2.1 Liquid Crystals

Liquid crystals have unique molecular structures, with physical properties intermediate between liquid and solid. Thermochromic liquid crystals have a unique helical structure that can selectively reflect the wavelength of incident white light. When the reflected wavelength is in the range of the visible band (300nm - 700nm), the liquid crystals display colours. Their helical structure changes according to the surrounding temperature causing the display of different colours. The behaviour of liquid crystals is initially applied on non-destructive tests, then frequently applied to temperature visualisation and measurement, and also in heat transfer studies.

The key to temperature measurement using liquid crystals is the colour hue. Several ideas were proposed to identify the hue that is related to the wavelength of the light.

2.1.1 Thermochromic liquid crystals

Liquid crystals have mobility and, like liquids, will take up the shape of their containers. Liquid crystals have the optical properties of solids. The liquid crystalline state has more order in the arrangement of its molecules than the liquid state, but less than the three-dimensional structure of the solid state. Reinitzer, 1888 (see Reinitzer, 1989), an Austrian biologist, observed that certain organic compounds appeared to possess two melting points, an initial melting point that turned the solid phase to a cloudy liquid and a second melting point at which the cloudy liquid turned clear. Further research revealed that an intermediate phase, or "mesophase", did indeed exist between the pure solid phase and pure liquid phase of some organic compounds. Their structures are such that they exhibit solid like behaviour, yet their internal forces are not strong enough to prevent flow, hence the name "liquid crystals". Since Reinitzer's original work, a great deal of research concerning the structure of liquid crystals has been carried out. Excellent papers on the molecular structures of liquid crystals have been published by Fergason(1964), Fergason and Brown(1968), Castellano and Brown (1973), Brown (1973a, 1973 b) and McDonnell (1987).

Liquid crystals are conventionally classified into one of three categories: smectic, nematic or cholesteric, as determined by the molecular structure of the liquid crystal. Because of their unique molecular structures, liquid crystals have several unusual properties which are:

(1) optical activity in the spontaneously twisted nematic liquid crystal; (2) sensitivity of cholesteric liquid crystals to change of temperature, which results in colour change; and (3) formation of monocrystals with application of a magnetic field or an electric field.

A variety of externally applied fields including electrical, magnetic, shear, pressure, and thermal fields have been found to produce a change in the optical properties of liquid crystals. Although a host of applications have, and more than likely will, continue to be found for the nematic and smectic type crystals (Brown 1973, Castellano and Brown 1973, Beck 1986), of immediate concern in the investigation in this thesis is the response of cholesteric liquid crystals to thermal field, and the use of this response to obtain both qualitative and quantitative temperature information.

The molecular structure of cholesteric liquid crystals is characteristic of a large number of compounds that contain cholesterol. Cholesterol by itself does not have a liquid-crystal phase. The molecules in cholesteric liquid crystals are arranged in layers. Within each layer however, the parallel alignment of molecules is more reminiscent of the nematic phase. The molecular layers in a cholesteric substance are very thin, with the longitudinal axes of the molecules parallel to the plane of the layers. Because of the peculiar shape of the cholesterol molecules, the direction of the longitudinal axes of the molecules in each layer is displaced slightly from the corresponding direction in the adjacent layers; the overall displacement traces out a helical path. It is this helical structure, which changes according to the surrounding temperature, that gives the cholesteric phase its characteristic iridescent colour when it is illuminated by a white light (Fergason 1964, McDonnell 1987). The particular combination of colour depends on the material, the temperature and the angle of the incident beam. The cholesteric liquid crystals will progressively exhibit all the colours of the visible spectrum as it is heated through the event temperature range (Cooper et al. 1975, Moffat 1990). Both the width of the event temperature range and its placement on the temperature scale can be controlled by selecting the appropriate cholesteric esters and the proportions used in a given formulation. At present, liquid crystals are commercially available with event temperatures ranging from a few degrees below zero to several hundred degrees Celsius. Liquid crystals can be obtained with event temperature spans as small as 0.5°C to as large as 50°C (Cooper et al. 1975, Moffat 1990). The phenomenon is reversible, repeatable and, with proper care, colour can be accurately calibrated with temperature. Liquid crystals with colour band-widths of 5°C or less will be called "narrow-band" materials, while those whose band-widths exceed 5°C will be called "wide-band" (Moffat 1990).

2.1.2 Encapsulated liquid crystals

The molecular structure of a cholesteric liquid-crystal substance is very delicately balanced and can be easily upset. Thus any small disturbance that interferes with the weak forces can produce marked changes in colour. TLCs were first used in wind tunnel experiments by Klein (1968) and Klein and Margozzi (1969), primarily to evaluate the feasibility of their use in determining the location of laminar and turbulent boundary layer transitions on aircraft models. The pure liquid crystals were applied directly to the model surface. Although Klein was able to obtain qualitative information using the liquid crystal technique, he was unsuccessful in attempts to obtain accurate quantitative data due to the adverse effects that surface contamination, ultraviolet light and flow induced shear stress produced on the pure liquid crystals (Ogden and Hendricks 1984).

McElderry (1970), in an investigation similar in principle to the one conducted by Klein, used encapsulated cholesteric liquid crystals as a means of determining boundary layer transition on a flat plate placed in a supersonic air stream. McElderry found that the encapsulated liquid crystals produced colour displays that were not affected by the adverse sensitivity to shear and contamination that Klein had experienced with the pure liquid crystals.

For temperature visualisation in fluids, pure liquid crystals display brighter colours than encapsulated liquid crystals. Pure liquid crystals were used by Hiller et al. (1989) for bright colour patterns. They dissolved pure materials in ether and sprayed the mixture into the air above a free-surface of glycerol. The ether evaporated in mid-air, leaving small drops of liquid crystal material that fell into the glycerol forming an "almost mono-dispersed" suspension of particles approximately 50 mm in diameter.

Many of the problems associated with the use of pure cholesteric liquid crystals have either been eliminated or greatly reduced through an encapsulating process. The encapsulated liquid crystals are coated with gelatine in a polyvinyl alcohol binder. This coating results in the formation of small spheroids with typical diameters of the order of 20-200 microns. In addition to extending the life of the liquid crystals to as long as several years, by protecting the raw crystals from the damaging effects of ultraviolet light and atmospheric contaminants, the encapsulation procedure also greatly reduces the variation of colour due to viewing angle (McElderry 1970). Further, unlike pure liquid crystals, the encapsulated liquid crystals are relatively insensitive to the effects of normal and shearing forces. The time for liquid crystals to change its colour for responsing to its surrounding temperature is called the temperature response time. The temperature response time of encapsulated liquid crystals is in the order of 0.1 second (Dabiri and Gharib 1990, Platzer 1992).

2.1.3 Temperature measurement using TLCs

TLCs have been employed in a number of interesting applications over the past thirty years. The majority of uses have involved qualitative and quantitative interpretation of the temperature fields displayed so colourfully by the liquid crystals. The applications of thermochromic liquid crystals on solid surface for temperature measurement or heat transfer studies have been reviewed by Cooper et al. (1975), Simonich and Moffat (1984), Moffat (1990) and Ashforth-Frost (1996).

For temperature visualisation and measurement in fluids, it is important that the sensors indicating temperature changes do not alter the flow structure when placed in the flow and must therefore be quite small. Cholesteric liquid crystals used as temperature sensors for applications to temperature visualisation in fluids, conveniently satisfy these requirements. By mixing the experimental fluid with thermochromic liquid crystal particles, the temperature field can be viewed while the fluid is illuminated by a white light sheet so long as the temperature is within the temperature range of the liquid crystals.

Encapsulated liquid crystals are fragile and are easily damaged (Ashforth-Frost and Jambunathan 1993), thus limiting their application. Tanaka (1988) and Tanaka and Furuta (1989) used the technique for temperature visualisation in thermal storage tanks. The liquid crystals used in the experiment ceased to show reactions after one week, because the encapsulated liquid crystal particles were physically damaged by a water circulation pump. Rhee et al. (1984, 1986) used a thermally conductive copper belt for lid-driven cavity flow avoiding to destruction of the liquid crystal particles. Dabiri and Gharib (1991) used a piston tube where the fluid was pushed into a water tank, instead of using a pump. More research work was carried out on natural convection flows (Akino et al. 1986, Bergman and Ungan 1988, Nishimura et al. 1990, 1992, Ota et al. 1991, Dzodzo 1993, Wozniak and Wozniak 1993). Nishimura et al. (1992) used two narrow band liquid crystals to represent two different temperature ranges which can be made simply by physically mixing liquid crystals of the desired temperature ranges.

Temperature field visualisation using TLCs yields only qualitative results; hot and cold regions are observed without regard to precise temperature levels. Instead of qualitatively visualising temperature, quantitative measurement of temperature was carried out in several experimental studies (Hiller and Kowalewski 1987, Kimura et al. 1990, Dabiri and Gharib 1991, Ozawa et al. 1992, Braun et al. 1993 and Dzodzo et al. 1994). Quantitative temperature measurement is achieved by measuring colour. Similar colour measurement methods were used in both solid surface and in fluid tests. The key to TLCs temperature measurement is to interpret colour and to formulate a relationship between colour and temperature. There are three broad classes of colour identification techniques - human observation, intensity based image processing and true colour image processing utilising different colour spaces (Kueppers 1980, Wyszecki and Stiles 1982).

2.1.3.1 Human Observation

Human observers can interpret liquid crystal images by direct visual inspection of the system during operation, or by visual inspection of colour photographs or tape recorded video images, usually using narrow-band liquid crystals. Calibrations for such use are generally limited to determination of a single temperature associated with a particular colour; often the yellow-green colour near the centre of the colour-play band, because the human eye is most sensitive to the yellow-green light at which maximum intensity occurs (Ashforth-Frost 1996). Cooper et al. (1975) used 8 different types of narrow-band liquid crystals to determine qualitatively, and quantitatively, temperature changes on solid surfaces (cylinder in cross-flow) subjected to forced convection environments. Ichimiya et al. (1988) described eight different colours which depend on temperature.

For narrow-band liquid crystals, accurate temperature measurement for a particular colour (usually yellow-green) could be achieved (Cooper 1975, Moffat 1990), but Cooper (1975) stressed that the observer who calibrated the liquid crystals also made all colour determinations during the actual experimental runs. Akino et al. (1989b) pointed out that the errors may be caused by individual differences and non-consistency of human sense.

2.1.3.2 Monochromatic image processing

Because errors may be caused by individual difference and non-consistency of human eyes, objective methods to identify colours are required. Kasagi et al. (1981) and Simonich and Moffat (1982) illuminated liquid crystals with a monochromatic light source in order to obtain an isothermal contour which corresponded to a certain temperature. Akino et al. (1989) used 18 optical filters which have very narrow wavelength transmittance bands to obtain monochromatic images corresponding to the characteristic temperature of each filter. The temperature field was obtained in isothermal lines. Metzger et al. (1989) and Metzger and Kim (1993) developed an experimental technique for the measurement of local heat transfer coefficients on rotating surfaces. This colour measurement procedure is fundamentally similar to that of Akino's narrow band filter method. The temperature of the surface is determined using an analytic filter (green) which detects colour only in this monochromic colour. Hiller et al. (1989) quantitatively measured the temperature in thermal convection flow with the help of a series of optical interference filters. Even though a series of filters can be used to provide isothermal lines of a steady temperature field, this method has its problem in dealing with transient cases. Treuner (1995) used Hiller's temperature calibration curve to study a thermocapillary flow.

Utilising a monochromic light source to illuminate the liquid crystals, or utilising optical filters, are both intended to obtain the monochromic image picture in order to extract the temperature data from the isothermal contours. This technique provides an objective method to identify a colour. For transient cases, it is difficult to use multiple filters or several monochromic light sources in order to obtain different isothermal contours.

2.1.3.3 True colour image processing

Human observers and intensity-based image processors generally prefer narrow-band liquid crystal materials. It is difficult to provide full-field quantitative information, especially in transient cases, using these interpretation techniques.

Relying on colour films, Wilcox et al. (1985) utilized digitised colour photographs and used three interference filters to separate the primaries in an effort to remove the human factor. By doing so, he created the additional work of calibrating each roll of film, since each roll was slightly different from the other used. Furthermore, once the film was calibrated, three separate digitisation's of the same image, each filtered through a different interference filter, were required to calibrate the liquid crystals. Using a video, Akino et al. (1989b) used a multiple regression of three colour components, obtained by changing three optical filters for the video camera, to measure temperature, and a hue based method was proposed in the same paper.

After 1989, a true image processing board played an important role in temperature measurements using TLCs. True-colour image processors, which work with true colour-temperature descriptions in their calibration, work well with wide-band materials. Hollingsworth et al. (1989) applied true colour image processing to the measurement of the heat transfer coefficients. The colour measurement method used a chromaticity coordinate system that is common to the standard colour video practice. Camci et al. (1991) proposed a new hue computer based processing technique that would be primarily responsible for the determination of the temperatures. The authors reported in detail their calibration procedures and the effects of light intensity and angle of view on the accuracy of the hue determination as a function of temperature. The hue of HSI (hue, saturation and intensity) colour space used for interpretation of colour for temperature measurement has become popular in recent years because of the efficiency of the method. Dabiri and Gharib (1990, 1991) used a 3-chip video colour camera to capture the flow image onto a videotape. The temperature flow field was obtained through a calibration scheme in HSI rather than RGB (red, green and blue) colour space. A similar scheme was used by Ozawa et al. (1992), Braun et al. (1993) and Dzodzo et al. (1994). Even though they all used hue values in HSI space their HSI mathematical formulations are different.

2.2 Particle Image Velocimetry (PIV)

Full velocity measurement can be achieved by analysing the seeded particles suspended in a flow. It involves inferring the velocity of the fluid at a particular point and time from measurements of the motion of small particles mixed with the fluid. This avoids the introduction of probes into the fluid that is an important advantage of the method. There are two major steps to the technique: obtaining the particle images/photographs and extracting the velocity data from the particle images. Particle tracking method and statistical analysis are frequently used, depending on the characteristic properties of images/photographs. A survey of the extraction methods is presented below. Optimal parameter analysis for PIV and post-processing techniques are reviewed.

Particle Image Velocimetry (PIV) is a non-intrusive technique for full field flow measurement. It has been developed over the past twenty years in order to make it a useful and usable tool for fluid velocity measurements by combining flow visualisation with quantitative measurements. PIV has been used in routine research applications and is now being applied in industrial laboratories. With its ability to yield full flow field maps from instantaneous pictures, PIV represents a major step forward in experimental fluid dynamics.

Previous velocity measurements at single points are traditionally made using the techniques of laser Doppler velocimetry (Durst et al. 1976, Adrian and Yao 1983, and Cenedese et al. 1994) and Hot Wire anemometry (Hussein 1995). Flow patterns are studied extensively using the technique of flow visualisation such as dye tracer, Schlieren photography, hydrogen bubble wires and smoke wires. Flow visualisation methods provide valuable information about the behaviour of the entire flow field, but they are not usually intended to provide quantitative velocity data. In single-phase flow the need for multi-point measurements is not acute when the flow is steady, because the vector flow field can be found from a series of single-point measurements. However, when the flow is unsteady, full field measurement techniques are capable of creating instantaneous pictures of the flow field that are unavailable from single-point measurements. Quantitative multi-point measurements can be performed using modified single-point probes. These approaches are limited by cost, or by blockage of the flow by physical probes (Adrian 1986b). Efforts to combine the accuracy of single-point methods with the full field nature of flow visualisation techniques have been undertaken by numerous research groups during the last twenty years. PIV is the achievement of twenty years of effort and is now well established in providing the full field velocity information.

The roots of PIV lie in speckle velocimetry (Barker and Fourney 1977, Simpkins and Dudderar 1978). Laser Speckle Velocimetry, Particle Image Velocimetry and Particle Tracking Velocimetry fall into the category of Pulsed Light Velocimetry (PLV) (Adrian 1991). In principle, the techniques record optical images of flow tracers and deduce velocity from the displacements of the flow tracers during short time intervals. Consider a flow that has been seeded with small tracer particles. These particles are supposed to accurately follow the motions of the fluid. A light sheet is passed through a seeded flow field, illuminating the particles at time, t. At a known time later, $t+\Delta t$, a second sheet of light is sent through the same plane in the flow field. The images of the particles from both light sheets are stored on a recording medium. Measurement of the separation between two images of the same particle throughout the field of view can provide the local fluid velocities from:

$$u(\mathbf{x}, t) = \Delta\mathbf{x}(t) / \Delta t \tag{2.1}$$

where x is the particle location and, Δx is the particle displacement at time t over a time interval, Δt. When the density of seeding particles is low, multiple images of particles with a constant time interval can be recorded instead of double images for velocity analysis. In this case, the signal to noise ratio of the multiple images is better than that of double images for velocity extraction. Reviews of the PIV techniques can be found in articles by Adrian and Yao (1983), Adrian (1986b), Dudderar et al. (1988), Kobayashi (1988), Adrian (1989), Adrian (1991), Buchhave (1992), Cenedeses and Paglialunga(1990), Gray and Greated (1995), which also provide a background of theoretical and experimental analysis for the techniques.

Adrian and Yao(1983) and Adrian (1984) described the appearance and information content of the recorded image by two dimensionless numbers, the source density (N_s) and the image density (N_I).

$$\begin{aligned} N_s &= C\Delta Z_0 \frac{\pi}{4}\frac{d_t^{\,2}}{M^2} \\ N_I &= \frac{C}{M^2} A\Delta Z_0 \end{aligned} \tag{2.2}$$

where C is the number of tracer particles per unit volume, d_τ the image particle diameter, ΔZ_0 the thickness of the illumination light sheet, M magnification of the camera and A the area of the interrogation spot. The source density means the mean number of tracer particles lying within one image particle intensity distribution, indicating that the image consists of individual image particles (i.e.N_s << 1), or that image particles overlap and - for a coherent illumination - interference of light comes into play (i.e. N_s >> 1). The number of N_I, the image density, means the mean number of effective image particles lying in one interrogation window or spot in the image plane, and represents the number of image particles within a particular area around a point at which we would like to determine the flow velocity. This area is referred to as the interrogation area. Adrian and Yao (1983), Adrian (1991) classified the technique into several categories, such as Particle Tracking Velocimetry (PTV N_s <<1, N_I <<1), Laser Speckle Velocimetry (LSV N_s >> 1, N_I >>1) and Particle Image Velocimetry (PIV N_s <<1, N_I >>1), according to the source density and image density of tracers. In this survey, the techniques of extracting velocity data from the particle images are established. Attempts to improve the limits of resolution, frame speed of the video based PIV are reviewed.

The light source for PIV illumination is usually a laser. Non-coherent light was also tried. Cloud et al. (1980) attempted to measure fluid velocity using non-coherent light speckle photography, but the quality of particle images using a non-coherent light source was poor. Bernal and Kwon (1988) used the method to measure surface flow velocity.

2.2.1 Individual particle tracking

Tracking techniques are used to observe individual image particles (N_s <<1), while the average distance between distinct image particles is much larger than the mean displacement and the expected number of image particles in the interrogation area is low (N_I << 1). Because of the large distance between distinct image particles, with respect to the mean displacement, it is reasonably easy to identify image particle pairs that correspond to the same tracer particle in the flow, and thus obtain the local flow velocity.

2.2.1.1 Particle path-lines

After long time exposure of the particles, the particles' path-lines are recorded. By tracking particle path-lines, their lengths and directions are measured. The path-lines could be tracked by human observation (Brüker and Althaus 1992), or using a threshold method for good contrast images (Kobayashi and Saga 1988), or utilising various masks/templates (Gharib et al. 1985, Wu et al. 1991, Ciccone et al. 1989, 1990). Human observation is tedious for large quantity data. Automatic tracking methods are thus favoured by researchers. The method of tracking particles' path-lines has its disadvantages. When the flow movements are three dimensional, the particles will follow the flow and move in and out the light plane, resulting in errors of measuring the lengths of the particles' path-lines.

2.2.1.2 Tracking particle pairs

By recording multiple exposures of particle images in single or multiple frames, the individual particle pairs can be determined if N_s <<1, N_I << 1. Because the displacement is expected to be much smaller compared to the distance between neighbouring particles, most of the particles in the first exposed image can be related automatically to their closest neighbour in the second exposed image (Nishino et 1988, Ramer and Shaffer 1992).

Marko and Rimai (1985) tracked the end points of particle pairs using a cursor and Braun and Canacci (1992) using human observation.

Considering the particle trajectory is in a straight line in a short time period, a track is based on the minimum variance of length, angle, average size and average grey level of all possible tracks from starting particles (Cenedese and Paglialunga 1989, Hassan et al. 1990, Cenedese and Romano 1991). Seeley et al. (1991) tracked particles through at least four sequential images by finding the particle spots that have the least deviation from a constant curvature line. Wernet (1991) illuminated the particle flow in different intensities for different exposure, then tracked particle pairs. Wernet and Pline (1991) applied the technique to investigate surface tension driven convection. Ushijima and Tanaka (1994) used a second order regression curve fit to track the centres of points located on the multiple frames.

The cross-correlation methods, especially binary cross-correlation methods have been proposed to individually track particle pairs by Uemura et (1989, 1993), Kobayashi and Saga (1988), Seeley et al. (1988), Hassan et al. (1993) and Reese and Fan (1994).

Humphreys Jr. (1991) proposed a histogram based technique for extraction of velocity vectors from double-pulsed particle images. The technique relied on the analysis of magnitude and direction histograms constructed from all possible vector pairings. Keane and Adrian (1995) combined particle image velocimetry and particle tracking velocimetry together, investigating the average velocity by PIV and further tracking individual particles inside the interrogation window. These techniques combine tracking with statistical techniques.

2.2.1.3 Direction determination

There is a direction ambiguity for the single frame particle tracking method. Direction is determined either by observation of the flow, or by the difference between the intensities of the starting and finishing points (Gharib et al. 1985, Wernet 1991 and Wu et al. 1991), or by neighbouring vectors Wu et al. (1991) and Murata (1993).

The tracking method investigates individual particle displacements in fluids, providing velocity data with the highest resolution among the PLV techniques. However, since the image density is low, the velocity cannot be determined at any arbitrary position, but only at a position where a tracer particle happens to be present. The result is a random sampling of the flow field. The sampling is, in general, not optimal.

2.2.2 Statistical analysis

For LSV and PIV, the interrogation spot always contains a sufficient number of image particles to determine the (local average) flow velocity in any position because $N_I >> 1$. However, it is no longer possible to identify individual image particle pairs unambiguously. Therefore statistical methods have to be used to determine the most probable displacement. Young's fringes and auto-correlation methods have an ambiguity in determining the direction of velocity vectors. The cross-correlation method has a higher signal to noise ratio than Young's fringes and auto-correlation methods, and has the advantage of avoiding the direction ambiguity and reconstructing images to improve accuracy.

2.2.2.1 Young's fringes and Auto-correlation methods

Barker and Fourney (1977) first extended the laser speckle photography and interferometry techniques to measure surface displacement of a solid surface to measure fluid velocities. The detailed Young's fringes technique can be found in articles by Keane and Adrian (1989, 1990), Greated et al. (1992) and Farrel (1993).

Normally, Young's fringes method is used for double-exposed or multiple-exposed high image density photographs. After the film, which recorded the exposed images, is developed, it is illuminated by a laser light beam (diameter around 1mm). For a group of particles that have undergone the same translation between two exposures, illumination of the film will generate a Franhofer diffraction pattern corresponding to the position of the particle pairs on the film. Franhofer diffraction produces the Fourier transform of the light amplitudes at a pin hole. Typically the Fraunhofer diffraction pattern in the far field is a set of Young's fringes modulated by a low frequency diffraction halo, whose spacing is inversely proportional to the pair spacing and whose orientation is perpendicular to the displacement vector (Farrell and Goetsch 1989) when a lens is used behind the film, it brings the fringe pattern to its focus plane,

$$E(x_0,y_0)=\frac{\exp(jkz)}{jkz}\exp[\frac{jk}{2z}(x_0^2+y_0^2)]\int_{-\infty}^{\infty}\int_{-\infty}^{\infty}E(x_1,y_1)$$
$$\cdot\exp[\frac{-j2\pi}{\lambda z}(x_0x_1+y_0y_1)]\,dx_1dy_1 \quad when\ \ z\ll\frac{k(x_1^2+y_1^2)}{2} \tag{2.3}$$

where E is the local light amplitude, k is a wave number, λ is the wavelength of the illumination light, x_0 and y_0 are coordinates in the fringe plane, x_1 and y_1 are coordinates in the film plane and z is the axial coordinate between the pupil and the image plane, see Figure 2.1. Note that apart from a multiplicative factor, Fraunhofer diffraction produces the Fourier transform of the light amplitude E at the film plane.

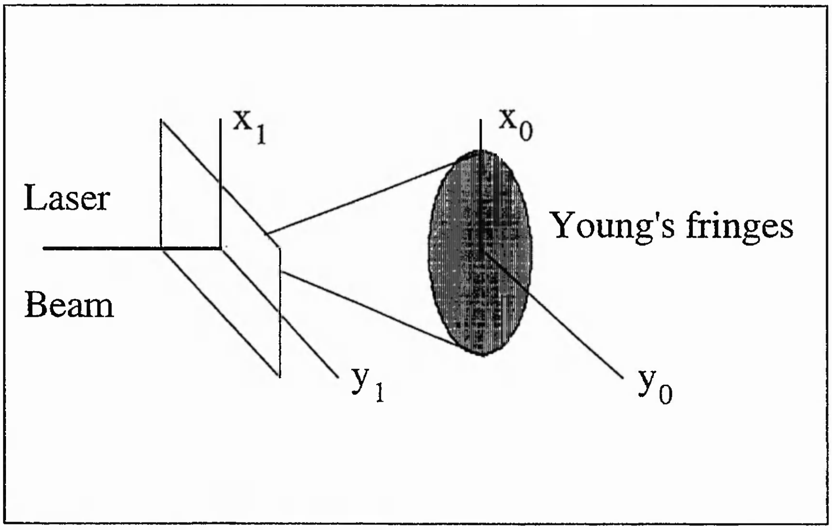

Figure 2.1 Young's fringes method

Direct analysis of the Young's fringes spacing and orientation results in velocity vectors (Brandt and Merzkicth 1994). Meynart (1982, 1983) digitised the Young's fringes into a frame grabber for analysis. Erbeck (1985) and Reynolds et al. (1985) described an automatic approach to analysing Young's fringes including searching for data on the photographic record, recognition of fringe patterns of sufficient quality, and finally analysis of these fringes. An auto-correlation function was calculated from the Young's pattern for extracting displacement and orientation of the fringes. To improve the fringe quality, optical and numerical methods were proposed using a partially coherent light beam for interrogation (Ferrari 1983), placing a compensation plate before the fringes and a rotating ground-glass for fringes screen (Erbeck 1985), or numerically subtracting or dividing with a hole function (Shapiro 1993).

Another frequently used technique for analysis of the Young's fringes is numerically taking a two dimensional Fourier Transform of the digitised Young's fringe data (Adrian and Yao 1983, Adrian 1986b). In fact, there is one optical Fourier Transform and one numerical Fourier Transform of the particle pattern. Liu et al. (1991), McCluskey et al. (1993), Shepherd and Fontaine (1993) applied the technique. The method of taking two optical Fourier transforms of the particle images was applied by using a Spacial Light Modulator (SLM) (Farrell and Goetsch 1989, Kompenhans et al. 1989, Moraitis and Riethmuller 1989, and Nakamura 1994). One side of the SLM is illuminated with the Young's fringe pattern and the other side is then illuminated coherently to achieve the second transformation.

The intensity of the fringe pattern is

$$I_f(\mathbf{x}_f) = |E(\mathbf{x}_f)|^2 = E(x_f) \cdot E^*(x_f) \tag{2.4}$$

It can be digitised by an electronic camera and analysed by two-dimensional Fourier transformation, e.g.

$$G(\mathbf{s}) = \frac{1}{4\pi}\int \exp(\frac{2\pi\cdot\mathbf{i}}{\lambda\cdot f}\mathbf{s}\ \mathbf{x}_f) I_f(\mathbf{x}_f) d\mathbf{x}_f \tag{2.5}$$

where *s* is the variable in the numerically computed Fourier transform plane. By the convolution theorem (Gonzalez and Wintz 1987), *G(s)* is equal to the convolution of the Fourier transforms:

$$G(\mathrm{s}) = \frac{f^2\lambda^2}{4\pi^2}\int E(\mathbf{X}) E^*(\mathbf{X} - \mathrm{s}) d\mathbf{X}. \tag{2.6}$$

This convolution is the auto-correlation of the transmitted light amplitude ***E(X)***. Repeating interrogation for each interesting position of the film results in the whole field velocity distribution. The film is usually mounted on a transfer mechanism. The processing speed is limited by the mechanism which transfers the interrogation from the current one to the next one (Greated et al. 1992).

Instead of interrogating particle images using a laser beam, the local images may be digitised and numerically analysed directly to obtain their orientation and spacing by detecting the peaks of an auto-correlation function. The ability to undertake these image processing tasks is enhanced through the use of high speed digital image processing hardware. Two numerical fast Fourier transforms (FFTs) were calculated from the local particle images to generate one self-correlation peak and two displacement peaks related to local mean velocity vectors (Reuss et al. 1989, Keane and Adrian 1989, 1990, Cenedese and Pagliaunga 1990, Landreth and Adrian 1990, Lee et al. 1993 and Molezzi and Dutton 1993).

When the double-exposure or multi-exposure images of flow seeded with particles are recorded in a single frame, two exposures (sampled at time t and $t+\Delta t$) are recorded in a linear unsaturated photograph and the transmissivity of the photographic recording is additive:

$$\tau(\mathbf{X}) = \tau_1(\mathbf{X}) + \tau_2(\mathbf{X}) \tag{2.7}$$

When a photograph is interrogated by a sampling window, $w(X - X_I)$, centred at X_I, the transmitted intensity is

$$I(\mathbf{X}) = w(\mathbf{X} - \mathbf{X}_I)\tau(\mathbf{X}) \tag{2.8}$$

The spatial auto-correlation of $I(X)$ with separation s is approximated by the following spatial average estimator over an interrogation spot

$$\begin{aligned} R(\mathrm{s}) &= \int I(\mathbf{X})I(\mathbf{X} + \mathrm{s})d\mathbf{X} = \int w(\mathbf{X} - \mathbf{X}_I)(\tau_1(\mathbf{X}) + \tau_2(\mathbf{X})) \\ &\quad \cdot w(\mathbf{X} - \mathbf{X}_I + \mathrm{s})(\tau_1(\mathbf{X} + \mathrm{s}) + \tau_2(\mathbf{X} + \mathrm{s}))d\mathbf{X} \\ &= \int w(\mathbf{X} - \mathbf{X}_I)w(\mathbf{X} - \mathbf{X}_I + \mathrm{s})[\tau_1(\mathbf{X})\tau_1(\mathbf{X} + \mathrm{s}) + \tau_2(\mathbf{X}) \\ &\quad \cdot \tau_2(\mathbf{X}+\mathrm{s}) + \tau_1(\mathbf{X})\tau_2(\mathbf{X}+\mathrm{s}) + \tau_2(\mathbf{X})\tau_1(\mathbf{X}+\mathrm{s})]d\mathbf{X} \end{aligned} \tag{2.9}$$

The sum of the first and the second terms in the square brackets represents the sum of auto-correlation of first exposure image and the second exposure image with themselves (Figure

2.2). It will reach a maximum value when $s = 0$ and vanish when ½*s*½ is much greater than the diameter of particle, d_τ. It is independent of the velocity field. (Adrian and Yao 1983). The third term is the cross-correlation of the first exposure image and the second exposure image, which corresponds to the positive velocity. The last term is the cross-correlation of the second exposure image and the first exposure image, which corresponds to the negative velocity. When the photograph is recorded with multiple-exposed images, there will be more cross-correlation peaks which correspond to the correlation of the first and the third exposures, etc. The auto-correlation function cannot distinguish the sign of the velocity because the recording cannot distinguish the first exposure from the second exposure, which leads to direction ambiguity.

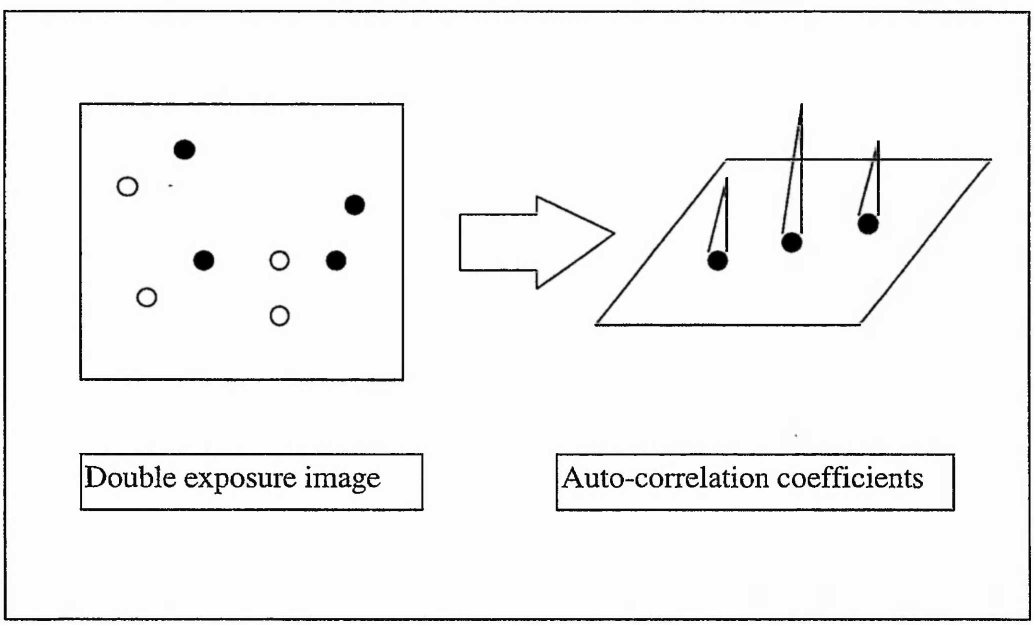

Figure 2.2 Auto-correlation method

There is a direction ambiguity inherent in Young's fringes and auto-correlation methods. To solve the direction ambiguity, Adrian (1986a), Grant et al. (1989), Lourenco (1993) and

Reuss (1993) used an image shifting technique. Lawson et al. (1994) used adaptive optics to improve the shift technique. Molezzi and Dutton (1993) used the shift technique in high-speed separated flows. Höker and Kompenhans (1989) managed to eliminate the direction ambiguity by checking the velocity vector field in the neighbourhood of each data point.

The minimum velocity is limited by the particle size. It is not possible for Young's fringes and Auto-correlation methods to measure the particle's displacement, which is less than one diameter of the particle size, because the signal of the cross-correlation will vanish in the self-correlation signal.

2.2.2.2 Cross-correlation method

As opposed to Young's fringes and auto-correlation methods, cross-correlation methods record double-exposed images in two separate frames using video camera or films using high speed cinematography. Goss et al. (1989) and Stucky et al. (1994) used a two-colour photography technique to record the double exposures in different colours then separated the double exposures into different frames for cross-correlation analysis. The cross-correlation method does not suffer from the problem of direction ambiguity because the images are recorded in different frames. It is easy to distinguish the first particle image and the second particle image. There is no limitation for minimum velocity measurement.

When the flow images are recorded in separated frames, the transmissivity of photographic recordings of the first and the second single exposure flow field are $\tau_1(\boldsymbol{x})$ at time t and $\tau_2(\boldsymbol{x})$

at time $t+\Delta t$, respectively. When the first frame image is sampled with a window function, $w(X-X_I)$, centred at X_I, the transmitted intensity is

$$I_1(\mathbf{X}) = w(\mathbf{X}-\mathbf{X}_I)\tau_1(\mathbf{X}) \tag{2.10}$$

and for the second frame image, the transmitted intensity is

$$I_2(\mathbf{X}) = w(\mathbf{X}-\mathbf{X}_I)\tau_2(\mathbf{X}) \tag{2.11}$$

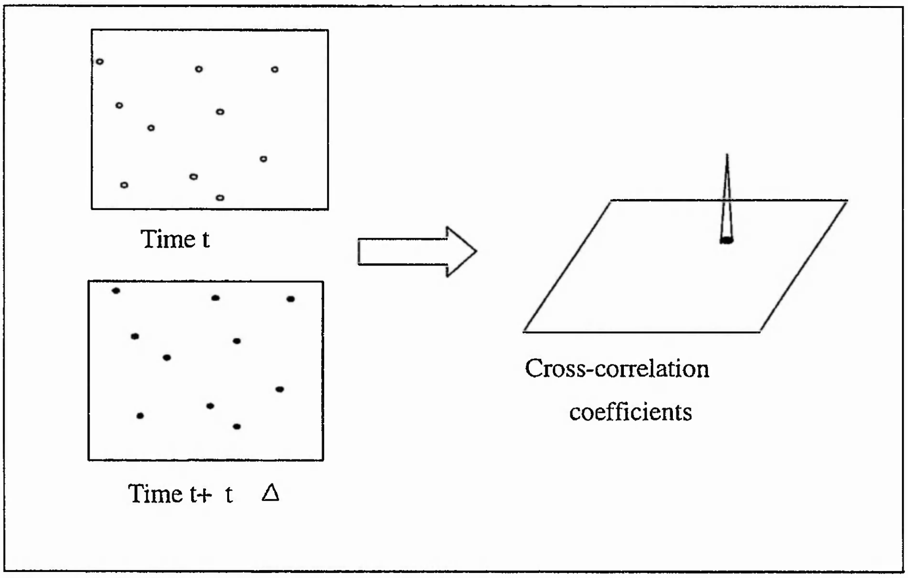

Figure 2.3 Cross-correlation method

In this case, the spacial cross-correlation coefficients $R(s)$ of I_1 and I_2 with separation vectors s

$$\begin{aligned} R(\mathbf{s}) &= \int I_1(\mathbf{X})I_2(\mathbf{X}+\mathbf{s})d\mathbf{X} \\ &= \int w(\mathbf{X}-\mathbf{X}_I)w(\mathbf{X}-\mathbf{X}_I+\mathbf{s})[\tau_1(\mathbf{X})\tau_2(\mathbf{X}+\mathbf{s})]d\mathbf{X} \end{aligned} \tag{2.12}$$

is used to determine the image displacement by locating the peak position of the cross-correlation (Yano 1983, Kimura and Takamori 1987, Yamamoto et al. 1988, 1989, Utami et al. 1991, Keane and Adrian 1992 and Willert and Gharib 1991, and Uemura et al. 1993, 1994), see Figure 2.3.

Willert and Gharib (1991) and Kemmerich and Rath (1994) calculated the local spatial cross-correlation between two sequential video recorded single-exposed particle images. Video based cross-correlation methods have development potential, although normally the time interval between exposures with video based cross-correlation methods is limited by the video frame rate - 25 frames per second and the resolution of each frame is 512´512 pixel with 8 bits grey levels. The frame rate limit can be overcome by utilising the odd and even fields of the video frames (Kobayashi and Saga 1988, Wernet 1991, Wernet and Pline 1991). Huang and Fielder (1994) reduced the time interval between successive exposures of video particle image velocimetry by means of external hardware synchronised with the video camera. These exposures with shorter time interval are recorded in separated video fields. A two camera system proposed by Hassan et al. (1993), Philip (1993) and Philip et al. (1994) achieved a fast frame rate of 100 to 320 ms per frame. Hassan et al. (1990) used a high resolution camera with 1024´1024 pixel and Wormell and Sopchak (1993) used a high resolution CCD camera (2048×2048) for high resolution velocity investigation. The high resolution image system combined with time interval control and the video based cross-correlation method has potential applications in the future. Conventional cross-correlation method has poor velocity measurements in areas with high velocity gradients. Huang et al.

(1993), Ashforth-Frost et al. (1993) proposed methods to eliminate the effects of velocity gradients. Jambunathan et al. (1995) proposed an improved cross-correlation method to suppress the effects of the local non-uniformity.

Young's fringes, auto-correlation and cross-correlation methods all interrogate velocity at a small local region. The interrogation is repeated at every interested position for full field velocity extraction, which is time consuming. Farrell (1992) and Huntley et al. (1993) proposed a simultaneous multiple points interrogation method. Meinhart et al. (1993) used parallel array processing technology incorporating the cross-correlation technique to achieve computational speeds to extract velocity data from PIV images. This technique required good hardware support.

Compared with the Young's fringes and auto-correlation method, the cross-correlation method has no problem of direction ambiguity. The signal to noise ratio is around two times higher than Young's and auto-correlation methods (Farrell 1993) because there are double the number of particles contributing to the noise background for the two methods than for the cross-correlation method. Further, the second image can be reconstructed for better velocity extraction.

2.2.3 Other methods

In order to speed up PIV extraction, digital filtering and rapid calculation algorithms have been proposed. Grousson and Mallick 1977, Meynart 1980, Grant and Qiu 1990 proposed a method which converts the particle images to whole field velocity pattern. Yao and Adrian (1984) used an orthogonal compression technique to measure two dimensional displacements. Ashforth-Frost et al. (1993) tried used XOR and subtraction methods to extract the velocity data from two sequential images. All these methods sacrificed accuracy of velocity measurement for rapid velocity information extraction.

Teo et al. (1991), Grant and Pan (1994) applied neural networks to particle image velocimetry. Carosone et al. (1995) used neural networks to recognize the overlapping image particles. Wernet (1993) used fuzzy logic to track particle pairs. Neural networks and fuzzy logic methods provide bright prospects for PIV although there are several obstacles to overcome in terms of speed and accuracy.

2.2.4 Analysis of optimal parameters

A number of parameters in pulsed light velocimetry affect the spatial resolution, accuracy and reliability of PIV, such as the interrogation spot size, the particle source density and image density and the seeded particle size, etc. Moraitis and Riethmuller (1988) theoretically analysed the performance of particle image displacement velocimetry (PIDV) experiments and pointed out that the success of a PIDV experiment cannot be absolutely guaranteed, unless parameters actually escaping from the control of the experimentalist are optimized. Usually, digital simulations were carried out for optimal parameter investigations (Grant et al. 1989, Guzennec and Kiritsis 1989, Keane and Adrian 1990, 1991 and 1992). Farrel (1993) made the particle images by drilling one to five small

(200mm) holes in a small region of an aluminum plate. Ashforth-Frost et al. (1993) and Jambunathan et al. (1995) used a black cardboard with randomly distributed white dots.

Kimura and Tanamoru (1987) used the cross-correlation method to obtain velocity vectors in a two-dimensional flow field and investigated the effects of the interrogation spot size for correlation. In the following year, Kimura investigated the effect of interrogation window size and rotation angle of particle image on the accuracy but did not arrive at a proper solution.

In fact, the interrogation spot size determines the resolution of the velocity measurement. The number of particles in the interrogation spot affects the accuracy and reliability of the velocity measurement. The accuracy increases as the number increases but there is a limit. Edwards (1988) mentioned that if there were three or more particles in the measurement region, the probability of making a false reading is very small. If there were three or more particles in a measurement region, the magnitude of the optical pattern from true velocity simply overwhelms the magnitude of the false vectors. Coupland et al. (1988) investigated the statistical variation of this signal to noise ratio appropriate to particle image velocimetry as a function of the seeding particle concentration. They indicated that when $1 < N_I < 7$ the expected signal to noise ratio increased monotonically but reaches a constant value when $N_I > 7$ for the Young's fringes method. Keane and Adrain (1992) pointed out that $N_I > 7$ for single exposure analysis or $N_I > 10$ for a double exposure analysis.

Bjorkquist (1991) pointed out that the optimum pixel resolution for PIV analysis strikes a balance between processing time and accuracy. He found an optimum resolution for analysis of a PIV photograph with 25mm diameter image particles and 1x1 mm^2 interrogation spot size. Image particle size has an effect on accuracy also. As the image particle size increases the errors decreases but less rapidly, tailing off for image particle diameters larger than 4 pixels, where little improvement in accuracy is achieved. Scherer and Bernal (1993) studied the resolution characteristics of Holographic Particle Image Velocimetry. They found $N_I = 3$ was best for their Holographic PIV. Guzennec and Kiritsis (1989, 1990) pointed out that when the particle overlapped the accuracy decreased as N_I increased, where N_I was between 20 and 150.

2.2.5 Effect of flow movements

Meynart (1985) theoretically investigated non-Gaussian statistics for speckle noise of Young's fringes. He pointed out that the strains resulting from the velocity gradients are usually much larger in fluid flows than for solid objects. As a result, to increase the spatial resolution, the photograph has to be illuminated with a narrow beam.

Adrian and Yao (1983), and Adrian (1986c) pointed out that the local non-uniformity led to the velocity measurement being biased to the lower velocity in the interrogation region, because the lower velocity particles stayed in the region and the larger velocity particles moved outside the region.

Grant et al. (1989) found that the large scale turbulence present in wake flow influenced the quality of the Young's fringes. Grant and Owens (1990) discussed the confidence attached to the estimates of mean velocity and turbulence intensity obtained by PIV measurements, pointing out that there was a high correlation between the local turbulence level and the error in measurement of mean velocity.

The conventional cross-correlation method provides poor velocity measurements where there are high velocity gradients. Huang (1993a) investigated the effects of the velocity gradients and in-plane motions by supposing that the particles were uniformly distributed. Huang (1993b), Ashforth-Frost et al. (1993) proposed a method to suppress the effects of the velocity gradients by reconstructing the interrogation pattern considering the velocity gradients. Jambunathan et al. (1995) improved the cross correlation method to decrease the effects of non-uniform velocity by reconstructing the second image considering the effects of flow. Three peak-finding methods were investigated. Tokumaru and Mimotakis (1995) estimated the displacement using a Taylor series expansion and used a least squares technique to determine velocity and velocity gradients within a correlation volume.

2.2.6 Post processing

After the velocity vectors are extracted from the particle images, post processing of the vectors is necessary because experimentalists cannot guarantee that the optimal parameters are satisfied in every individual interrogation spot. Kimura et al. (1988) checked the effects of figure rotation and proposed a method of correction of erroneous velocity vectors by comparing each estimated velocity vector with the mean of 8-neighbouring vectors. He assumed that the velocity vectors of which ending points are out of their own 8 neighbouring vectors were regarded as erroneous vectors. Landreth and Adrian (1988), Reuss et al. (1990) removed spurious vectors by comparing each vector with other vectors near it. An erroneous vector was discarded and estimated from its neighbours if its value falls out of the bounds of the average value of its neighbouring vectors. The final vectors were smoothed out using an axisymmetric Gaussian kernel. Hassan et al. (1993) used Hardy multi-quadratic equations for interpolating the whole field velocity data to eliminate the erroneous vectors. Spedding and Rignot (1993) studied interpolating methods for processing the velocity data of PIV. Alahyari and Longmire (1994) extracted velocity information from double-exposed photographs by the auto-correlation technique. He described the post-processing module performing data validation, removal of bad vectors, and replacement of drop-out vectors by interpolated vectors. Westerweel (1994) investigated three major post-processing approaches - the global-mean, local mean and local-median procedures - to eliminate spurious vectors. He proved that the local-median test has the highest efficiency.

2.2.7 Three-dimensional measurement

Chang and Tatterson (1983), Chang and Tatterson (1983), and Chang et al. (1984), Arroyo and Greated (1992) and Hinsch (1995) constructed a practical velocimeter based on stereo photogrammetry. Cenedese and Paglialunga (1988) used two colour planes, Suter et al. (1989) used three colour planes to reconstruct the three-dimensional flow. Kasagi and

Nishino (1991) used three cameras to reconstruct the three-dimensional flow. Grant et al. (1991) used stereoscopic particle image velocimetry and holographic velocimetry for measuring three components of the velocity. Westerweel and Nieuwstadt (1991) studied the performance of three dimensional particle image velocimetry using two-camera digital particle image velocimetry. Raffel et al. (1995) utilized parallel light sheet planes trying to extract the third components of velocity right to the light planes. Gray and Greated (1993) achieved three dimensional velocity measurements using holograms. Prasad and Adrian (1993) used a two camera stereoscopic system to extend conventional high image-density particle image velocimetry to three-dimensional vectors on planar domains. Kent et al. (1993) proposed photogrammetric calibration to improve three-dimensional particle tracking velocimetry. Huang et al. (1993) applied the cross-correlation technique to three-dimensional images to measure the three-dimensional flow.

2.3 Simultaneous measurement of velocity and temperature

Simultaneous flow and temperature visualisation proposed by Rhee et al. (1984, 1986), Akino et al. (1986), Bergman and Ungan (1988) and Treuner et al. (1995), provided qualitative velocity and temperature information. Quantitative velocity and temperature measurement was attempted by Hiller and Kowalewski (1987), Kimura et al. (1990), Ozawa et al. (1992) and Wozniak and Wozniak (1993). Hiller and Kowalewski used stroboscopic illumination, recording the colour flow pattern on photographs. Velocity data was obtained by tracking individual particles but temperature calibration gave problems because of pure liquid crystals and the colour film used. Wozniak and Wozniak (1993) used a similar method; velocity data was extracted by Young's fringes method. Because the flow was illuminated by a non-coherent light source, visibility of the Young's fringes was poor. Kimura et al. (1990) and Ozawa et al. (1992) used the direct digital images for velocity and temperature measurements; the temperature measurement tested on linear relationship of temperature and hue but the plotted data showed that one hue value was related to two temperature values, while velocity measurement was not attainable in regions with high velocity gradients. In this thesis, accurate velocity and temperature results will be provided.

2.4 Conclusions

Temperature measurement using thermochromic liquid crystals and full field velocity measurement are reviewed in this chapter. Several conclusions are reached.

a) Thermochromic liquid crystals can display different colours at different surrounding temperatures because their unique helical molecular structure adjusts according to temperature. Pure liquid crystals can display brilliant colours but their colour property is easily disturbed, being not only affected by temperature but also by normal and shear forces, view angles and atmospheric contamination. They can be easily damaged by ultraviolet light. Encapsulated liquid crystals are sensitive to temperature and relatively insensitive to other effects.

b) Encapsulated liquid crystals are frequently used for temperature visualisation and measurement on solid surfaces. Most applications to fluids are on natural convection because there is a problem of recirculation of fluid seeded with encapsulated liquid crystals where the encapsulated liquid crystals could be damaged by a pump.

c) The temperature can be obtained by measuring the colour displayed by liquid crystals. There are three major methods - human observation, intensity based image processing and true colour image processing. True colour image processing is becoming the favoured routine for researchers due to improved accuracy. HSI space was frequently used, several different researchers using different hue representations.

d) Full field velocity measurement was achieved by pulsed light velocimetry. Individual particle tracking provides randomly-sampled velocity data for low image particle density. Young's fringes, auto-correlation and cross-correlation are traditionally used for velocity extraction in the case of higher image particle density.

e) The Young's fringes method and auto-correlation method are usually applied for velocity extraction from the negative film, providing high resolution velocity data but with a direction ambiguity. The direction ambiguity could be resolved by shift techniques.

f) Velocity data can be extracted directly from digital particle images by means of the cross-correlation method (Video based PIV). The low resolution and frame rate of the image facility have side effects on the velocity measurement. Local non-uniformity will strongly affect the performance of the video based PIV.

g) Optimal parameter analysis carried by researchers indicates that the image particle density for single exposure analysis is more than 7 and for double exposure analysis more than 10. The interrogation spot size and particle size have an effect on the accuracy of experiments also.

Now, two ways of combination of paused light velocity with encapsulated thermochmic liquid crystals are available by carefully selecting the seeding particle density and the particle diameter. Firstly, the colour flow could be recorded on a colour film, Young's fringes and the auto-correlation method could be used for velocity measurement, but the calibration should be carried through the transmittance vector of the colour film with temperature and then the relative exposure and exposure ratio vectors, which is cumbersome and not reliable. Secondly, as used in this thesis, the colour flow could be directly digitalized, the colour and temperature being calibrated through true colour and temperature. The velocity could be measured by the cross-correlation method. The side effects will be investigated and deduced through an improved cross-correlation method proposed in this thesis.

Chapter 3 Analysis of cross-correlation

In chapter 2 the PIV techniques were reviewed. Generally, all the PIV techniques can be divided into two steps: firstly, recording the images of a flow seeded with particles and secondly, extracting velocity vectors from the recorded images. The PIV techniques are often categorised into photographic PIV and video based PIV, according to the recording media used (Willert and Gharib 1991). Video based particle image velocimetry is proposed for velocity measurement and a white light source is chosen for illumination, considering the utilities of the colour property of the thermochromic liquid crystals, in order to measure velocity and temperature simultaneously.

In this chapter ensemble statistical properties of the particle images are studied based on theoretical work of Adrian and Yao (1983), Adrian (1986c), Keane and Adrian (1990, 1991 and 1992) and Westerweel (1993). A CCD sensor is used for recording the images of flow seeded with fine particles in video based PIV. The optical density of the electric charge collected with a CCD sensor, is proportional to the image intensity field. Therefore, the image intensity is dealt with directly for particle image analysis. Major sources which affect the accuracy of velocity measurement are now discussed.

3.1 Principles of PIV

Flow visualisation techniques make the flow movement visible by adding air bubbles, dyes or fine particles to the fluid. For quantitative velocity measurement, the movements of individual particles or clusters of particles inside the flow are tracked, by assuming that the particles follow the motion of the fluid exactly. In addition they should neither alter the flow, nor interact with each other. This is only the ideal situation and in practice approximations are made.

In two-dimensional PIV, simultaneous in-plane velocity measurements at many points in the flow region are obtained by recording small particles that move with the flow and are illuminated in a thin white light sheet, of thickness Δz_O, as shown in Figure 3.1. At any moment t and a time interval Δt later, the exposures of particle images are recorded in the image plane. Assuming that the system consists of an aberration-free, thin circular lens with a focal length f and a diameter D and all observed particles are in focus, the object distance d_O and image distance d_i satisfy the geometrical lens law:

$$\frac{1}{d_O} + \frac{1}{d_i} = \frac{1}{f} \tag{3.1}$$

With the magnification M defined by $M = d_i / d_O$, the position of the particle image in the image plane $\boldsymbol{X} = (X, Y)$ can be related to the particles position $\boldsymbol{x} = (x, y)$ by the following expression

$$\mathbf{X} = M(x \cdot \mathbf{i} + y \cdot \mathbf{j}) \tag{3.2}$$

Thus the local in-plane image displacement between pulses, dX, can be related to the particles velocity $\boldsymbol{u} = (u,v)$ by

$$d\mathbf{X} = (dX,\ dY) = M(u\cdot\mathbf{i} + v\cdot\mathbf{j})\Delta t = M(dx\cdot\mathbf{i} + dy\cdot\mathbf{j}) \tag{3.3}$$

In the paraxial recording, when the image displacements are small compared to the distance from the light sheet to the lens, d_O, the thickness of the light sheet is negligible. Then the in-plane velocity components of the particle can be obtained from the local in-plane image displacements.

The measurement of the local displacements dX is interrogated in a small interrogation spot, centred on a position X_I. The mean displacement of image particle pairs, $\Delta X(X_I)$, in the interrogation spot is determined and a scan over the entire flow picture produces mean displacements over the entire image plane. The measured in-plane velocity components are determined by

$$\mathbf{u}(\mathrm{x_I}) = \Delta\mathbf{X}(\mathbf{X}_I)\,/\,M\Delta t \tag{3.4}$$

This measured velocity $\mathbf{u}(\mathbf{x})$ is a close approximation to the particle's in-plane velocity when paraxial approximations are made. After the particle images are obtained, the task of PIV velocity measurement becomes local displacement interrogation from the particle images.

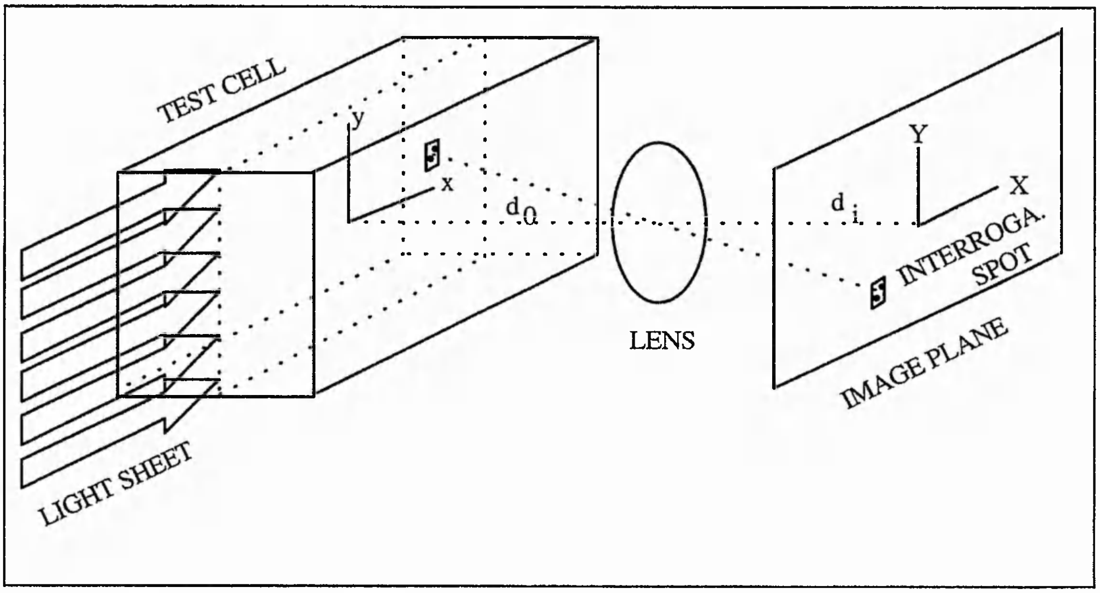

Figure 3.1 Schematic diagram of PIV set-up

3.2 Image of Flow Seeded With Particles

When the source particle density (N_s << 1) is low (Adrian 1984), the possibility of overlapping image particles in the light sheet is fairly small. The image of individual particles is determined by the particle size and the image system. Locations of the particles in the light sheet are distributed randomly. The image of the flow seeded with particles is a combination of all randomly distributed individual particles in the light sheet. Assuming all particle images are in-focus over the depth of the illuminating sheet and the fields of views paraxial, individual

$$\tau_0(\mathbf{X}) = \tau_0(X,Y) \tag{3.5}$$

particle intensity τ_0 is independent of z.

$$g(\mathrm{x},\ t) = \sum_{i=1}^{N_I} \delta(\mathrm{x} - \mathrm{x}_i(t)) \tag{3.6}$$

The locations of particles in the interrogation spot at time t is defined as

where N_I is the number of particles within the interrogation volume. Supposing the mean concentration of particles is constant and the velocity is uniform over an area the size of an

$$\begin{aligned} &g(x,t) = C(x) + \Delta g(x,t) \\ &< g(x,t)g(x',t+\Delta t) >= C(x,t)^2 + \\ &C(x,t)\delta(x'-x-\mathbf{u}(x,t)) \end{aligned} \tag{3.7}$$

interrogation spot, this yields

where $C(x)$ is the mean number of particles per unit volume and is assumed to be time independent and $<\Delta g> = 0$ (Adrian and Yao 1983, Adrian 1986c, Keane and Adrian 1992).

The appearance of flow image intensity $I(x)$ depends on the concentration of particles in the light sheet. At low source density ($N_s << 1$) image particles do not overlap, hence the intensity of particle images is given by a superposition of the intensity of all the individual particles

$$I(\mathbf{X}) = \sum_{i=0}^{N} I_0(\mathbf{x}_i)\tau_0(\mathbf{X} - M\mathbf{x}_i) \tag{3.8}$$

within the light sheet of intensity $I_0(x)$ and thickness ΔZ_0,

Alternatively, the intensity of the particle image is written as

$$I(\mathbf{X}) = \int I_0(\mathbf{x}) g(\mathbf{x}, t) \tau_0(\mathbf{X} - M\mathbf{x}) d\mathbf{x}. \tag{3.9}$$

which is a convolution between the position function of particles and the intensity of the individual particle.

The intensity distribution of the image pattern within an interrogation spot (window) is

$$I(\mathbf{X}) = w(\mathbf{X} - \mathbf{X}_1) \int I_0(\mathbf{x}) g(\mathbf{x}, t) \tau_0(\mathbf{X} - M\mathbf{x}) d\mathbf{x}. \tag{3.10}$$

where $w(X\text{-}X_I)$ is a window function centred at X_I with the size of the interrogation spot.

3.3 Cross-correlation of the particle images

In the small interrogation spot centred at X_I, the image of the flow at time t is a pattern of randomly distributed particles, $I_I(X_I)$. Assuming that the fluid velocity within the interrogation area is a constant $\boldsymbol{u}$ during a short time Δt, the image of flow at time $t+\Delta t$ will be shifted $\boldsymbol{u}\Delta t$ centred at location of $X_I + \boldsymbol{u}\Delta t$, represented as $I_2(X_I + \boldsymbol{u}\Delta t)$. The flow acts on a random particle field I_I at the "input" to yield the random field I_2 at the "output". A description of how the output I_2 relates to the input sample I_I can be given as:

$$I_2(\mathbf{X}) = \int I_I(\mathbf{t}) d(\mathbf{t} - \mathbf{X}) dt \tag{3.11}$$

The displacement function is a Dirac delta function, displaced from the origin by $\boldsymbol{u}\Delta t$, $d(X-\boldsymbol{u}\Delta t)$.

The method of detecting the displacement is to find the match of the particle image $I_1(X_1)$ in the image $I_2(X_1)$ to find out $\boldsymbol{u}\Delta t$. There are many possible ways of measuring the degree of match or mismatch between two images $I_1(X_1)$ and $I_2(X_1)$. For example, one can use as mismatch measures such expressions as

$$\max|I_1 - I_2| \quad or \quad \iint|I_1 - I_2|\,d\mathbf{X} \quad or \quad \iint(I_1 - I_2)^2 d\mathbf{X} \tag{3.12}$$

and so on (Rosenfeld and Kak 1982).

If the square of the difference is used as a measure of mismatch, a measure of match or mismatch can be derived from the mean-square error given as,

$$\begin{aligned} Error &= \int(I_1(\mathbf{X}) - I_2(\mathbf{X}+\mathbf{s}))^2 d\mathbf{X} \\ &= \int I_1(\mathbf{X})^2 d\mathbf{X} + \int I_2(\mathbf{X}+\mathbf{s})^2 d\mathbf{X} - 2\int I_1(\mathbf{X}) I_2(\mathbf{X}+\mathbf{s}) d\mathbf{X} \end{aligned} \tag{3.13}$$

where the first and second terms represent the energy from each function and the third term is the cross-correlation of $I_1(\mathbf{X})$ and $I_2(\mathbf{X})$. Thus, the mean-square error is small if and only if the third term is large as compared to the previous terms. From the Cauchy-Schwarz inequality (Gonzalez and Wintz 1987),

$$\int I_1(\mathbf{X}) I_2(\mathbf{X}+\mathbf{s}) \leq [\int I_1(\mathbf{X})^2 d\mathbf{X} \int I_2(\mathbf{X}+\mathbf{s})^2 d\mathbf{X}]^{\frac{1}{2}} \tag{3.14}$$

with equality if and only if $I_1(\mathbf{X}) = I_2(\mathbf{X} + s)$. In this case, $s = u\Delta t$. Thus, the value of the cross-correlation is a measure of the degree of match,

$$R(s) = \int I_1(\mathbf{X}) I_2(\mathbf{X}+s)\, d\mathbf{X} \qquad (3.15)$$

and normalizing this with the right-hand-side of (3.14) would give the relative degree of

$$R(s) = \frac{\int I_1(\mathbf{X}) I_2(\mathbf{X} + s) d\mathbf{X}}{\left[\int I_1(\mathbf{X})^2 I_2(\mathbf{X} + s)^2 d\mathbf{X}\right]^{\frac{1}{2}}} \qquad (3.16)$$

match.

When the best match occurs, the value of $R(s)$ is 1.0. That is the theoretical base for the improved cross-correlation method for PIV presented in chapter 5.

The maximum of this correlation peak coincides with the location of the displacement delta function $d(X-u\Delta t)$, while the cross-correlation peak may be interpreted as moving self-correlation peak of $I_1(X)$ away from the origin by the spacial displacement of particles in the interrogation spot. To illustrate this, the cross-correlation may be rewritten as:

$$\begin{aligned} R(s) &= \int I_1(\mathbf{X}) I_2(\mathbf{X}+s) d\mathbf{X} \\ &= \int I_1(\mathbf{X}) \int I_1(\mathbf{t}) d(\mathbf{t} - \mathbf{X} - s) d\mathbf{t} d\mathbf{X}. \end{aligned} \qquad (3.17)$$

By replacing $\boldsymbol{t}$ with $X+\boldsymbol{m}$,

$$
\begin{aligned}
R(\mathbf{s}) &= \int I_I(\mathbf{X}) \int I_I(\mathbf{X}+\mathbf{m}) d(\mathbf{m}-\mathbf{s}) d\mathbf{m} d\mathbf{X} \\
&= \int d(\mathbf{m}-\mathbf{s}) \int I_I(\mathbf{X}) I_I(\mathbf{X}+\mathbf{m}) d\mathbf{X} d\mathbf{m} \\
&= \int R_s(\mathbf{m}) d(\mathbf{m}-\mathbf{s}) d\mathbf{m}
\end{aligned}
\tag{3.18}
$$

where $R_s(\mathbf{m})$ represents the auto-correlation function of the input function $I_I(\mathbf{X})$. The location of the individual particles is a stationary random process such that the input function $I_I(\mathbf{X})$ correlates with itself only at the origin. The cross-correlation peak corresponding to the displacement appears as a shift in $R_s(\mathbf{m})$.

Substituting equation (3.10) into (3.15) yields

$$
\begin{aligned}
R(\mathbf{s}) &= \int (w(\mathbf{X} - \mathbf{X}_I) w(\mathbf{X} - \mathbf{X}_I + \mathbf{s}) \int I_0(\mathbf{x}) g(\mathbf{x}, t) \\
&\quad \tau_0(\mathbf{X} - M\mathbf{x}) d\mathbf{x} \int I_0(\mathbf{x}') g(\mathbf{x}', t+\Delta t) \tau_0(\mathbf{X} - M\mathbf{x} + \mathbf{s}) d\mathbf{x}') d\mathbf{X} \\
&= \int (w(\mathbf{X} - \mathbf{X}_I) w(\mathbf{X} - \mathbf{X}_I + \mathbf{s}) \int\int I_0(\mathbf{x}) I_0(\mathbf{x}') \\
&\quad g(\mathbf{x}, t) g(\mathbf{x}', t+\Delta t) \tau_0(\mathbf{X} - M\mathbf{x}) \tau_0(\mathbf{X} - M\mathbf{x} + \mathbf{s}) d\mathbf{x} d\mathbf{x}') d\mathbf{X}.
\end{aligned}
\tag{3.19}
$$

3.4 Ensemble statistical properties

The cross-correlation $R(s)$ is random because the particles are randomly located. Hence, it is best viewed as an estimate of the true, ensemble average correlation function which provides general guidelines for the cross-correlation method. Assuming that the fluid velocity within the small interrogation spot is a constant $\boldsymbol{u}$ during Δt, the expected ensemble average value of $<R(s)>$ is obtained directly from (3.19) by taking the averaging operation inside of the integral (Adrian and Yao 1983). The statistical properties of the cross-correlation function is determined by an ensemble average of $\boldsymbol{R(s)}$. Combining (3.7) and (3.19), yields the ensemble average of the cross-correlation as

$$
\begin{gathered}
< R(\mathbf{s}) >= \int(w(\mathbf{X}-\mathbf{X}_I)w(\mathbf{X}-\mathbf{X}_I+\mathbf{s})\iint I_O(\mathbf{x})I_O(\mathbf{x}')\tau_O(\mathbf{X}- \\
M\mathbf{x})\tau_O(\mathbf{X}-M\mathbf{x}'+\mathbf{s}) < g(\mathbf{x},t)g(\mathbf{x}',t+\Delta t) > \mathrm{d}\mathbf{x}\,\mathrm{d}\mathbf{x}')\mathrm{d}\mathbf{X} \\
= \int(w(\mathbf{X}-\mathbf{X}_I)w(\mathbf{X}-\mathbf{X}_I+\mathbf{s})\iint I_O(\mathbf{x})I_O(\mathbf{x}')\tau_O(\mathbf{X}-M\mathbf{x})\tau_O(\mathbf{X}- \\
M\mathbf{x}'+\mathbf{s})C(\mathbf{x},t)^2 d\mathbf{x}d\mathbf{x}')d\mathbf{X} + \int(w(\mathbf{X}-\mathbf{X}_I)w(\mathbf{X}-\mathbf{X}_I+\mathbf{s}) \\
\iint I_O(\mathbf{x})I_O(\mathbf{x}')\tau_O(\mathbf{X}-M\mathbf{x})\tau_O(\mathbf{X}-M\mathbf{x}'+\mathbf{s}) \\
C(\mathbf{x},t)\delta(\mathbf{x}'-\mathbf{x}-\mathbf{u}\Delta t)\mathrm{d}\mathbf{x}\,\mathrm{d}\mathbf{x}')\mathrm{d}\mathbf{X}
\end{gathered}
\tag{3.20}
$$

For simplicity, four assumptions were proposed (Adrian and Yao 1983, Adrian 1986c)

a. Intensity of light sheet is constant along the x and y direction, so that it may be approximated by a function of z, only.

b. All images are in-focus over the depth of the illuminating sheet and the field of views paraxial $\tau_O(X)$ is independent of z.

c. The mean concentration of particles is constant over areas the size of an interrogation spot.

d. The function $\tau_O(X)$ is narrow compared to the variations of the intensity of light sheet.

The narrow extent of τ_0 permits a fundamental simplification of the equation (3.20). The integrand vanish unless τ_0 functions are simultaneously large, requiring $\mathbf{X} \cong M\mathbf{x} \cong M\mathbf{x}' - s$, hence

$$\begin{aligned} < R(\mathbf{s}) > &= \frac{C^2 A \Delta z^2 I_0^2}{M^2} F_w F_z \tau_\infty^{\ 2} + \\ &\Delta z\, I_0^2 N_I F_w F_z \tau_\infty^{\ 2} F_\tau(\mathbf{s} - M\mathbf{u}\Delta t) \end{aligned} \qquad (3.21)$$

$$\begin{aligned} F_w(\mathbf{s}) &= \int w(\mathbf{X}) w(\mathbf{X}+\mathbf{s})\, \mathrm{d}\mathbf{X} / A \\ F_z(\Delta z) &= \int I_0(z - z_{01}) I_0(z - z_{02} + \Delta z)\, \mathrm{d}z / I_0^2 \\ F_\tau(\mathbf{s}) &= \int \tau_0(\mathbf{X}) \tau(\mathbf{X}+\mathbf{s})\, \mathrm{d}\mathbf{X} / \tau_\infty^{\ 2} \\ \tau_\infty &= \int \tau_0\, \mathrm{d}\mathbf{X} \\ N_I &= \frac{CA\Delta z}{M^2} \end{aligned} \qquad (3.22)$$

where A is the area of the interrogation spot and N_I represents the number of particles within the interrogation window.

F_z is the normalised correlation of the intensities of two successive light pulses in terms of the out-of-plane displacement Δz_0 between time t and $t+\Delta t$, which function width is of order of the light sheet thickness Δz_0. F_z is defined as the out-of-plane loss-of-pairs function (Adrian 1986c). For nearly two-dimensional flow, the velocity component perpendicular to the light sheet plane is small. When $\max(w\Delta t) < (1/2)\, \Delta z_0$, $F_z = 1$.

F_w is the normalised correlation of the mean intensity across the interrogation spots, whose width is of the order of the interrogation spot size. For a uniform window $W_{i,j}$ and window size N:

$$F_w(i, j) = (1 - \frac{|i|}{N})(1 - \frac{|j|}{N}) \tag{3.23}$$

Uniform windowing can cause the correlation to be biased but the effect is negligible. Westerweel (1993) pointed out that the existence of F_w causes the correlation peak to be biased towards the centre. He proposed to compensate the bias by

$$R^*(\mathbf{m}) = \frac{R(\mathbf{m})}{F_w(\mathbf{m})} \tag{3.24}$$

The width of the function F_τ is of the order of the diameter of particles d_τ, and its amplitude at $s = 0$ is proportional to d_τ^2. In the limit of vanishing d_τ its amplitude becomes infinite, and its width vanishes while its strength remains constant:

$$\int F_\tau(\mathrm{s})\mathrm{d}\mathrm{s} = 1 \tag{3.25}$$

showing that F_τ approaches a Dirac delta function (Adrian 1986c, Keane and Adrian 1992, Westerweel 1993). Because the minimum size of the image particle on a CCD will be no less than one pixel, F_τ covers more than one pixel. This makes it possible to estimate the centroid of the displacement at sub-pixel accuracy (see section 3.6).

The first term of equation (3.21) is the cross-correlation of the mean intensities. The second term is the cross-correlation of the intensity fluctuations which corresponds to the mean velocity in the interrogation spot. Discarding the first term, we have

$$< R(\mathbf{s}) > \;=\; \Delta z\, I_0^{\,2} N_I F_w F_z \tau_\infty^{\,2} F_\tau(\mathbf{s} - M\mathbf{u}\Delta t) \tag{3.26}$$

3.5 Digital particle image velocimetry

Traditional particle image velocimetry uses photographic films or plates for the recording of the particle images. Rapid development of digital image techniques in recent years has led to CCD camera becoming the most popular for recording PIV.

The image intensity $I(X)$ is commonly discretized with a CCD that integrates the light intensity over a small area, usually referred to as a pixel. Assuming that the device has a linear response with respect to light intensity, and it is made up of square and contiguous pixel with area Δ^2, the relation between the discrete image I_k and the continuous image $I(X)$ is given by:

$$I_k \;=\; \int p(\mathbf{X} - \mathrm{K}\Delta) I(\mathbf{X})\, \mathrm{d}\mathbf{X} \tag{3.27}$$

where $k = (i, j)$ represents the position of the pixel on the CCD. $p(X)$ is the sampling function:

$$p(X) = \frac{1}{\Delta^2} \quad \textit{while } X \in \Delta, \ \ \textit{0 elsewhere} \tag{3.28}$$

Note that $p(X)$ is a symmetric function (viz., $p(X) = p(-X)$) and that $\int p(X)\mathrm{d}X = 1$ (Westerweel 1993).

Given the cross-correlation of the continuous PIV images on equation (2.28), the cross-correlation of the Video PIV images is

$$\begin{aligned} < R(\mathrm{k},\mathrm{l}) > &= \int p(\mathbf{X} - \mathrm{k}\Delta) \int p(\mathbf{X}' - \mathrm{l}\Delta + \mathbf{s}) < R(\mathbf{s}) > \mathrm{d}\mathbf{X}\,\mathrm{d}\mathbf{X}' \\ &= \Delta z\, I_0^{\,2} N_I F_w F_z \tau_\infty^{\,2} F_\tau((\mathrm{l} - \mathrm{k})\Delta - M\mathbf{u}\Delta t) \end{aligned} \tag{3.29}$$

The peak position of the $<R(k, l)>$, at $(\mathbf{l}$-$\mathbf{k})$ of the discrete correlation coefficient plane with respect to the origin, is related to the local mean velocity.

3.6 Sub-pixel accuracy

For each interrogation spot of digitised image, the maximum of $R(\boldsymbol{k}, \boldsymbol{l})$ yields only a rough estimate of the displacement (with a resolution of one pixel). Supposing that the peak position of the cross-correlation coefficient sited at $\boldsymbol{m} = \boldsymbol{l} - \boldsymbol{k} = (i, j)$, then the displacement (x, y) will be

$$x = (i + \delta_i)\Delta \quad y = (j + \delta_j)\Delta \tag{3.30}$$

where d_i and d_j are the sub-pixel displacements, with

$$|\delta_i| \leq 0.5, \quad |\delta_j| \leq 0.5 \tag{3.31}$$

For a 32×32 pixel interrogation spot, a displacement of 10 pixels will yield a relative error 0.5/10, equal to 5%. In order to obtain sub-pixel accuracy, Willert and Gharib (1991) used a three-point curve fit to find the sub-pixel position. Prasad et. al. (1992) demonstrated that parabolic and Gaussian curve fits yielded *rms* errors that were about one-half of those from the centre of mass technique (Willert and Gharib, 1991). They also argued that this trend was true only for flows where the velocity gradient is negligible and, consequently, they selected the centre of mass method. To establish the difference in accuracy of the three above methods, they have been compared directly to each other, as discussed below and reported in Jambunathan et al. (1995).

3.6.1 Centroid of mass

After locating the integer position $k(i, j)$ which is nearest to the peak position, a small area A centred at $k(i, j)$ is defined to calculate the sub-pixel position as

$$\delta_{\mathbf{k}} = \frac{\int_A \mathbf{s}R(\mathbf{s}-\mathbf{k})d\mathbf{s}}{\int_A R(\mathbf{s}-\mathbf{k})} \tag{3.32}$$

In fact, the sub-pixel value is the mass centre of the cross-correlation coefficients inside the area, A.

3.6.2 Parabolic fit

Supposing a parabolic function $y = ax^2 + bx + c$ passes three points $(-1, y_{-1})$, $(0, y_0)$ and $(1, y_1)$, its peak position will lie at

$$x = -\frac{b}{2a} \quad while \quad a \neq 0 \tag{3.33}$$

for dy/dx = 0. Three y values $y_{-1} = R(i-1, j)$, $y_0 = R(i, j)$ and $y_1 = R(i+1, j)$ and three corresponding x positions are -1, 0 and 1 respectively, hence

$$\begin{aligned} R(i-1, j) &= a - b + c \\ R(i, j) &= 0 + 0 + c \\ R(i+1, j) &= a + b + c \end{aligned} \tag{3.34}$$

Solving the equations, the sub-pixel value along column j is

$$\delta_j = \frac{R(i-1,j) - R(i+1,j)}{2(R(i-1,j) + R(i+1,j) - 2R(i,j))} \tag{3.35}$$

similarly for the value along row i

$$\delta_i = \frac{R(i,j-1) - R(i,j+1)}{2(R(i,j-1) + R(i,j+1) - 2R(i,j))} \tag{3.36}$$

3.6.3 Gaussian fit

Another method that is very similar to the parabolic fit is the Gaussian fit using the fact that the cross-correlation is approximately a Gaussian curve (Adrian and Yao 1983). Taking logs on both sides of

$$y = e^{ax^2 + bx + c} \tag{3.37}$$

yields

$$\ln y = ax^2 + bx + c \tag{3.38}$$

Applying a similar operation as that of treating the parabolic function with three values around the peak position, yields

$$\delta_i = \frac{\ln R(i,j-1) - \ln R(i,j+1)}{2(\ln R(i,j-1) + \ln R(i,j+1) - 2\ln R(i,j))}$$
$$\delta_j = \frac{\ln R(i-1,j) - \ln R(i+1,j)}{2(\ln R(i-1,j) + \ln R(i+1,j) - 2\ln R(i,j))} \tag{3.39}$$

Prior to the sub-pixel interpolation, the corresponding coefficients are compensated according to equation (3.24).

3.7 Conclusions

The particle image can be expressed as a convolution between the position function of the seeded particles and the intensity function of the individual particle.

Cross-correlation coefficient is a measure of match of two images. If the two images are identical, the normalised cross-correlation coefficient of them equals 1.0.

Assuming the uniform velocity distribution within the interrogation spot, function F_t reaches its maximum value at $Mu\Delta t$, which is the local displacement between the first image and the second image. The position of maximum cross-correlation coefficient corresponds to the local velocity.

Out-of-plane and in-plane movements of particles due to flow movements affect the peak value of the cross-correlation coefficients, leading to a reduction in the number of paired particles. $N_I F_w F_z$ represents the number of paired particles within the interrogation spot. For two-dimensional flow, the effect of out-of-plane movement is small, $F_z = 1$. F_w is the normalised correlation of the interrogation intensity across the interrogation spot. It is affected by uniform displacement/velocity.

The peak value of the cross-correlation coefficient is accumulated from cross-correlations of $N_I F_w F_z$ paired particles. When the velocity distribution within the interrogation spot is not uniform, the peak value will be decreased and the peak will be broader.

For two digital particle images, the cross-correlation peak always covers more than one pixel because the size of the imaged particle is at least one pixel. The sub-pixel accuracy of the velocity measurement can be achieved through the interpolation of the neighbouring values around the peak.

Chapter 4 Effects of velocity distribution

The ensemble analysis of the cross-correlation provides general guidelines for experiments. Uniformity of velocity within the interrogation spot is required for the cross-correlation method. For video based PIV, the assumption of uniform velocity within the interrogation spot is invalid due to the limitation of the image facility. The individual case of cross-correlation of two images is studied. Estimations of the effects of three movements - uniform displacement, rotation and bi-axial shear - are presented. Simulations are carried out to investigate the effects of the local non-uniformity.

4.1 Cross-correlation method

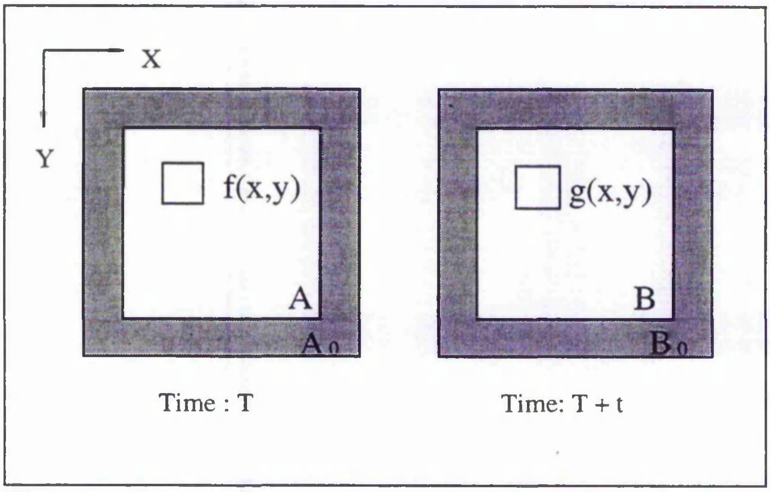

Figure 4.1 Image A and B

Having obtained two sequential images, cross-correlation was employed to extract the velocity vectors from the images via a $N´N$ pixel interrogation window, shown schematically in Figure 4.1. The area of interest in the first frame is $\boldsymbol{A}$ and outside of this window is labelled $\boldsymbol{A_o}$. Their counterparts in the second frame are $\boldsymbol{B}$ and $\boldsymbol{B_o}$ respectively. An interrogation spot $f(i,j)$ centred at a particular position (x, y) is sampled within $\boldsymbol{A}$. Its counterpart is $g(i,j)$ within $\boldsymbol{B}$. The cross-correlation coefficient $\boldsymbol{R(k,l)}$ is calculated between the patterns $f(i,j)$ and $g(i,j)$ using (Kimura and Takamori, 1986):

$$R(k,\ l) = \frac{\sum_{i=-\infty}^{\infty}\sum_{j=-\infty}^{\infty} f(i,\ j)g(i-k,\ j-l)}{\sqrt{\sum_{i=-\infty}^{\infty}\sum_{j=-\infty}^{\infty} f^2(i,\ j)\ \sum_{i=-\infty}^{\infty}\sum_{j=-\infty}^{\infty} g^2(i-k,\ j-l)}} \tag{4.1}$$

According to convolution theory, the correlation operation in the space domain becomes multiplication in the frequency domain (Gonzalez and Wintz, 1987)

$$f \circ g \Leftrightarrow F \cdot G^* \tag{4.2}$$

Where $\circ$ denotes correlation, F and G are the Fourier transforms of f and g, and G^* is the conjugate of G. A Fast Fourier Transform (FFT) is employed to simplify and significantly speed up the cross-correlation process. The procedure is shown schematically in Figure 4.2.

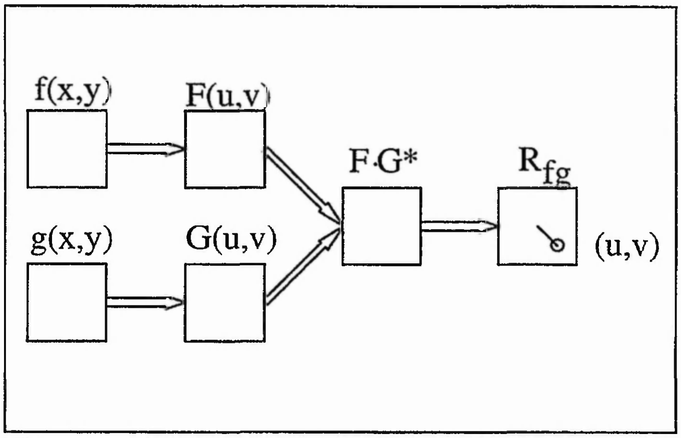

Figure 4.2 FFT

FFT requires that the number of rows and columns of the input and output must have an exponent of 2; the size of the interrogation window must therefore have corresponding dimensions. A high cross-correlation value near 1 is observed when many particle images in the first image match their corresponding spatially shifted partners in the second image. Small cross-correlation peaks may be observed when individual particle images match with other particle images. The highest correlation peak is considered to represent the best match of particle images between the *f(i,j)* and *g(i,j)*. The offsets $(\Delta x, \Delta y)$ of the peak, which are measured from the origin of the cross-correlation coefficient map, represent the average spatial shift of particles from image **A** to **B** at position *(x, y)*.

4.2 Limitations of image facility

For video based PIV, the particle images of the flow grabbed by a frame grabber are directly used for velocity interrogation. The resolution of the frame grabber is 512×512 pixels per frame (around 100 mm^{-1}) and the frame rate is 25 frames per second.

The low frame rate of video based PIV defines the smallest time interval as 0.4 ms, and thus limits the technique to low velocity measurement. For higher velocity measurement, the synchronised device of CCD needs to be adjusted or two CCD camera could be used. That is beyond the scope of this thesis.

The resolution of a CCD sensor is 10 times lower than that of a film. In this case, the assumption of the local uniform velocity within the interrogation is not sustained. For video based PIV, an interrogation spot of 32×32 pixels is not small enough to ignore the local non-uniformity in the velocity distribution.

4.3 Effects of local velocity distribution

Adrian and Yao (1983) pointed out that local non-uniformity of the velocity distribution leads to the peak position being biased to the lower velocity value. Since particles with higher velocity tend to move in and move out the interrogation spot and the particles with lower velocity tend to stay in the spot, more particle pairs with lower velocity are found. The statistical cross-correlation peak is thus biased to the lower velocity value.

The ensemble statistical properties of the cross-correlation makes it difficult to establish how far the local non-uniformity affects the accuracy of the velocity measurement. Huang et al. (1993a) further analyzed the effects of velocity gradients in the interrogation spot, assuming the intensity distribution is ensemble average uniform. The analysis of the ensemble cross-correlation function provides some insight into the performance of the cross-correlation procedure, but does not directly address questions concerning probabilities of measurement and the fluctuation in the statistics of individual velocity measurements. In this thesis, individual cases of particle images are examined to predict the effects of the local non-uniformity. Optimal parameters of image particle density, particle size and local non-uniformity are investigated.

Considering a flow element of a general two dimensional flow, Helmholz velocity theory divides a flow movement into three subsidiary terms (Wu 1982):

$$\mathbf{u} = \mathbf{u}_0 + \frac{1}{2}\Delta\mathbf{u} \cdot \delta\mathbf{r} + \nabla\phi \qquad (4.3)$$

where $\boldsymbol{u}$ represents the mean velocity in the fluid element and $\boldsymbol{u}_0$ represents the velocity of the spatial transfer of the fluid element. The three terms on the right-hand side of equation (4.3) are translation, rotation and element bi-axial shear respectively. The three terms acting on two images with a time interval result in uniform displacement, rotation and shearing movements in an interrogation spot. Generally, they cause only some of the particles in the interrogation spot to contribute to the cross-correlation peak, resulting in the maximum normalized cross-correlation value to be less than one.

4.3.1 Uniform displacement

Pure uniform displacement leads the particles within the interrogation spot to be shifted by an identical distance. The term $g(x, t)g(x', t{+}\Delta t)$ of equation (3.19) becomes a Dirac function for each particle pair within the interrogation spot. Because of uniform displacement, some particles move into the interrogation spot and some particles move out. Only part of particles of N_I contributes to the cross-correlation peak. Supposing that the size of the interrogation spot is N and the uniform displacement in x and y direction are equal to $y_d N$, the mean number of the particles which contribute to the correlation peak is

$$N_{pair} = \frac{(N - \psi_d N)^2}{N^2} N_I = (1 - \psi_d)^2 N_I \tag{4.4}$$

If the particles are modelled as randomly distributed points, the probability $p(k)$ of finding k particle pairs in a interrogation spot obeys a Poisson distribution (Adrian 1991), i.e.

$$p(k) = \frac{N_{pair}{}^{k}}{k!} e^{-N_{pair}} \tag{4.5}$$

where N_{pair} is the number of particle pairs within the interrogation spot. Because of the uniform displacement, the probability $p(k)$ of finding k particles in the interrogation spot decreases.

Edwards (1988) stated that if there were three or more particle pairs in the measurement region, the probability of making a false reading is very small. For whole field velocity interrogation the possibility of finding less than 3 particle pairs contributing to the cross-correlation peak is

$$\begin{aligned} p(k<3) &= p(0)+p(1)+p(2) \\ &= e^{-(1-\psi_d)^2 N_I}[1+(1-\psi_d)^2 N_I+((1-\psi_d)^2 N_I)^2] \end{aligned} \tag{4.6}$$

meaning that *p(k<3)* of all interrogated velocity vectors are not reliable data. This depends on the image particle density and the uniform displacement.

It has been stated previously that the larger image particle size results in a broadening of the correlation peak and poor accuracy of the measurement.

4.3.2 Rotation movement

When there is only pure rotation movement around the centre of the interrogation spot, the measured mean velocity at the centre must be zero. In the case of rotation, the energy of the difference for the best match for the two images is

$$Error = \sum_{1}^{NI} (\mathbf{r}_i \theta)^2 \tag{4.7}$$

In fact, every particle within the interrogation spot has a unique displacement, which is dependant on its location $\boldsymbol{r}_i$ and rotation angle q. The procedure to find the match of the first image in the second image rests with finding the minimum energy of the difference of the two images (see section 3.3), where the minimum energy

$$Error = \sum_{1}^{NI} (\mathbf{r}_i\theta - \varepsilon)^2 \tag{4.8}$$

is located at the position of

$$\varepsilon = \theta \sum_{1}^{NI} \mathbf{r}_i \tag{4.9}$$

Here, the value of e is the error of the velocity measurement for each interrogation position in the case of pure rotation movement. It is related to the mass centre of the random distributed particles and the rotation angle.

From equation (3.25), the integrand vanishes when the distance of the particle pairs is larger than the diameter of the image particle. Larger image particle size will tolerate larger rotation angle than the smaller image particle size, because the larger size image particle requires larger rotation to move the particle apart for a fixed location.

4.3.3 Bi-axial shearing movement

As with rotation, the mean velocity will be zero when there is only bi-axial shearing movement, the shear is

$$\zeta = \alpha + \beta \tag{4.10}$$

where a and b are the shear angle in x and y directions respectively. For simplicity, let $a = b = z/2$. The shear movement for each particle located at $\boldsymbol{r}_i$ is

$$\mathbf{i}x \cdot \mathrm{tg}\frac{\zeta}{2} + \mathbf{j}y \cdot \mathrm{tg}\frac{\zeta}{2} = \mathbf{r}_i tg\frac{\zeta}{2} \tag{4.11}$$

In the case of shearing movement, the energy of the difference for the best match for the two images is

$$Error = \sum_{1}^{N_I} (\mathbf{r}_i \mathrm{tg}\frac{\zeta}{2})^2 \tag{4.12}$$

In fact, every particle within the interrogation spot has a unique displacement, which is dependant on its location $\boldsymbol{r}_i$ and shear z. The minimum energy

$$Error = \sum_{1}^{N_I} (\mathbf{r}_i \mathrm{tg}\frac{\zeta}{2} - \varepsilon)^2 \tag{4.13}$$

is located at the position of

$$\varepsilon = \mathrm{tg}\frac{\zeta}{2}\sum_{1}^{N_I} \mathbf{r}_i \tag{4.14}$$

Here, the value of e is the error of the velocity measurement for each interrogation position in the case of pure shearing movement. It is related to the weight centre of the random distributed particles and the shear.

The image particle size plays the same role in the case of shearing movement as it does in the case of rotation. Larger imaged particle sizes will tolerate larger shear movement than the smaller ones.

4.4 Simulation analysis

Ensemble analysis of the cross-correlation provides general guidelines for the PIV experiments. The individual particle images are studied with uniform displacement, rotation movement and shear movement applied. The effects of image particle density, particle size and local non-uniformity of velocity are investigated. This predicts that the correlation zone decreases due to the movements within the interrogation spot. In this section, the numerical simulations of the PIV images are used to investigate the errors of the cross-correlation method in the cases of different parameters. The parameters of video based PIV interrogation spot size, particle image density and particle size are investigated for optimal experimental design during the simulations.

4.4.1 Generating Particle Images

The particle images are formed from the seeded particles in fluids illuminated with a light sheet. Noting Adrian's four assumptions (see section 3.4), the intensity of the light sheet is regarded as a constant value, neglecting the variation in the z direction. In the case of a digital image, it is 255 where the grey scale varies from 0 to 255.

The particle number in a volume follows the law of Poisson's distribution. The image particle positions $G(X)$ in the image plane could be generated for fixed average particle image density, which is governed by the Poisson statistics. In fact $G(X)$ represents randomly distributed points with grey level 255.

The seeding particles are identical resulting in the same diameter of image particles d_τ. The intensity distribution of an individual particle image per unit of illuminating intensity is represented as $\tau_0(X)$. The first particle image $A(X)$ in the simulation is created by calculating the convolution of $G(X)$ and $\tau_0(X)$.

$$A(\mathrm{X}) = G(\mathrm{X}) * \tau_0(\mathrm{X}) \tag{4.15}$$

The second image $B(X)$ is obtained by mathematical transformation of image A in two dimensional Cartesian coordinates.

For uniform transform, there is

$$
\begin{aligned}
X_B &= X_A - d_x \\
X_B &= X_A - d_y
\end{aligned} \tag{4.16}
$$

where d_x and d_y are the shift in x and y direction respectively.

In the case of rotation, angle q around the centre $c(c_x, c_y)$, this becomes

$$
\begin{aligned}
X_B &= X_A \cos\theta - Y_A \sin\theta + c_x(1-\cos\theta) + c_y \sin\theta \\
Y_B &= X_A \sin\theta + Y_A \cos\theta - c_x \sin\theta + c_y(1-\cos\theta)
\end{aligned} \tag{4.17}
$$

In the case of bi-axial-shear z around the centre $c(c_x, c_y)$, this becomes

$$
\begin{aligned}
X_B &= X_A + Y_A \operatorname{tg}(\frac{\zeta}{2}) - c_y \operatorname{tg}(\frac{\zeta}{2}) \\
Y_B &= X_A \operatorname{tg}(\frac{\zeta}{2}) + Y_A - c_x \operatorname{tg}(\frac{\zeta}{2})
\end{aligned} \tag{4.18}
$$

4.4.2 Simulation procedure

There are many parameters that need to be considered for PIV experiments, such as the source particle density, the particle size, the thickness of the light sheet and the light source.

After the images are obtained, the interrogation spot size of the cross-correlation method needs to be chosen. For analysis of particle images using the cross-correlation method, three major parameters affect the measurement, namely the image particle density, the interrogation spot size and the image particle size. When the three parameters are determined, other experimental parameters can be adjusted.

Given the image particle density, the image particle size, the first image of a particle image representing a flow seeded with particles with the same diameter is created. The second image is generated by numerical transformations of the first image (shift, rotatation or shear). After these two images are created, the movements between two images at points of interest are interrogated using the cross-correlation algorithm with the given interrogation spot size. Finally the errors of the cross-correlation method are estimated by comparing the results with the known values of movements.

4.5 Results

The displacements calculated from the cross-correlation method are compared with known values; the mean errors of the measurements at 225 points are presented. The interrogation spot size, the image particle density and the image particle size and the flow movements are interrelated to affect the accuracy of the measurement. The effects of the interrogation size on the time for each interrogation are investigated. The errors of the velocity measurements using different interrogation spot sizes (window size), in the case of uniform displacements, rotation and shearing movements, are given in Figure 4.3, 4.4 and 4.5 respectively. The errors of the velocity measurements using the different image particle densities, in the case of uniform displacements, rotation and shearing movements, are given in Figure 4.6, 4.7 and 4.8 respectively. The errors of the velocity measurements using the different image particle sizes, in the case of uniform displacements, rotation and shearing movements, are given in Figure 4.9 Finally, the effects of the flow movements on the cross-correlation coefficients are given in Figure 4.10, 4.11 and 4.12.

4.5.1 Interrogation spot size

The velocity measurement of an interested point is the mean value of the velocity distributed within the interrogation spot. The size of the spot determines the resolution of the measurement. On the other hand, larger interrogation spots require longer calculation time. A FFT algorithm is employed to speed up the cross-correlation process, which requires that the size of the interrogation spot must have an exponent of 2. In this case, the size must be 8, 16, 32 and 64, etc. The larger size of the spot means longer calculation time, because the cross-correlation operation requires three FFT operations and one matrix multiplication. The time consumed increases rapidly as the size increases (Table 4.1).

Table 4.1 Time consumed for an interrogation

Interrogation spot size (pixel)	Time (second)
8×8	0.05
16×16	0.06
32×32	0.11
64×64	0.44

For a fixed image source density, a larger interrogation spot means larger image particle density. In the case of uniform displacement, large image particle density will help the cross-correlation to provide accurate values (see section 4.5.2). The larger size of the interrogation spot also means a larger measurement range. The mean error increases as the displacement increases. As long as the displacement is less than one third of the size of the spot, the mean error of the measurements is fairly small. Figure 4.3 shows the mean errors of the measurements for interrogation spot size of 8, 16, 32 and 64 with the image particle size varying from 1 to 7.

Figure 4.3 Mean errors for uniform displacements using different interrogation spot sizes

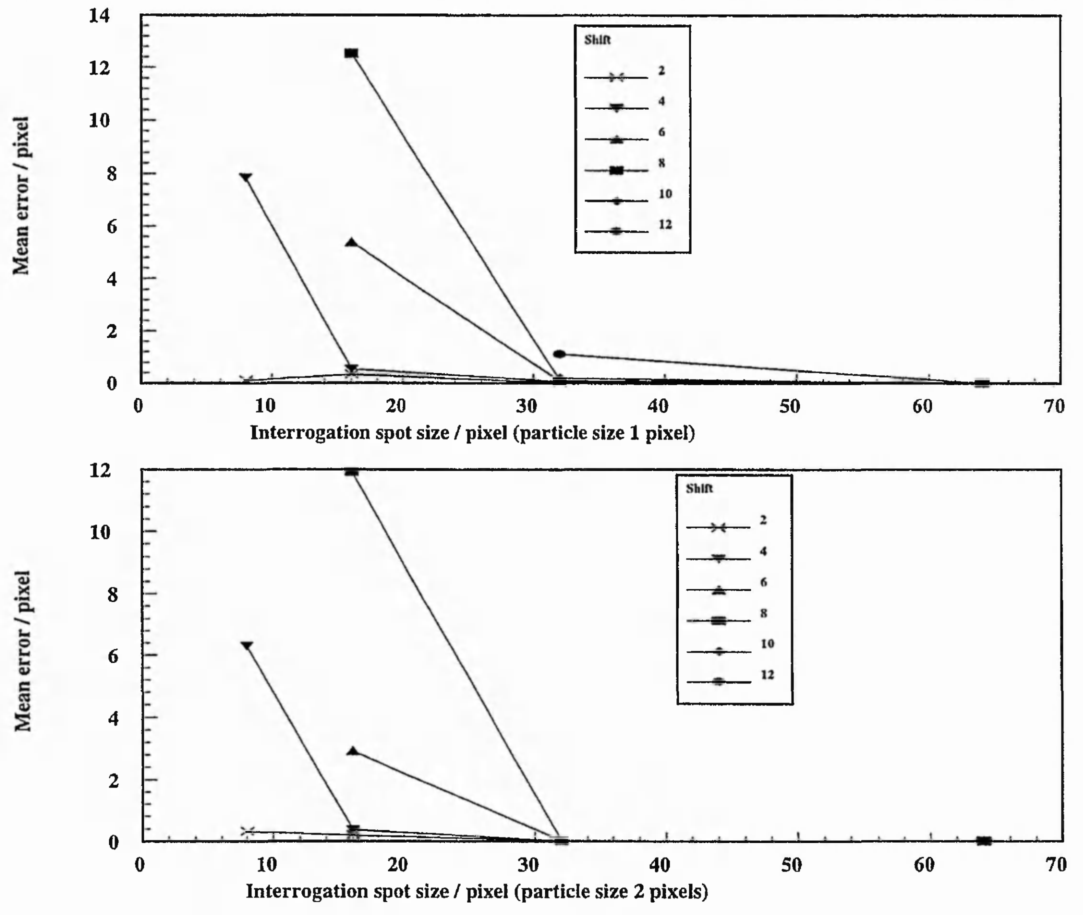

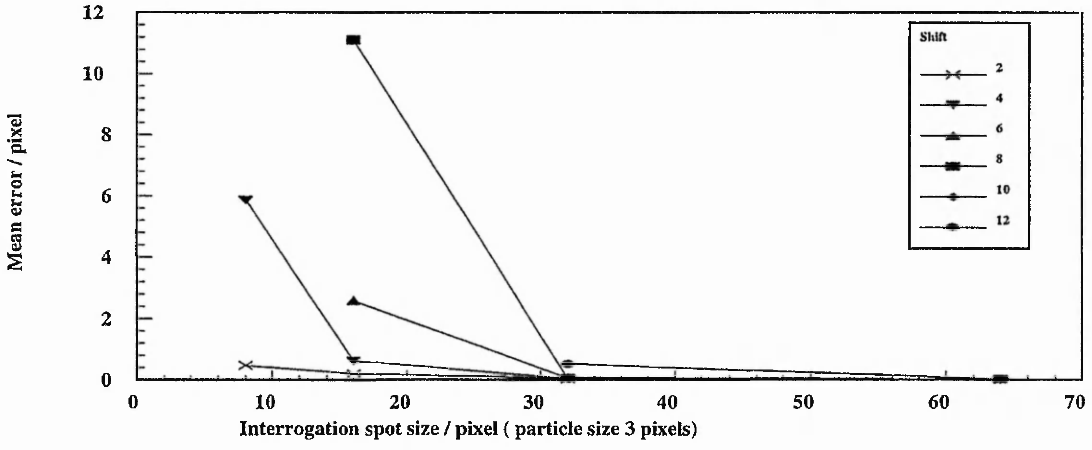
Mean error / pixel
12
10
8
6
4
2
0
0
10
20
30
40
50
60
70
Interrogation spot size / pixel (particle size 3 pixels)
Shift
2
4
6
8
10
12

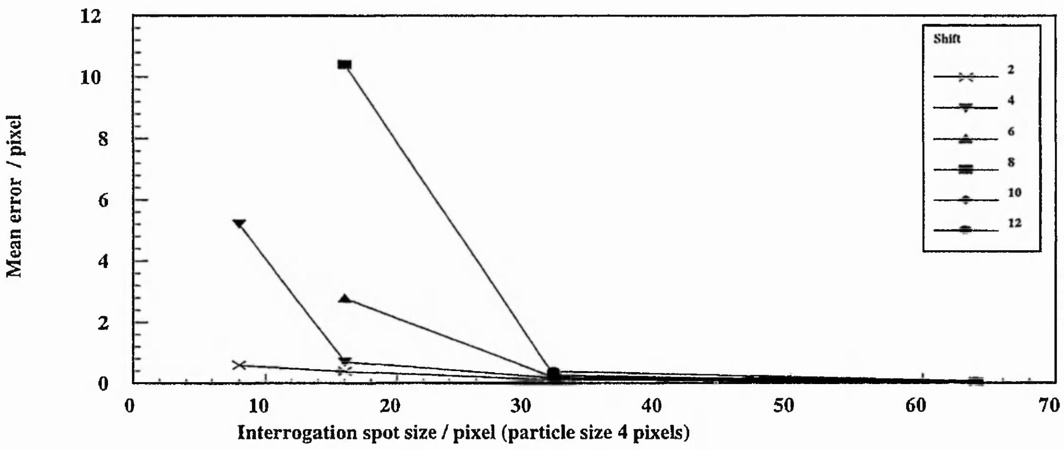
Mean error / pixel
12
10
8
6
4
2
0
0
10
20
30
40
50
60
70
Interrogation spot size / pixel (particle size 4 pixels)
Shift
2
4
6
8
10
12

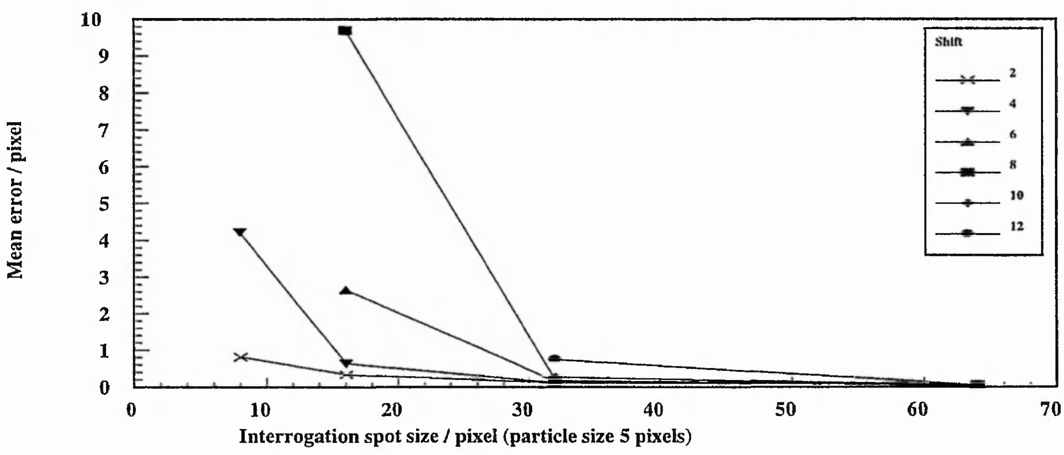
Mean error / pixel
10
9
8
7
6
5
4
3
2
1
0
0
10
20
30
40
50
60
70
Interrogation spot size / pixel (particle size 5 pixels)
Shift
2
4
6
8
10
12

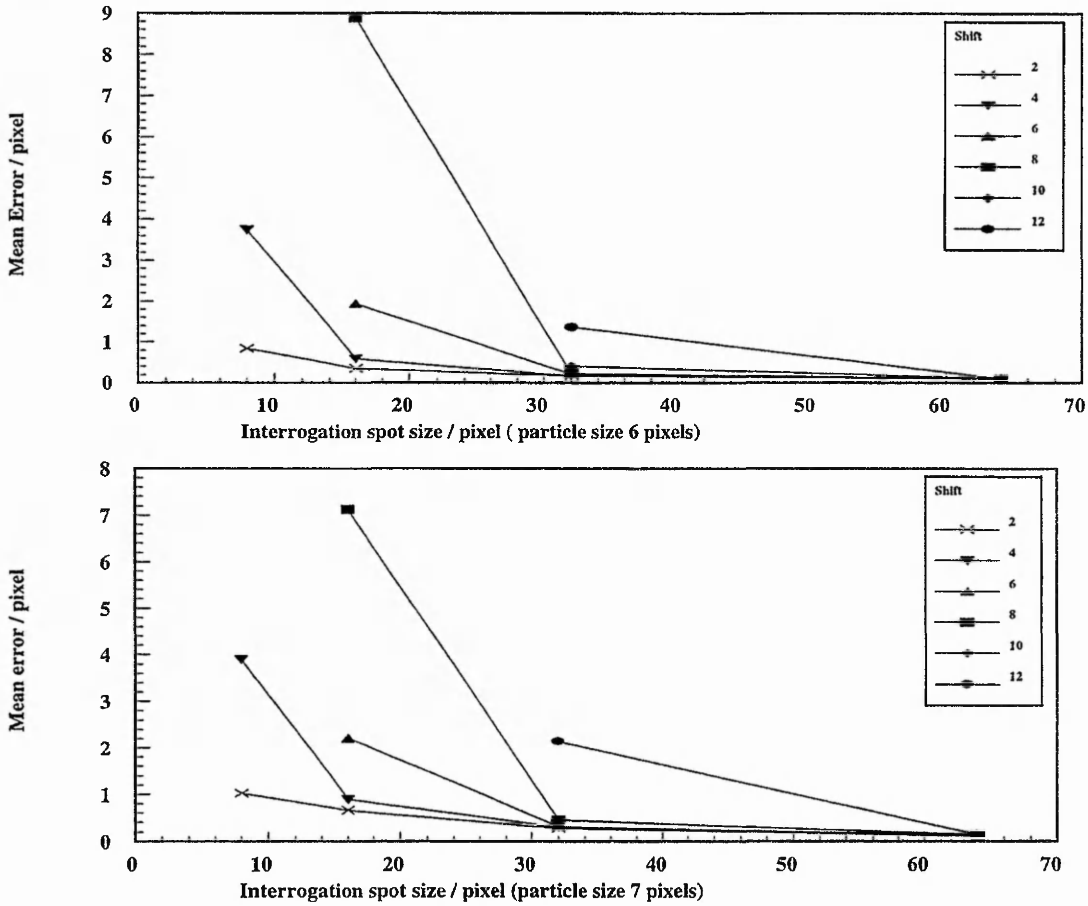

Figure 4.3 Mean errors for uniform displacements using different interrogation spot sizes

Because the error of the measurement for pure rotation is related to the rotation angle, the mean error increases as the rotation angle increases. Changing the interrogation spot to a larger size affects the location of the weight centre of the particles, in most cases, it makes things worse. The large interrogation spot size does not help to get accurate measurements, see Figure 4.4.

Figure 4.4 Mean errors for rotation movements using different interrogation spot sizes

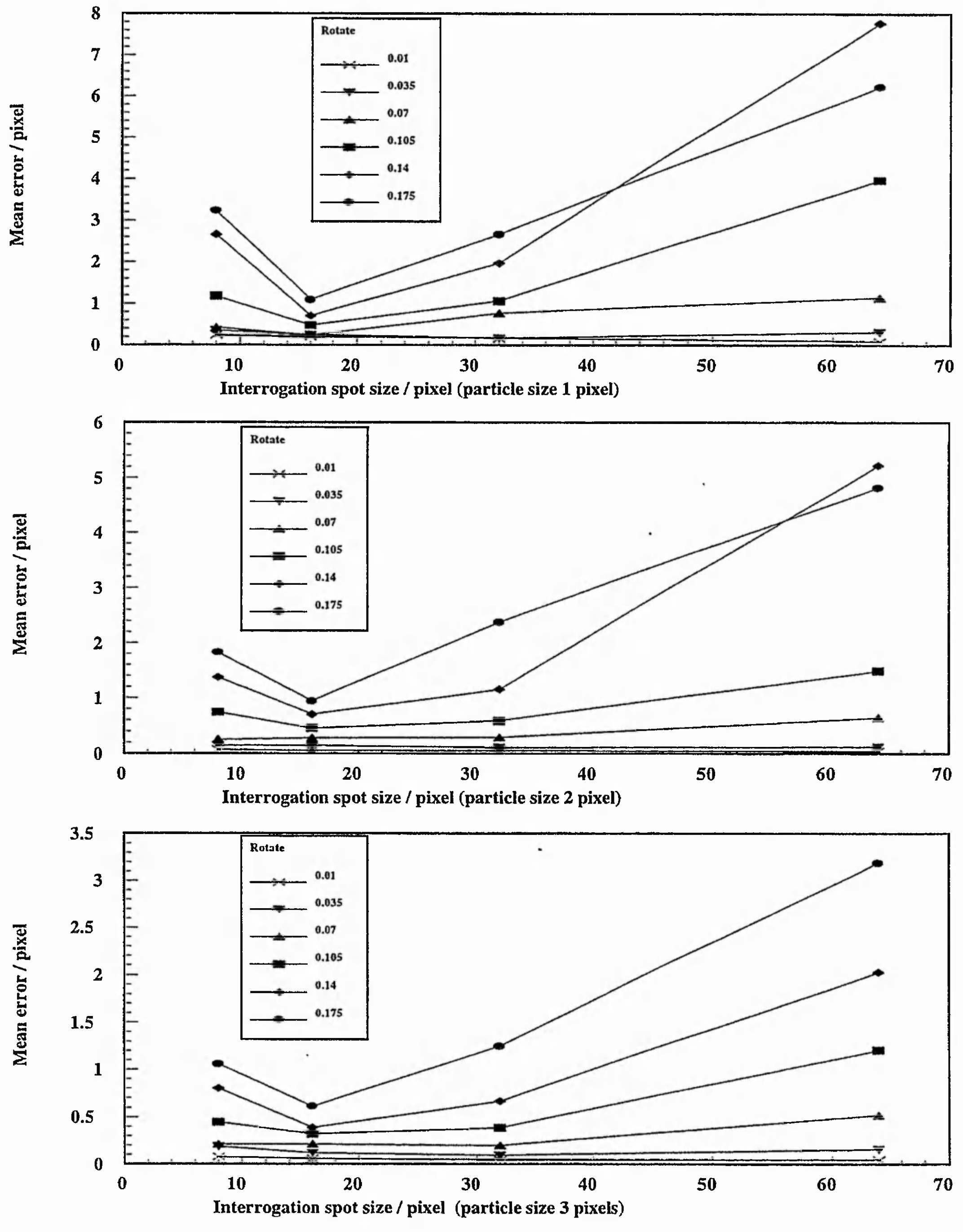

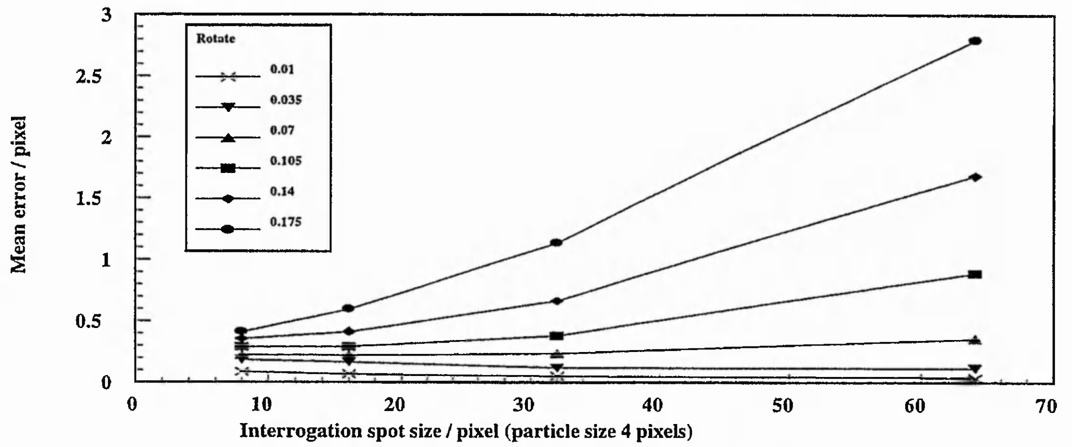
Rotate
0.01
0.035
0.07
0.105
0.14
0.175
Mean error / pixel
Interrogation spot size / pixel (particle size 4 pixels)

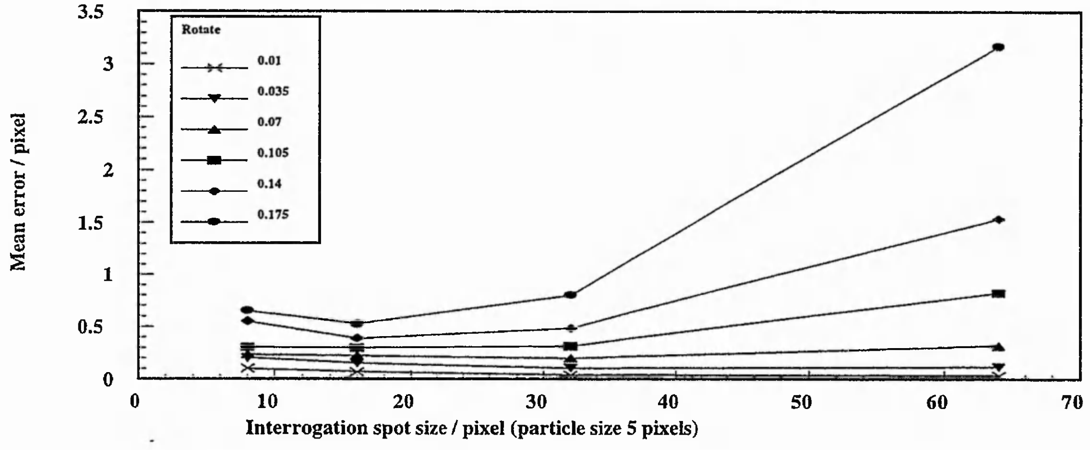
Rotate
0.01
0.035
0.07
0.105
0.14
0.175
Mean error / pixel
Interrogation spot size / pixel (particle size 5 pixels)

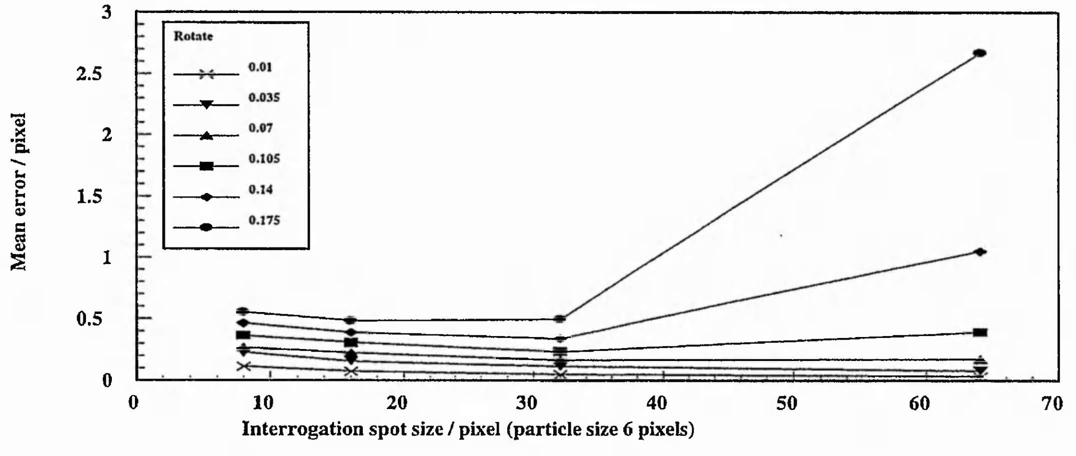
Rotate
0.01
0.035
0.07
0.105
0.14
0.175
Mean error / pixel
Interrogation spot size / pixel (particle size 6 pixels)

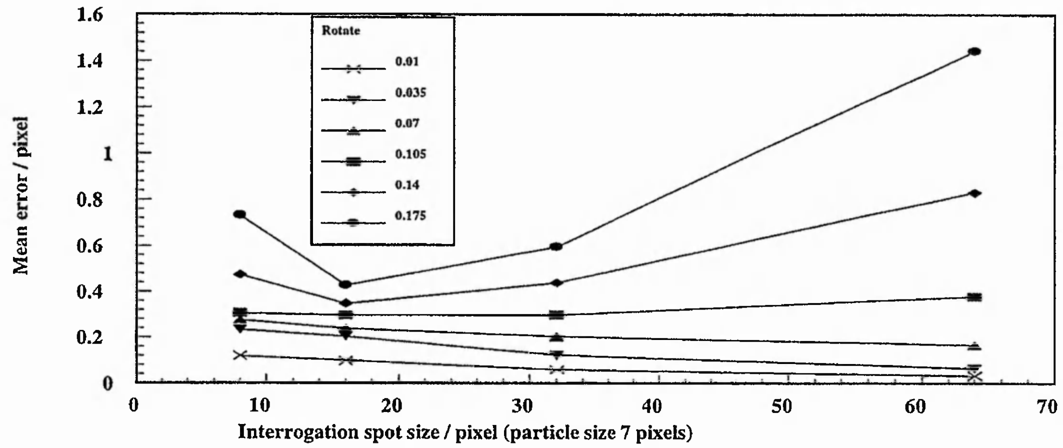

Figure 4.4 Mean errors for rotation movements using different interrogation spot sizes

A similar situation happens with the case of shearing movements, the mean errors increase as the shear increases. Similarly , increasing the interrogation spot size does not help to produce accurate measurement, see Figure 4.5.

Figure 4.5 Mean errors for shear movements using different interrogation spot sizes

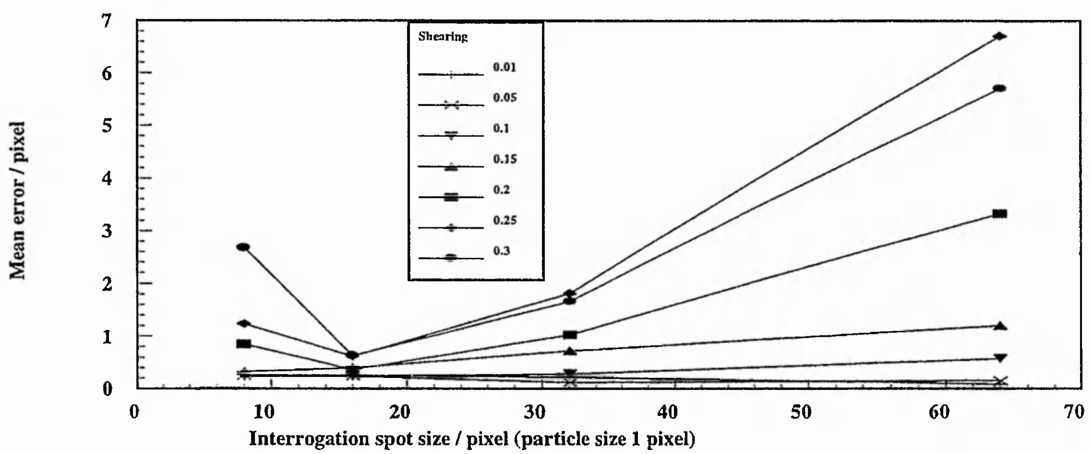

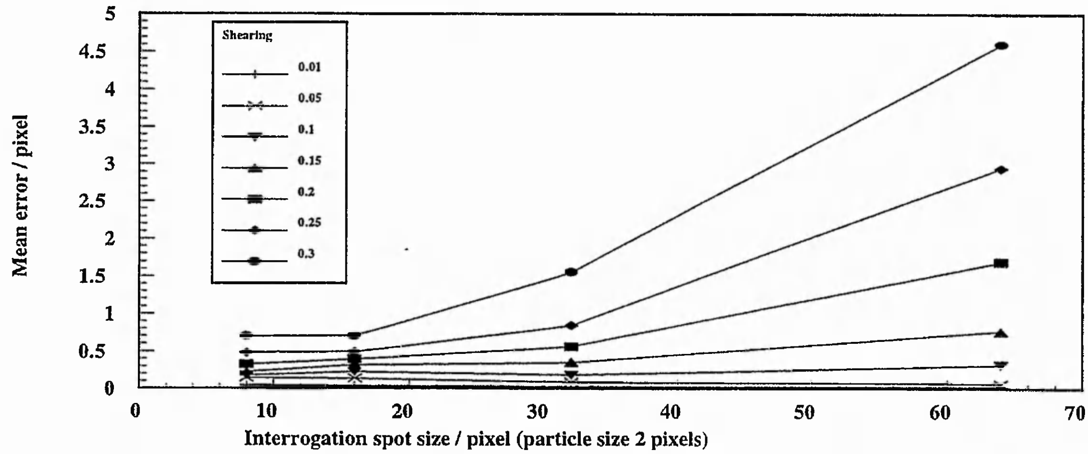
Shearing
0.01
0.05
0.1
0.15
0.2
0.25
0.3
Mean error / pixel
0
0.5
1
1.5
2
2.5
3
3.5
4
4.5
5
0
10
20
30
40
50
60
70
Interrogation spot size / pixel (particle size 2 pixels)

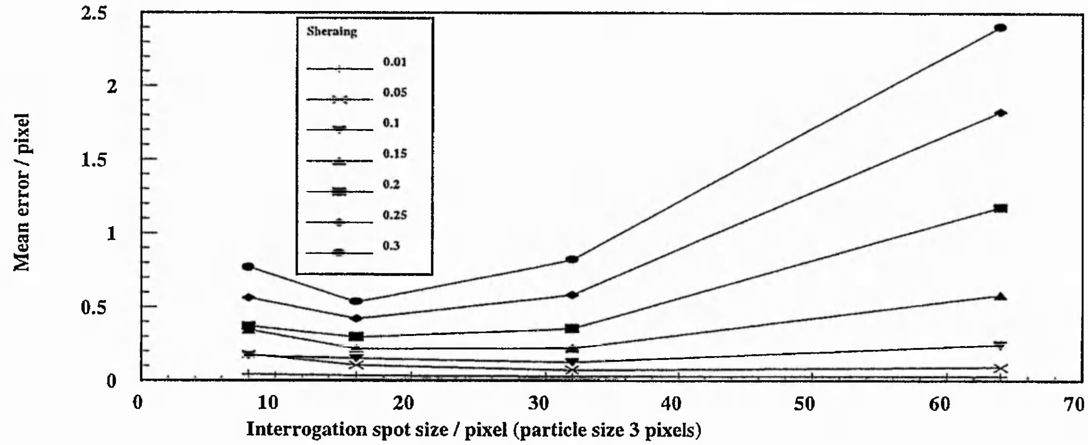
Sheraing
0.01
0.05
0.1
0.15
0.2
0.25
0.3
Mean error / pixel
0
0.5
1
1.5
2
2.5
0
10
20
30
40
50
60
70
Interrogation spot size / pixel (particle size 3 pixels)

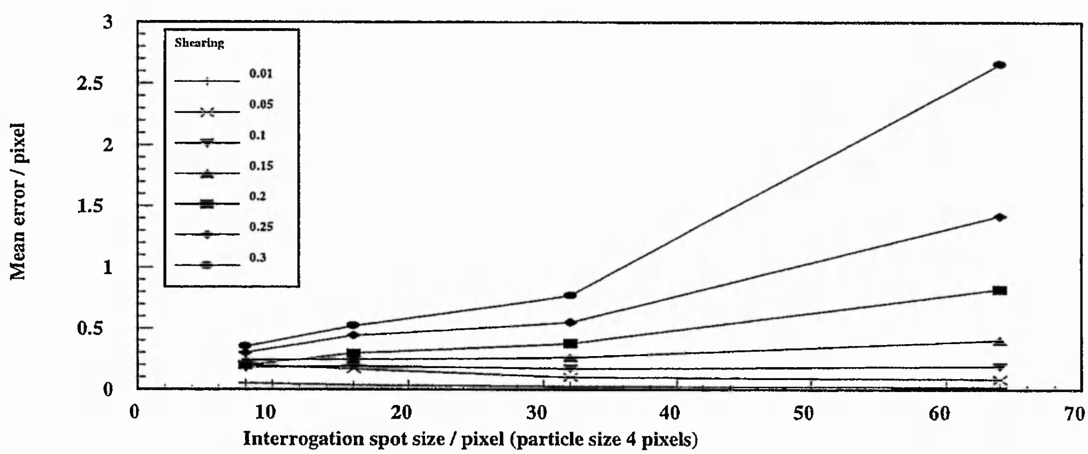
Shearing
0.01
0.05
0.1
0.15
0.2
0.25
0.3
Mean error / pixel
0
0.5
1
1.5
2
2.5
3
0
10
20
30
40
50
60
70
Interrogation spot size / pixel (particle size 4 pixels)

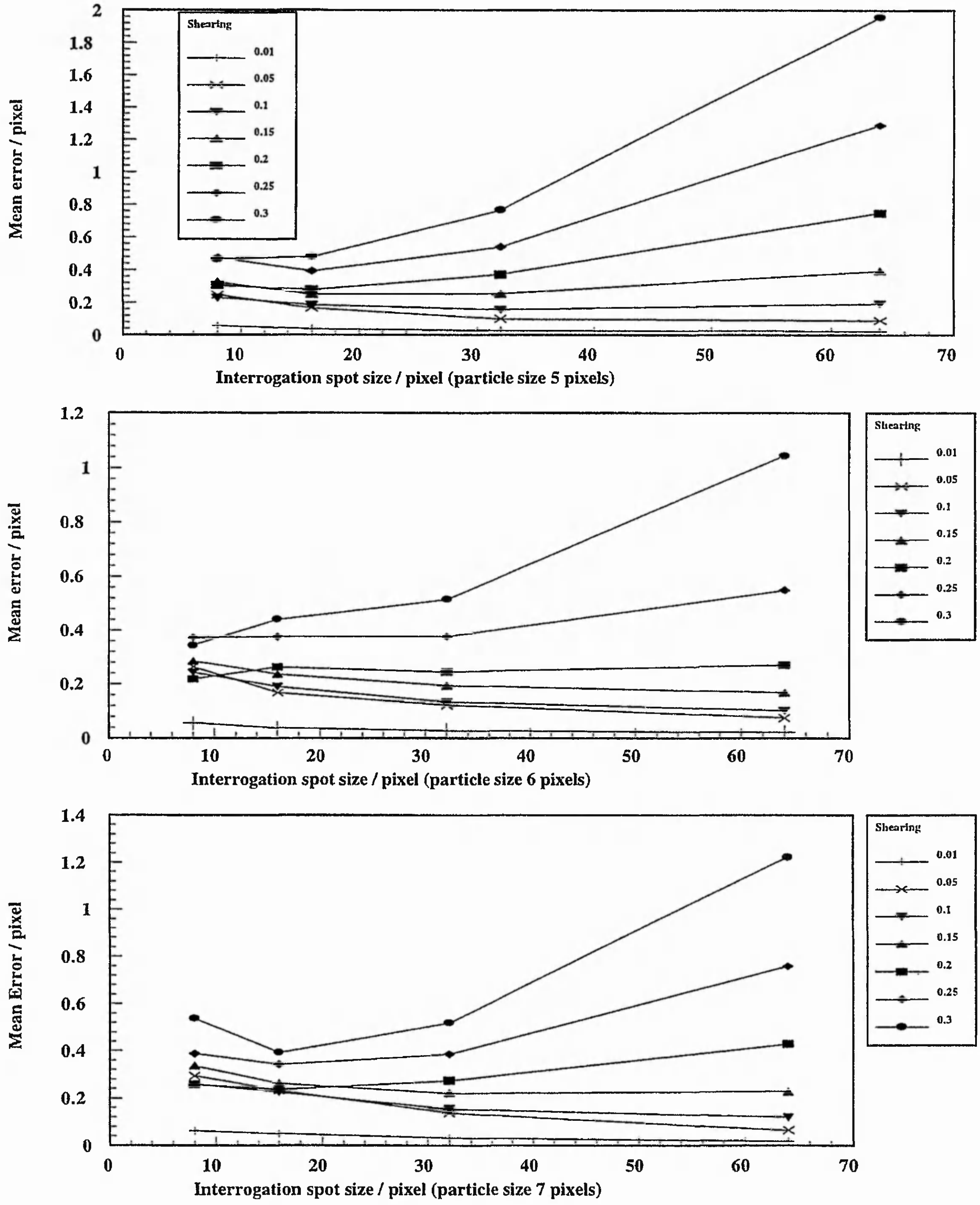

Figure 4.5 Mean errors for shear movements using different interrogation spot sizes

4.5.2 Image particle density

The image particle density has a strong influence on the measurement of the uniform displacements. The mean errors decrease as the density increases. Figure 4.6 shows the results of the mean errors of the measurements for the image particle density varying from 1 to 20 with an interrogation spot size of 32 pixels.

Figure 4.6 Mean errors for uniform displacements with different image particle densities

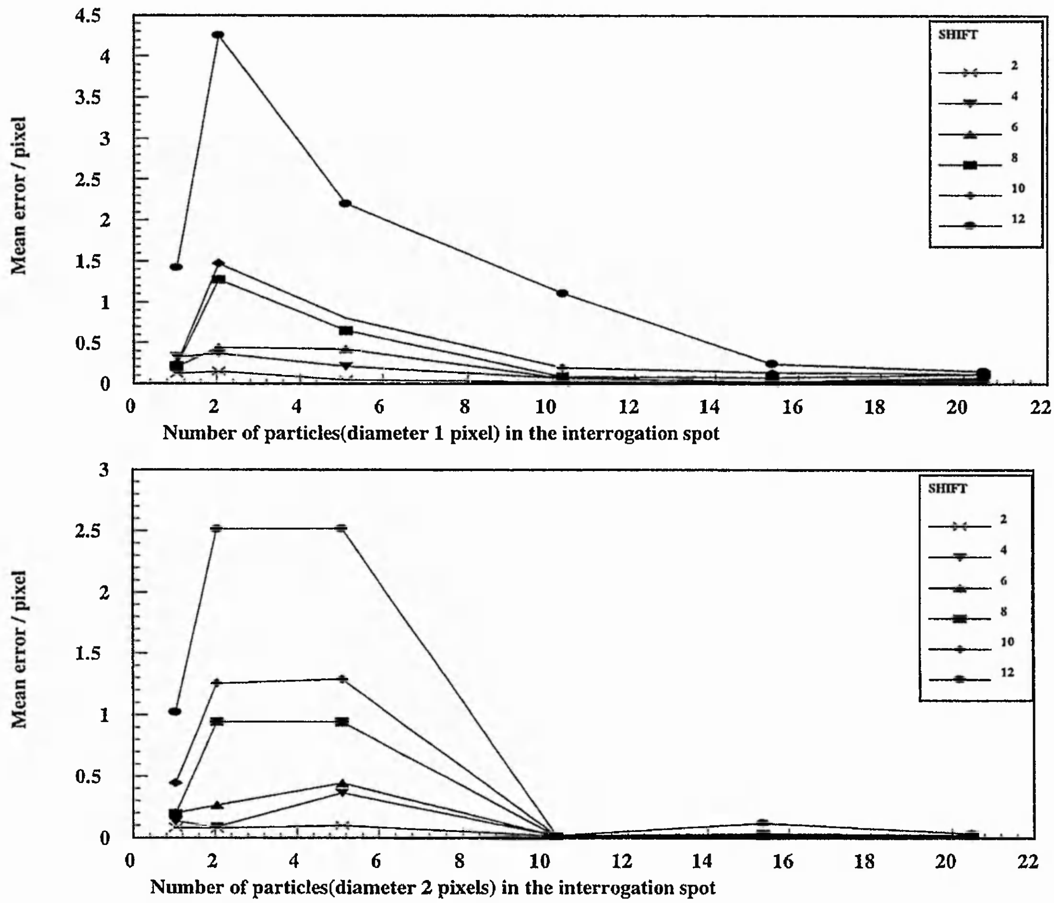

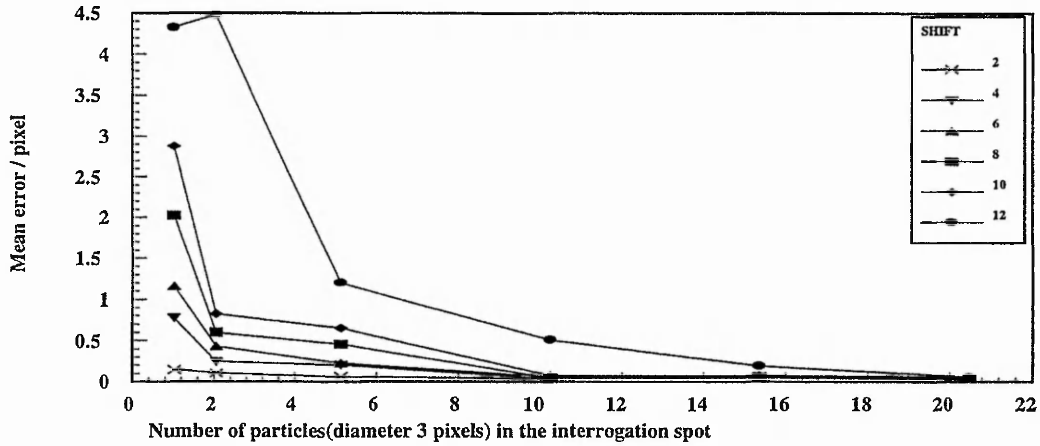
Mean error / pixel
Number of particles(diameter 3 pixels) in the interrogation spot
SHIFT
2
4
6
8
10
12

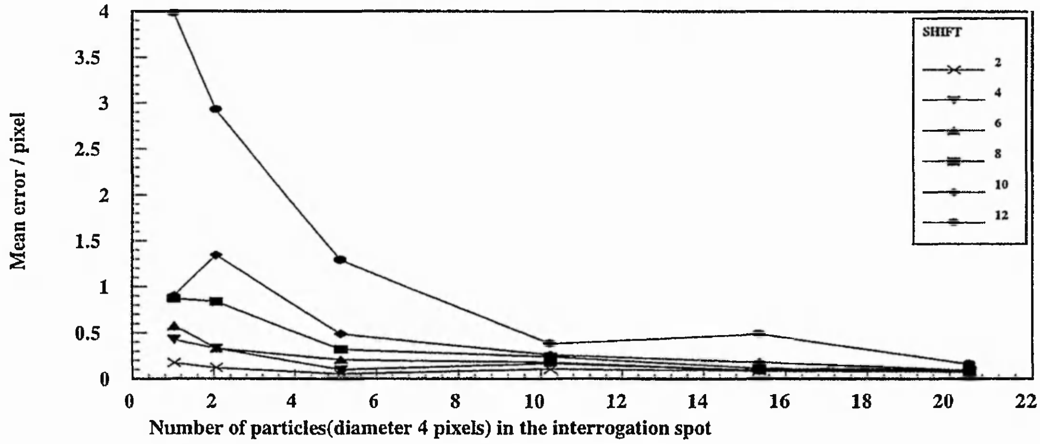
Mean error / pixel
Number of particles(diameter 4 pixels) in the interrogation spot
SHIFT
2
4
6
8
10
12

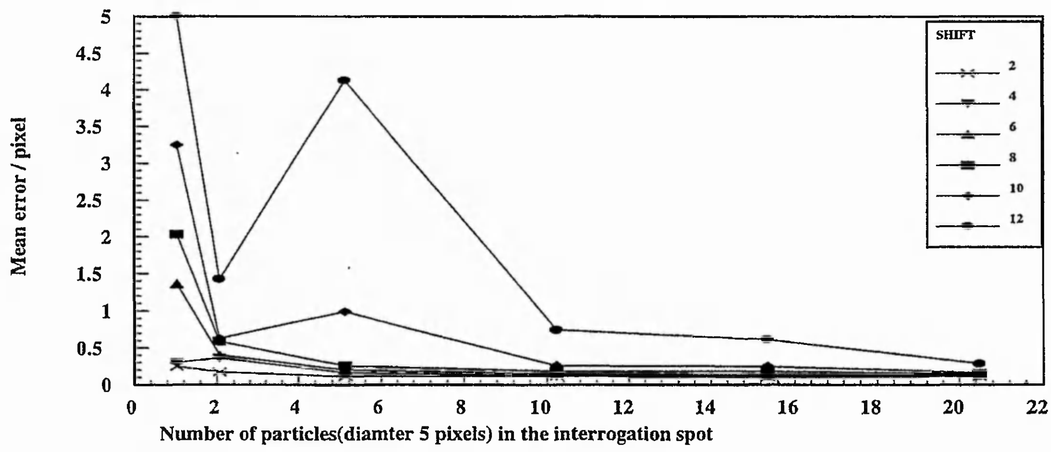
Mean error / pixel
Number of particles(diamter 5 pixels) in the interrogation spot
SHIFT
2
4
6
8
10
12

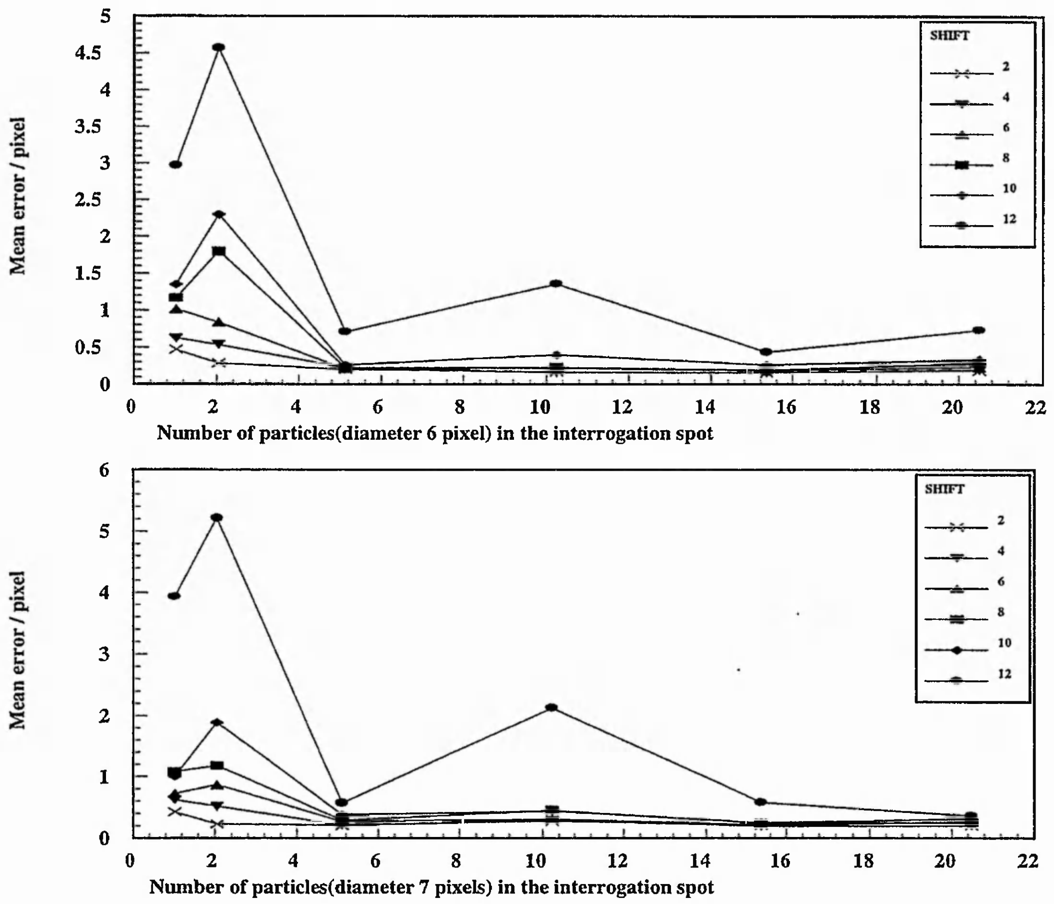

Figure 4.6 Mean errors for uniform displacements with different image particle densities

The image particle density has small influence for the cases of pure rotation movement and shear movement, because the image particle density affects the weight centre of the particles with the interrogation spot. The mean error decreases as the density increases (Figure 4.7, 4.8). The influence of the density becomes significant for large image particle size.

Figure 4.7 Mean errors for rotation movement with different image particle densities

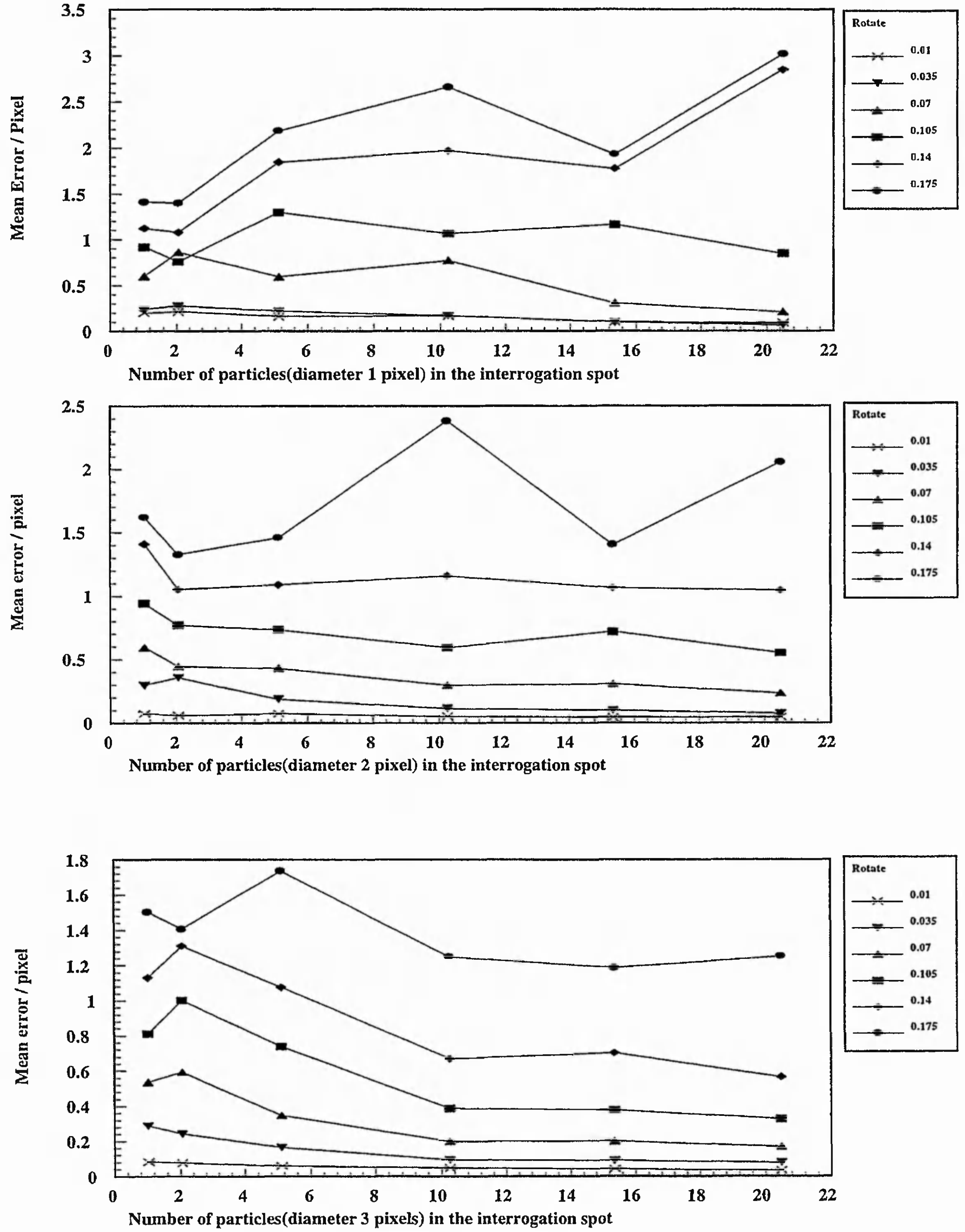

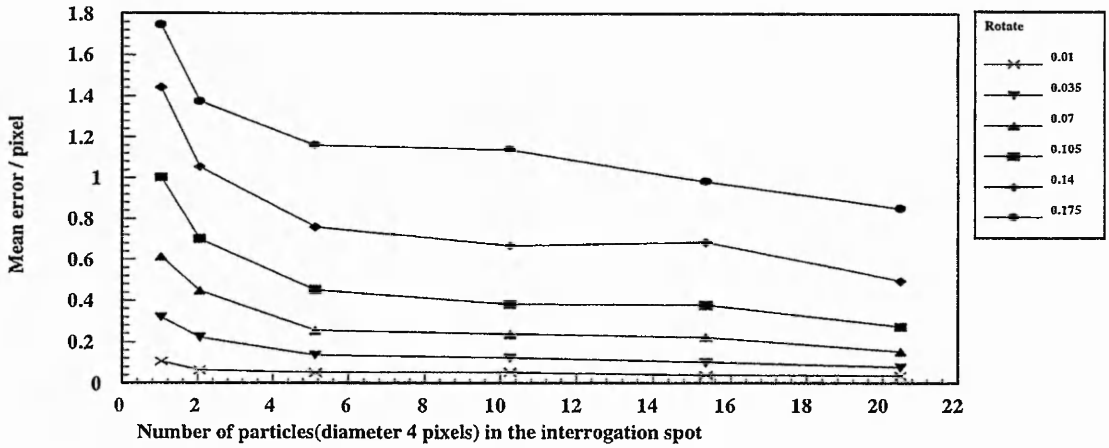
Mean error / pixel
1.8
1.6
1.4
1.2
1
0.8
0.6
0.4
0.2
0
0
2
4
6
8
10
12
14
16
18
20
22
Number of particles(diameter 4 pixels) in the interrogation spot
Rotate
0.01
0.035
0.07
0.105
0.14
0.175

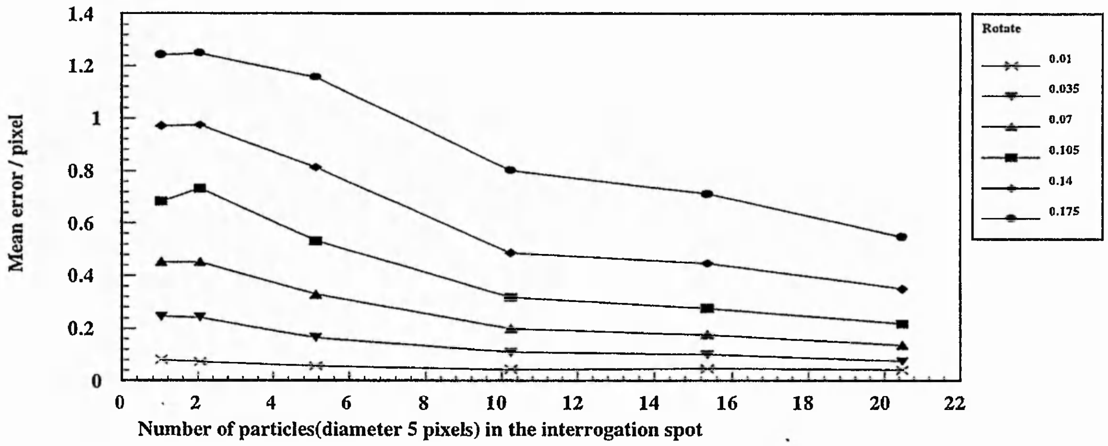
Mean error / pixel
1.4
1.2
1
0.8
0.6
0.4
0.2
0
0
2
4
6
8
10
12
14
16
18
20
22
Number of particles(diameter 5 pixels) in the interrogation spot
Rotate
0.01
0.035
0.07
0.105
0.14
0.175

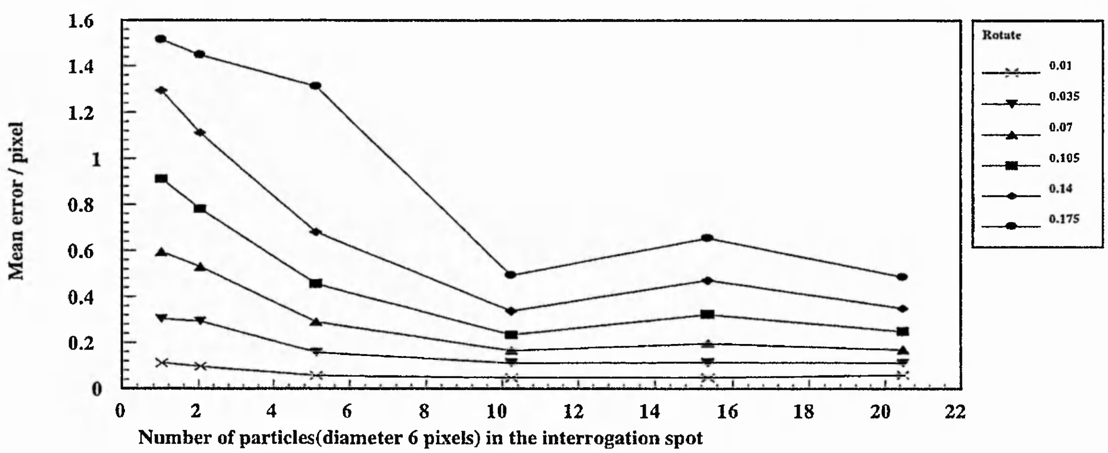
Mean error / pixel
1.6
1.4
1.2
1
0.8
0.6
0.4
0.2
0
0
2
4
6
8
10
12
14
16
18
20
22
Number of particles(diameter 6 pixels) in the interrogation spot
Rotate
0.01
0.035
0.07
0.105
0.14
0.175

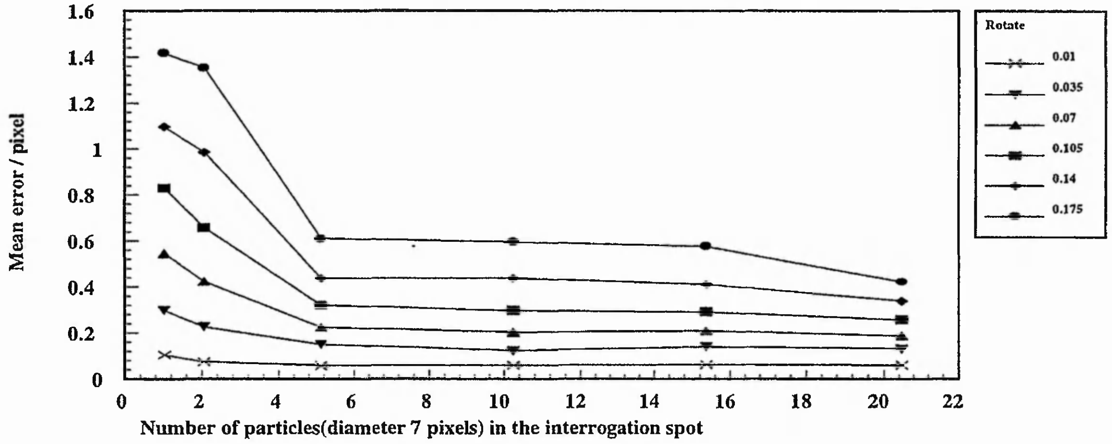

Figure 4.7 Mean errors for rotation movement with different image particle densities

Figure 4.8 Mean errors for shearing movement with different image particle densities

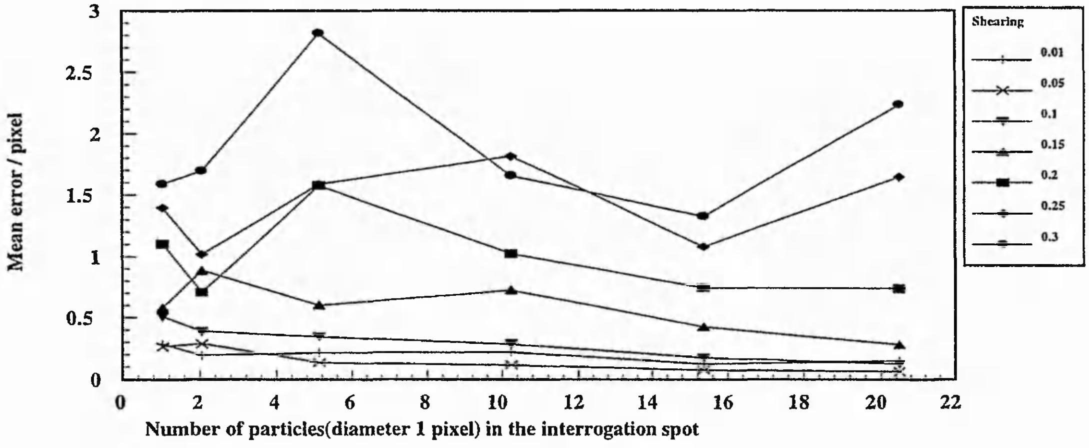

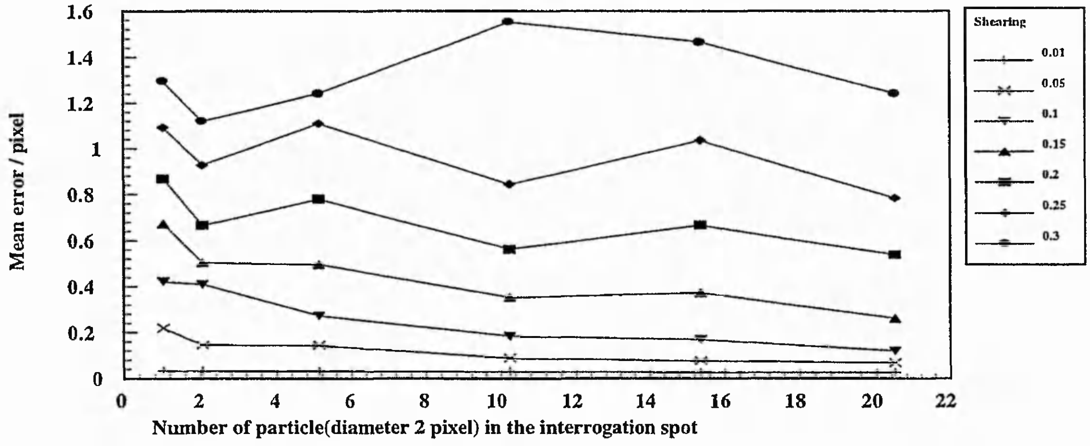

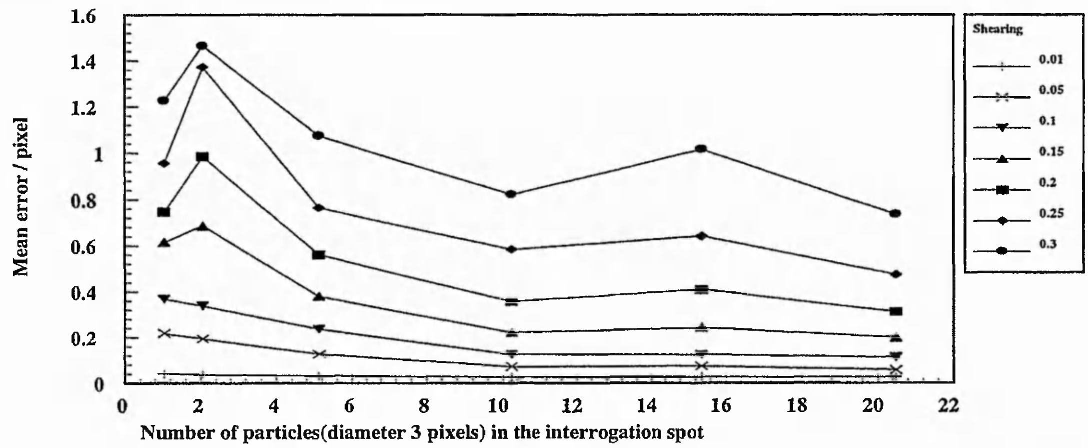
Mean error / pixel
Number of particles(diameter 3 pixels) in the interrogation spot
Shearing
0.01
0.05
0.1
0.15
0.2
0.25
0.3

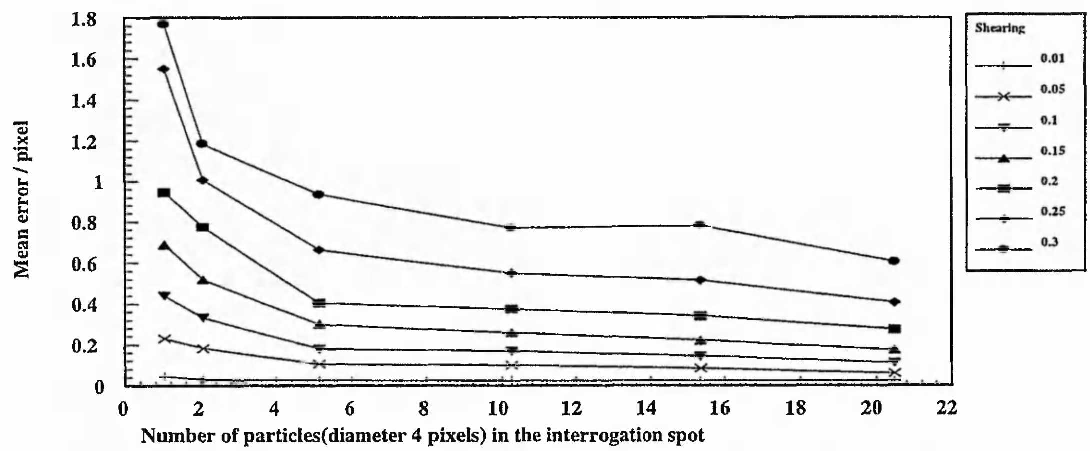
Mean error / pixel
Number of particles(diameter 4 pixels) in the interrogation spot
Shearing
0.01
0.05
0.1
0.15
0.2
0.25
0.3

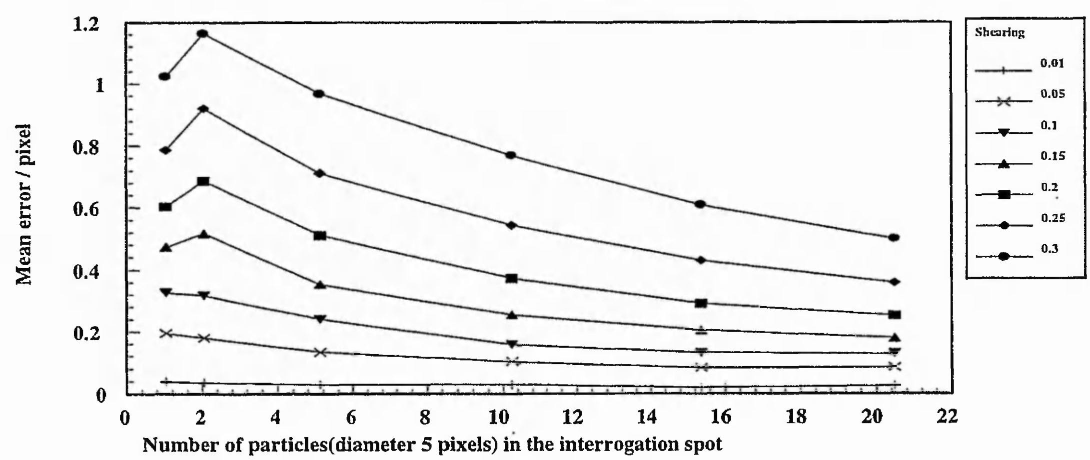
Mean error / pixel
Number of particles(diameter 5 pixels) in the interrogation spot
Shearing
0.01
0.05
0.1
0.15
0.2
0.25
0.3

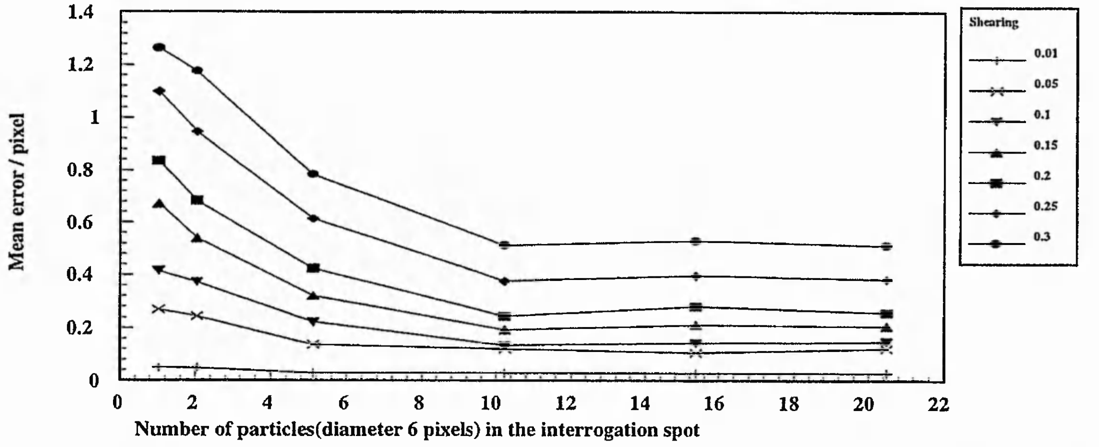

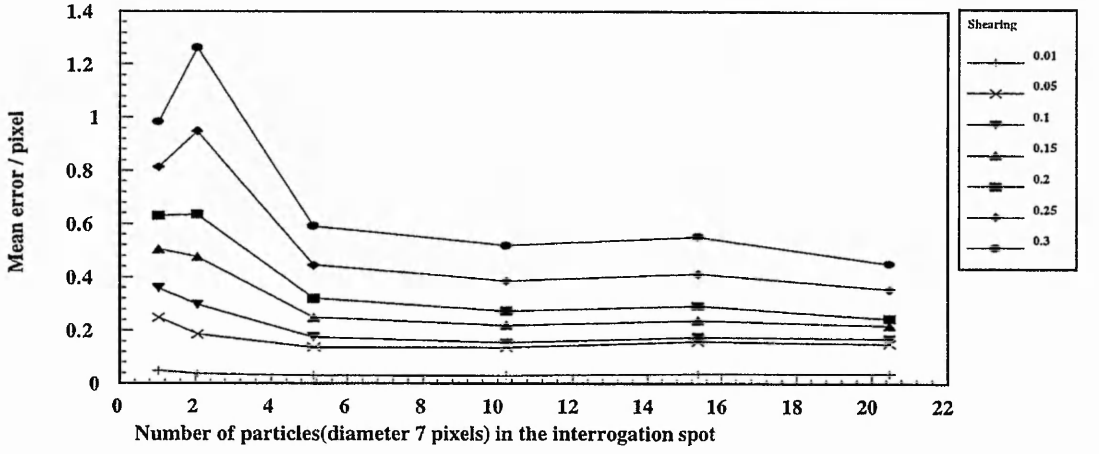

Figure 4.8 Mean errors for shearing movement with different image particle densities

4.5.3 Image particle size

The size of the image particle plays an important role in the measurement, it determines the width of the cross-correlation peak. Larger image particle size leads to broadening of the correlation peak, which then leads to error of the measurement (Figure 4.9).

In the case of pure rotation and shearing movements, the large image particle size helps to provide accurate measurement because larger size image particle tolerates larger rotation/shearing movement (see section 4.3.2 and 4.3.3).

4.5.4 Cross-correlation coefficients

The cross-correlation coefficients are collected in the cases of various values of uniform displacements, rotation and shear movements. The correlation peaks are biased due to rotation and shear. The values of the correlation peaks decrease as the values of the movements increase and vice versa (Figure 4.10, 4.11, 4.12).

Figure 4.9 Mean errors for three modes of movement with different particle sizes

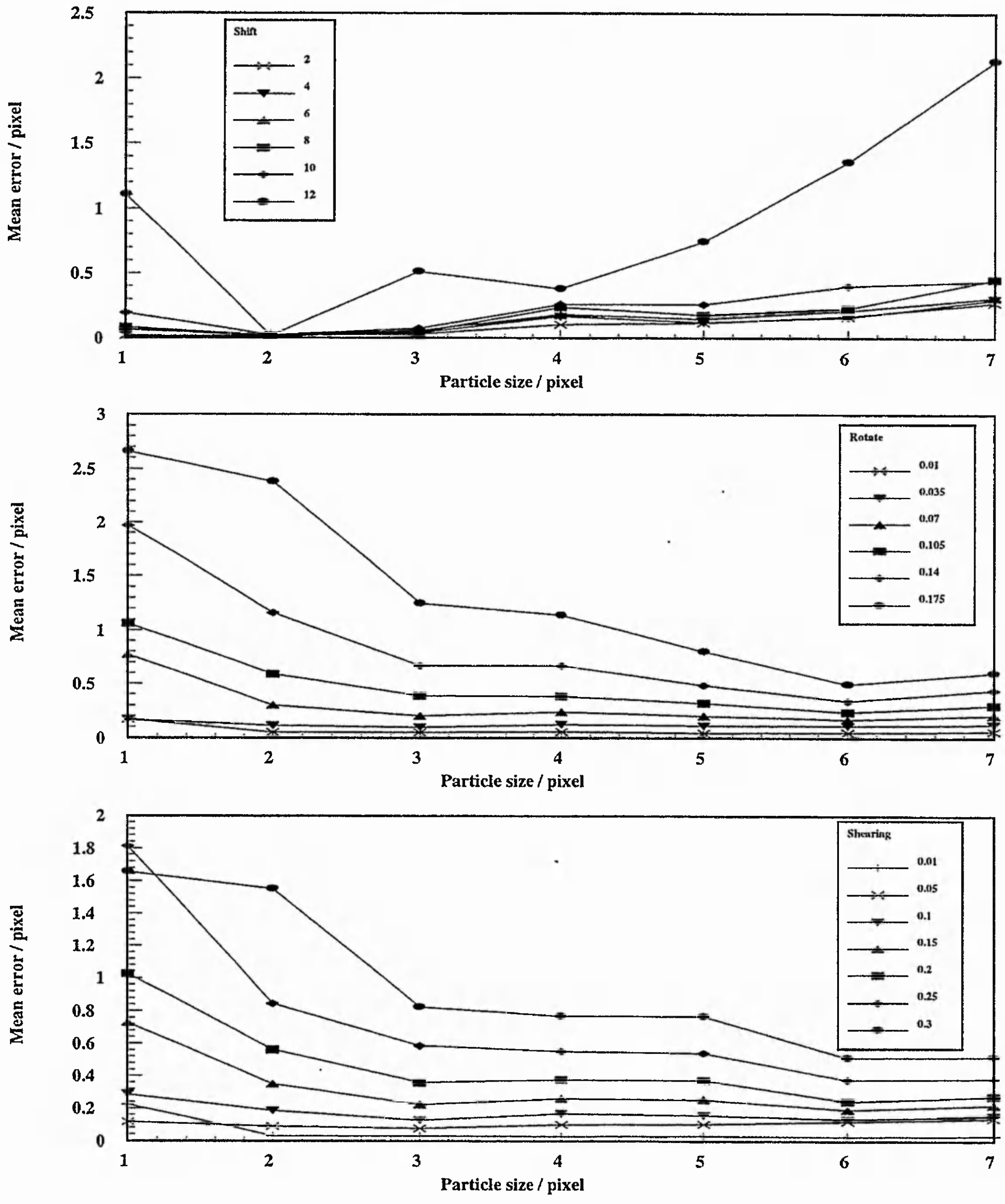

Figure 4.9 Mean errors for three modes of movement with different particle sizes

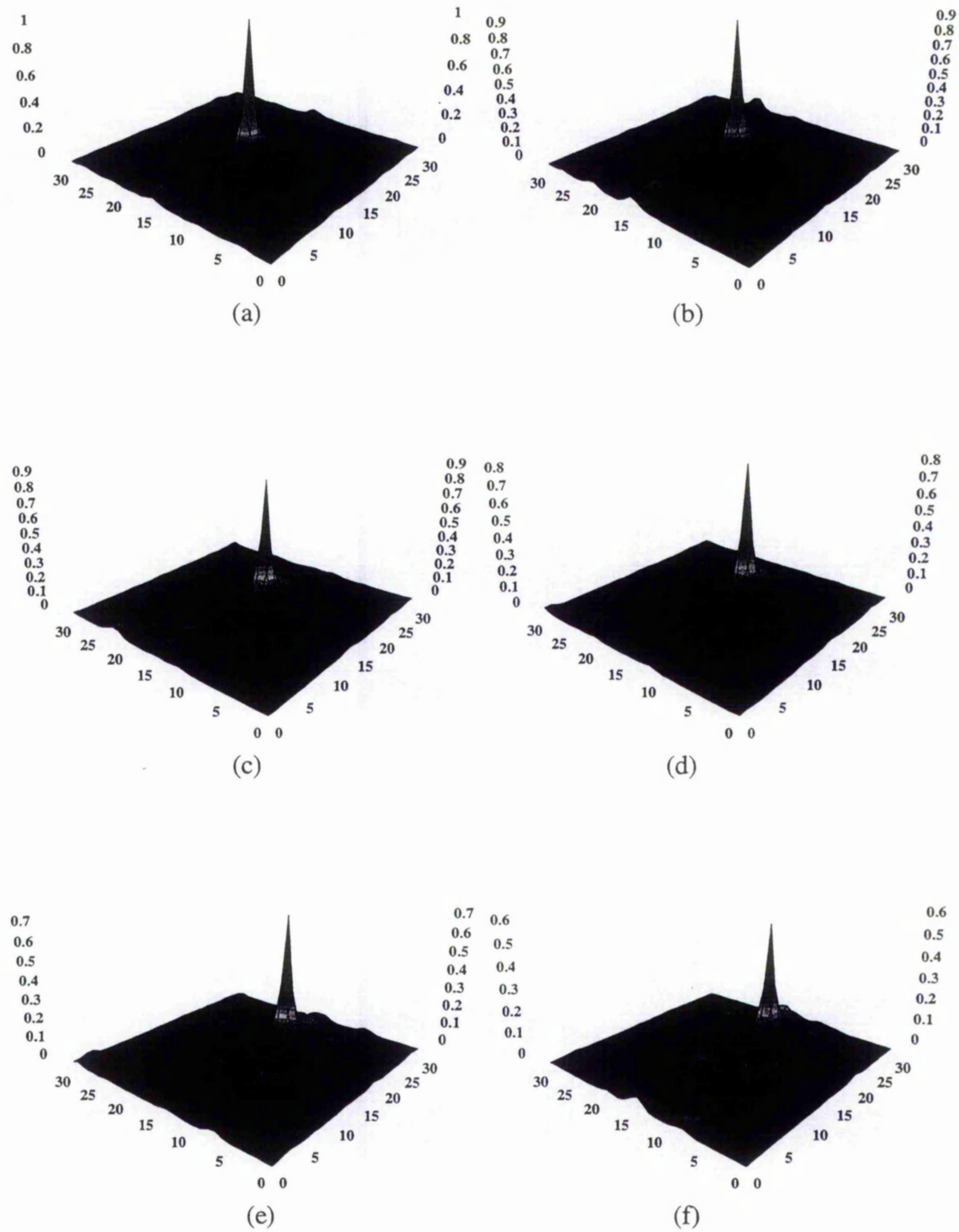

Figure 4.10 Cross-correlation coefficient distribution in the case of uniform displacements (a.0 pixel b. 2 pixels. c. 4 pixels d. 6 pixels e. 8 pixels f. 10 pixels)

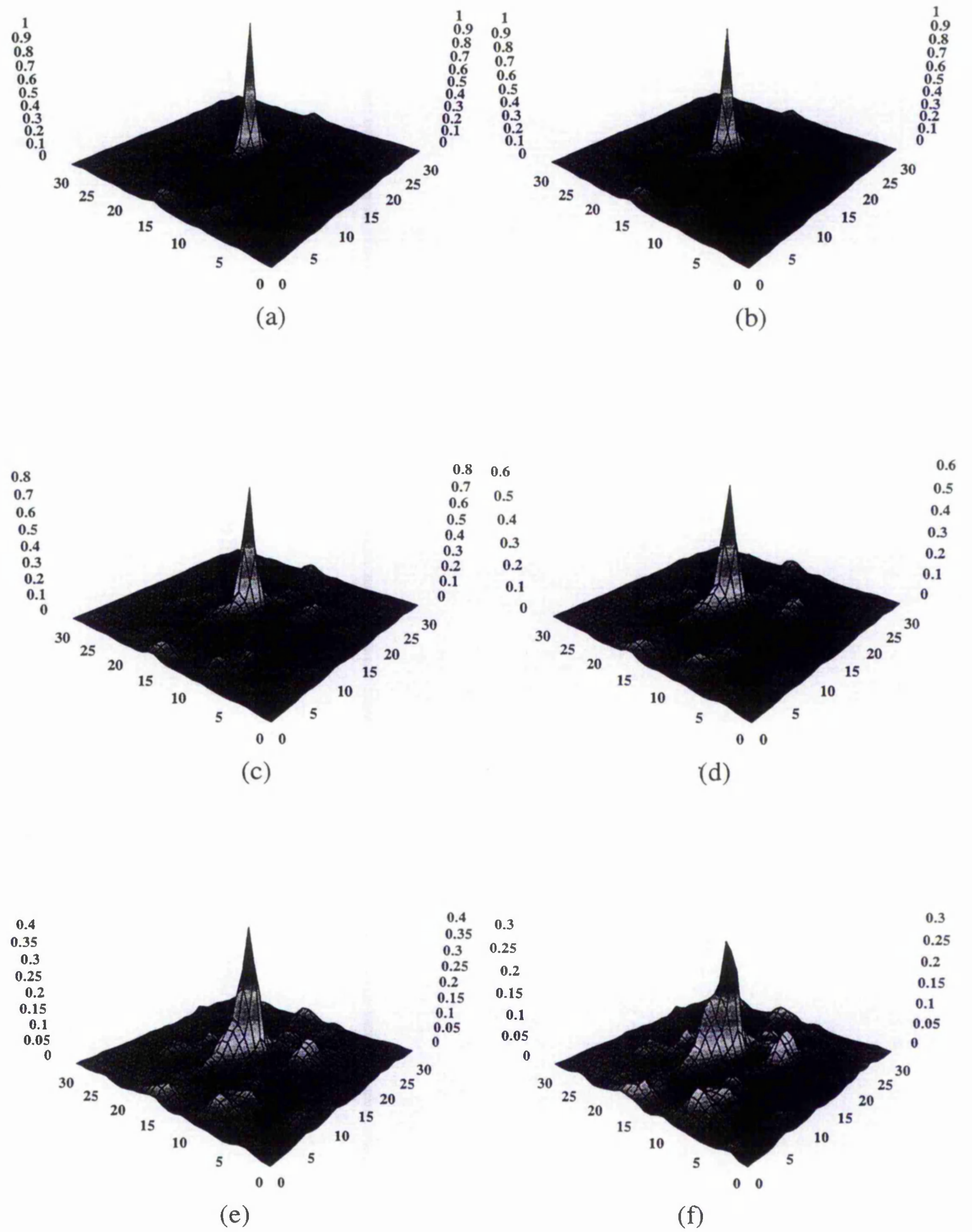

Figure 4.11 Cross-correlation coefficient distribution in the case of rotation movements (a. 0.01 radian b. 0.035 radian c. 0.070 radian d. 0.105 radian e. 0.140 radian f. 0.175 radian)

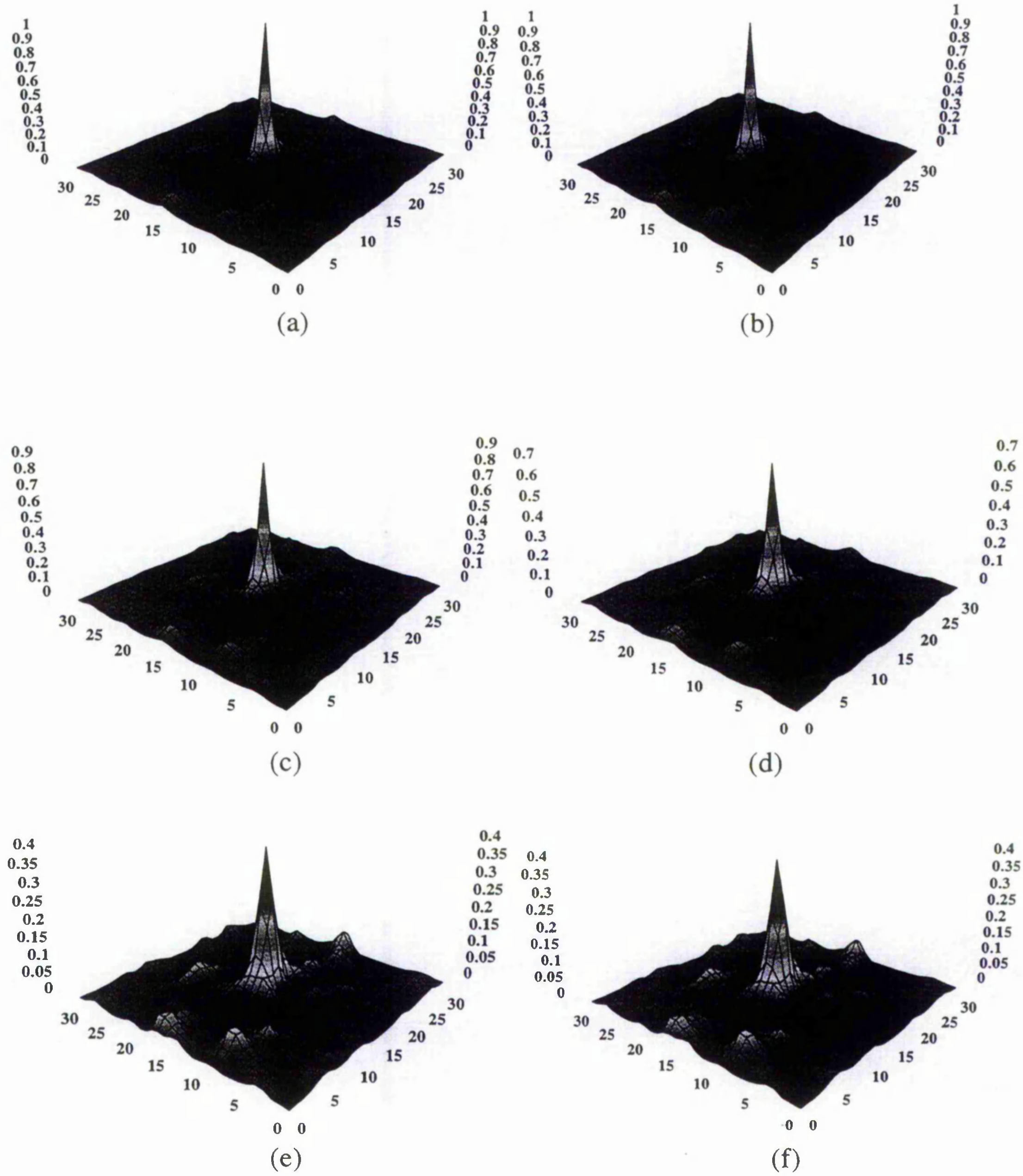

Figure 4.12 Cross-correlation coefficient distribution in the case of shearing movements (a. 0.01 b. 0.05 c. 0.10 d. 0.15 e. 0.20 f. 0.25)

4.6 Optimal parameter analysis

The image particle density strongly influences the accuracy of the measurement of uniform displacement. When the image particle density $N_I > 10$, the cross-correlation method provides good measurement as long as the displacement is less than one third of the interrogation spot size.

After the requirement of the image particle density is fixed, the interrogation spot size determines the source particle density. The size of the interrogation spot will affect the measurement resolution, the calculation time, the measurable range and the accuracy of the measurement. For better measurement resolution, a smaller interrogation spot size is required. Smaller spot means higher source particle density, which will affect the flow. A larger interrogation spot gives poor measurement resolution and requires longer calculation time. The interrogation spot size 32 is selected for the cross-correlation method in this thesis, considering calculation time, resolution of velocity measurement and image particle density.

The larger image particle size can tolerate larger rotation/shearing movements, but broadens the cross-correlation peak, resulting in poor measurement for uniform displacements. Large size of the image particle also requires large seeding particles in the flow for a fixed magnification, and too large particles will affect the flow movement. The image particle size at least of 3 pixels for a 32×32 interrogation spot is required for a optimal measurement, considering effects of flow movements. N_I is required not less than 10.

4.7 Conclusions

Because of the limitation of the video based PIV, the effects of local non-uniformity cannot be ignored. Uniform displacement causes the probability of finding particle pairs to be decreased, resulting in more erroneous measurement. The errors for rotation movements are related to the rotation angles and the weight centres of the particles within the interrogation spot. The errors for shearing movements are related to the shear and the weight centres of the particles within the interrogation spot. The larger image particle size broadens the correlation peak, which decreases the accuracy of the uniform displacement measurement but helps to tolerate larger rotation or shearing movements.

Simulations have been carried out to investigate the relationships between the measurement error and the interrogation spot size, the image particle density and the particle size. For uniform displacement, the large interrogation spot size and high image particle density will improve the measurement accuracy. In the case of the rotation and shear movements, the rotation angle, the shear and the particle size determine the accuracy of the measurement. Increasing the spot size and the image particle density has little effect on improving the accuracy of the measurement. The value of the cross-correlation peak increases as the values of the uniform displacements, rotation and shearing movements decrease. For an optimal experiment, the required image particle density must be larger than 10 with the interrogation spot size 32×32 pixel and the image particle size of 3 pixels.

Chapter 5 Improved cross-correlation algorithm

There are two major steps in PIV, firstly the particle images are recorded and secondly the velocity data are extracted from the particle images. Before recording the image, the seeding particle density, the seeding particle and its size, the light source and the thickness of the light sheet, the image system and the recording media are chosen. These parameters determine the characteristic properties of the particle images. After recording the particle images, a suitable velocity extraction method is selected based on the characteristic property of the image.

According to the recording media, PIV methods are categorized into photographic PIV and video based PIV (Willert and Gharib 1991). For video based PIV, the resolution of particle images and the time interval between the images are limited by the image facility. Application of the conventional cross-correlation method assumes that the velocity distribution inside the interrogation spot is uniform, ignoring the non-uniformity of the velocity. In the case of using particle images directly from the frame grabber, the non-uniformity of the velocity cannot be ignored because of the low image resolution of the frame grabber. The accuracy of the velocity measurement is affected by the local non-uniformity within the interrogation spot, that has been investigated in chapter 4.

In this chapter, an improvement to the conventional cross-correlation method is proposed to eliminate the effects of the local non-uniformity. A new second image of PIV can be created from the original second image using the velocity data obtained by the conventional cross-correlation method. The difference between the first image and the new second image is used to compensate the velocity data obtained. The compensation is based on the fact that the normalized cross-correlation coefficient of two identical functions is unity, and the true velocity distribution will enable the new second image to be identical to the first image. The more favourable data are kept while the less favorable data are rejected. The procedure is iterated until all the cross-correlation coefficients of the interrogated points reach their maximum value. Simulation results have proved that the accuracy of velocity data are improved using this technique.

5.1 The improved cross-correlation method

The ensemble statistical property of cross-correlation of the particle image is given in equation (3.29),

$$< R(\mathbf{k},\mathbf{l}) >= \Delta z\, I_0^2 N_I F_w F_z \tau_\infty^2 F_\tau((\mathbf{l}-\mathbf{k})\Delta - M\mathbf{u}\Delta t) \qquad (5.1)$$

The local non-uniformity inside the interrogation spot affects the function F_τ. The function F_τ becomes narrower as the velocity distribution vanishes.

For individual interrogation, the possibility of having more than three paired particles inside the interrogation spot is high when the three velocity movements - uniform displacement, rotation and shear is small and vice versa, as given in section (4.6).

Above all, both the ensemble analysis and the individual case studies proved that velocity measurement at the interrogation spot with smaller non-uniformity in velocity distribution has better accuracy.

An improved cross-correlation method is proposed to compensate for the effects of non-uniformity within the interrogation spot, reconstructing the second image utilizing the velocity data $\boldsymbol{u}'$ calculated from equation (4.1). By calculating the cross-correlation of the first image and the reconstructed second image, the velocity compensation can be found:

$$< R(\mathbf{k}',\mathbf{l}') >= \Delta z\, I_0^2 N_I F_w F_z \tau_\infty^2 F_\tau((\mathbf{l}'-\mathbf{k}')\Delta - M(\mathbf{u}-\mathbf{u}')\Delta t) \qquad (5.2)$$

In fact, the reconstruction method decreases the scale of the three movement terms within the interrogation spot between the first image and the new second image. That increases the signal to noise ratio of the cross-correlation coefficients. The compensation procedure is iterated until the cross-correlation coefficients $<R>$ at each interested position of full flow reach their maximum values.

In the procedure of the iteration, the velocity data with higher maximum cross-correlation coefficients than their old values are saved to replace the old data. The higher correlation coefficients prove that those velocity data can rebuild the second image with greater similarity to the first image than the previous data.

If whole field displacement vectors $(\Delta x, \Delta y)$ are known between images ***A*** and ***B***, and the flow is two-dimensional, the second image pattern can be rebuilt to be similar to the first image. The whole field displacement vectors are

$$\begin{aligned} x_B &= x_A + \Delta x \\ y_B &= y_A + \Delta y \end{aligned} \tag{5.3}$$

where (x_A, y_A) is the position of a particle in image ***A*** at time ***T*** and (x_B, y_B) is the position of the same particle in image ***B*** at time $T+t$. A digitized particle image is represented by the pixel's grey distribution. This means that the grey $I(x_B, y_B, T+t)$ in image ***B*** is equal to $I(x_A, y_A, T)$ in image ***A***.

A new image ***B'*** can be reconstructed from image ***B***. The grey $I(x_{B'}, y_{B'}, T)$ in ***B'*** is the grey $I(x_B, y_B, T+t)$ in ***B***, where $(x_{B'}, y_{B'})$ is identical to (x_A, y_A). Noticing that x_A and y_A must be integers and the displacements $(\Delta x, \Delta y)$ are usually non-integers, the pixel intensity of position (x_B, y_B) is obtained using bi-linear interpolation:

$$I(x_B, y_B) = \sum_{i=0}^{3} N_i \cdot I_i \tag{5.4}$$

where

$$
\begin{aligned}
i_B &= integer(x_B) \quad \varepsilon_i = x_B - i_B \\
j_B &= integer(y_B) \quad \varepsilon_j = y_B - j_B \\
I_0 &= I(i_B, j_B) \qquad I_1 = I(i_B, j_B+1) \\
I_2 &= I(i_B+1, j_B) \quad I_3 = I(i_B+1, j_B+1) \\
N_0 &= (1-\varepsilon_i)(1-\varepsilon_j) \quad N_1 = (1-\varepsilon_i)\varepsilon_j \\
N_2 &= \varepsilon_i(1-\varepsilon_j) \qquad N_3 = \varepsilon_i \ \varepsilon_j
\end{aligned}
\tag{5.5}
$$

$I(x_B, y_B)$ is set at position $(x_{B'}, y_{B'})$ in ***B'***. After all the pixels' grey levels are calculated, ***B'*** is constructed. The image ***B'*** is sampled by a window $g'(x,y)$ centred at position (x,y). If the displacement data is accurate and the particle flow is two-dimensional, neglecting electronic noise and the averaging effect of bi-linear interpolation, the highest cross-correlation coefficient of $f(x,y)$ and $g'(x,y)$ will be 1.

The whole field displacement is currently unknown. The displacement data $(\Delta x,\Delta y))$ at each point can be calculated using the conventional cross-correlation method. Supposing the actual displacement is $(\Delta x+dx,\Delta y+dy)$, where (dx,dy) is a measure of the non-uniformity of the displacement around the point, then if the second image ***B'*** is built based on $(\Delta x,\Delta y)$ and the window $g'(x,y)$ is sampled, the peak position of the cross-correlation between $f(x,y)$ and $g'(x,y)$ will be offset from the origin by $(d'x,d'y)$. $(d'x, d'y)$ is an average over the interrogation NxN window and normally small compared to $(\Delta x,\Delta y)$ so that the effects of non-uniformity are reduced. A new displacement vector $(\Delta x+d'x,\Delta y+d'y))$ is found which is more accurate because of lower scale of the three terms of movement.

5.2 Algorithm

Before the new procedure is introduced, an assumption is made that the higher the correlation coefficient, the higher will be the accuracy of the velocity data.

Since the initial velocity data is unknown it is necessary to use an iterative procedure, which includes six major steps:

1). Use the conventional cross-correlation velocity method to extract initial full field displacement vectors. Eliminate error vectors using a median filtering subroutine (Westerweel 1993).

2). Bi-linear interpolation of the displacement at every pixel inside the first image $\boldsymbol{A}$ using the extracted velocity. Find the grey level of every pixel of the new second image $\boldsymbol{B'}$ by the procedure introduced in the previous section.

3). Copy $\boldsymbol{A_o}$ as the outside image of $\boldsymbol{B'}$ for velocity extraction at the points around its boundary, in case parts of $f(x,y)$ and $g'(x,y)$ have been sampled from the outside image $\boldsymbol{A}$ and $\boldsymbol{B}$.

4). Set a correction count to record the correction time and null it.

5). Calculate the cross-correlation of $f(x,y)$ and $g'(x,y)$. Find the peak position of the coefficient map. If the highest coefficient is larger than the recorded coefficient of position (x,y), add the offset to the recorded displacement at position (x,y) and add 1 to the correction count. Otherwise, omit this position and continue at next position.

6). Continue until all full field velocity vectors have been corrected, check the correction number, if no null, return to step 3, if null, exit.

5.3 Validation of the improved method

Synthetic flow images were generated for simulating uniform, recirculating and biaxial shearing flows for validation of the improved cross-correlation method. The first recorded image was obtained using a simulation package which is introduced in chapter 3. The second image was generated by translating, rotating or bi-axially shearing the first image to simulate uniform, recirculating and biaxial shearing fluid flows using imaging techniques. The second image of the synthetic uniform flow was generated by shifting the first image in the X direction by a known distance. Distances of 2, 4, 6, 8 and 10 pixels were applied and the resulting second images were saved separately for velocity extraction. The second images of simulated recirculating flow were obtained by rotating the first image by angles of 0.035, 0.07, 0.105, 0.14 and 0.175 radians around the centre of the first image. Shearing flow was simulated by shearing the first image with shear strains of 0.05, 0.1, 0.15, 0.2, 0.25 and 0.3. After the images were generated, the conventional method and the improved method were applied to extract the velocity data which were compared with the expected data.

The mean errors for the measurements of uniform displacement, rotation and shear movements decrease after median filtering, because the obvious erroneous vectors are eliminated. The improved cross-correlation method further decrease the errors of the measurement (Figure 5.1).

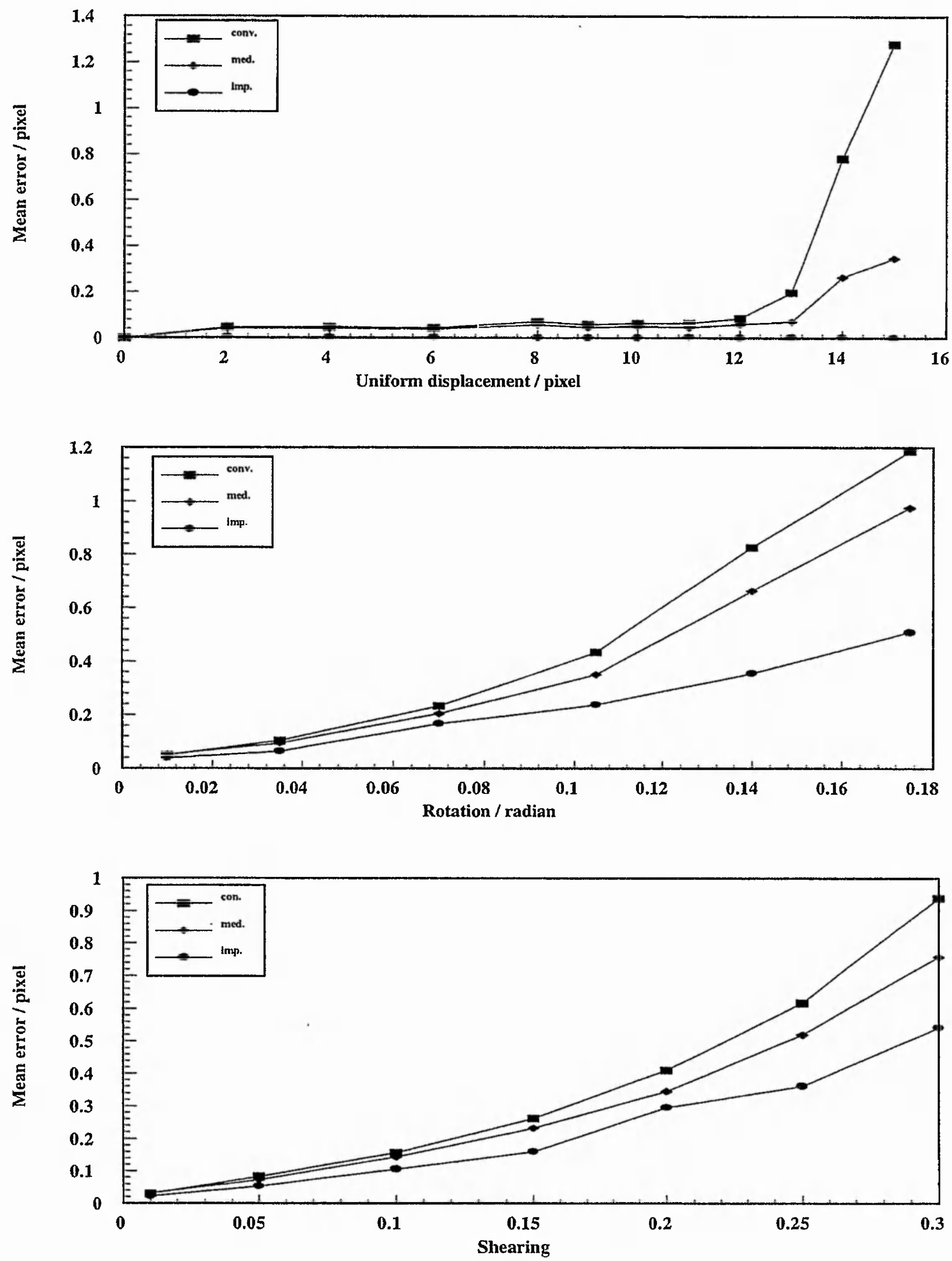

Figure 5.1 Comparison of mean errors
(conv - conventional PIV, med - median filtered result, imp - improved result)

For uniform displacements, the errors are suppressed. The new second image could be rebuilt to be the same as the first image because of the simple uniform displacements. The conventional PIV results provide a good initial point for the improved method to commence iteration, resulting in better reconstruction.

For rotation and shear movement, the errors have been decreased by 30% comparing the filtered results of the conventional PIV, but cannot be eliminated throughout, see Figure 5.1. Ignoring the electronic noise, there are two reasons for this. Firstly, the velocity of each pixel in the second image is interpolated from the extracting velocities. By-linear interpolation could not provide precise velocity for every pixel, the reconstruction of the second image could not provide the exact copy of the first image. Secondly, the random distribution of particles within the interrogation spot biased the correlation peak, that can only be partly compensated by the improved method because of the first reason.

Figure 5.2 shows the comparison of the mean value of the maximum correlation coefficients of points inside the area of interest obtained from the conventional method and the improved method using the parabolic curve fit procedure. For the three modes of movement, the value of the maximum correlation coefficient is approaching 1.0 as the improved cross-correlation method is applied. The results of cross-correlation coefficients indicate: a) the improved cross-correlation method provides more accurate velocity data which could be used to

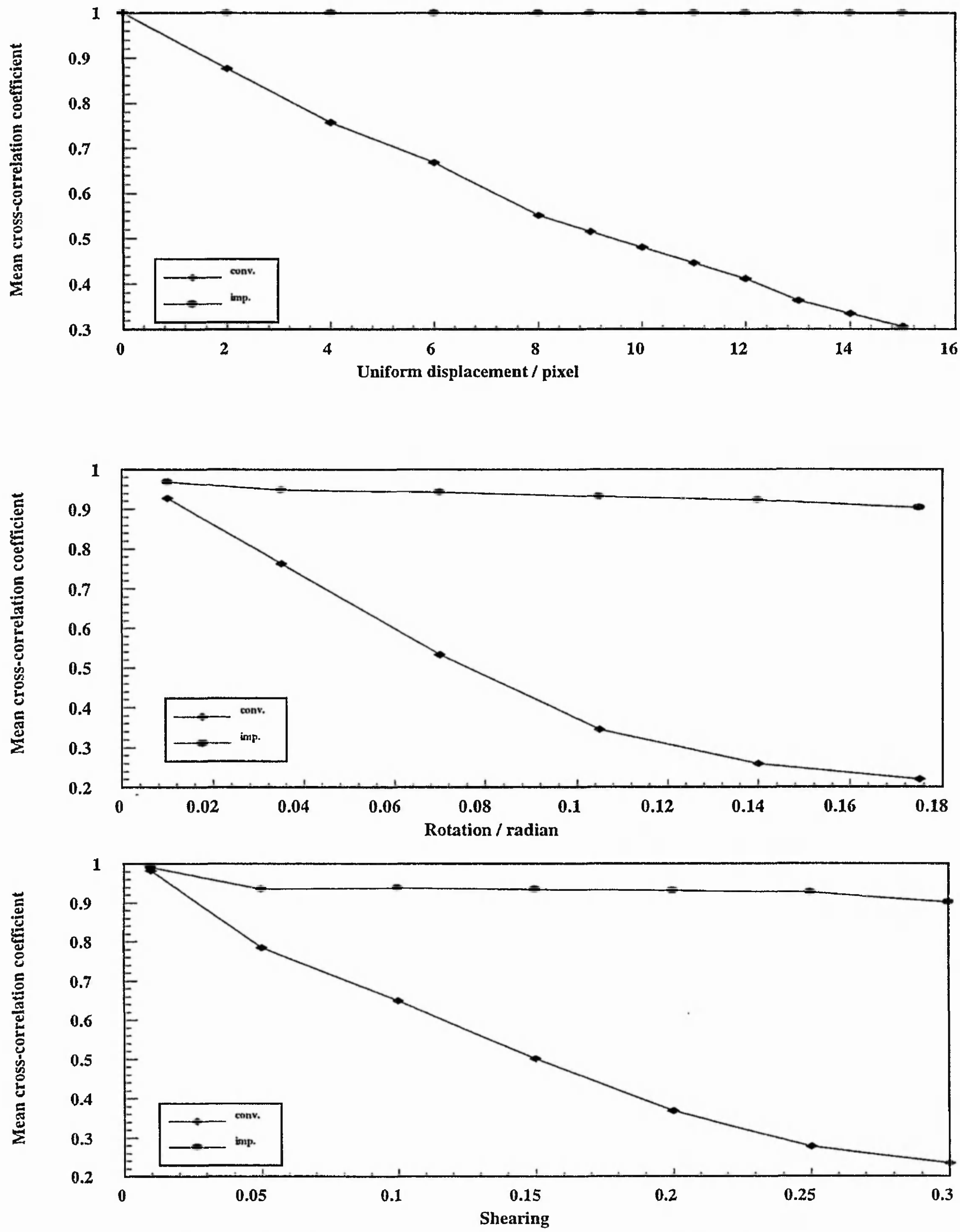

Figure 5.2 Comparison of cross-correlation coefficients
(conv - conventional PIV, imp - improved result)

generate the new second image, similar to the second image. b) the lower the value of the three modes of movement, the higher the cross-correlation coefficients. Comparison of Figure 5.1 with Figure 5.2 shows that higher accuracy is obtained with a high correlation coefficient since the displacement errors are smaller for higher coefficients.

5.4 Conclusions

An improved cross correlation technique has been proposed to overcome errors, in the analysis of video images for Particle Image Velocimetry (PIV), due to appreciable local non-uniformity velocity distributions.

Simulations proved that the improved cross-correlation method is good at suppressing the errors for the uniform displacement and partly correcting the errors for the rotation and shear movements. In the case of rotation and shear movements, the errors decrease by 30%.

The final maximum values of the cross-correlation coefficients show that the improved method provides more accurate velocity data, because the correlation coefficient is a measure of the image match.

Chapter 6 Temperature measurement

Thermochromic liquid crystals display different colours at different temperatures because of a special crystalline feature namely the periodic helical structure. Temperature measurement can be achieved by identifying the corresponding colour. The colour displayed by the liquid crystals is subjective. Three highly interrelated factors must be taken into account - light source, type of liquid crystals and the colour sensor. Colour interpretation is essential for temperature measurement. In this chapter the concepts of colour are introduced. Hue of the HSI space is used for colour identification. Several hue representations are investigated. The effect of viewing angle has been shown to be negligible if the variation of viewing angle is within +/- 10°. Two hue representations are recommended to be used for the types of liquid crystals used in this thesis.

6.1 Colour

The outside world is colourless. It consists of colourless matter and colourless energy (Kueppers 1980). There is no such thing as colour in the absence of an observer; 'colour' is in fact a subjective sensation, experienced by an observer through the light-sensitive receptor mechanism of the eye. The colours displayed from liquid crystals at different temperatures are not within the liquid crystals. Liquid crystals do not reveal any fixed, specific colour. They are merely transmitters of information. The information, of course, is transmitted to the observer through the selected portion of the light that reaches the eye as a "colour stimulus". They tell us how this colour stimulus differs from the spectral make-up of the general illumination. Colour materialises only if this colour stimulus causes the intact visual system of an observer to produce a colour sensation. Their appearances instead are relative. It depends on illumination, environmental temperature and exists exclusively as a sensory perception on the part of the viewer.

To determine specific parameters that describe a colour displayed by liquid crystals, three highly interrelated factors must be taken into account. 1) Spectral distribution of the light source illuminating the temperature field. 2) Spectral reflectivity of the liquid crystals being observed. 3) Spectral sensitivity of the imaging sensor (Camci et al. 1991). Most of the available present day imaging sensors such as colour CCD arrays simulate the spectral sensitivity of the "standard human eye". The main task of the presently developed image processing system hardware and algorithms is to bridge the perceived quantitative colour information and the local temperature at a given point.

6.1.1 Light sources

In order to obtain the full-colour patterns of flows seeded with liquid crystal particles, a white light illumination is required. What one recognizes as a natural white light is daylight (sunlight reflected back from the sky); that part of the electromagnetic spectrum which falls between wavelengths 380nm and 770nm (1nm = 10^{-9}m = 10 A^0). Daylight is really not homogeneous, but is a mixture of component bands containing a continuous contribution from radiation of each wavelength between these stated limits. These component bands appear as different colours, that is they produce sensations in the brain different from each other and different from the sensation of white which is the effect of the mixture.

In real life one seldom meets the pure colour of radiation of a single wavelength (monochromatic radiation), but any disturbance of the spectrum produces the sensation of a coloured light, because some part is emphasized at the expense of another. Thus by removing some parts of the continuous spectrum of light the conditions are produced for seeing colour.

A light source itself may be coloured because it is deficient in some wavelengths, e.g. sodium light produced by an electric discharge through sodium vapour contains visible energy mainly at 589nm and 589.6nm, and hence causes the sensation of yellow orange. Many other gas discharge lamps which produce energy through atomic excitation are highly coloured for similar reasons. Monochromic light sources were used by Kasagi et al. (1981) and Simonich and Moffat (1982) in order to obtain an isothermal contour.

Fluorescent lamps produce energy principally by the atomic excitation of mercury vapour, but the resulting gaps in the mercury spectrum are filled as well as possible by the fluorescence of the powders with which the inside of the tube is coated, and which are activated by the ultraviolet radiations of the excited mercury vapour. This gives an acceptable illumination, but the rendering of colours of objects is distorted because of the inequality of distribution of the energy throughout the visible spectrum.

Incandescent lamps with metal filaments, e.g. tungsten, produce light as a function of the temperature to which the metal filament is raised, and this has a continuous spectrum of energy output which, although emphasising the red and yellow part of the visible spectrum, is nevertheless acceptable as a warm white light source, although most of the energy produced is in the non-visible infrared region.

Two such lamps could give an equivalent colour appearance when observed directly, because differences between them balance out visually. However, they could render colours of objects differently, because one of them is deficient in some wavelength which is critical to the object. The more continuous the spectrum of a source in the visible range, the better the colour rendering, because it approximates better to daylight, or 'norm'.

An RGB laser was tried (Tanaka and Furuta 1989) instead of using a Xenon slit light, but the spectrum of the RGB laser was not continuous. Chan et al. (1994) examined four lamps - fluorescent lamp, metal halide lamp, tungsten lamp and tungsten-halogen lamp. The fluorescent lamp produced flicker problems, the metal halide lamp produced a high proportion of ultraviolet light, which is highly undesirable in the liquid crystal application, and the colour and lighting quality of the tungsten lamp deteriorated in use, as its filament evaporated and blackened the bulb. The tungsten-halogen lamp produced an excellent colour rendering even over a long run, with a reasonably high efficacy, high luminance and compact size. A tungsten-halogen lamp (Oriel Model 66187 1000W) is used in this thesis. A cool-mirror is mounted on the lamp to isolate the heat from the experimental rig which the lamp illuminates.

6.1.2 Thermochromic liquid crystals

If an object reflects the whole of the incident light without discrimination it is called 'white', while if it is so constituted that it absorbs all the light it is designated black. Neither 100% absorption nor 100% reflectance are attainable in practice, but there is an infinity of gradations between black and white through grey in objects which are non-selective in their reflectance. This is called the achromatic range.

Thermochromic liquid crystals have the inherent quality of differentially reflecting some part of the incident light, they will modify the light seen, giving only a selected part of the spectrum and causing the sensation of colour in the brain of an observer. Its colour will depend on the illumination by which it is viewed.

Cholesteric liquid crystals are composed of layers of liquid crystal sheets. However, in each sheet the molecules are aligned in a slightly different orientation with respect to their adjacent layers. (Fig 6.1). It is this property of the cholesteric liquid crystal that is responsible for its colour reflection behaviour. The cholesteric (Ch) mesophase is closely related to the nematic (N) phase but differs significantly in that the direction (the unit vector describing the average direction of the molecular long axes) is not constant in space, but undergoes a helical distortion (Figure 6.1). The director of each individual layer is rotated through a small angle. When the director turns through 360°, the thickness represents the pitch length for the helix.

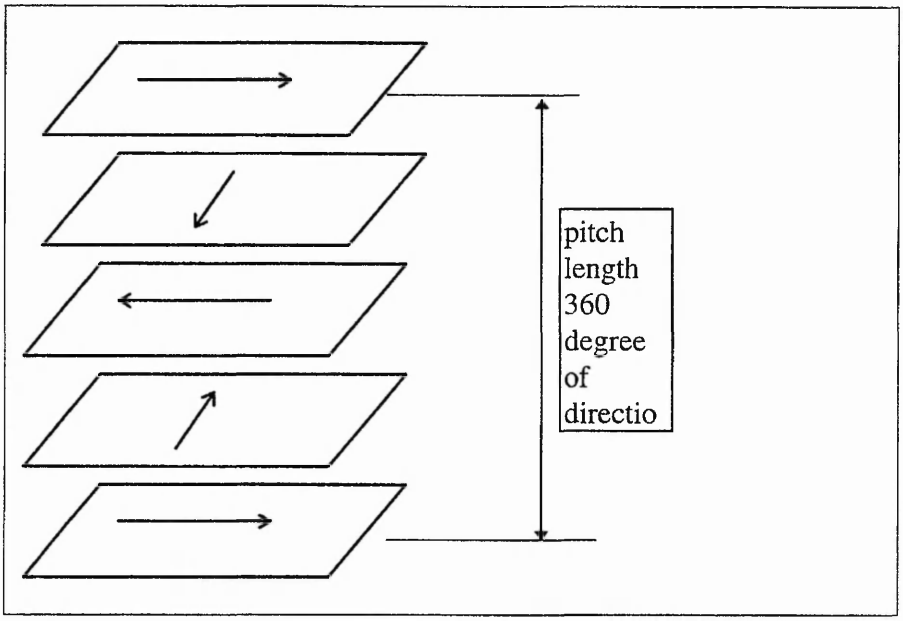

Figure 6.1 Idealized helical model of a cholesteric liquid crystal

Classically, isotropic liquids or solutions containing chiral molecules, e.g. sugar solutions, are described as optically active since the right and left-handed components of plane polarized light propagated at different velocities, causing the plane of polarization of the emergent beam to be rotated. This property is often referred to as circular birefringence and gives rise to rotations of about 10°/mm. In the case of cholesteric liquid crystals (ChLCs), there is therefore a twofold optical activity: (1) molecular and (2) macromolecular - associated with the helical structure. When unpolarized light hits the liquid crystal, it is split into two linear polarized components. Due to the anistropy of the liquid crystal, the right-handed and the left-handed components of the polarized light each see a different refractive index, resulting in the rotation of the light's polarized plane. The important difference in this case is that the rotation is much greater, of the order of $10^{3\circ}$/mm.

A further unique feature of the helical structure occurs when its optical wavelength (*np*) is equal to that of the incident light:

$$\lambda = np \tag{6.1}$$

where

n = the average refractive index of the liquid crystal

p = pitch length

In this case, circularly polarized light with the same sense as the helix is selectively reflected in a manner that is analogous to Bragg X-ray reflection (Treuner et al. 1995). When the light wavelength, the reflection angle and the pitch length of the helix have a relationship as the equation (6.2), there is a maximum reflection of the light,

$$p \cdot \cos\varphi = \frac{m \cdot \lambda}{n} \tag{6.2}$$

where φ is the reflection angle, *m* the order of reflection and n the average refractive index of the liquid crystals. The smaller the reflection angle φ, the longer the reflected wavelength λ.

In order to visualize how this occurs, it is convenient to consider the helical structure as depicted in Figure 6.1. The arrows in this model represent the director orientation in each N-like layer. Therefore, for each layer or sheet, two refractive indices may be defined: n_e parallel to the director and n_o at right angle to it in the same plane. If a plane polarized beam with the same wavelength as the helix enters the structure with its plane of polarization parallel to the director, and if the helix enters the structure with its plane of polarization parallel to the director, and if the helix is right-handed, then one circularly polarized component will propagate seeing some average refractive index and be transmitted. However, the other component will see a sinusoidal variation in refractive index along the helix axis with n_e repeated at every 180° rotation or *p/2* spacing and be scattered. The scattered light from each *p/2* plane constructively interferes and is reflected as right-handed circularly polarized light, whose wavelength is given by

$$\lambda = n_e p \tag{6.3}$$

By the same process, incident plane polarized light with its plane orthogonal to the director will have 50 percent of its intensity reflected and its wavelength is given by

$$\lambda' = n_o p \tag{6.4}$$

When ordinary white light is incident on the helix, all wavelengths between λ and λ' are reflected so that the bandwidth is given by

$$\Delta\lambda = p(n_e - n_o) \tag{6.5}$$

As the temperature of the liquid crystal changes, the distance between the sheets of liquid crystal layers changes tending to increase the pitch, and the angular direction of each layer of liquid crystals increases with respect to its adjacent layers tending to decrease the pitch. The second effect dominates over the first, and as will be seen in the calibration curve, is highly non-linear with respect to temperature changes. Due to these effects, the colour reflection of the liquid crystals is highly dependent upon the angle from which it is viewed with respect to the incident illumination. Thus, any changes in the viewing angle results in changes of perceived colours. The pitch of the liquid crystal layers is not only sensitive to temperature, but also shear stress and to magnetic fields (McDonnell 1987).

The selective reflection and thermochromic properties of the cholesteric phase are undoubtedly very interesting phenomena and have stimulated imaginative ideas for applications. The property of interest, from a heat transfer point of view, of the cholesteric type liquid crystal concerns its response to temperature. Over a known, reproducible range of temperature, the "event temperature range", the cholesteric liquid crystal will progressively exhibit all colours of the visible spectrum as it is heated through the event temperature range. This phenomena is reversible, repeatable and with proper care, colour can be accurately calibrated with temperature.

Estimated time response of the liquid crystals is in the order of 0.1 second (Fergason 1964, Dabiri and Gharib 1991 and Platzer et al. 1992). Black background was recommended for better colour rendering (Cooper 1975, Moffat 1990).

The encapsulated liquid crystal particles are commercially available for different temperature ranges and particle sizes (Appendix I).

6.1.3 The colour sensor

The trichromatic theory postulates three different types of cones, which are located in the centre of the retina of the human eye and sensitive to different bands of wavelengths. The 'red-sensitive' cones are thus brought into action chiefly by light of the longer visible wavelengths, the second type respond chiefly to light of wavelengths in the middle of the visual spectrum and are called 'green-sensitive', while a third type (the 'blue-sensitive' cones) are most affected by light of the short wavelength part of the visible spectrum (Kuepper 1980).

According to the trichromatic theory, when both the red-sensitive and the green sensitive cones are activated and sending their respective response, the brain interprets the message as somewhere intermediate in the spectrum and records a yellow sensation, either orange or yellow-green according to which message predominates. Similarly, cyan colour is the result of green and blue responses simultaneously. If all three types are stimulated at the same time, the message is white, although a continuous spectrum may not be present. This can be demonstrated by mixing three beams of coloured light of quite narrow wavebands in the red green and blue areas: although it is clear that there are gaps in the spectrum, the brain will nevertheless insist that the result is white, although such a "white" light will be quite inadequate in colour rendering properties.

In terms of video camera and CCD sensors, colour video signals are transmitted as unique combinations of red, green and blue (RGB) light. What human eyes perceive as red, yellow, pink, purple, etc., on a colour monitor are actually mixtures of the primary additive colours of red, green and blue.

6.2 Colour spaces

Almost all modern colour measurement is based on the CIE system of colour specification. The initials come from the French title of the international committee (Commission Internationale de l'Eclairage) which set up the system in 1931. Although additions have been made since, the basic structure and principles are unchanged (Wyszecki and Stiles 1982, Rigg 1987).

The CIE method of colorimetric specification is based on the rules of colour matching by additive colour mixture. Observations made over many years of additive colour mixture experimentation were elucidated by Hermann Günter Grassman and have come to be known as Grassman's laws of colour mixture (Grum and Bartleson 1980). By additive mixture we mean the combination of two stimuli acting in such a manner that they enter the eye simultaneously or in rapid succession and are incident on the same area of the retina or are incident in the form of a mosaic too fine to be resolved as such. Grassman's laws for such colour mixture are three in number: (1) Three independent variables are necessary and sufficient for specifying a colour mixture. (2) Stimuli evoking the same colour appearance produce identical results in additive colour mixtures, regardless of their spectral compositions. (3) If one component of a colour mixture changes, the colour of the mixture changes in a corresponding manner.

6.2.1 RGB colour space

The three principles of additive colour mixture imply certain analogies with mathematical relations that are very powerful. The first establishes what is called "trichromacy". The experimental choices are monochromic lights with spectral centroids of 700.0nm, 546.1nm, and 426.8nm. Symbolizing the unit vectors of this primary system as $R\ G\ B$, a colour stimulus C can be written as

$$C = Rr + Gg + Bb. \tag{6.6}$$

The tristimulus values R, G, B may be determined as the radiance of the primaries necessary to match each, in turn, of a large series of other monochromatic lights. These quantities are called "spectral tristimulus values", and if the power of each spectral stimulus is the same, the unit normalised spectral tristimulus values are symbolised as $r\ g\ b$ at each wavelength of 700.0nm, 546.1nm and 436.8nm respectively.

The tristimulus values may be expressed as dimensionless ratios called "chromaticity coordinates". They are related to the trismulus values simply as

$$r = \frac{R}{R+G+B}$$
$$g = \frac{G}{R+G+B}$$
$$b = \frac{B}{R+G+B} \tag{6.7}$$

Chromaticity coordinates provide the advantage that a knowledge of any two determines the value of the third as well, since, r+g+b =1.0.

6.2.2 XYZ colour space

It is found that mixtures of the primaries, although the most saturated obtainable, are unable to match in saturation the intermediate colours, while matching perfectly as regards hue. In other words, the path of the spectral colours falls outside the triangle except at the three fixed points (Figure 6.2).

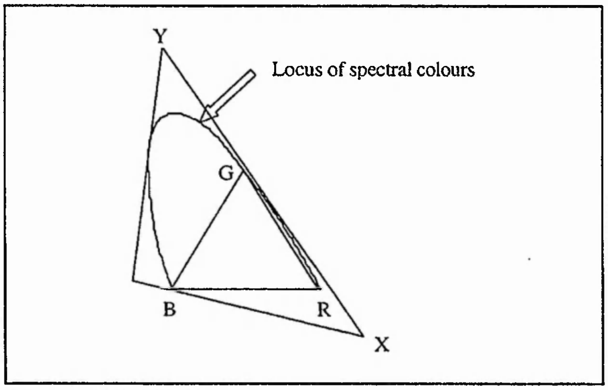

Figure 6.2 XYZ coulur space

The CIE also adopted a tristimulus specification based on imaginary primaries that are a linear transformation of the RGB, which formed a triangle enclosing the whole of the spectrum locus without having to use negative values when the sample has to be desaturated before matching. This was done as a matter of computational and interpretive convention. The tristimulus values for these imaginary primaries are symbolized X, Y, Z and they have become the fundamental specification metric of CIE colorimetry (Chamberlin and Chamberlin 1980).

Based on the Standard Observer data, and using real red, green and blue primary stimuli with units adjusted such that equal quantities are required to match white, the definition adopted

$$\begin{aligned} X &= 2.3646R - 0.5151G + 0.0052B \\ Y &= -0.8965R + 1.4264G - 0.0144B \\ Z &= -0.4681R + 0.0887G + 1.0092B \end{aligned} \qquad (6.8)$$

was (when R is 700nm, G is 546.1 nm, and B is 436.8nm)

Note, that equal quantities of both stimuli XYZ and RGB are required to match white. Tristimulus values X, Y, Z represent quantities and can be reduced to relative proportions, or chromaticity coordinates (designated x, y, z) thus:

$$\begin{aligned} x &= \frac{X}{X+Y+Z} \\ y &= \frac{Y}{X+Y+Z} \\ z &= \frac{Z}{X+Y+Z} \end{aligned} \qquad (6.9)$$

6.2.3 Uniform colour space

The colour triangle (RGB, XYZ) so far considered is subject to severe aberrations. This is because the eye is not equally sensitive to all colours, and can easily distinguish very small differences in some areas while being relatively insensitive in others. Very many transformations have been suggested to correct this distortion, in order to provide an equally sensitive colour space to all colours, but none of these are satisfactory. In the CIE 1960 recommendations, the transformation into the co-ordinates u, v, w of the CIE Uniform Colour Scale was given as (Chamberlin and Chamberlin 1980):

$$
\begin{aligned}
u &= \frac{4x}{-2x+12y+3} \\
v &= \frac{6y}{-2x+12y+3} \\
w &= \frac{3y-3x+1.5}{6y-x+1.5}
\end{aligned}
\qquad (6.10)
$$

6.2.4 HSI colour space

When colour is described in an image, it is not described in terms of its relative proportions of red, green and blue light. Rather, it is described according to our own perception of colour.

Colour is described in the psychological concepts of hue, saturation and intensity. These are the parameters of human visual perception. These parameters are what we use to describe colour. Figure 6.3 shows the Munsell colour system used to illustrate how we perceive colour in these terms.

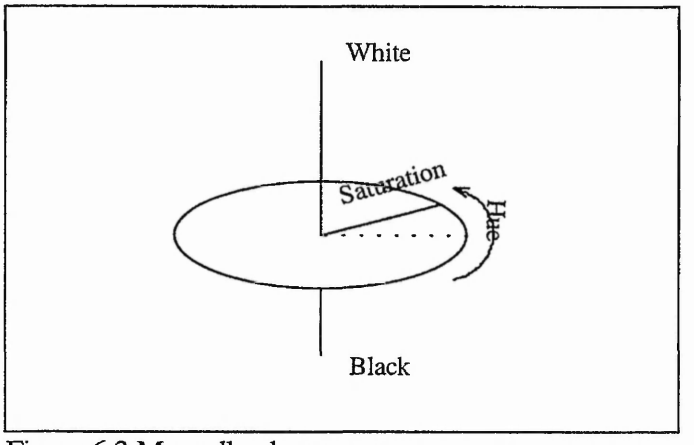

Figure 6.3 Munsell colour space

Hue is relevant to the wavelength of a colour. It is a colour attribute that describes a pure colour, such as pure red, pure yellow, etc. Primary hues produce all other hues. Colour video signals use red, green and blue light as the primary hues. These additive primaries create white when mixed equally.

Saturation refers to the purity of a colour or hue. Highly saturated colours are vivid. Less saturated colours are perceived as dull or faded. Complete desaturation is white.

Intensity is the relative brightness of an object. It is a measure of the amount of light reflected from an object. It can best be described as what an object would look like if its colour was subtracted out. That is, the object appears white, black, or some intermediate shades of grey. Objects with a high intensity appear white while those with a low intensity appear black.

XYZ and UVW are the linear conversions of RGB, they can be derived form RGB colour space. HSI colour is based on human perception. The conversion of HSI from RGB is non-linear. The DT2871 (HSI) Colour Frame Grabber digitizes the incoming analog red, green and blue video signals and converts this data to their hue, saturation and intensity values to form a colour image having 512 x 512 x 24-bit resolution. The colour image is stored in three separate onboard frame-store memory buffers. The three buffers are output simultaneously to an HSI-to-RGB converter producing the colour image on the display monitor.

The DT2871 follows the HSI triangle model for colour conversion. In the HSI colour space, the relationship of the colour data can be explained as follows: In the HSI triangle model, HUE and SATURATION lie on a flat triangular plane. The third colour component, INTENSITY, lies perpendicular to the plane and intersects it at the point of equal energy (red = green = blue) inside the triangle (Figure 6.3). There is a separate hue/saturation plane at each intensity level. The hues lie on the perimeter of the HSI triangle. Pure red lies at 0 degrees, pure green at 120 degrees and pure blue at 240 degrees. Saturation is maximum along the perimeter of the triangle and minimum in the centre of the triangle. The hue, saturation and intensity values are each 8 bits. Their numeric values range from 0 to 255.

6.3 Reliability of image board

Before the hue-temperature calibration the reliability of the image system was checked. The colour image system consists of one Pulnix colour CCD camera, one DT-2871 frame grabber and one DT-2878 co-processor, and the DT-2871 and DT 2878 boards are installed in an

IBM PC SX 386 computer. A colour board with colour changes ranging gradually from red to blue was mounted in front of the colour CCD camera. Six different colours were observed in 9 different situations ((1) light stop numbers of the CCD camera 2, (2) 2.8, (3) 4, (4) 5.6, (5) 8, (6) 11.2, (7) 16, (8) poor illumination and (9) dark room). When the light stop was 2 and 2.8, the pictures were over-exposed. Nine HSI pictures were captured into the computer for investigation. The intensities of the nine pictures decline (Figure 6.4) as the light stop number increases because less energy of light reached the CCD sensor. The intensity of the ninth picture (situation of dark room) reaches the lowest grey level of 15. Its values of hue and saturation are random. In the case of poor illumination, the hue value is biased. When the picture is over-exposed, its hue value is not reliable either, its saturation value is also very low. Apart from the situations of poor illumination and over-exposure, the hue values of the other picture are fairly constant. In order to obtain accurate temperature data, the condition of illumination, the light stop of the CCD camera and the view angle should be fixed for hue-temperature calibration and colour picture acquisitions.

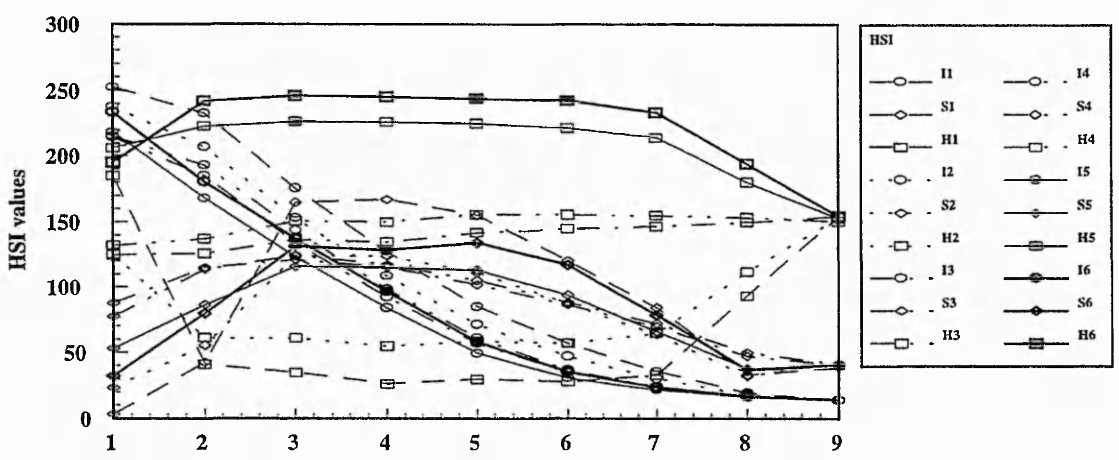

Figure 6.4 H S I values of the same colour under different conditions

6.4 Colour identification for temperature measurement

There are three major methods of determining the relationship between the colour which is displayed by liquid crystals and the temperature surrounding the liquid crystals.

The first is human observation, which is based on the naked eye. The human eye is sensitive to green colour (Cooper et al. 1975), and is good at identifying the temperature contour of the green line of narrow bandwidth liquid crystals. The second method is intensity based image processing and avoids the non-consistancy of the human observer. Either monochromatic light sources (Kasagi et al. 1981, Simonich and Moffat 1982) or optical filters can be used (Akino et al. 1989b).

The third method is based on true colour image processing and has benefitted recently from the development of advanced digital image technology and computers. This method is welcomed by many researchers (Hollingsworth et al. 1989, Moffat 1990, Camci et al. 1991, Farina et al. 1993 and Chan et al. 1994) because of its accuracy and time efficiency. The true colour image system works like a standard human eye, further, it can identify thousands of different colours so is more sensitive than a human eye.

The image facility used in this thesis - DT2871 colour frame grabber can grab a colour image either in RGB mode or in HSI mode. A series of images of the fluid seeded with liquid crystal particles (case 1: water seeded with BM100/R29C/4W/S33, case 2: glycerol seeded with

BM100/R45C/15W/S33) at different constant temperatures were captured. The relationships between temperature and RGB or HSI were obtained.

In RGB space, the three parameters R, G and B define a colour. The colour changes from red to blue as the temperature changes from low to high in the temperature range of the liquid crystals. The parameter R has a major contribution in the red domain and the

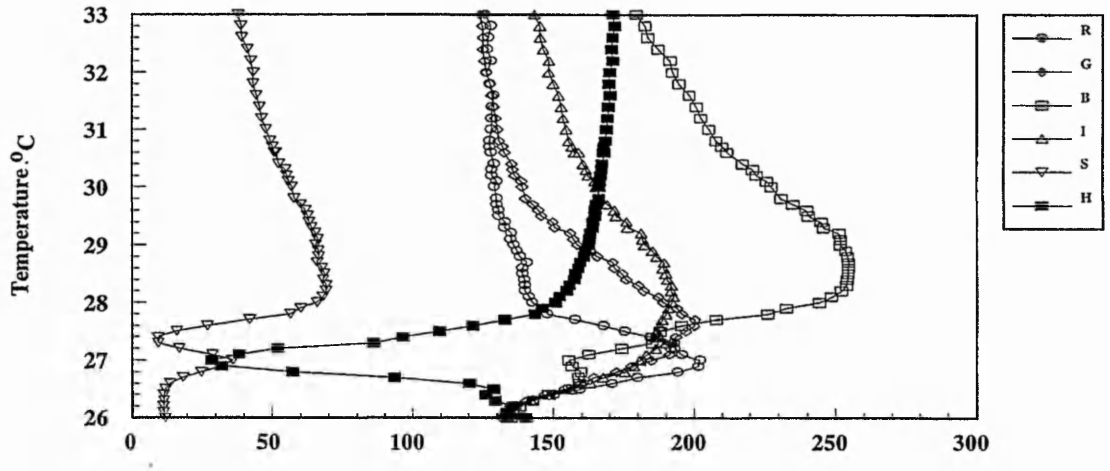

(BM100/R29C/4W/S33)

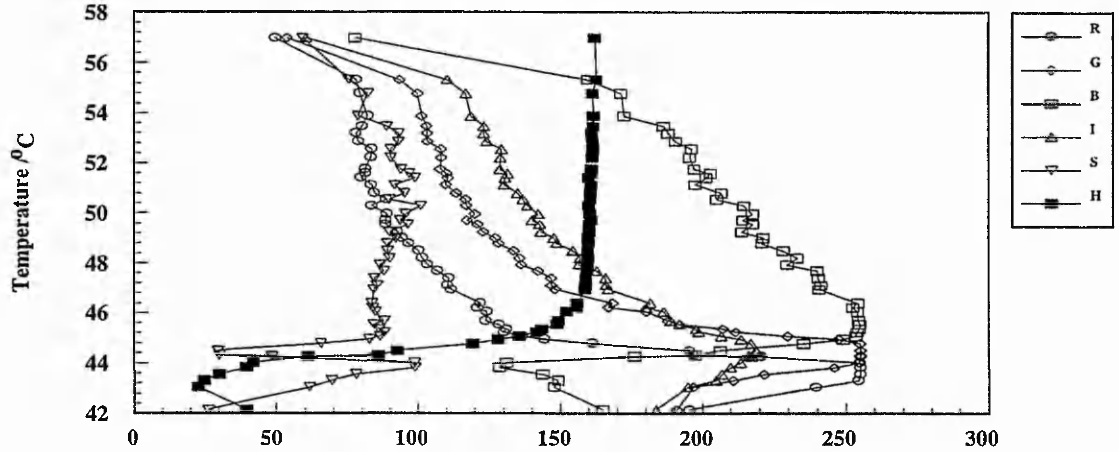

(BM100/R45C/15W/S33)

Figure 6.5 R G B and H S I values against temperature parameter B has a major contribution in blue domain (Figure 6.5). The ratio between R, G and B is relevant to the wavelength of the colour, which is affected by the environment temperature (Figure 6.6). Three normalised R, G and B values r, g and b were used to calibrate the colour - temperature in RGB space by Akino et al. (1989a).

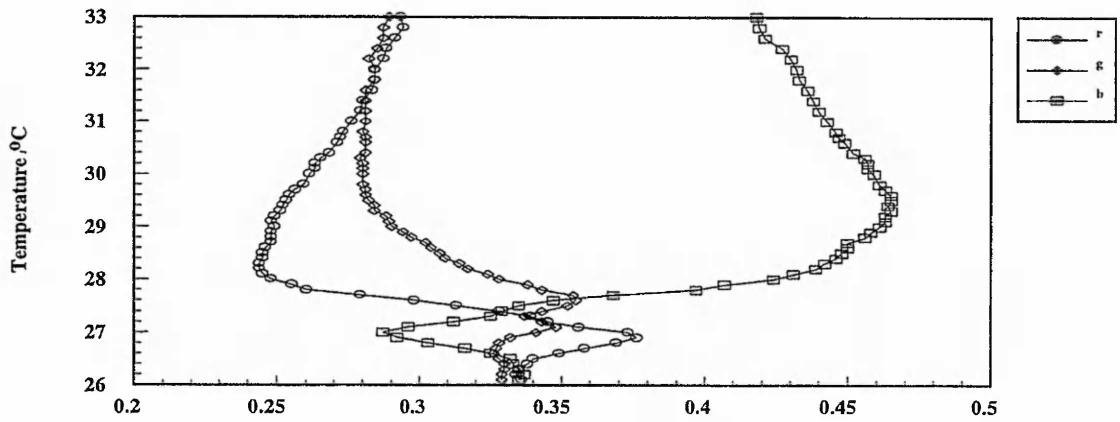

(BM100/R29C/4W/S33)

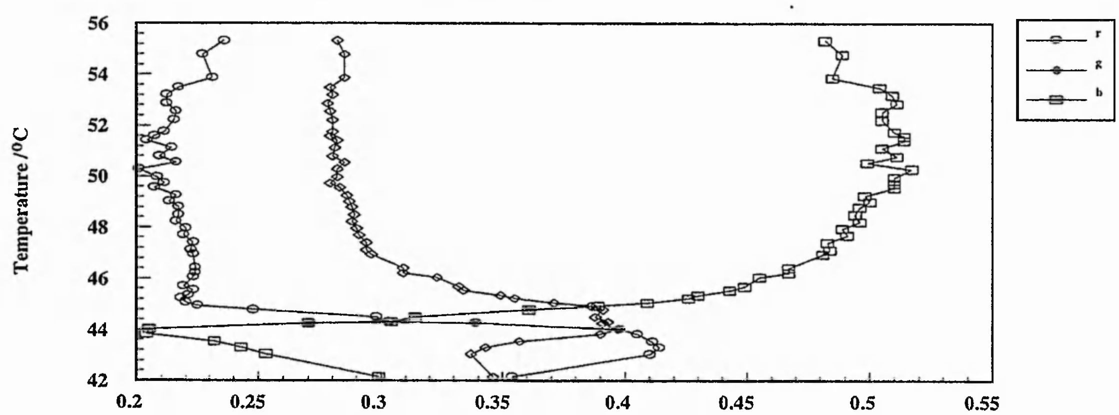

(BM100/R45C/15W/S33)

Figure 6.6 r g b values against temperature

In HSI space, saturation and intensity have nothing to do with the wavelength of the colour only hue, as long as they are over a certain limit (e.g. 15 grey levels). Hue has a monotonic relationship with the temperature in certain temperature ranges (Figure 6.5), and has been recommended to be used for temperature measurement (Akino et al. 1989b, Camci et al. 1991).

DT-2871 has its own definition of HSI, its hue-temperature relationship is monotonic when the temperature is higher than a certain degree certigrade (27°C for BM100/R29C/4W/S33, 43°C for BM100/R45C/15W/S33). Experiments designed for temperature measurement must control the temperature to be higher than a prescribed value. If there are temperatures lower than this prescribed value, there will be two temperature values corresponding to the same hue value and one of the temperature values is false.

6.5 Hue representations

Many researchers calibrate the hue-temperature relationship for temperature measurement because the true colour image facility is available and the relationship is simple. They might describe the measurement in the same name of HSI, but they may mean different hue representations.

Akino et al. (1989b) and Ozawa et al..(1992) used hue representation as

$$hue = \cos^{-1}\left(\frac{2r-g-b}{\sqrt{6\left[\left(r-\frac{1}{3}\right)^2+\left(g-\frac{1}{3}\right)^2+\left(b-\frac{1}{3}\right)^2\right]}}\right)\bullet\frac{255}{\pi} \qquad (6.11)$$

Braun et al. (1993) eliminated the white part from the R, G and B by subtracting the smallest value among R, G and B. The remaining values were used for hue calculation.

Chan et al. (1994) obtained hue value as follows:

$$\begin{aligned}
hue &= \left(\frac{\pi}{2} - \mathrm{tg}^{-1}(z)\right)\bullet\frac{255}{2\pi} && G > B \\
or &= \left(\frac{3\pi}{2} - \mathrm{tg}^{-1}(z)\right)\bullet\frac{255}{2\pi} && G < B \\
or &= \left(\pi - \mathrm{tg}^{-1}(z)\right)\bullet\frac{255}{2\pi} && R = 0 \text{ and } G = B \qquad (6.12)\\
or &= 0 && R = 255 \text{ and } G = B \\
& where \quad z = \frac{2R-G-B}{\sqrt{3}(G-B)}
\end{aligned}$$

Dabiri and Gharib (1991) transferred the RGB to hue through the transformation

$$V_1 = \frac{1}{\sqrt{6}}(2R - G - B)$$

$$V_2 = \frac{1}{\sqrt{6}}(G - B) \qquad (6.13)$$

$$hue = \mathrm{tg}^{-1}(\frac{V_2}{V_1}) \bullet \frac{255}{2\pi}$$

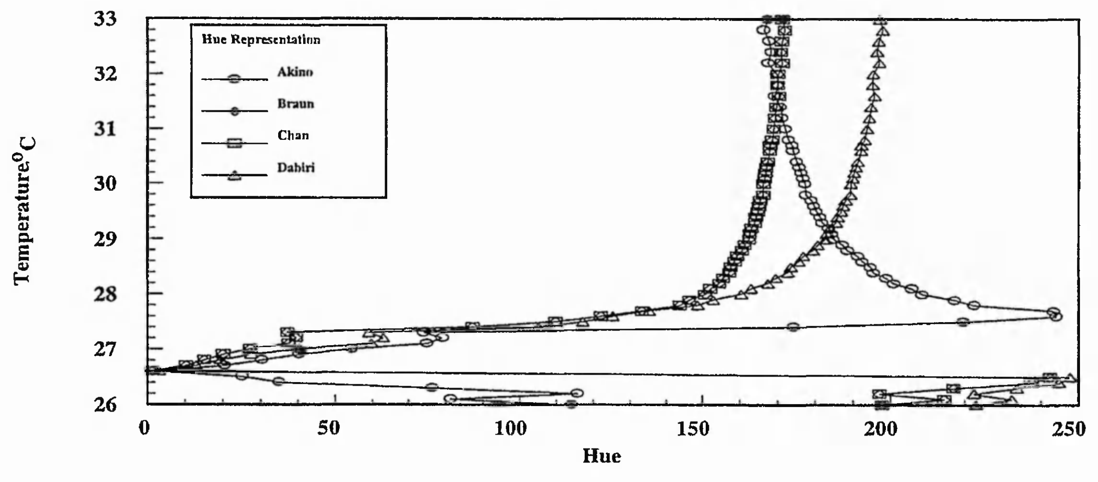

(BM100/R29C/4W/S33)

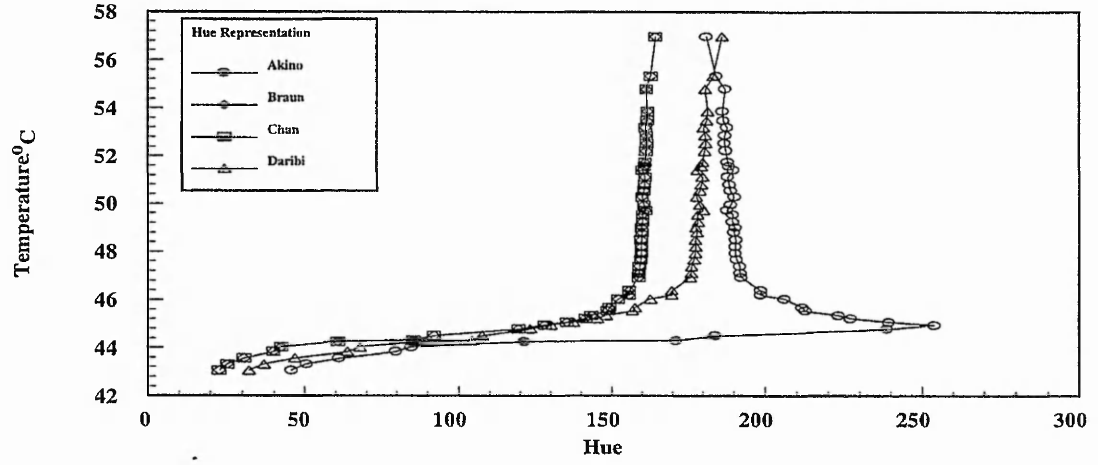

(BM100/R45C/15W/S33)

Figure 6.7 Hue representations of Akino, Braun, Chan and Dabiri

All the above hue representations are used to plot the hue-temperature curves (Figure 6.7). The curve of Akino reverses in the higher temperature range because of the circulation of the hue, which could be modified through simple mathematical operations. All these four representations provide similar curves, the hue value changing rapidly at lower temperature and slowly in higher temperature. The relationships could be divided into two linear regions and one higher order region in between.

Hollingsworth et al. (1989) chose the uniform colour space - UVW system, though it was designed to minimise nonlinearities (Figure 6.8)

$$
\begin{aligned}
U &= 0.405R + 0.116G + 0.133B \\
V &= 0.299R + 0.587G + 0.114B \\
W &= 0.145R + 0.827G + 0.627B \\
T &= U + V + W \\
u = \frac{U}{T} \quad & v = \frac{V}{T} \quad w = \frac{W}{T} \\
u_o = 0.201 \quad & v_o = 0.307 \\
hue &= \mathrm{tg}^{-1}\left(\frac{v - v_o}{u - u_o}\right)
\end{aligned}
\tag{6.14}
$$

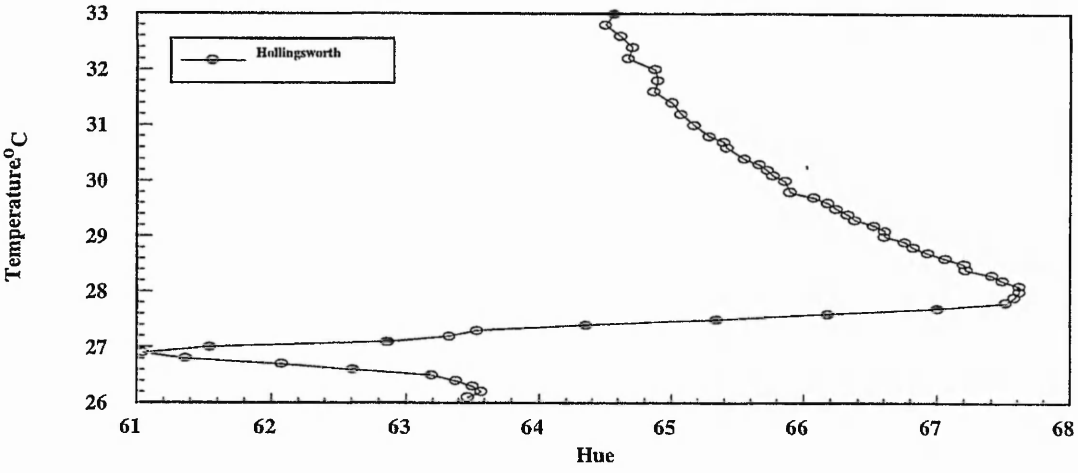

(BM100/R29C/4W/S33)

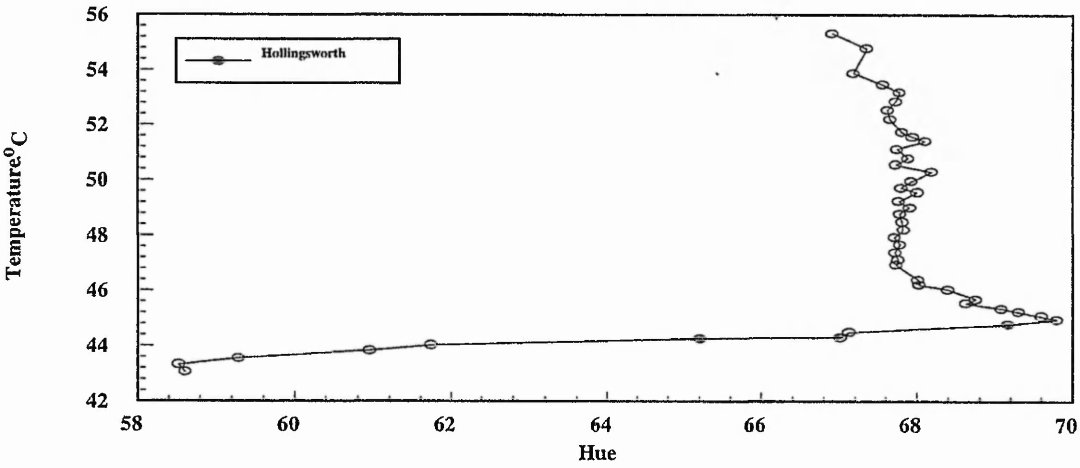

(BM100/R45C/15W/S33)

Figure 6.8 Hollingsworth's Hue representation

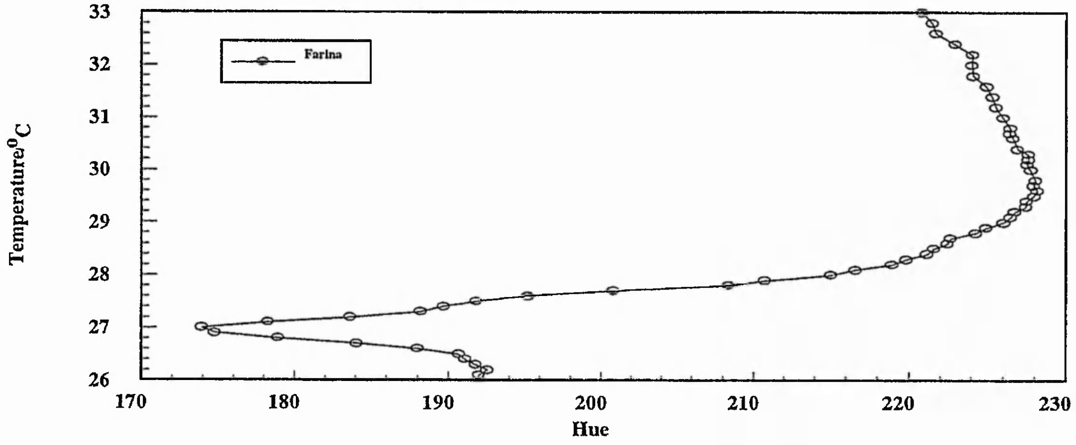

(BM100/R29C/4W/S33)

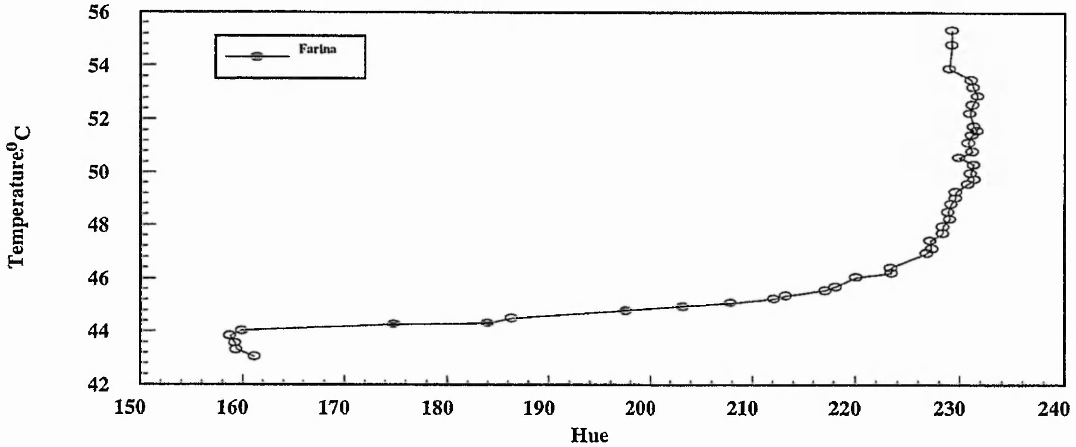

(BM100/R45C/15W/S33)

Figure 6.9 Farina's Hue representation

Farina et al. (1993) converted the RGB to the hue value (Figure 6.9) in the following equations

$$
\begin{aligned}
V_1 &= -\frac{1}{4}(R+G-2B) \\
V_2 &= \frac{1}{4}(R-2G) \\
hue &= tg^{-1}(\frac{V_2}{V_1})\bullet\frac{255}{2\pi}
\end{aligned}
\tag{6.15}
$$

Although Hollingsworth's and Farina's (Figure 6.9) representations provided good hue-temperature relationships in their applications (Hollingsworth et al. 1989, Farina et al. 1993), their representations confined the hue into small ranges, and required good temperature control during heat convection/transfer experiments for the liquid crystals used in this thesis.

Two transforms are proposed in this thesis for hue representation. The first converts the RGB to XYZ using equation (6.8) then to uniform UVW colour space using equations (6.9) and (6.10). The hue is calculated from

$$hue = tg^{-1}(\frac{v}{u})\bullet\frac{255}{2\pi} \tag{6.16}$$

The relationship of hue and temperature is similar to Hollingsworth's result (Figure 6.10).

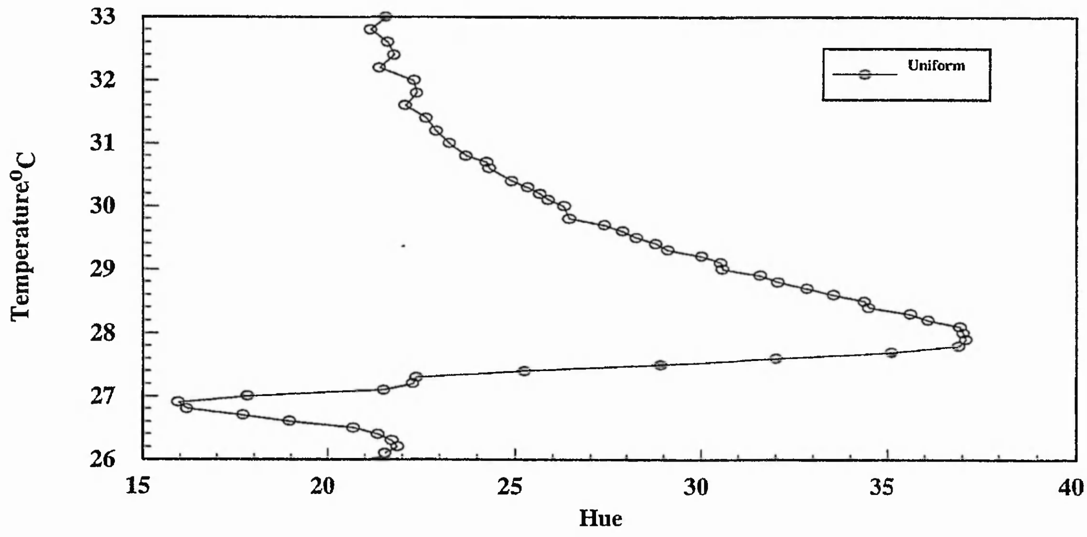

(BM100/R29C/4W/S33)

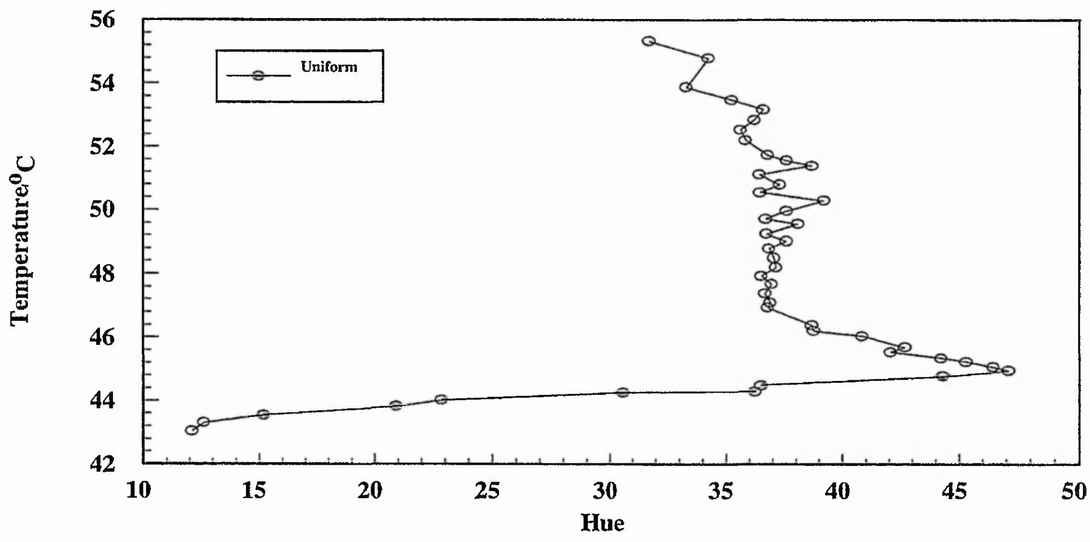

(BM100/R45C/15W/S33)

Figure 6.10 Uniform Hue representation

The second derives the hue simply from the RGB triangle

$$hue = (\pi - tg^{-1}(\frac{2R - G - B}{G - B})) \bullet \frac{255}{2\pi} \tag{6.17}$$

which provides a good hue-temperature relationship (Figure 6.11).

Comparing all the above hue representations, two hue representations are applied for the temperature measurement in this thesis for the liquid crystals used - the HSI mode of DT2871 colour image board, and the simple hue conversion proposed in this thesis.

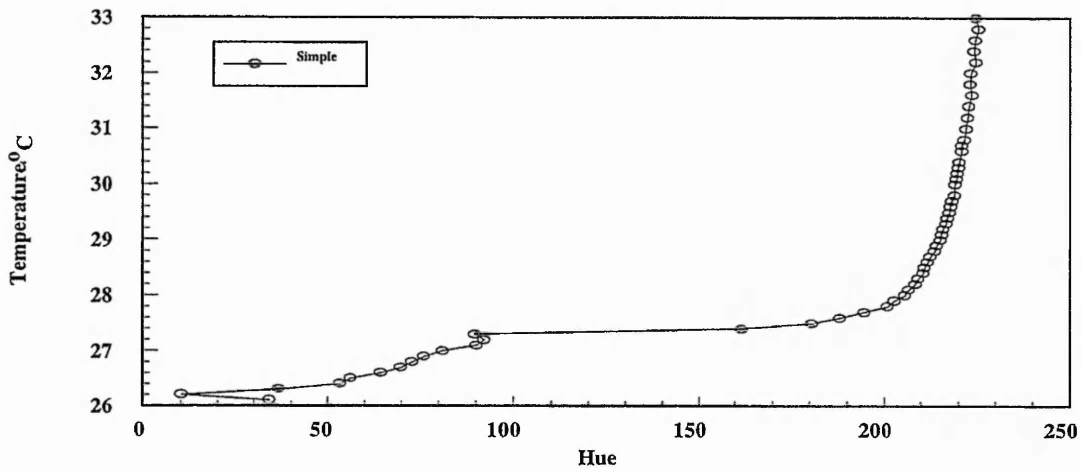

(BM100/R29C/4W/S33)

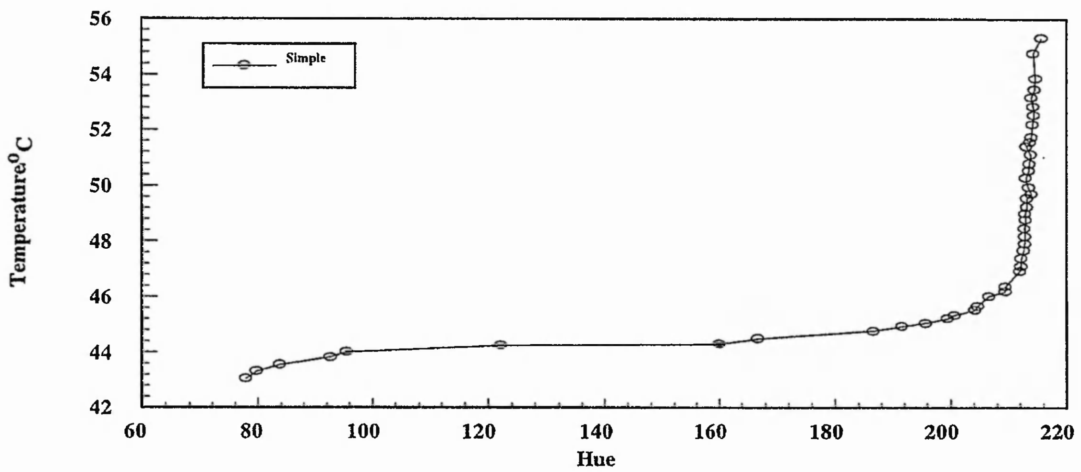

(BM100/R45C/15W/S33)

Figure 6.11 Simple Hue representation

6.6 Effect of viewing angle

The temperature dependence of the selective reflection of thermochromic liquid crystals is a specific feature of the liquid crystals' periodic helical structure. The light wavelength λ reflected parallel to the helical axis, is proportional to the spatial period p (pitch length) between the twisted layers, p being a function of temperature. The viewing angular dependence of the selective reflection of pure liquid crystals is similar to a Bragg reflection (Equation 6.2), where the viewing angle is related to the reflection angle (Figure 6.12).

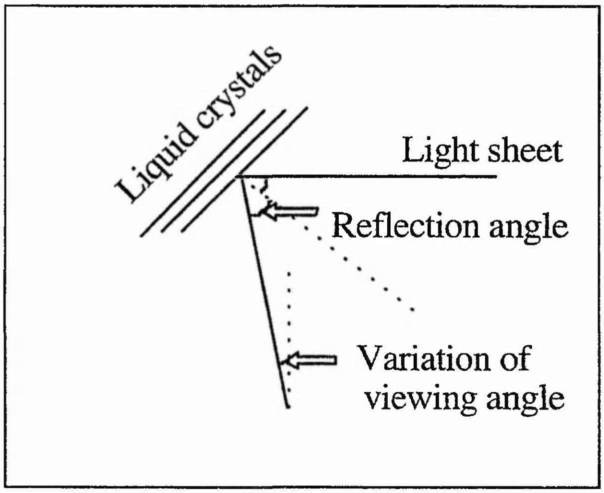

Figure 6.12 Viewing angle and reflection angle

Usually the temperature field is observed at right angle to the light sheet, the reflection angle being *45*°. Supposing the viewing angle changes by $\mathrm{d}\theta$, then the reflection angle changes by $\mathrm{d}\varphi = \mathrm{d}\theta/2$. From Equation 6.2, we have

$$-p \cdot \sin\varphi \cdot \frac{d\theta}{2} = \frac{m}{n} d\lambda \tag{6.18}$$

Assuming a small change in viewing angle of say $d\theta = 0.174$ radian (10°), and noting that $p = \lambda/n$ (Equation 6.1), yields

$$d\lambda = -\lambda \cdot \sin\frac{\pi}{4} \cdot \frac{0.174}{2} \approx -0.06\lambda \tag{6.19}$$

For the DT2871 colour image grabber, the hue values corresponding to red (700nm), green (546.1nm) and blue (436.8nm) are 0, 85 and 170, that yields hue value h

$$h \approx -0.640\lambda + 443.8 \tag{6.20}$$

Further ,

$$dh = 0.06h \tag{6.21}$$

This means that a *10°* change in viewing angle cause a 6 per cent variation in hue value. Experiments have shown that the encapsulation procedure greatly reduces the variation of colour due to viewing angle (McElderry 1970). Calibration data collected from different viewing angles (Figure 6.13) prove that the effect of viewing angle on the hue-temperature relationship is negligible if the change of viewing angle is small (-8.5° to 8.5° for BM100/R29C/4W/S33 and -4° to 4° for BM100/R45C/15W/S33).

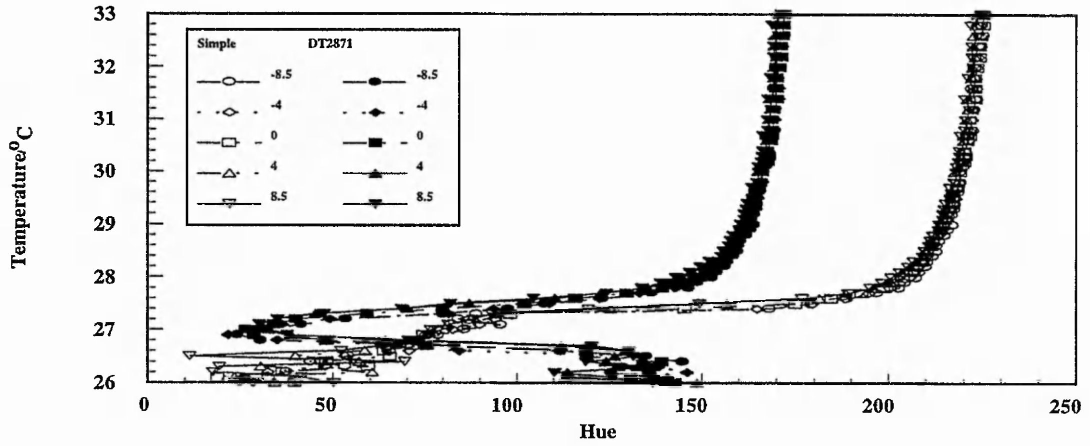

(BM100/R29C/4W/S33)

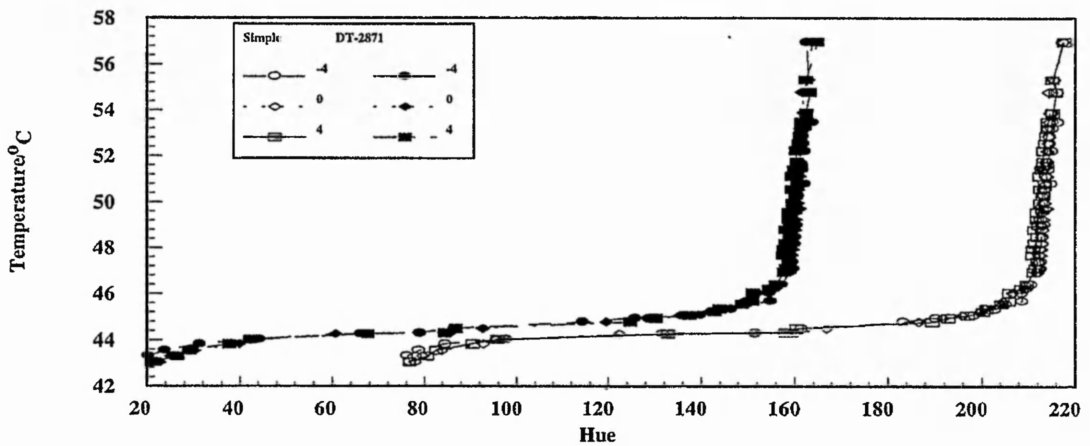

(BM100/R45C/15W/S33)

Figure 6.13 Effects of viewing angles

6.7 Conclusions

Temperature measurement can be achieved by measuring the colour reflected by liquid crystals at a given point. Three highly interrelated factors must be taken into account - light source, type of liquid crystals and CCD sensor, because colour is a special quality of a mental image perceived by an observer.

A tungsten-halogen lamp is selected for illumination because its continuous spectrum is good for rendering colour. Most of the energy of the lamp is produced in the infrared region, a cool mirror being installed to isolate the experimental rig from the heat of the lamp.

Colour identification depends on the colour spaces utilised. XYZ and UVW colour spaces are linear conversions of the RGB colour space. HSI colour space is based on physiological concepts. It is a non-linear conversion of the RGB colour space. Comparing the relationships between temperature and R, G, B , H, S, I, hue is selected for identification of colour reflected by liquid crystals; this simplifies the calibration procedure. Various hue representations are compared. In the main, they can be divided into two categories - uniform conversion and simple conversion. Although uniform colour space is designed to minimise nonlinearities, it does not provide a good hue-temperature relationship for the liquid crystals used in this thesis. Simple conversions provide similar curves - hue increases rapidly at lower temperature and slowly at higher temperature.

The effect of viewing angle is theoretically and experimentally investigated. The effect is negligible when the variation of viewing angle is within +/-10°, when the encapsulated liquid crystal particles are used.

Chapter 7 Simultaneous measurement

In this chapter, the improved cross-correlation method combined with encapsulated liquid crystals is applied to the investigation of natural convection. Two cases are studied using different liquid crystal particles - BM100/R29C/4W/S33 and BM100/R45C/15W/S33 seeded in different fluids. The simultaneous velocity and temperature distributions at particular moments are presented. Uncertainties of the measurements are investigated.

7.1 PIV using liquid crystal particles

Liquid crystals in micro-encapsulated form can not only act as particles for establishing the velocity field but, due to their responsiveness to temperature also enable the temperature field to be measured. Velocity and temperature measurements are interrelated for the purpose of simultaneous measurement. Fine liquid crystals are required in order to obtain the continuous colour distribution for convenient temperature measurement, whilst for the cross-correlation method of PIV, a characteristic pattern uniquely related to the particle group is necessary. The selection of the seeding density and the particle size must provide visible particle images on the CCD target and, at the same time, the continuous hue distribution. For good velocity measurement, the image particle size must be larger than 3 pixels. Suitable seeding density will provide a fairly continuous hue distribution.

The motion of a particle in a viscous fluid is governed by so-called Basset-Bossinesq-Oseen (BBO) equations (Emrich 1981).

$$\frac{\pi d^3}{6}\rho_P\frac{\mathrm{d}u_P}{\mathrm{d}t} = F+\frac{\pi d^3}{6}\frac{\mathrm{d}u_F}{\mathrm{d}t}-\frac{\pi d^3}{6}\chi\rho_F\frac{\mathrm{d}V}{\mathrm{d}t}$$
$$-R[1+\frac{d}{2V(\pi\nu)^{1/2}}\int_{t_0}^{t}\frac{\mathrm{d}V/\mathrm{d}t'}{|t-t'|^{1/2}}\mathrm{d}t'] \qquad (7.1)$$

where d is the particle diameter, F is proportional to the external force, acting on the particle, v is kinematic viscosity of the experimental fluid, u_P and u_F are the velocities of particle and fluid, and $V = u_P - u_F$, r_P and r_F are densities of the particle material and the experimental fluid, c is added mass coefficient. The coefficient R in the fourth term is proportional to the viscous resistance of the fluid to the motion of the particle. The physical laws which govern the hydrodynamic resistance experienced by a single undeformable particle have been extensively investigated. The general solution of equation (7.1), i.e., the general form for the particle dynamic characteristics in rectilinear flow, is given by the transfer function H, where

$$U_P(i\omega) = H(i\omega)U_F(i\omega) \qquad (7.2)$$

where U_P and U_F are the Fourier transform of the velocities u_P and u_F, and ω is frequency of periodic motion. Defining the amplitude function as $h = |U_P|/|U_F|$ and the phase angle α, the equation (7.2) can be written as (Emrich 1981)

$$H(St,\sigma) = \eta\exp(i\alpha)$$
$$\sigma = \frac{\rho_P}{\rho_F} \qquad (7.3)$$

The amplitude ratio h and the phase angle α are functions of the Stokes number

$$St^2 = \nu / (\omega d^2) \tag{7.4}$$

where n is viscosity, ω the frequency of periodic motion and d the particle diameter. While the Stokes number $St >> 1$ and density s is close to 1.0, the amplitude ratio h is 1.0 and the phase angle α is zero. In this case, the particles follow the flow exactly. When the density of the particle is less than that of the fluid, the particle moves faster than the fluid ; when the density of the particle is higher than that of the fluid, the particle moves slower than the fluid. In this thesis, the relative density of liquid crystal particles, water and glycerol are 1.02, 0.998 and 1.27 respectively, the density ratio σ for particles and water is 1.022 and particles and glycerol is 0.807. Natural convections studied in this thesis change slowly, so that the Stokes number is large and hence the liquid crystal particles follow the convection flow very well (Emrich 1981).

The temperature response time of the liquid crystals is an important consideration since a slow response time would result in erroneous temperature values. Since the liquid crystal fluid is encapsulated, the response time of both the liquid crystal and the encapsulating shell should be taken into account. Both of the these effects can be taken into account by modelling the micro-encapsulated liquid crystal particle as a sphere of diameter d initially at temperature T_0, and the surrounding ambient fluid at temperature T_s. Dimensional analysis suggests two dimensionless parameters with a particular solution:

$$\frac{T_s - T_c}{T_s - T_o} = f(\frac{\alpha t}{d^2}) \tag{7.5}$$

T_c is the transient temperature of the sphere at its centre, t is the time, and α is the thermal diffusivity of the liquid crystal (Dabiri and Gharib 1991). For a sphere,

$$\frac{T_s - T_c}{T_s - T_o} = 0 \quad when \quad \frac{\alpha t}{d^2} \approx 0.15 \tag{7.6}$$

In this thesis, the average diameter (d) of particles is 100μm and the thermal diffusivity of liquid crystals is 10^{-7}, giving a temperature response time is 0.015 second.

Thus, seeding the fluid with correctly-sized neutrally buoyant liquid crystals, the problem of altering the flow can be avoided, and at the same time the particles follow the flow accurately and liquid crystals respond quickly.

7.2 Image system for simultaneous measurement

After selecting suitable seeding particle density and particle size, the particles are mixed with the working fluid which is illuminated by a white light sheet.

The natural convection flows are viewed through a colour CCD camera at right angles (Figure 7.1) to the light sheet and, the analog signals from the CCD camera being converted into digital data and stored in three buffers (HSI/RGB) of a colour frame grabber DT2871. DT2871 can freeze the image and save it in a computer (IBM 386SX). For the purpose of the simultaneous measurement, DT2871 grabs the first image in HSI mode and saves the INTENSITY in a co-processor DT2878, then grabs the second image in HSI or RGB mode with a time delay. The intensity of the first image is transferred from DT2878 to the fourth buffer of DT2871. All the four buffers are saved. The intensity images are used for extracting velocity data and the hue values of the second image are extracted for temperature measurement.

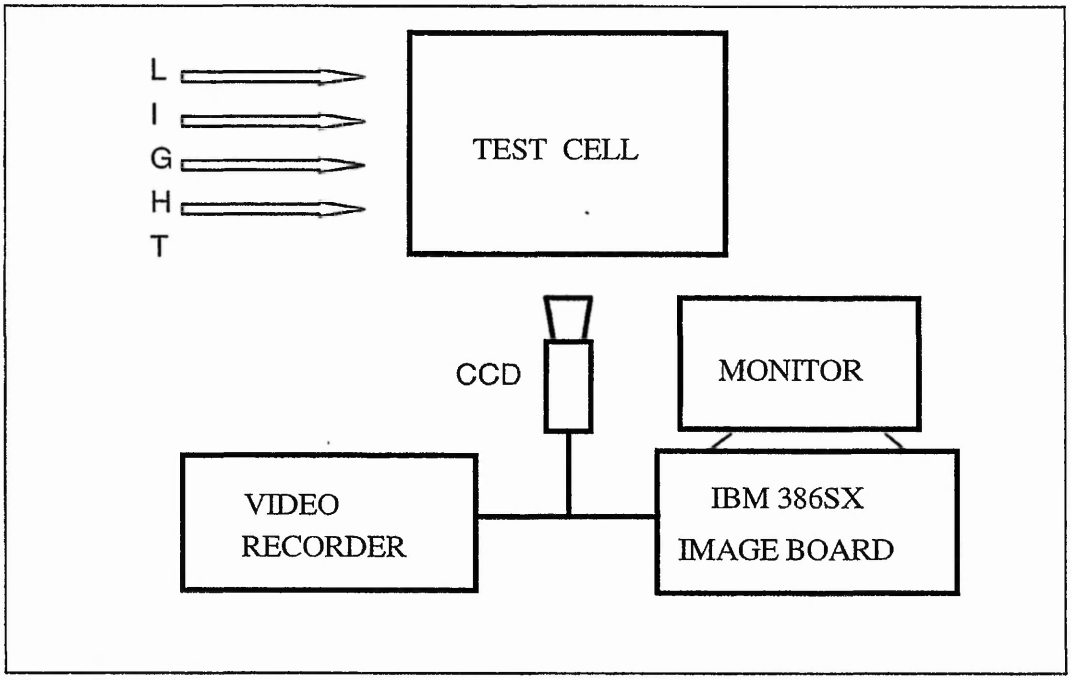

Figure 7.1 Schematic diagram of image acquisition arrangement

7.3 Case studies

Two natural convection flows are investigated using the simultaneous measurement technique. The first is the natural convection from an heated steel tube and the second the natural convection within a square Perspex box.

There are three relevant dimensionless parameters which govern the behaviour of the convection flows: the Renolds number *Re* which is the ratio of inertial to viscous forces,

$$Re = \frac{Vl}{\nu} \tag{7.7}$$

the Prandtl number *Pr* which is the ratio of momentum diffusivity to thermal diffusivity,

$$Pr = \frac{\nu}{\alpha} \tag{7.8}$$

and the Rayleigh number *Ra* which is the ratio of thermal buoyancy to viscous forces,

$$Ra = \frac{g\beta\Delta T\, l^3}{\nu\alpha}$$
$$\beta = -\frac{1}{\rho}\left|\frac{\partial\rho}{\partial T}\right| \tag{7.9}$$

where ν is the kinematic viscosity, V the fluid velocity, l a characteristic dimension in the flow field, α the thermal diffusivity, ΔT the temperature difference, T the temperature, g the acceleration due to gravity and ρ the density of the fluid. All the three parameters are given in the following two cases.

7.3.1 Natural convection from a hot pipe

7.3.1.1 Experimental rig

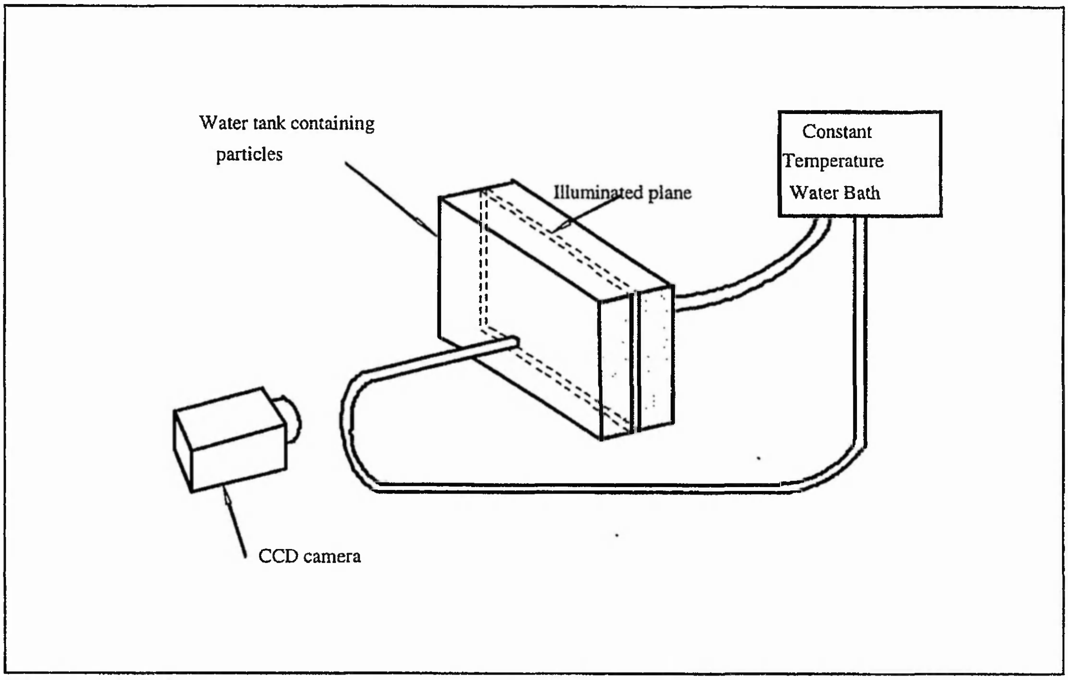

Figure 7.2 Schematic diagram of experimental arrangement

The first natural convection experiment is the natural convection from a heated horizontal cylinder. The proposed simultaneous measurement technique is applied for the analysis of recorded images of natural convection. The test cell consisted of a transparent Perspex tank (150 ´ 186 ´ 100 mm) containing water at 25°C heated by a thin seamless stainless steel tube (diameter 13 mm) through which warm water at ~50°C from a constant temperature water bath was circulated. The flow was artificially seeded with 0.01% micro-encapsulated liquid crystal particles (BM100/R29C/4W/S33) of 100mm mean diameter. A thin plane of the flow domain was illuminated using white light and images were recorded at right angles to this plane using a Pulnix TLC-X colour CCD camera (Figure 7.2).

7.3.1.2 Calibration of Hue and Temperature

Calibration of Hue and Temperature relationship was performed by means of a calibrated mercury-glass thermometer (0.1°C scale). The bulb of the thermometer was located on the centre of the test cell. The water temperature in the test cell increased from 26°C to 33°C by step of 0.1/0.2°C. The water was stirred frequently in order to obtain a uniform temperature distribution all over the test cell. The colour images and their corresponding temperatures were saved in the IBM 386SX computer. The hue values at different viewing angles of -8.5°, -4.0°, 0,0°, 4.0°, 8.5° have been collected and plotted in Figure 6.13 (BM100/R29C/4W/S33). Simple hue conversion (Equation 6.17) was used. The curve of the simple conversion was divided into three regions for curve fitting, allowing for the errors introduced by variation of viewing angle.

Region 1: 27.0 - 27.8°C

$$Temperature = 0.0059Hue + 26.612$$

with standard error deviation of 0.108°C.

Region 2: 27.8 - 29.0°C

$$Temperature = 0.0032\,Hue^2 - 1.269Hue + 152.174$$

with standard error deviation of 0.337°C.

Region 3: 29.0 - 33.0°C

$$Temperature = 0.37256Hue - 51.280$$

with standard error deviation of 0.401°C

The hue-temperature relationships in the three regions were used to build a look-up-table of hue and temperature conversions (Appendix III) for conversion of the data in the hue buffer to temperatures.

7.3.1.3 Velocity and temperature results

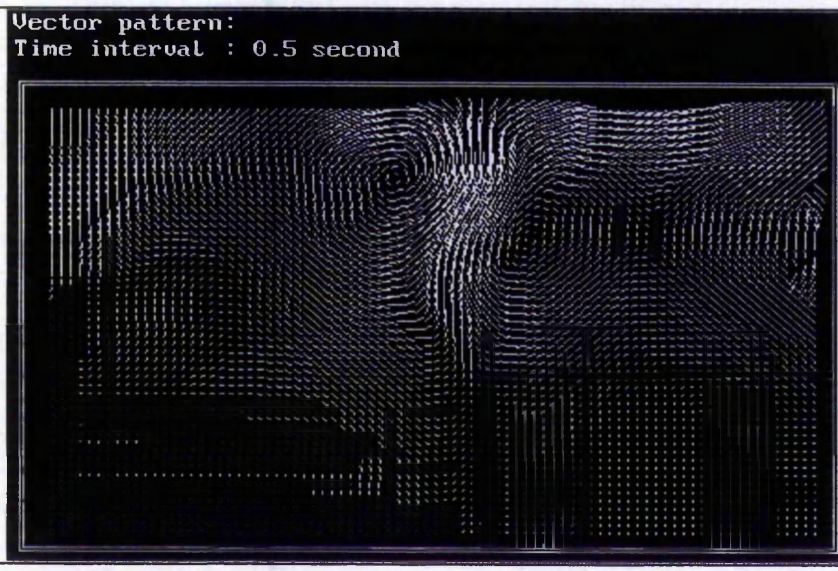

Figure 7.3 Velocity vectors

Prior to the cylindrical tube being heated, no convective motion was present within the test section. On opening the hot water supply to the cylinder, the upward convected flow was immediately visible in a central core directly above the cylinder. As the flow reached the free surface of the water, two counter-rotating recirculation regions were formed, but the flow was not entirely symmetric. Having allowed a velocity field to develop, two sequential colour images were acquired at a 0.5 second interval using the HSI mode for the first colour image and RGB mode for the second colour image. The proposed improvement to the algorithm was applied on the two intensity images to extract the velocity distribution. Figure 7.3 shows the resulting velocity field. The maximum velocities recorded were of the order of 0.1 m/s, at Re » 1300, Pr » 7 and Ra » 8.9´10^4 based on the outside diameter of the steel tube.

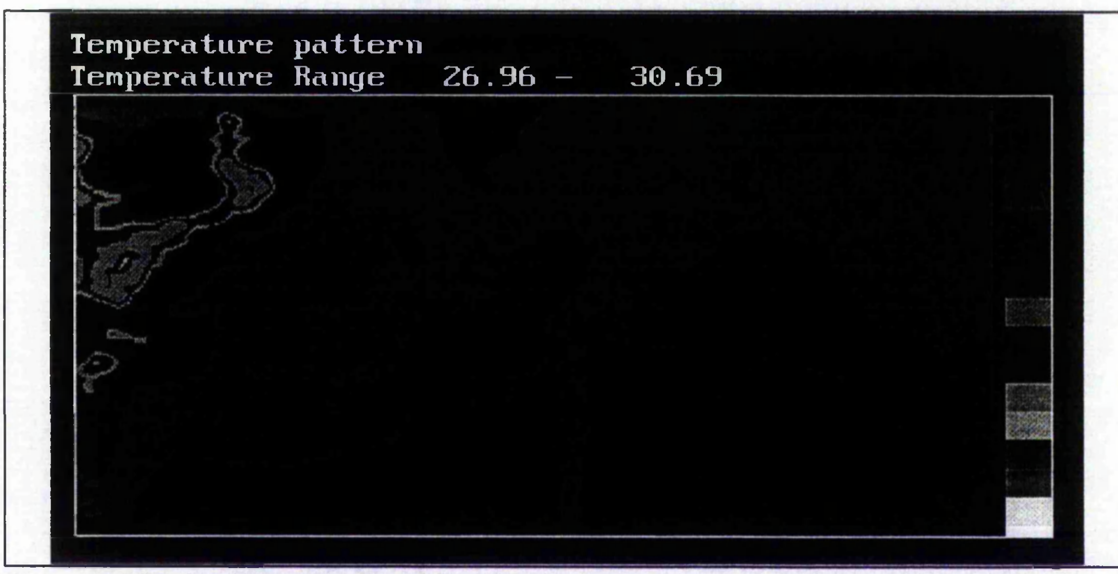

Figure 7.4 Temperature distribution

The RGB values of the second image were first converted to hue values using the simple conversion (Equation 6.17). The hue values were saved in one DT2871 buffer, then converted to temperature values according to the looking up table. The hue Figure 7.4 shows the temperature distribution in the test cell where the range of the liquid crystal temperature varied from 27°C to 31°C. The white and black patches indicate the range from low to high values respectively. The grey vertical lines in the centre of Figure 7.4 show the path of the rising hot stream directly above the heated cylinder.

Figure 7.5 shows the temperature contours of step 0.1°C.

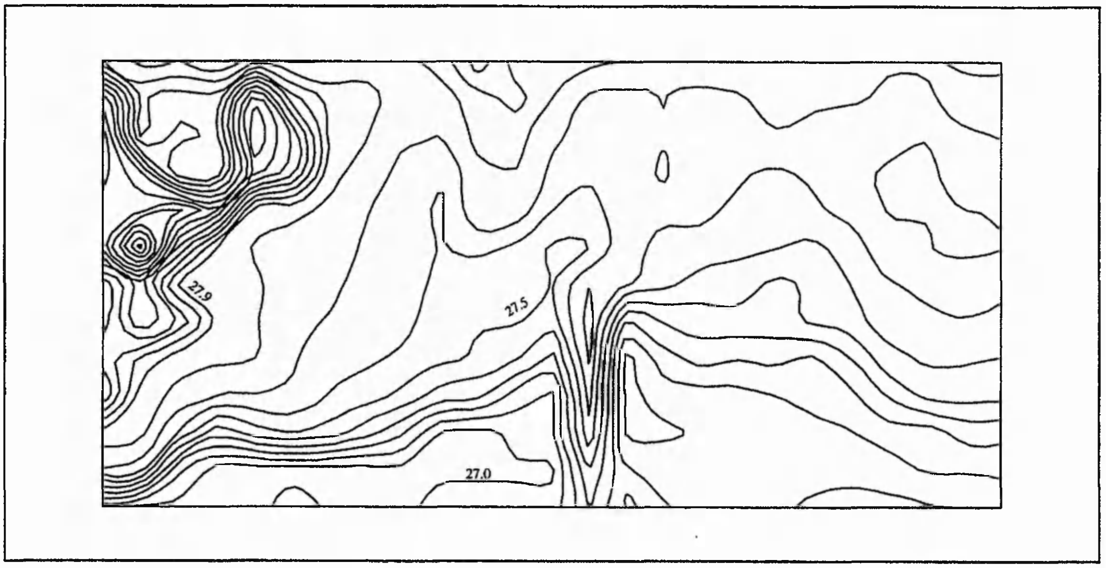

Figure 7.5 Temperature contours

7.3.1.4 Uncertainties

The sources of error in using the colour images to measure the velocity and temperature simultaneously are electronic noise, screen deformation, lens distortions, refraction index changes and information extraction techniques. Usually the electronic noise, the screen deformation and lens distortion are not significant, since noise can be filtered out by image pre-processing and, screen deformation and lens distortion can be corrected by

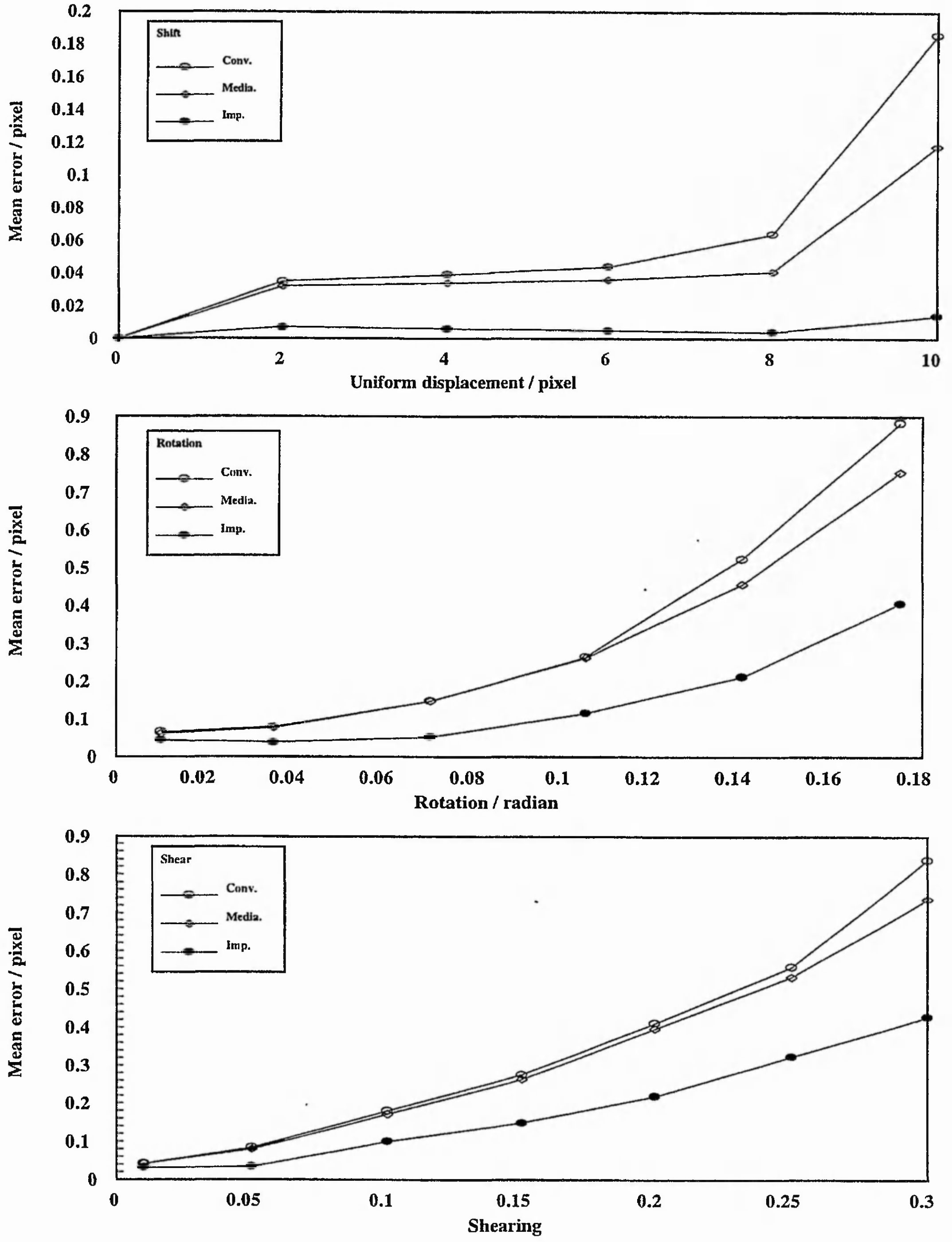

Figure 7.6 Comparsion of mean errors using true particle image of BM100R29C4WS33

calibrating the system before the measurement is done. The temperature changes the refraction index of fluid resulting in the flow images being distorted. This problem has not been addressed in this thesis.

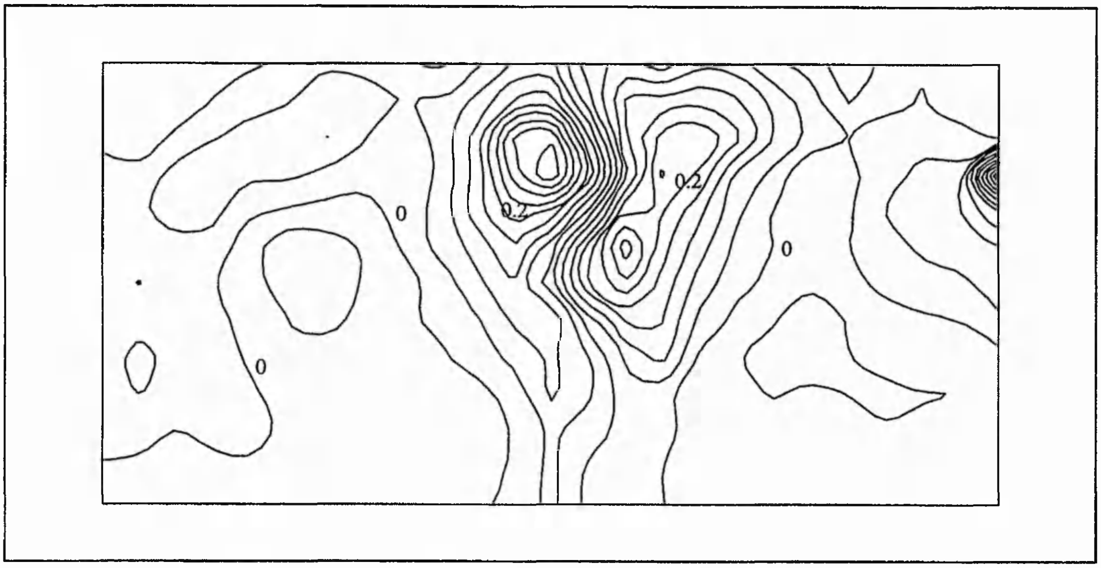

Rotation angle distribution

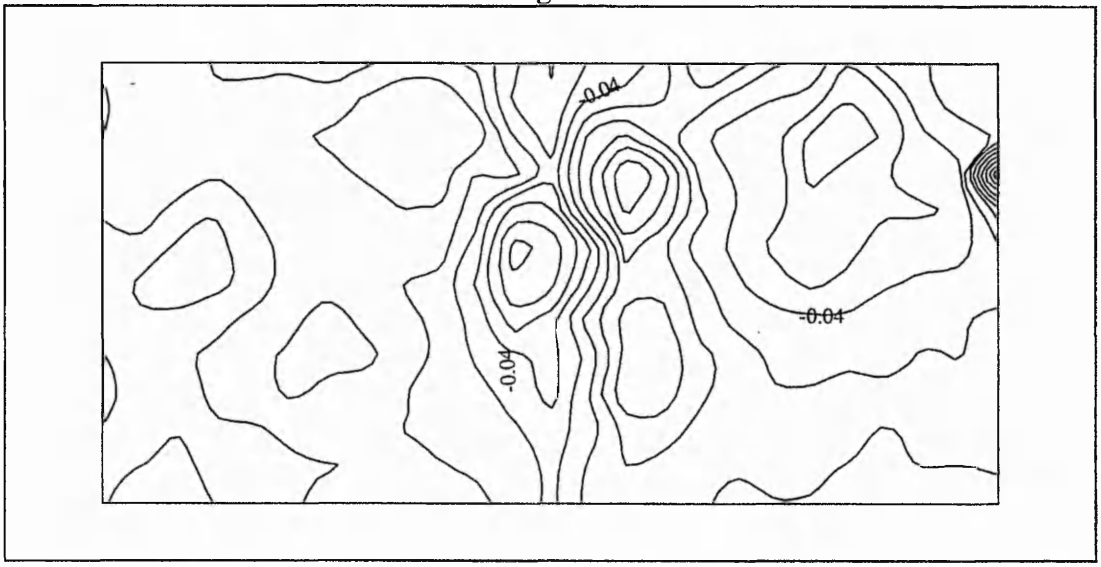

Shearing distribution

Figure 7.7 Rotation and shearing distribution

A true image of fluid seeded with liquid crystal particles is shifted, rotated and bi-axial sheared to generate a second image. The PIV techniques are applied on these two images to investigate the uncertainties of velocity measurements (Figure 7.6). The major source of velocity measurement uncertainty is non-uniformity of velocity distribution within the interrogation spot. Uniform displacements contribute little error to velocity measurement, and rotation and shearing movements lead to large error of velocity measurement. The rotation angle and shearing distributions are calculated for the velocity data, and plotted in Figure 7.7.

The maximum displacement is 6.79 pixels, rotation angle varies from -0.418 to 0.455 radians and shearing changes from -0.231 to 0.335, where the poorest velocity measurement is located at highest rotation and shearing values. The average rotation angle is 0.0502 radians and average shearing is 0.0397, so that the average error is less than 0.1 pixels. The average relative error based on the maximum displacement is less than 1.5%.

The error of temperature measurement is from the hue-temperature calibration. In fact the hue-temperature curve depends on the inherent property of the liquid crystals and the hue interpretation. The hue interpretations (Equation 6.17) provide accurate temperature data for BM100/R29C/4W/S33 in the red to green colour region, where the standard error of regression is less than 0.1°C. In the blue colour region, the error of temperature measurement is around 0.4°C.

7.3.2 Natural convection of square box

7.3.2.1 Experimental rig

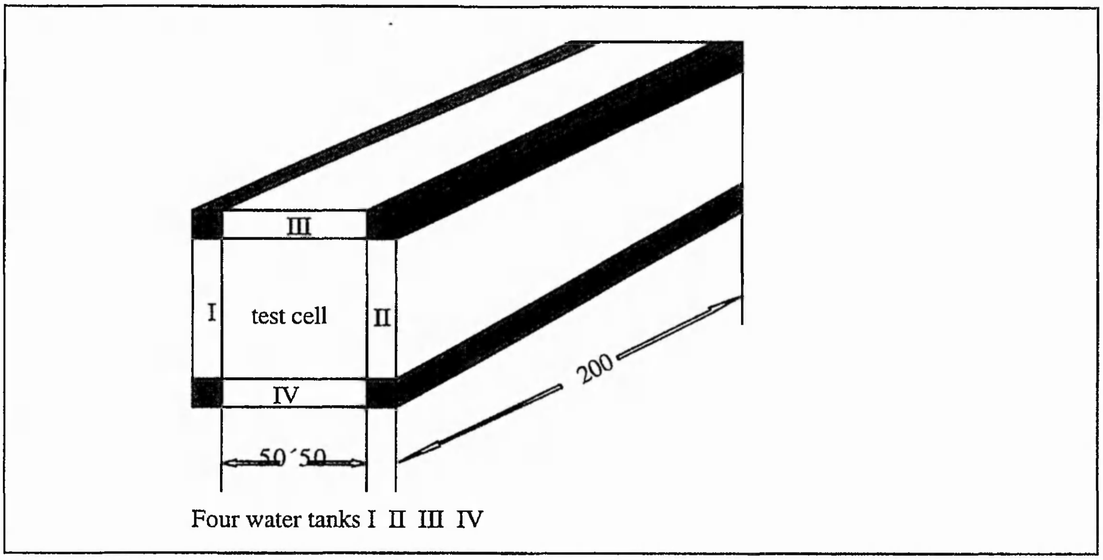

Figure 7.8 Schematic diagram of the second experimental rig

The second experiment is the natural convection within a square box. The test cell consisted of a transparent Perspex tank (50 ´ 50 ´ 200 mm) containing glycerol at 45°C heated by four water baths in which warm water at ~60°C was circulated from two constant temperature water reservoirs. The test cell could be heated from both side walls or heated from bottom to top walls (Figure 7.8). The flow was artificially seeded with 0.01% micro-encapsulated liquid crystal particles (BM100/R45C/15W/S33) of 100mm mean diameter. A thin (5mm) plane of the flow domain was illuminated using white light and images were recorded at right angles to this plane using a Pulnix TLC-X colour CCD camera.

7.3.2.2 Calibration of Hue and Temperature

Calibration of the Hue and Temperature relationship was performed by means of a calibrated thermocouple. The thermocouple was located on the centre of the test cell. The water temperature in the test cell increased from 43°C to 56°C in steps of 0.1-0.5°C. The glycerol was stirred frequently in order to obtain uniform temperature distribution all over the test cell. The colour images and their corresponding temperatures were saved in the IBM 386SX computer. The hue values at viewing angles of -4.0^0, 0.0^0, 4.0^0 have been plotted at Figure 6.13 (BM100/R45C/15W/S33). DT2871 hue conversion was used. The curve of the simple conversion was divided into three regions for curve fitting, considering the errors introduced by variation of the viewing angle.

Region 1: 43.544 - 45.230°C

$$Temperature = 0.0126Hue + 43.347 \qquad (7.10)$$

with standard error deviation of 0.095°C.

Region 2: 45.230 - 47.392°C

$$Temperature = 0.0031\,Hue^2 - 0.849Hue + 103.391 \qquad (7.11)$$

with standard error deviation of 0.188°C.

Region 3: 47.392 - 56.967°C

$$Temperature = 1.700Hue - 222.263 \qquad (7.12)$$

with standard error deviation of 0.857°C

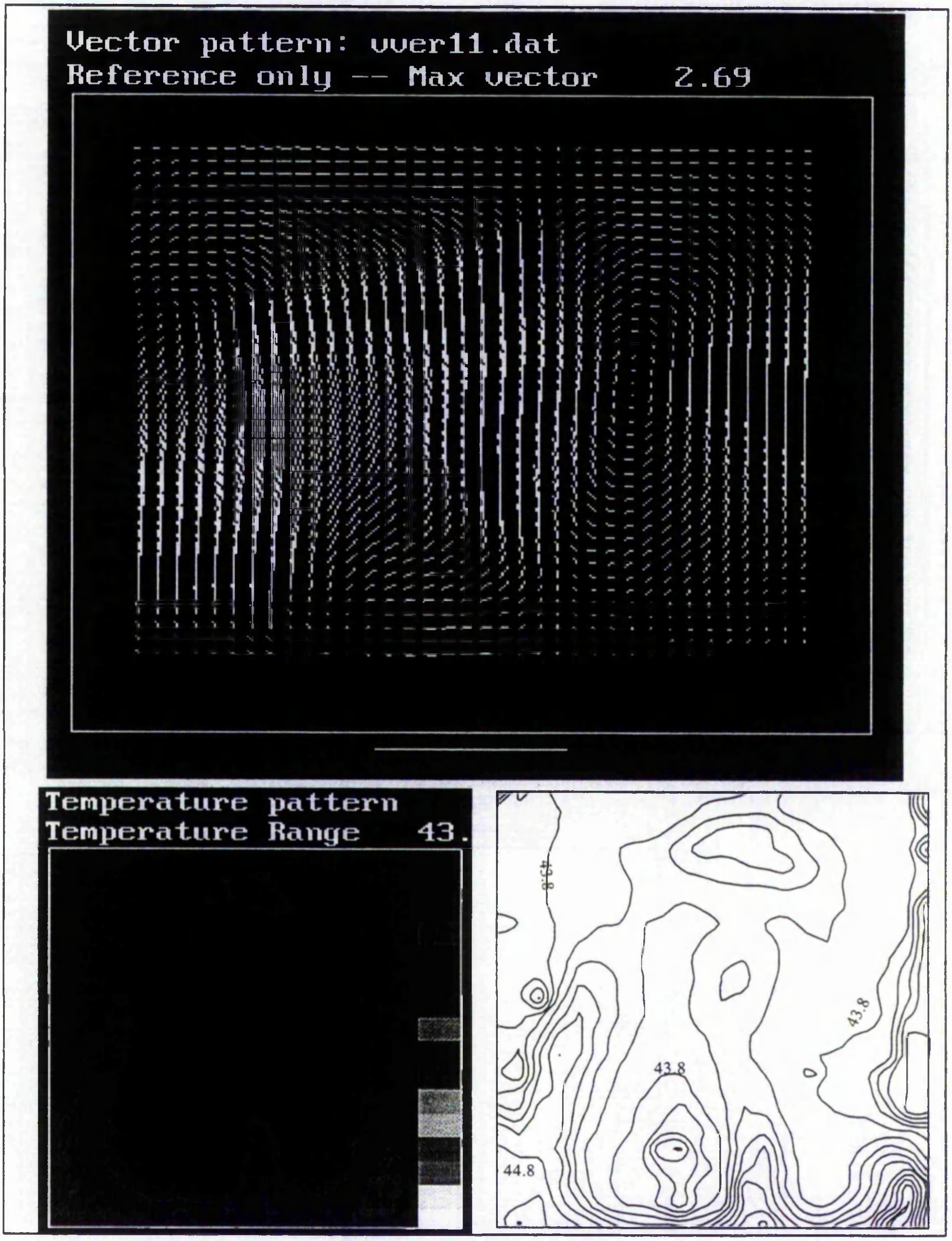

Figure 7.9 Velocity and temperature distribution of the natural convection studied

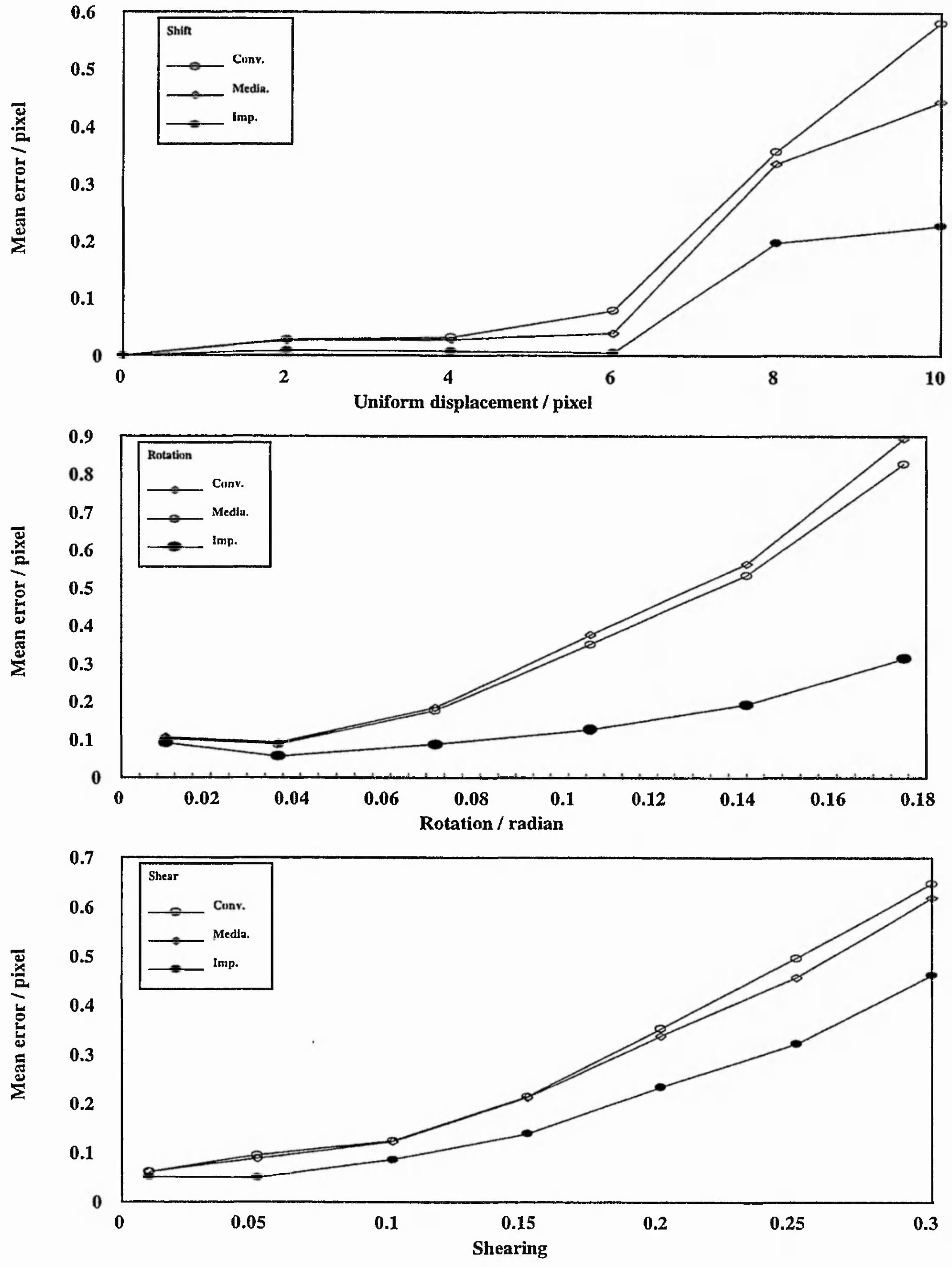

Figure 7.11 Comparsion of mean errors using true particle image of BM100R45C15WS33

The hue-temperature relationships in the three regions were used to build a look-up-table of hue and temperature conversions (Appendix IV) for conversion of data in the hue buffer to temperatures.

7.3.2.3 Velocity and temperature results

While the bottom plate of the square box was heated by the bottom tank with water at 60°C and both side tanks with water at 45°C, the flow was rising from the center of the bottom line to the top, and developing into circulating flows to both sides (Re » 0.426, Pr » 1.3´10^{7} and Ra » 8.6´10^{4} based on the box size 50 mm). The flow images at a particular moment were grabbed, the intensity image of the first colour image was saved in the fourth buffer of DT-2871, and the second colour image, with 3.02 seconds delay, was saved in the HSI buffers in HSI mode. The velocity distribution was extracted by the improved PIV and temperature was measured using DT-2871 hue interpretation.

7.3.2.4 Uncertainties

The PIV techniques are applied on true images of flow seeded with liquid crystal particles BM100/R45C/15W/S33 to investigate the uncertainties of velocity measurements (Figure 7.10). The rotation angle and shearing distribution are derived from the velocity data and plotted in Figure 7.11.

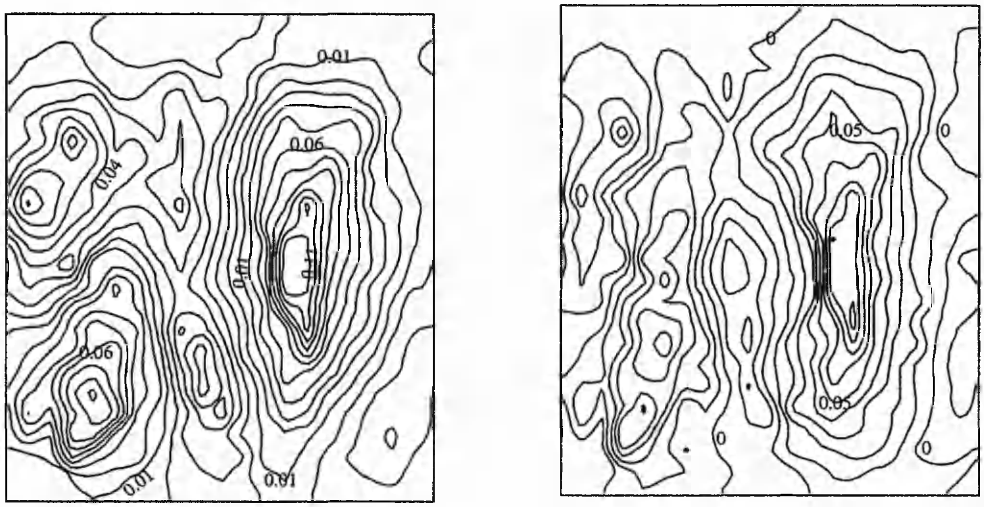

Figure 7.11 Rotation angle and shearing distributions (Rotation angle - left; shaering - right)

The maxmum displacement is 2.69 pixels, the rotation angle varies from -0.086 to 0.131 radians and shearing changes from -0.048 to 0.107. For worst case, the error is less than 0.25 pixel, the relative error is less than 10%. The average rotation angle is 0.0248 and shearing is 0.0183, that the average error is less than 0.13 pixels and the average relative error is less than 5%.

The hue interpretations of DT-2871 provide accurate temperature data for BM100/R45C/15W/S33 in the red to green colour region, where the standard error of regression is less than 0.1°C. In the blue colour region, the error of temperature measurement is around 0.8°C.

7.4 Conclusions

Simultaneous measurement of velocity and temperature is demonstrated in two case studies. Intensity images of the colour images of flow are used for velocity measurement, while the hue images are used for temperature measurement.

The main source of error of velocity measurement is from the non-uniformity of velocity distribution within the interrogation spot of PIV. The error increases as the rotation angle and shear of flow increase. The error in velocity measurement is dependant on the flow itself. The average relative error of the improved cross-correlation method is less than 6% for the measurements of the two natural convection flows, which is a significant improvement when compared with errors of the conventional PIV method.

Temperature measurement using liquid crystal particles gives accurate temperature (error less than 0.1°C) in the red to green colour region of the liquid crystals but a large error (error of 0.4/0.8°C) is associated with the temperature data obtained in the blue region of the liquid crystals. It is reccommended to carry out temperature measurement in the red to green colour region. In all colour ranges the relative error is less than 2%.

Chapter 8 Conclusions and recommendations

The thesis is summarized in this chapter. Conclusions and further investigations are presented. The main achievement of this thesis is simultaneous measurement of velocity and temperature by combining particle image velocimetry with thermochromic liquid crystals. The errors caused by the flow movements which cannot be ignored for video based particle image velocimetry have been significantly suppressed by the improved cross-correlation method. Best hue interpretations have been used for temperature measurements. Accurate temperature measurement has been achieved in the red to green colour region of thermochromic liquid crystals used in this thesis. The simultaneous measurement technique has been applied for two cases of natural convection flows. Accurate velocity and temperature data have been obtained.

8.1 Thermochromic liquid crystals

Different colour spaces for temperature measurement have been examined, especially the hue representations. XYZ and uniform colour spaces are linear transformations of RGB colour space; HSI colour space is non-linear transferred from RGB colour space. Identification of colour displayed by liquid crystals is simplified in HSI colour space because only hue value is of interest of temperature measurement, while the value of saturation and intensity are within certain range.

Several hue representations in HSI colour space are compared for the liquid crystals used in this thesis. Results reveal that a particular hue representation may be suitable for a particular liquid crystals but may not be suitable for others. Two hue representations are used for colour identification for the liquid crystals BM100R29C4WS33 and BM100R45C15WS33. The effects of viewing angle are studied. While the variation of viewing angle is within ±10°, the error in hue value is less than 6% for pure liquid crystals. Further, encapsulation procedure greatly reduces the variation of colour due to viewing angle.

Thermochromic liquid crystals in encapsulated form can act as particles, while the liquid crystals display colours at different temperature. Analysis of the movement of particles following the flow leads to full field velocity measurement. Encapsulated liquid crystals enable the simultaneous measurement of velocity and temperature, being assisted by the true colour image facilities.

8.2 Particle image velocimetry

Theoretic analysis of cross-correlation has been carried out in chapter 3 based on particle image velocimetry theories of Adrian and Yao (1983), Adrian (1986c), Keane and Adrian (1990, 1992), Westerweel (1993) and digital image processing theory, which provides a theoretical base for cross-correlation analysis. Assuming the velocity distribution is uniform at a small area, the velocity field acts on flow images in the small area as a linear filter, where the location of the peak of cross-correlation between the first image and the second image with a time delay, corresponding to the displacement between the two images in the short time period. The peak position depends on the velocity distribution, but it is biased because of uniform movement between the two images. The signal to noise ratio is dependant on the particle image density (N_I) and strength of in-plane movement, assuming two-dimensional flow only. For video based PIV, because the minimum size of the particle image on the CCD camera will not be less than one pixel, then the peak of cross-correlation always covers more than one pixel. This makes it possible to estimate the centroid of the displacement at sub-pixel accuracy. Three sub-pixel position method has been compared and parabolic fit is selected due to its superior accuracy and simplicity.

The accuracy of locating the correlation peak is investigated in chapter 4. Particular attention has been paid to the effects of flow movements on velocity measurement. There are several experimental parameters that affect the spatial resolution, accuracy and reliability of video based particle image velocimetry, such as the interrogation spot size, the particle source density, the particle image density and the particle size. Flow movements have effects on the velocity measurement, especially for video based particle image velocimetry which has low image resolution and limited frame rate. Few researchers paid attention to the effects of flow movements. A theoretical investigation found that uniform displacement leads to a decrease of particle pairs within the interrogation spot that decreased the accuracy of the velocity measurement. The peak location is biased due to the rotation movement (Equation 4.9) and shearing movement (Equation 4.14). Considering interactive effects of experimental parameters (interrogation spot size, particle image density and particle image size) and flow movements, simulations are carried out to investigate the effects of the experimental parameters and the local flow movements. Results show that a suitable interrogation size is 32×32 pixel, particle image density should be larger than 10 and image particle size should be bigger than 3 pixels. The errors of velocity measurement increase as the scales of the flow movements increase. The cross-correlation coefficients increase as the scales of the flow movements decrease, while the errors decrease. The cross-correlation coefficient could be treated as a reliability measure of velocity measurements.

An improved cross-correlation method is proposed to obtain accurate velocity measurement in chapter 5, because higher cross-correlation coefficient leads to more accurate velocity result. Simulation results prove that the accuracy of velocity measurement is significantly improved by the proposed cross-correlation method. For uniform displacements less than 10 pixels, the errors are eliminated. For rotation and shearing movement, the errors are 30% less compared to the median filtered results of the conventional PIV.

8.3 Simultaneous measurement

Simultaneous measurement has been achieved by combining particle image velocimetry with thermochromic liquid crystals. It has been validated by using synthetic particle images and true colour particle images and applied for two natural convection flows. One is natural convection from a heated steel tube and another is the convection with a square Perspex box. Simple hue conversion (Equation 6.17) was applied on temperature measurement using

BM100/R29C/4W/S33 and hue conversion of DT-2871 was applied on temperature measurement using BM100/R45C/15W/S33. The accuracy of velocity measurement depends on the flow measured, varying with the rotation angle and shearing. The average relative error of velocity measurement is less than 6%. The accuracy of temperature measurement varies in different colour regions of liquid crystals. High accuracy temperature data can be measured in the red to green colour region. The relative error of temperature measurement is less than 2%.

A menu driving package has been completed for the purpose of the simultaneous measurement.

8.4 Further investigations

For temperature measurement using thermochromic liquid crystals, accurate colour identification is essential. Colour identification depends on the structural properties of liquid crystals and the colour space theory applied. Further investigations on colour theory and structure property of liquid crystals are required for a suitable hue representation for temperature measurement.

For velocity measurement, the cross-correlation algorithm is good at extracting the uniform displacement, but has poor performance in the cases of rotation and shearing movements. The improved cross-correlation method suppresses the errors caused by image distortions but it is time consuming. To find an algorithm which is good at extracting uniform displacement and at the same time tolerates larger distortions of image pattern, neural networks and fuzzy logic algorithms are of interest for further investigations.

Simultaneous measurement of velocity and temperature is achieved for investigation of natural convection. For high speed velocity flow, higher resolution colour image facilities and a synchronic signal controller are required. Three-dimentional velocity and temperatue information are required for complex three dimensional flows, which will require further study.

References

Alahayari A and Longmire E K 1994 Particle image velocimetry in a variable density flow: application to a dynamically evolving microburst. Experiments in Fluids 17. 434-440.

Adrian R J and Yao C S. 1983 Development of pulsed velocimetry (PLV) for measurement of turbulent flow. *Proc 8th Symposium on Turbulence.* University of Missouri Rolla. 170-186.

Adrian R J 1984 Scattering particle characteristics and their effect on pulsed laser measurements of fluid flow: speckle velocimetry vs particle image velocimetry. *Applied Optics.* Vol **23**. No. **11**.

Adrian R J. 1986a Image shifting technique to resolve directional ambiguity in double-pulsed velocimetry, *Applied Optics* Vol.**25** No **21**.

Adrian R J. 1986b Multi-point optical measurements of simultaneous vectors in unsteady flow a review. *Int J Heat & Fluid Flow* 0142-727x/86 127-145.

Adrian R J. 1986c Statistical properties of particle image velocimetry measurements in turbulent flow. *Laser Anemometry in Fluid. Mechanics - III.* 115-129.

Adrian R J. 1989 Engineering applications of particle image velocimeters. *ICALEO'89 Optical Methods in Flow and Particle Diagnostics.* 56-71.

Adrian R J. 1991 Particle-Imaging Techniques for Experimental Fluid Mechanics. *Annu. Rev Fluid Mech.* **23**: 261-304.

Akino N, Shiina Y, Kunugi T, Seki M and Okamoto Y. 1986 Visualization of natural convection in enclosures with complex Geometries by thermo-sensititive liquid crystal particles suspended in fluids Flow Visulizaton in Japan Vol.6 No 22 July.

Akino N Kunugi T, Shiina Y, Ichimiya K and Kurosawa A 1989a Fundamental study on visualization of temperature fields using thermosensitive liquid-crystals. Proc. of 5th Int. Symposium on flow visualization. 87-92.

Akino N, Kunugi T, Ichimiya K, Mitsushiro K and Ueda M 1989b Improved liquid-crystal thermometry exclusing human color sensation. Part I: Concept and calibration. J. Heat Transfer Vol 111 585-565.

Arroyo M P and Greated C A 1991 Stereoscopic particle image velocimetry. Meas. Sci. Technol. Vol 2 1181-1186.

Arroyo M P and Greated C A 1992 A three dimensional particle image velocimetry system and its application to the measurement of acoustic streaming. Proceeding of Euromech Colloquium 279.

Ashforth-Frost S and Jambunathan K 1993 Flow visualisation using liquid crystals. SPIE Vol 2005. 237-245.

Ashforth-Frost S, Dobbins B N, Jambunathan K, Wu X P and Ju X Y. 1993 A comparison of interrogation methods for particle Image Velocimetry. SPIE Vol. **2005** 478-489.

Ashforth-Frost S 1996 Quantitative thermal imaging using liquid crystals. Int. J. Biomedical Optics, 1(1), 18-27.

Beck F 1986 Use of liquid-crystal thermography for defect location on seminconductor device. Quality and reliability engineering international vol 2 143-151.

Barker D B and Fourney M E. 1977 Measuring fluid velocities with speckle patterns. Optics Letters Vol 1 No 4 October 1977.

Bergman T L and Ungan A U 1988 A note on lateral heating in a double-diffusive system J Fluid Mech 1988 Vol 194 pp 175-186.

Bernal L P and Kwon J T. 1988 Surface flow velocimetry field measurement by laser speckle photography. *Proc 4th international symp on appl of laser anemometry to fluid mechanics.*

Bjorkquist D C. 1991 Reduced pixel resolution PIV analysis Laser anemometry - Volume 1 *ASME* 303-308.

Brandt A and Merzkirch W 1994 Particle Image Velocimetry applied to a spray jet. *Part. Part. Syst. Charact.* **11** 156-158.

Braun M J and Canacci V A 1992 Full field flow visualization and computer aided velocity measurements in a bank of cylinders in a wind tunnel. Experiments in Fluids 13. 117-127.

Braun M J, Dzodzo M and Lattime S B 1993 Automatic computer based non-intrusive temperature measurements in laminar natural convection using TLC in enclosured with variable aspect ratio. FED-Vol 172, Experimental and Numerical Flow Visualization ASME. 111-119.

Brown G H 1973a Properties and applications of liquid crystals. Journal of Electronic Materials, Vol 2, No 3. 403-430.

Brown G H 1973b Structure property and some applications of liquid crystals. Journal of the Optical Society of America, Vol 62 No 12 1505-1514.

Buchhave P 1992 Particle image velocimetry - Status and trends. Experimental thermal and fluid science 5, 586-604.

Brüker C and Althaus W 1992 Study of vortex breakdown by particle tracking velocimetry (PTV). Experiments in Fluids 13. 339-249.

Camci C, Kim K and Hippensteele S A 1991 A new hue capturing technique for the quantitative interpretation of liquid crystal images used in convective heat transfer studies. ASME 91-GT-122. 1-13.

Carosone F, Cenedese A and Querzoli G 1995 Recognition of partially overlapped particle images using the Kohonen neural networks. Experiments in Fluids 19. 225-232.

Castellano J A and Brown G H 1973 Thermotropic liquid crystals. Part II Current uses and future ones. Chemtech April 1973 229- 235.

Cenedese A and Paglialunga A. 1988 A new technique for the determination of the third velocity component with the PIV. *Proc 4th international symposium on application of laser anemometry to fluid mechanics.*

Cenedese A and Paglialunga A 1989 Automatic tracking procedure for the analysis of a multiexposed photograph Flow Visualization V Proceeding of the fifth international symposium on flow visualization August 21-25 1989 Prague Czechoslovakia.

Cenedese A and Paglialunga A 1990 Digital direct analysis of a multiexposed photograph in PIV Experiments in Fluids 8 pp 273-280 1990.

Cenedese A and Romano G P 1991 Space derivatives and largangian correlations evaluation with PIV technique Laser anemometry - Volume 1 1991.

Cenedese A, Doglia G and Romano G P 1994 LDA and PIV velocity measurements in free jets. Experimental Thermal and Fluid Science 9 125-234.

Chamberlin G J and Chamberlin D G 1980 Colour - its measurement, compututation and application. Edited by Thomas L C. Heyden.

Chan T L, Jambunathan K, Leung T P and Ashforth-Frost 1994 A surface temperature calibration method for thermochromic liquid crystals using true-colour image processing. 10th Int. Heat Transfer Conference. Vol 2 201-206.

Chang T P and Tatterson G B. 1983 An automated analysis method for complex three dimensional mean flow fields. Proc. Third Int. Symp. Flow Visualization. 266-273.

Chang T P, Wilcox N A and Tatterson G B. 1984 Application of image processing to the analysis of three-dimensional flow fields. Opt. Eng. 23(3), 283-287.

Ciccone A D, Kawall J G and Keffer J F 1989 Scientific visualization of saltating particle trajectories Flow Visualization V Proceeding of the fifth international symposium on flow visualization August 21-25 Prague Czechoslovakia.

Ciccone A D, Kawall J G and Keffer J F 1990 Flow visualization/digital image analysis of saltating particle motions Experiments in Fluids 9 pp 65-73.

Cloud G, Falco R, Radke R and Peiffer J 1980 Noncoherent-light speckle photography for measurements of fluid velocity fields SPIE Vol 243 Applications of speckle phenomena 1980 pp 150-157.

Cooper T E, Field R J and Meyer J F 1975 Liquid crystal thermography and its application to the study of convective heat transfer Transactions of the ASME August 1975.

Coupland J M, Pickering C J D and Halliwell N A 1988 Particle image velocimetry: confidence criteria at low seeding densities Proc 4th international symposium on applications of laser anemometry to fluid mechanics.

Dabiri D and Gharib M 1990 Digital particle image thermometry and its application to a heated vortex-ring. ASME FED V95, 27-34.

Dabiri D and Gharib M 1991 Digital particle image thermometry: the method and implementation Experiments in Fluids 11 77-86 1991.

Dudderar T D, Meynet R and Simpkins P G 1988 Full field laser metrology for fluid velocity measurement. Optics and lasers in engineering. Vol 9. 163-189.

Durst F, Melling A and Whitelaw J H. 1976 *Principles and Practice of Laser-Doppler Anomometry*. Acadamic Press.

Dzodzo M B 1993 Visualization of laminar natural convection in romb-shaped enclosures by means of liquid crystals. Imaging in Transport Processes. 183-193.

Dzodzo M, Braun M J and Lattime 1994 A non-intrusive computer automated investigation of natural convection using thermochromic liquid crystals and comparison with numerical simulation. 10th
Int. Heat Transfer Conference Vol 2, 225-230.

Edwards R V 1988 Some practical considerations of the resolution and accuracy of particle image velocimetry Proc 4th international symposium on applications of laser anemometry to fluid mechanics. 2.16

Emrich, R J edited.1981 Methods of Experimental Physics - Fluid dynamics. Vol **18**. Part A.

Erbeck R 1985 Fast image processing with a microcomputer applied to speckle photography Applied Optics Vol.24 No 22 15 November 1985 pp 3838-3841.

Farina D J, Hacker J M, Moffat R J and Eaton J K 1993. Illumination invarient calibration of thermochromic liquid crystals. HTD-Vol. 252, Visualization of Heat Transfer Porcesses ASME. 1-11.

Farrel P V and Goetsch D 1989 Optical analysis of particle image velocimetry data ICALEO'89 Optical Methods in Flow and Particle Diagnostics. 80-89.

Farrel P V 1992 Optical evolution methods in particle image velocimetry. Optics and lasers in engineering 17. 187-207.

Farrel P V 1993 Application of numerical and optical evaluation schemes for particle image velocimetry. Experiments in Fluids 14, 433-446.

Fergason J L 1964 Liquid Crystals. Sci. Amer. 211(2), 77-85.

Fergason J L and Brown G H 1968 Liquid Crystal in Nondestructive Testing. Applied Optics, Vol 7, No. 9. 1729-1737.

Ferrari T, Saulnier J Fagot H, Smigielski P and Harertig J 1983 Instantaneous velocity fluid measurement in a sheet of fluid by means of chronophotography in coherent light: improvement of the method ICIASF'83 IEEE. 23-29.

Gharib M, Hernan M A, Yavrouian A H and Sarohia V 1985 Flow velocity measurement by image processing of optically activated tracers AIAA 23rd aerospace sciences meeting January 14-17 1985 Reno Nevada pp 1-6.

Gonzalez and Wintz 1987 Digital Image Processing. (Reading, MA: Addison-Wesley).

Goss L P, Post M E, Trump D D and Sarka B 1989 Two-color particle velocimetry ICALEO'89 Optical Methods in Flow and Particle Diagnostics. 99-109.

Grant I and Owens 1990 Confidence interval estimates in PIV measurements of turbulent flows. Applied Optics Vol 29. No 10. 1400-1403.

Grant I and Qiu J H 1990 Digital convolution filtering techniques on an array processor for particle image velocimetry Applied Optics Vol 29. No 29. 4327-4331.

Grant I, Smith G H, Liu A, Owens E H and Yan Y-Y 1989 Measuring turbulence in reversing flows by particle image velocimeter ICALEO'89 Optical Methods in Flow and Particle Diagnostics. 90-98.

Grant I, Zhao Y, Tan Y and Stewart J N 1991 Three component flow mapping: experiences in stereoscopic PIV and holographic velocimetry Laser anemometry - Volume 1 ASME.

Grant I and Pan X 1994 The neural network method applied to particle image velocimetry. SPIE Vol 2005 437-447.

Gray C and Greated C A 1993 A processing system for the analysis of particle displacement holograms. SPIE Vol 2005 636-647.

Gray C and Greated C A 1995 Evolution of the particle image velocimetry measuring technique. "Strain" Feb.

Greated C A, Skyner D J and Brauce T 1992 Particle image velocimetry (PIV) in the coastal engineering laboratory. 23rd Int. Conf. on Coastal Engineering.

Grousson R and Mallick D 1977 Study of flow pattern in a fluid by scattered laser light Applied Optics Vol 16 No 9 September.

Grum F and Bartleson C J edited. 1980 Colour Measurement. Optical Radition Measurements Vol 2. New York : London Academic Press.

Guezennec Y G and Kiritsis N 1989 Statistical investigation of errors in particle image velocimetry ICALEO'89 Optical Methods in Flow and Particle Diagnostics.

Guezennec Y G and Kiritsis N 1990 Statistical investigation of errors in particle image velocimetry Experiments in Fluids 10 pp 138-146 1990.

Hassan Y, Blanchat T and Hild R 1990 Full-field velocity imaging technique using high-energy pulsed laser velocimetry SPIE Vol 1244 Image processing algorithms and techniques 1990 pp 130-142.

Hassan Y A, and Canaan R E 1991 Full-field bubbly flow velocity measurements using a multiframe particle tracking technique Experiments in Fluids 12 pp 49-60 1991.

Hassan Y A, Philip O G and Schmidlt 1993 Bubble collapse velocity measurements using a particle image velocimetry technique with fluorescent tracers, FED-Vol 172 Experimental and Numerical Flow Visualization ASME, 85-92.

Hiller W J and Kowalewski 1987 Simultaneous Measurement of Temperature and Velocity Fields in Thermal Convection Flows. Flow Visualization. Vol 4. 617-622.

Hiller W J, Koch S and Kowalewski T A 1989 Three-dimensional structures in laminar natural convection in a cubic enclosure. Experimental Thermal and Fluid Science 2, 34-44.

Hinsch K D 1995 Three-dimensional particle image velocimetry. Meas. Sci. Technol. 6. 742-753.

Hollingsworth D K, Boehman A L, Smith E G and Moffat R J 1989 Measurement of temperature and heat transfer coefficient distributions in a complex flow using liquid crystal thermography and true-color image processing. ASME winter meeting. ASME HTP 123. 35-42.

Höker R and Kompenhans J 1989 Some technical improvements of particle image velocimetry with regard to its application in wind tunnels. ICIASF'89. 545-554.

Huang H T, Fiedler H E and Wang J J 1993a Limitation and improvement of PIV Part I: Limitation of conventional techniques due to deformation of particle image patterns Experiments ion Fluids 15 pp 168-174 1993.

Huang H T, Fiedler H E and Wang J J 1993b Limitation and improvement of PIV Part II: Particle image distortion, a novel technique. Experiments ion Fluids 15 pp 263-273 1993.

Huang H T and Fielder H E 1994 Reducing time interval between successive exposures in video PIV. Experiments in Fluids 17 356-363.

Huang K, Slepicka J and Cha S S 1993 Cross-correlation of three-dimensional images for three-dimensional three-component fluid measurements. SPIE Vol 2005. 655-659.

Humphreys W M Jy 1991 A histrogram-based technique for rapid vector extraction from PIV photographs Laser anemometry - Volume 1 ASME 1991.

Huntley J M, Goldrein H T and Benckert L R 1993 Parallel processing system for rapid analysis of speckle photography and particle-image-velocimetry data. Applied optics Vol 32. No 17. 3152-3155.

Hussein H J 1995 Bias correlation for measurements of particle-velocity correlations in turbulent flows. Experiments in Fluids 18 462-467.

Ichimiya K, Akino N, Kunugi T and Mitsushiro K 1988 Fundamental study of heat transfer and flow situation around a spacer (in the case of a cylinderical rod as a spacer). Int J. Heat Mass Transfer. Vol 31, No 11 2215-2225.

Jambunathan K, Ju X Y, Dobbins B N and Ashforth-Frost S 1995 An improved cross correlation technique for particle image velocimetry. Meas. Sci. Technol. 6 507-514.

Kasagi N, Hirata M and Kumada M 1981 Studies of full-converge film cooling part I: cooling effectiveness of thermally conductive wall.

Kasagi N and Nishino K 1991 Probing turbulence with three-dimensional particle-tracking velocimetry Experimental thermal and fluid science 1991; 4:601-612.

Keane R D and Adrian R J 1989 Optimization of particle image velocimeters ICALEO'89 Optical Methods in Flow and Particle Diagnostics.

Keane R D and Adrian R D 1990 Optimization of particle image velocimeters. Part I: Double pulsed systems. Meas. Sci. Technol. 1 1202-1205.

Keane R D and Adrian R D 1991 Optimization of particle image velocimeters. Part I: Multiple pulsed systems. Meas. Sci. Technol. 2 963-974.

Keane R D and Adrian R D 1992 Theory of cross-correlation analysis of PIV images. Applied Scientific Research, Vol. 49, pp. 191-215.

Keane and Adrian 1993 Prospect for super-resolution with particle image velocimetry. SPIE Vol 2005. 283-293.

Keane and Adrian 1995 Super-resolution particle imaging velocimetry. Meas. Sci. Technol. 6. 754-768.

Kent J C, Trigui N, Choi W C, Guezennee Y G and Brodkey R S 1993 Photogrammetric calibration for improved three dimensional particle tracking velocimetry (3DPTV). SPIE Vol 2005. 400-412.

Kemmerich T and Rath H J 1994 Multi-level convolution filtering technique for digital laser-speckle-velocimetry. Experiments in Fluids 17 315-322.

Kimura I and Takamori T 1986 Image processing of flow around a circular cylinder by using correlation technique Flow visualization IV pp 221-226 Washington; Hemisphere pub 1986.

Kimura I and Takamori T 1987 Image processing of flow around a circular cylinder by using correlation technique. Flow visualization IV. 221-226.

Kimura I, Kimura H and Takamori T 1988 Image processing of flow velocity vector distributions (Improvement of spatial resolution) 2nd international symposium on fluid - control measurement mechanics - and flow visualisation 5-9 September 1988 Sheffield England. 189-193

Kimura I, Takamori T, Ozawa M, Takenaka N and Sakaguchi T 1990 Simultaneous measurement of flow and temperature fields based on color image information. Flow Visualization. 29-34.

Klein E J 1968 Liquid Crystals in Aerodynamic Testing. Aeronutics and Astronautics, 6, 70-73.

Klein E J and Margozzi A P 1969 Explratory Investigation on Measurement of Skin Friction by Means of Liquid Crystals. NASA TM X-1774, May.

Kobayashi T and Saga T 1988 A real-time velocity measurement algorithm for two-dimensional flow fields 2nd international symposium on fluid - control measurement mechanics - and flow visualisation 5-9 September 1988 Sheffield England. 174-178.

Kobayashi T 1988 Flow visualixation image analysis review 2nd international symposium on fluid - control measurement mechanics - and flow visualisation 5-9 September 1988 Sheffield England.

Kompenhans J, Reichmuth J and Höcker R 1989 Data evaluation in particle image velocimetry by means of a spatial light modulator ICALEO'89 Optical Methods in Flow and Particle Diagnostics.

Kueppers H. 1980 The basic law of colour theory. Barron's Educational Series.

Landreth C C and Adrian R J 1988 Measurement and refinement of velocity data using high image density analysis in particle image velocimetry Proc 4th int symp on appl of laser anemometry to fluid mechanics. 6.14

Landreth C C and Adrian R J 1990 Impingement of a low Reynolds number turbulent circular jet onto a flat plate at normal incidence. Experiments in Fluids 9. 74-84.

Lawson N J, Halliwell N A and Coupland J M 1994 Particle image velocimetry: image labeling by use of adaptive optics to modify the point-spread function. Applied Optics Vol 33, No 19. 4241-4247.

Lee J, Valentino G, Kaufman D and Farel P V 1993 Experimental and Numerical Flow visualization. FED-Vol 172. ASME 65-72.

Liu Z C Landreth C C Adrian R J and Hanratty T J 1991 High resolution measurement of turbulent structure in a channel with particle image velocimetry Experiments in Fluids 10 301-312 1991.

Lourenco L M 1993 Velocity bias technique for particle image velocimetry measurements of high speed flows. Applied optics Vol 32. No. 12. 2159-2163.

Marko K A and Rimai L 1985 Video recording and quantitative analysis of seed particle track images in unsteady flows Applied Optics Vol.24 No 21. 3666-3672.

McCluskey D R, Elgaard C, Easson W J and Greated C A. 1993 The application of PIV to turbulent Two-phase flows. Flow Visualization and Image Analysis. Edited by Nieuwstadt F T M. 207-226.

McDonnell D G. 1987 Thermochromic cholesteric liquid crystals Thermochromic Liquid Crystals. Edited by Gray G W. New York: Wiley.

McElderry E D 1970 Boundary Layer Transition at Supersonic Speeds Measurement by Liquid Crystals. Air Force Flight Dynamics Laboratory. FDMG Tm 70-73, June.

Meinhart C D, Prasad A and Adrian R J 1993 A parallel digital processor system for particle image velocimetry. Meas. Sci. Technol. 4. 619-628.

Metzger D E, Bunker R S and Bosch G 1989 Transient liquid crystal measurement of local heat tranfer on a rotating disk with jet impingement. ASME paper 89-GT-287.

Metzger D E and Kim Y K 1993 Local heat transfer measurement with liquid crystals on rotating surface including non-axisymetric cases. AGARD Conf. Proc 527. Paper 17.

Meynart R 1980 Equal velocity fringes in a Rayleigh-Benard flow by a speckle method Applied Optics Vol 19 No 9 1 May 1980.

Meynart R 1982 Digital image proceeding for speckle flow velocimetry Rev Sci Instrum 53(1) Jan 1982 American institute of Physics.

Meynart R 1983 Speckle velocimetry study of vertex pairing in a low-Re unexcited jet Phys Fluids 26 (8) August 1983 American Institute of Physics. 2074-2079.

Meynart R 1985 Non-Gaussian statistical of speckle noise of Young's fringes in speckle velocimetry Applied Optics Vol 24 No 10. 1448-1453.

Moffat R 1990 Experimental Heat Transfer. Proc 9th Int. Heat Transfer Conference Vol 1 187-209.

Molezzi M J and Dutton J C 1993 Applied of particle image velocimetry in high speed separated flow. AIAA Journal Vol 31, No 3. 438-446.

Moraitis C S and Riethmuller M.L 1988 Stochastic modelling and performance prediction of PIDV experiments Proc 4th Int Symp on appl of Laser anemometry to fluid mechanics 1988.

Moraitis C S and Riethmuller M.L 1989 A real time holographic autocorrelator for the analysis of pulsed laser velocimetry images based on a $Bi_{12}SiO_{20}$ spatial light modulator ICALEO'89 Optical Methods in Flow and Particle Diagnostics.

Murata S 1993 Study of unsteady separated flows by numerical analysis and image processing PhD thesis 1993 Kyoto University Japan.

Nakamura J, Tomita Y and Honda S 1994 Real-time particle image velocimetry using liquid crystal display. IMTC'94 May 10-12.

Nishimura T, Fujiwara M and Miyashita H 1990 Visualization of temperature fields of transient natural convection with maximum density effect in a water-field enclosure by chiral nematic liquid crystals. Journal of Chenical Engineering of Japan Vol 23 No 2. 241-244.

Nishimura T, Fujiwara M and Miyashita H 1992 Visualization of temperature fields and double-diffusive convection using liquid crystals in an aqueous solution crystallizing along a vertical wall Experiments in Fluids 12 245-250.

Nishino K Kasagi N and Hirata M 1988 Study of streamwise vortical structures in a two-dimensional turbulent channel flow by digital image processing Proc 2nd Int Symp on transport phenomena in turbulent flows pp 157-170.

Ogden T R and Hendricks E W 1984 Liquid crystal thermography in water tunnels. Experiments in Fluids 2 65-66 1984.

Ota K, Imoh M and Takagi K 1991 Visualization of natural convection by micro-capsulated thermally sensitive liquid crystals FLUCOME '91 ASME 751-754.

Ozawa M, Muller U, Kimura I and Takamori T 1992 Flow and temperature measurement of natural convection in a Hele-Shaw cell using a thermo-sensitive liquid-crystal tracer Experiments in Fluids 12 213-222.

Philip O G 1993 High speed steam bubble collapse velocity measurements with a particle image velocimetry technique using fluorescent tracers. Trans. Am. NUCL. SOC. Vol 68 Part A. 488-490.

Philip O G, Schmidl W D and Hassan Y A 1994 Development of a high speed particle image velocimetry technique using fluorescent tracers to study stream bubble collapse. Nuclear Engineering and Design 149 375-385.

Prasad A F and Adrian R J 1992 Stereoscopic particle image velocimetry applied to liquid flows. Experiments in Fluids 15. 49-60.

Platzer K H, Hirsch C, Metzger D E and Wittig S 1992 Computer-based areal surface temperature and local heat transfer measurments with thermochromic liquid crystals (TLC). Experiments in Fluids 13 26-32 1992.

Raffel M, Gharib M, Ronneberger O and Kompenhans J 1995 Feasibility study of three-dimensional PIV by correlating images of particles within parallel light sheet planes. Experiments in Fluids 19 69-77.

Ramer E R and Shafer F D 1992 Automated analysis of multiple pulse particle image velocimetry data. Applied Optics. Vol 31. No 6. 779-784.

Reese J and Fan L S 1994 Transient flow structures in the entrance region of a bubble column using particle image velocimetry. Chemical Engineering Science. Vol 49. No 24B. 5623-5636.

Reinitzer F 1989 Contributions to the knowledge of chrolesterol. Liquid Crystals, Vol 5, No 1, 7-18. (A translation, from the German, of the original paper by Reinitzer F published in Monatshefte für Chemie, Vol 9, 421-441 1888).

Reuss D L, Adrian R J, Landreth C C, French D T and Fansler T D 1989 Instantaneous planar measurements of velocity and large-scale vorticity and strain rate in an engine using particle image velocimetry. SAE paper. 590616.

Reuss D L, Bardsley M, Felton P G, Landreth C C and Adrian R J 1990 Velocity, vorticity and strain rate ahead of a flame measured in an engine using particle image velocimetry. SAE paper 900053.

Reuss D L 1993 Two-dimensional particle image velocimetry with electroptical image shifting in an internal combustion engine. SPIE Vol 2005. 413-424.

Reynolds G A, Short M and Whiffen M C 1985 Automated reduction of instantaneous flow field images Optical Engineering Vol 24 No.3 May/June 1985.

Rhee H S, Koseff J R and Street R L 1984 Flow visualization of a recirculating flow by rheoscopic liquid and liquid crystal techniques. Experiments in Fluids 2, 57-64.

Rhee H S, Koseff J R and Street R L 1986 Simultaneous flow and temperature field visualization in a mixed convection flow. Flow visualization IV, 659-664.

Rigg B 1987 Colour physics for industry. Edited by Roderick McDonald.

Rosenfeld A and Kak A C 1982 Digital picture processing. 2nd edition. Vol 1, Vo1 2. New York : London Academic Press.

Scherer J and Bernal L P 1993 Resolution characteristics of holographic particle image velocimetry. AIAA Journal Vol 31. No 3. 434-437.

Seeley C H, Jr, Blanchat T K and Hassan Y A. 1991 Analysis of particle tracking techniques for particle image velocimetry. Trans. AM. NUCL. SOC. 29-31.

Shapiro V 1993 Automatic Young's fringe analysis in the source image plane. Optics and lasers in engineering 18. 307-324.

Shepherd I C and La Fontaine R F 1993 Mapping the velocity field in a centrifugal fan using particle image velocimetry. Journal of wind engineering and industrial aerodynamics 50. 373-382.

Simonnich and Moffat R J 1982 New technique for mapping heat-transfer coefficient contours. Rev. Sci. Instrum. 53(5) 678-683.

Simonnich and Moffat R J 1983 Liquid crystal visualization of surface heat transfer on a concavely curved turbulent boundary layer. 83 Tokyo IGTC 1, ASME 83 GTJ 7 1-11.

Simonnich and Moffat R J 1984 Liquid crystal visualization of surface heat transfer on a concavely curved turbulent boundary layer. Journal of Engineering for Gas Turbines and Power. Vol 106 619-627.

Simpkins P G and Dudderar T D 1978 Laser speckle measurements of transient Bénard convection. J Fluid Mech. Vol 89. part 4 665-671.

Spedding G R and Rignot E J M 1993 Performance analysis and application of grid interpolation techniques for fluid flows. Experiments in Fluids 15. 417-430.

Stucky M J, Nino E, Gajdeczko B and Felton P G 1994 Two-color particle image velocimetry technique for an internal combustion engine. Experimental Thermal and Fluid Science 8, 305-314.

Suter P, Revesz A and Tanner P A 1989 Reconstruction of velocity vectors in a three-dimensional flow field from photographed tracer trajectories Flow Visualization V Proceeding of the fifth international symposium on flow visualization. August 21-25 1989 Prague Czechoslovakia.

Tanaka T 1988 Visualization of the temperature field in thermal storage tanks by using the thermo-sensitive liquid crystal suspension method. 2nd international symposium on fluid - control measurement mechanics - and flow visualization 5-9 September 1988 Sheffield England.

Tanaka and Furuta Y 1989 Study on application of R.G.B laser to flow visualization by means of thermochromic liquid crystal suspension method. Flow Visualization IV.

Teo C L, Lim K B, Hong G S and Yao M H T 1991 A Neural Net Approach in Analyzing Photograph in PIV ISSN#0-7803-0233-8/91 1991 IEEE page 1535-1538.

Tokumaru P T and Dimotakis P E 1995 Image correlation velocimetry. Experiments in Fluids 19 1-15.

Treuner M, Rath H J, Duda V and Siekman N 1995 Thermocapillary flow in drops under low gravity analysed by the use of liquid crystals. Experiments in Fluids 19. 264-273.

Uemura T, Kawahara G and Yamamoto F 1989 High speed image analysis for measuring velocity distribution from pictures of particles Flow Visualization V Proceeding of the fifth international symposium on flow visualization August 21-25 1989 Prague Czechoslovakia.

Uemura T, Iguchi M and Morita Z I 1993 High speed algorithm for digital PIV analysis of multiple-exposure pictures. SPIE Vol 2005. 683-691.

Uemura T, Yamamoto F and Iguchi M 1994 A high speed algorithm for 2D and £D PTV and its application. Transport phenomena in thermal engineering, 1385-1394.

Ushijima S and Tanaka N 1994 Particle tracking velocimetry using laser-beam scanning and its application to transient flows driven by a rotating disk. Journal of Fluid Engineering. Vol 116 265-272.

Utami T, Blackwelder R E and Veno T 1991 A cross-correlation technique for velocity field extraction from particulate visualization Experiments in fluids 10 213-223 1991.

Wernet M P 1991 Particle displacement tracking applied to air flows Laser anemometry - Volume 1 ASME. 327-225.

Wernet M P and Pline A D 1991 Particle image velocimetry for the surface tension driven convection experiment using a particle displacement tracking technique Lase Anemometry - Volume 1 ASME 1991.

Wernet M P 1993 Fuzzy logic particle tracking velocimetry. SPIE Vol 2005. 701-708.

Westerweel J and Nieuwstadt F T 1991 Performance tests on 3-dimensional velocity measurements with a two-camera digital particle-image velocimeter Laser Anemometry Volume 1 ASME 1991.

Westerweel J 1993 Digital Particle Image Velocimetry. PhD Thesis.

Westerweel J 1994 Efficient detection of spurious vectors in particle image velocimetry data. Experiments in Fluids 16. 236-247.

Wilcox N A, Watson A T and Tatterson G B 1985 Color/temperature calibrations for temperature sensitive tracer particles. International Symposium on Physical and Numerical Flow Visualization, June 24-26, 65-74.

Willert C E and Gharib M 1991 Digital particle image velocimetry Experiments in Fluids 10 pp 181-193 1991.

Willert C E and Gharib M 1992 Three-dimensional particle imaging with a single camera Experiments in Fluids 12 pp 353-358 1992

Wormell D C and Sopchak J L 1993 A particle image velocimetry system using a high resolution CCD camera. Int. Conf. Optical Diagnostics in fluid and thermal flow. SPIE Vol 2005. 648-654.

Wozniak K and Wozniak G 1993 Experimental analysis of Benard-convection by combined application of liquid crystals and PIV. EUROTHERMP32. 54-59.

Wu W Y 1980 Fluid Mechanics (in Chinese). Beijing University Press.

Wu Z.-Q, Zhou J, Chen S, Yang L, Xu,H.-Q and Yang J.-L 1991 An image processing system for quantitatively analyzing the 2-D fluid velocity-field image Computers Fluids Vol 20 No 4 pp 359-371 1991.

Wyszecki G and Stiles W S. 1982 Color Science: Concepts and methods, Quantative Data and Formulae. 2nd Ed. pp 486-509, Wiley.

Yamamoto F, Uemura T and Koukawa M 1988 Application of flow visualization and digital image processing techniques to unsteady viscous diffusing free doublet flow (in the case of impulsive concentrated drag application) 2nd international symposium on fluid - control measurement mechanics - and flow visualisation. 184-188.

Yamamoto F, Koukawa M and Itoh M 1989 Flow visualization of elementary solution of unsteady two-dimensional oseen equation by digital image processing technique Flow Visualization V Proceeding of the fifth international symposium on flow visualization August 21-25 1989 Prague Czechoslovakia.

Yano M 1983 Velocity measurement using correlation concerning with digital tracer image Flow Visualization Vol 3 1983 Flow visualization Soc of Japan. (in Japanese).

Yao C-S and Adrian R 1984 Orthogonal compression and 1-D analysis technique for measurement of 2-D particle displacements in pulsed laser velocimetry Applied Optics Vol.23 No 11. 1687-1689.

APPENDIX I

In the experiments LC are used from Hallcrest.

The Hallcrest delivered samples that are identified by a code number which includes all essential information for usage.

The LC are available in different densities for the same type. The density is identified by the Specific Gravity (Sg).

BM	chiral-nematic	sg = 1.02
CM	Cholesteric	sg = 0.97
BCM	BM + CM	sg = 0.97 - 1.02

Further information by code number

R	red start temperature
G	mid green temperature
C	centigrade temperature scale
F	fahrenheit temperature scale
W	colour-play bandwidth
S33	flow visualisation includes 33.3% LC in capsule
C17-10	surface measurement include 10% LC in capsule

The number behind the chemical type is the diameter of the LC in micrometer.

Without number means 10-50 micrometers.

Example:

BM100R29C4W S33

BM	chiral nematic LC
100	diameter 100 micrometers
R29C	red start at 29 C
4W	4 band width
S33	flow visualisation 33.3% LC in capsule

A digital image processor is the heart of any image processing system. An image processor consists of a set of hardware modules that perform four basic functions: image acquisition, storage, low-level (fast) processing, and display. Typically, the image acquisition module has a TV signal as the input and converts this signal into digital form, both spatially and in amplitude. Most modern image processors are capable of digitizing a TV image in one frame-time. For this reason, the image acquisition module is often referred to as a frame grabber.

The storage module, often called a frame buffer, is a memory capable of storing an entire digital image. Usually, several such modules are incorporated in an image processor. The single most distinguishing characteristic of an image storage module is that the contents of the memory can be loaded or read at TV rates. This feature allows the image acquisition module to deposit a complete image into storage as fast as it is being grabbed. Alternatively, the memory can be addressed at TV rates by a display module, which outputs the image to a TV monitor.

The image system used in this project consists of a colour CCD camera (PULNIX TMC-X) a colour image frame grabber (DT-2871) and its co-processor (DT2878) and a RGB colour monitor. The image boards are installed in a IBM PC SX 386.

The TMC-X is an ultra small CCD colour video camera module which uses a CCD (Charge Coupled Device) sensor. The CCD used in the camera has 752×582 picture elements, and working at minimum illumination 4.5 lux F1.2 AGC: OFF (0 dB). The colour CCD sensor converts pictures into a composite signal to a RGB adaptor then RGB signals from the RGB adapter are passed to a colour image frame grabber (DT2871).

The DT2871 (HSI) colour frame grabber captures colour images from the colour CCD camera for image processing. The colour images are captured and displayed in real time at a rate of 25 frames per second. Red, green and blue colour video signals are digitized to form a colour image having 512×512×24-bit pixel resolution. The captured image is stored in three on-board frame-store memory buffers. The three buffers are output simultaneously producing the colour image on a display monitor(SONY KX-14CP1 colour monitor).

The DT2871 supports two different colour spaces: red-green-blue (RGB) or hue-saturation-intensity space (HSI). In its default mode, the DT2871 performs real-time RGB->HSI and HSI->RGB colour space conversions on the pixel data for capture and display.

The DT2878 uses the AT&T DSP32C digital signal processor chip, which feature 32-bit floating point arithmetic, high-throughput, support for large amounts of external memory and low power dissipation.

The DT2878 can be used as a standard DSP board for computation intensive applications. Data can be transferred between the host PC/AT and the DT2878 using the PIO-DMA mode, allowing the DSP32C to continue processing while the data is transferred.

The DT2878 can also be used as a companion co-processor with a frame grabber board (DT2871). An external port on the board supports DT-Connect, which provides high-speed transfer of data between the DT2878 and DT2871. This connection is made using two 26-pin flat ribbon cables, one for input transfers and one for output transfers. Each can transfer 8-bit or 16-bit data at speeds of up to 10 MHz, without involving the host system bus.

Appendix III Look-up-table for BM100/R29C/4W/S33

0-35	36-70	71-105	106-140	141-175	176-210	211-245	246-255
27.000	27.000	27.000	27.236	27.444	27.653	28.517	27.000
27.000	27.000	27.000	27.242	27.450	27.659	28.608	27.000
27.000	27.000	27.000	27.248	27.456	27.665	28.705	27.000
27.000	27.000	27.000	27.254	27.462	27.671	28.809	27.000
27.000	27.000	27.000	27.260	27.468	27.676	28.919	27.000
27.000	27.000	27.000	27.266	27.474	27.682	29.020	27.000
27.000	27.000	27.000	27.272	27.480	27.688	29.393	27.000
27.000	27.000	27.000	27.278	27.486	27.694	29.766	27.000
27.000	27.000	27.000	27.284	27.492	27.700	30.138	27.000
27.000	27.000	27.000	27.290	27.498	27.706	30.511	27.000
27.000	27.000	27.088	27.296	27.504	27.712	30.883	
27.000	27.000	27.093	27.302	27.510	27.718	31.256	
27.000	27.000	27.099	27.308	27.516	27.724	31.628	
27.000	27.000	27.105	27.314	27.522	27.730	32.001	
27.000	27.000	27.111	27.320	27.528	27.736	32.373	
27.000	27.000	27.117	27.325	27.534	27.742	32.746	
27.000	27.000	27.123	27.331	27.540	27.748	33.000	
27.000	27.000	27.129	27.337	27.546	27.754	27.000	
27.000	27.000	27.135	27.343	27.552	27.760	27.000	
27.000	27.000	27.141	27.349	27.557	27.766	27.000	
27.000	27.000	27.147	27.355	27.563	27.772	27.000	
27.000	27.000	27.153	27.361	27.569	27.778	27.000	
27.000	27.000	27.159	27.367	27.575	27.784	27.000	
27.000	27.000	27.165	27.373	27.581	27.790	27.000	
27.000	27.000	27.171	27.379	27.587	27.944	27.000	
27.000	27.000	27.177	27.385	27.593	27.964	27.000	
27.000	27.000	27.183	27.391	27.599	27.990	27.000	
27.000	27.000	27.189	27.397	27.605	28.023	27.000	
27.000	27.000	27.195	27.403	27.611	28.062	27.000	
27.000	27.000	27.201	27.409	27.617	28.108	27.000	
27.000	27.000	27.207	27.415	27.623	28.160	27.000	
27.000	27.000	27.212	27.421	27.629	28.218	27.000	
27.000	27.000	27.218	27.427	27.635	28.283	27.000	
27.000	27.000	27.224	27.433	27.641	28.355	27.000	
27.000	27.000	27.230	27.439	27.647	28.433	27.000	

0-35	36-70	71-105	106-140	141-175	176-210	211-245	246-255
43.000	43.789	44.231	44.673	45.115	43.000	43.000	43.000
43.000	43.802	44.243	44.685	45.127	43.000	43.000	43.000
43.000	43.814	44.256	44.698	45.341	43.000	43.000	43.000
43.000	43.827	44.269	44.711	45.376	43.000	43.000	43.000
43.000	43.839	44.281	44.723	45.417	43.000	43.000	43.000
43.000	43.852	44.294	44.736	45.464	43.000	43.000	43.000
43.000	43.865	44.307	44.748	45.517	43.000	43.000	43.000
43.000	43.877	44.319	44.761	45.576	43.000	43.000	43.000
43.000	43.890	44.332	44.774	45.641	43.000	43.000	43.000
43.000	43.903	44.344	44.786	45.713	43.000	43.000	43.000
43.000	43.915	44.357	44.799	45.791	43.000	43.000	
43.000	43.928	44.370	44.812	45.875	43.000	43.000	
43.000	43.940	44.382	44.824	45.965	43.000	43.000	
43.000	43.953	44.395	44.837	46.062	43.000	43.000	
43.000	43.966	44.408	44.849	46.165	43.000	43.000	
43.000	43.978	44.420	44.862	46.274	43.000	43.000	
43.000	43.991	44.433	44.875	46.389	43.000	43.000	
43.000	44.004	44.445	44.887	46.510	43.000	43.000	
43.000	44.016	44.458	44.900	46.537	43.000	43.000	
43.000	44.029	44.471	44.913	48.237	43.000	43.000	
43.000	44.041	44.483	44.925	49.937	43.000	43.000	
43.000	44.054	44.496	44.938	51.637	43.000	43.000	
43.000	44.067	44.509	44.951	53.337	43.000	43.000	
43.000	44.079	44.521	44.963	55.037	43.000	43.000	
43.000	44.092	44.534	44.976	56.737	43.000	43.000	
43.000	44.105	44.546	44.988	43.000	43.000	43.000	
43.000	44.117	44.559	45.001	43.000	43.000	43.000	
43.688	44.130	44.572	45.014	43.000	43.000	43.000	
43.701	44.142	44.584	45.026	43.000	43.000	43.000	
43.713	44.155	44.597	45.039	43.000	43.000	43.000	
43.726	44.168	44.610	45.052	43.000	43.000	43.000	
43.738	44.180	44.622	45.064	43.000	43.000	43.000	
43.751	44.193	44.635	45.077	43.000	43.000	43.000	
43.764	44.206	44.647	45.089	43.000	43.000	43.000	
43.776	44.218	44.660	45.102	43.000	43.000	43.000	

Appendix V Data

A. Data of thermocouple calibration

mv	Temperature(°C)	Residence
2.0221	28.0	0.084900
2.5301	40.0	0.017075
2.7026	44.0	-0.080756
2.9030	48.8	-0.041373
3.3660	59.7	-0.140190
3.6393	66.5	0.167412
3.9761	74.3	-0.033453
4.5124	87.1	0.026433

Temperature = $23.756 \times mv - 20.121$
Correlation 0.999988
Standard Error of Regression 0.104675

B. Physical property of water and glycerol

Liquid	Formula	Density $10^{3}kgm^{-3}$	Thermal Conductivity $Wm^{-1}K^{-1}$	Viscosity $10^{-3}Pa.s$
Water	H_2O	0.998	0.60	1.00
Glycerol	$C_3H_5(OH)_3$	1.270	0.28	1490

Liquid	Coeff. of Thermal Expansion (Volumetric) $10^{-3}K^{-1}$	Specific Heat Capacity $kJkg^{-1}K^{-1}$
Water	0.18	4.18
Glycerol	0.50	2.43

(Kempe's engineers year-book 1991 Vol 1 A1-F5)

Appendix VI introduces several simple image processing techniques which are frequently used in this thesis for image analysis.

1. Image smoothing

Smoothing operations are used primarily for diminishing spurious effects that may be present in a digital image as a result of a poor sampling system or transmission channel.

1.1 Neighbourhood averaging

Neighbourhood averaging is a straightforward spatial-domain technique for image smoothing. Given an $N \times N$ image $f(x, y)$, the procedure is to generate a smoothed image $g(x, y)$ whose grey level at every point (x, y) is obtained by averaging the grey level values of the pixels of f contained in a predefined neighbourhood of (x, y). In other words the smoothed image is obtained by using the relation

$$g(x, y) = \frac{1}{M} \sum_{(n,m) \in S} f(n, m)$$

for $x, y = 0, 1, ..., N-1$. S is the set of coordinates of points in the neighbourhood of the point (x, y), including (x, y) itself, and M is the total number of points in the neighbourhood.

1.2 Median Filtering

Median filters replace the grey level of each pixel by the median of the grey levels in a neighbourhood of the pixel, as opposed to, the average. This method is particularly effective when the noise pattern consists of strong, spike-like components.

Recall that the median *m* of a set of values is such that half of the values in the set are less than *m*. In order to perform median filtering in a neighbourhood of a pixel we first sort the values of the pixel and its neighbours, determine the median, and assign the value to the pixel. For example, in a 3×3 neighbourhood the median is the 5th largest value, in a 5×5 neighbourhood the 13th largest value, and so on. The principal function of median filtering is to force points with very distinct intensities to be more like their neighbours, thus actually eliminating intensity spikes that appear isolated in the area of the filter mask.

1.3 Low-pass Filtering

Image smoothing can be achieved via the frequency domain by attenuating a specified range of high-frequency components in the transform of a given image,

$$G(u,v) = H(u,v)F(u,v)$$

where $F(u,v)$ is the transform of the image we wish to smooth. The problem is to select a function $H(u, v)$ that yields $G(u, v)$ by attenuating the high-frequency components of $F(u, v)$.

The inverse transform of $G(u, v)$ will then yield the desired smoothed image $g(x, y)$. Since high-frequency components are "filtered out", and information in the low-frequency range is "passed" without attenuation, this method is commonly referred to as low-passing filtering.

1.4 Averaging of multiple images

Consider a noisy image $g(x, y)$ that is formed by the addition of noise $n(x, y)$ to an original image $f(x, y)$; that is

$$g(x, y) = f(x, y) + n(x, y)$$

where it is assumed that at every pair of coordinates (x, y) the noise is uncorrelated and has zero average value. The objective of the following procedure is to obtain a smoothed result by adding a given set of noise images $\{g_i(x, y)\}$.

2. Digital convolution filtering

Convolution of digital images is similar to that for continuous images except that the variables take on integral values and the double integral becomes a double summation.

Thus, for a digital image,

$$g(i, j) = f * h = \sum_m \sum_n f(m, n) h(i - m, j - n)$$

Since both f and h are non-zero only over a finite domain, the summations are taken only over the area of non-zero overlap. The function h is rotated 180° and its origin shifted to the coordinates i, j. The two functions are multiplied together point by point and the resulting products summed to give the output value. Different 3×3 array h are convolved with a lager digital image f result in different filtered images g.

3×3 High pass filter

-1 -1 -1
-1 9 -1
-1 -1 -1

3×3 Low pass filter

1/9 1/9 1/9
1/9 1/9 1/9
1/9 1/9 1/9

3×3 Laplacian filter

-1 -1 -1
-1 8 -1
-1 -1 -1

3×3 Vertical line enhancement

-1 2 -1
-1 2 -1
-1 2 -1

2.5 3×3 Horizontal line enhancement

-1 -1 -1

2 2 2
-1 -1 -1

3. Histogram equalization

A histogram of grey-level content provides a global description of the appearance of an image. Histogram equalization achieves enhancement by modifying the histogram of a given image in a specified manner.

Let the variable r represent the grey level of the pixels in the image to be enhanced. For simplicity, it will be assumed in the following discussion that pixel values have been normalized so that they lie in the range

$$0 \leq r \leq 1$$

with $r = 0$ representing black and $r = 1$ representing white in the grey scale.

For any r in the interval [0, 1], attention will be focused on transformations of the form

$$s = T(r)$$

which produce a level s for every pixel value r in the original image. It is assumed that the transformation function satisfies the conditions:

(a) $T(r)$ is single-valued and monotonically increasing in the interval $0 \leq r \leq 1$, and

(b) $0 \leq T(r) \leq 1$ for $0 \leq r \leq 1$.

Condition (a) preserves the order from black to white in the grey scale, while condition (b) guarantees a mapping that is consistent with the allowed range of pixel values.

The inverse transformation from s back to r will be denoted by

$$r = T^{-1}(s) \quad 0 \leq s \leq 1$$

where it is assumed that $T^{-1}(s)$ also satisfies conditions (a) and (b) with respect to the variables s.

The grey levels in an image are random quantities in the interval [0, 1]. Assuming for a moment that they are continuous variables, the original and transformed grey levels can be characterized by their probability density function $p_r(r)$ and $p_s(s)$, respectively. A great deal can be said about the general characteristics of an image from the density function of its grey levels.

Consider the transformation function

$$s = T(r) = \int_0^r p_r(w)\mathrm{d}w \quad 0 \leq r \leq 1$$

The right most side of equation is recognized as the cumulative distribution function (CDF) of r. Further we have

$$\frac{\mathrm{d}s}{\mathrm{d}r} = p_r(r)$$

yields

$$\begin{aligned} p_s(s) &= [\,p_r(r)\frac{\mathrm{d}r}{\mathrm{d}s}\,]_{r=T^{-1}(s)} \\ &= [\,p_r(r)\frac{1}{p_r(r)}\,]_{r=T^{-1}(s)} \\ &= 1 \quad 0 \leq s \leq 1 \end{aligned}$$

which is a uniform density in the interval of definition of the transformed variable s. It is noted that this result is independent of the inverse transformation function. This is important because it is not always easy to obtain $T^{-1}(s)$ analytically.

The foregoing development indicates that using a transformation function equal to the cumulative distribution of r produces an image whose grey levels have a uniform density. This implies an increase in the dynamic range of the pixels, which can have a considerable effect in the appearance of an image.

Appendix VII PIVT programmes

Particle image velocimetry using thermochromic liquid crystal particles measures velocity and temperature simultaneously. The package for this purpose is called PIVT, which is written in C++, DSP32C C.

The PIVT package is user friendly menu drive software. It has several levels of menus. The first level of menu is displayed after run PIVT.

1. Main Menu

F1Image Restore F2Board Setup F3Statistics F4Manage Buffer PgDnNext Image

Image Mode: HSI
Sync source: INTERNAL
Work Region: 0 0 512 512

Image Processing
Image Acquisition
Particle Image/Tracking Velocimetry
Thermographic Liquid Crystals
Exit

The top line of the screen is the list of functions, which includes image restore, image board set-up, statistics data display, buffer management and page down key for next image if there is a series images available. Press the function key F1 to F4 to run different functions. These functions can only be ran individually.

On the up-right corner, the state of the image board is displayed. The secondary menu is displayed on the middle of the screen. One of the menu items is highlighted, pressing ENTER to run this secondary menu item. The highlight can move up and down by pressing the arrow keys. Program can exit from Exit or press ESC.

After pressing F1, the menu for image restore will be displayed, saving and restoring one image, or a series of images, can be done in this menu.

F1Image Restore F2Board Setup F3Statistics F4Manage Buffer PgDnNext Image

Restore a picture
Save a picture
Series Images Information
Exit

Pressing F2 will run the set-up of image board.

F1Image Restore F2Board Setup F3Statistics F4Manage Buffer PgDnNext Image

Image Mode: HSI
Sync source: INTERNAL
Work Region: 0 0 512 512

Image Processing
Image Acquisition
Particle Image/Tracking Velocime
Thermographic Liquid Crystals
Exit

Start Row: 0
Start Col (module 16): 0
Height: 512
Width (module 16): 512
Acqu/Disp Mode (0:HSI, 1:RGB): 0
Do - [ENTER] Change - [SPACE]

F3 is for display of histogram of a buffer, mean value and most frequent value.

F1Image Restore F2Board Setup F3Statistics F4Manage Buffer PgDnNext Image

Image Mode: HSI
Sync source: INTERNAL
Work Region: 0 0 512 512

Image Processing
Image Acquisition
Particle Image/Tracking Velocime
Thermographic Liquid Crystals
Exit

Buffer Number[0-31]: 0
Start Row: 0
Start Col (module 16): 0
Height: 512
Width (module 16): 512
Do - [SPACE] Change - [ENTER]

F4 is for buffer management.

F1Image Restore F2Board Setup F3Statistics F4Manage Buffer PgDnNext Image

Clear a frame buffer
Clear picture plane 0
Set a constant Buffer
Exchange buffers
Copy a buffer region
Exit

Whilst one of the secondary menu items is highlighted, pressing ENTER leads to the running of the corresponding function of the item.

2. Image Processing

The first item of image processing is Read pixel values. Move the cursor to find the RGB/HSI values at interested position.

F1Image Restore F2Board Setup F3Statistics F4Manage Buffer PgDnNext Image

Image Mode: HSI
Sync source: INTERNAL
Work Region: 0 0 512 512

Read pixel values
Arithmetic operations
Logic operations
Image Enhancement

ARROW keys - Move Cursor.
INS key - change step.
Hit ENTER to quit.

Morphological Processing
Geometric Processing *ROW* *COL* *I/R* *S/G* *H/B*
Save Result --- --- --- --- ---
Exit *255* *255* *123* *100* *141*

Arithmetic operations: after pressing ENTER of the highlighted item, the dialogue menu will be displayed. Enter the correct figures, press SPACE to run.

F1Image Restore F2Board Setup F3Statistics F4Manage Buffer PgDnNext Image

Image Mode: HSI
Sync source: INTERNAL
Work Region: 0 0 512 512

Multiply a Constant
Divided by a Constant
Offset a Constant
Add Two Buffers
Subtract
Multiply Two Buffers
Division
Set Hue Pattern
Exit

Logic operations: after pressing ENTER of the highlighted item, the dialogue menu will be displayed. Enter the correct figures, press SPACE to run.

F1Image Restore F2Board Setup F3Statistics F4Manage Buffer PgDnNext Image

Image Mode: HSI
Sync source: INTERNAL
Work Region: 0 0 512 512

Set Active Region and Mode
Logic ADD a Constant
Logic OR a Constant
Logic XOR a Constant
Logic ADD Two Buffers
Logic OR Two Buffers
Logic XOR Two Buffers
Exit

Image enhancement: after pressing ENTER of the highlighted item, the dialogue menu will be displayed. Enter the correct figures, press SPACE to run.

F1Image Restore F2Board Setup F3Statistics F4Manage Buffer PgDnNext Image

Image Mode: HSI
Sync source: INTERNAL
Work Region: 0 0 512 512

3 x 3 High Pass
3 x 3 Low Pass
3 x 3 Laplacian
3 x 3 Vertical Line Enhancement
3 x 3 Horizontal Line Enhancement
Histogram Equalization
Linear Stretch
Median Filter
Local Average
Exit

Morphological processing: after pressing ENTER of the highlighted item, the dialogue menu will be displayed. Enter the correct figures, press SPACE to run.

F1Image Restore F2Board Setup F3Statistics F4Manage Buffer PgDnNext Image

Image Mode: HSI
Sync source: INTERNAL
Work Region: 0 0 512 512

Set Active Region and Mode
Binary Image Dilation
Erosion
Open
Close
Exit

Geometric processing: after pressing ENTER of the highlighted item, the dialogue menu will be displayed. Enter the correct figures, press SPACE to run.

F1Image Restore F2Board Setup F3Statistics F4Manage Buffer PgDnNext Image

Image Mode: HSI
Sync source: INTERNAL
Work Region: 0 0 512 512

Set Active Region and Mode
Transform and Rotation
Zoom
Exit

The image processed can be save through the item Save Result. Pressing ENTER, the dialogue menu will be displayed. Enter the correct figures, press SPACE to run.

F1Image Restore F2Board Setup F3Statistics F4Manage Buffer PgDnNext Image

Image Mode: HSI
Sync source: INTERNAL
Work Region: 0 0 512 512

Read pixel values
Arithmetic operations
Logic operations
Image Enhancement
Morphological Processing
Geometric Processing
Save Result
Exit

Image Name: c:\exp_pic\calib\flow02.img
Image Mode (0:B/W, 1:HSI, 2:RGB): 1
Start Row of Save/Restore: 0
Start Col of Sav/Res (module 16): 0
Height of Region: 512
Width of Region (module 16): 512
Do - [SPACE] Change - [ENTER]

3. Image Acquisition

When the item of image acquisition is highlighted, pressing ENTER to grab one image or a series of images.

F1Image Restore F2Board Setup F3Statistics F4Manage Buffer PgDnNext Image

Image Mode: HSI
Sync source: INTERNAL
Work Region: 0 0 512 512

Freeze a picture
Pass through
Acquire a series of pictures
Exit

To acquire a series of pictures, several figures are required which are used to define the area, image mode, time delay and acquisition methods.

F1Image Restore F2Board Setup F3Statistics F4Manage Buffer PgDnNext Image

Image Mode: HSI
Sync source: INTERNAL
Work Region: 0 0 512 512

Freeze a picture
Pass through
Acquire a series of pictures *Image Series Name[3 Characters]:*
Image Model (0:HSI 1:RGB) 0
Save (0:Double 1:Single): 0
Buffer doubled [0:I 1:S 2:H]: 0
Time Interval(>0.11s): 0.11
Save Temperature Value (1:Yes, 0:No): 0
Do - [SPACE] Change - [ENTER]

4. Particle Image/Tracking Velocimetry

Cross-correlation procedure is run through the item of Cross-Correlation method, figures required to defined the method to extract the velocity data.

<u>F1</u>Image Restore <u>F2</u>Board Setup <u>F3</u>Statistics <u>F4</u>Manage Buffer <u>PgDn</u>Next Image

Image Mode: HSI
Sync source: INTERNAL
Work Region: 0 0 512 512

<u>Cross-Correlation Method</u>
Display velocity vectors
Tracking Method
Comparison of All parameters
Check Accuracy of PIVs
Exit

<u>Improved PIV [Yes: 1 No:0]:</u> 0
Save Result In: Velocity.dat
First Frame in Dt2871 [0-3]: 0
Second Frame in Dt2871 [0-3]: 1
Row Start: 128
Col Start: 128
Height: 256
Width: 256
Row Step: 5
Col Step: 5
Interrogation Window Size [16 or 32]: 32
Fit Method[Wht:1 Pbolic:2 Gauss:3]: 2
Error detector[1 2 3]: 1
Display Procedure [Yes:1 No:0]: 0
Do [Space] Change [Enter]

Velocity vectors can be displayed through the next item.

<u>F1</u>Image Restore <u>F2</u>Board Setup <u>F3</u>Statistics <u>F4</u>Manage Buffer <u>PgDn</u>Next Image

Image Mode: HSI
Sync source: INTERNAL
Work Region: 0 0 512 512

Cross-Correlation Method
<u>Display velocity vectors</u>
Tracking Method
Comparison of All parameters
Check Accuracy of PIVs
Exit

<u>Velocity File Name:</u> Velocity.dat
Scale: 1.000000
Do [Space] Change [Enter]

Tracking method:

<u>F1</u>Image Restore <u>F2</u>Board Setup <u>F3</u>Statistics <u>F4</u>Manage Buffer <u>PgDn</u>Next Image

Image Mode: HSI
Sync source: INTERNAL
Work Region: 0 0 512 512

Cross-Correlation Method
Display velocity vectors
Tracking Method *Result Data File: Track.dat*
Comparison of All parameters *Start Row: 128*
Check Accuracy of PIVs *Start Col: 128*
Exit *Height: 256*
Width: 256
Do [Space] Change [Enter]

Comparison of All parameters

F1Image Restore F2Board Setup F3Statistics F4Manage Buffer PgDnNext Image

Image Mode: HSI
Sync source: INTERNAL
Work Region: 0 0 512 512

Cross-Correlation Method
Display velocity vectors
Tracking Method
Comparison of All parameters *Result File Name: Optimal.dat*
Check Accuracy of PIVs *Do [Space] Change [Enter]*
Exit

Check Accuracy of PIVs

F1Image Restore F2Board Setup F3Statistics F4Manage Buffer PgDnNext Image

Image Mode: HSI
Sync source: INTERNAL
Work Region: 0 0 512 512

Cross-Correlation Method
Display velocity vectors
Tracking Method
Comparison of All parameters
Check Accuracy of PIVs *Result File Name: Compare.dat*
Exit *Spacial Density: 0.0200003*
Particle Size: 3

Do [Space] Change [Enter]

5. Thermographic Liquid Crystals

Calibration of the hue and temperature relationship is carried out by reading hue or RGB and temperature values from the series of images saved previous.

F1Image Restore F2Board Setup F3Statistics F4Manage Buffer PgDnNext Image

Image Mode: HSI
Sync source: INTERNAL
Work Region: 0 0 512 512

Calibration
DT2871 Hue to Temperature
DT2871 RGB to Temperature
Exit

DT2871 hue values can be converted to temperature through the item of DT2871 Hue to Temperature, the temperature will be displayed on screen as a colour pattern, data can be saved. Look-up-table data are required.

F1Image Restore F2Board Setup F3Statistics F4Manage Buffer PgDnNext Image

Image Mode: HSI
Sync source: INTERNAL
Work Region: 0 0 512 512

Calibration
DT2871 Hue to Temperature Hue Buffer number: 2
DT2871 RGB to Temperature Hue-Temperature data file: Lut.dat
Exit Start Row: 128
Start Col: 128
Height: 256
Width: 256
Step Row: 5
Step Col: 5
Temperature data save in: Tempera.dat
T data mode [0-Matrix, 1-Triplets]: 0

Do [Space] Change [Enter]

DT2871 RGB values can be converted to temperature through the item of DT2871 RGB to Temperature, the temperature will be displayed on screen as a colour pattern, data can be saved. Look-up-table data are required.

F1Image Restore F2Board Setup F3Statistics F4Manage Buffer PgDnNext Image

Image Mode: HSI
Sync source: INTERNAL
Work Region: 0 0 512 512

Calibration
DT2871 Hue to Temperature
DT2871 RGB to Temperature *Hue Buffer number:* 2
Exit
Hue-Temperature data file: Lut.dat
Start Row: 128
Start Col: 128
Height: 256
Width: 256
Step Row: 5
Step Col: 5
Temperature data save in: Tempera.dat
T data mode [0-Matrix, 1-Triplets]: 0
Do [Space] Change [Enter]

A comparison of interrogation methods for Particle Image Velocimetry

S Ashforth-Frost, B N Dobbins, K Jambunathan

Department of Mechanical Engineering
Faculty of Engineering and Computing
The Nottingham Trent University
Burton Street, Nottingham NG1 4BU, UK

X P Wu and X Y Ju

Department of Modern Mechanics
University of Science and Technology of China
Anhui 230026, P R China

ABSTRACT

Two methods of extracting velocity vectors from particle image patterns are described. The results are compared with Particle Image Velocimetry (PIV) using the well established cross-correlation technique for a case of natural convection from a heated tube submerged in a water bath. In an endeavour to improve the accuracy of velocity extraction, velocity gradients have been introduced into the algorithm. The procedure is repeated to a chosen iterative limit. Results presented show the effect of the gradient operator on the velocities obtained in regions where the velocity gradient is large.

1. INTRODUCTION

Since Kinoshita[1] first applied the Particle Image Velocimetry (PIV) technique to obtain two-dimensional information of velocity vectors on the surface of a flood flow in a river by the manual operation of a stereograph-image plotter, others[2,3] have used PIV intensively for measurement of fluid flow fields. Essentially there are two methods to record flow patterns of fluid fields, one utilizes film or plate and the other utilizes video records. The film method employs point by point analysis - Young's fringes[2] or the auto-correlation method[4] to investigate the double/multi-exposed film or plate to extract velocity data which has direction ambiguity. Adrian[5] and Grant et al.[6] tried to resolve directional ambiguity by using an image shifting technique. Goss[7] introduced two-colour PIV attempting to remove the directional ambiguity. The video method employs the cross-correlation method[3,8,9] or other tracking methods[10,11] to analyze two image frames, obtaining velocity data, removing directional ambiguity which is characteristic for both Young's fringe and the auto-correlation techniques. An important advantage of the video method is its easy applicability for flow velocity measurements due to the absence of photographic and opto-mechanical processing steps inherent to non-video based PIV techniques. Yano[12] applied the correlation technique to a fairly simple steady flow field without any reverse flow and proved that the technique was effective. Kimura et al.[8,9] used correlation techniques to analyze flow around a circular cylinder, in an attempt to decrease erroneous velocity vectors.

In this paper, two methods of extracting the velocity vectors from particle image patterns are described. The results are compared with the well established cross-correlation technique for a case of natural convection from a heated tube submerged in a water bath. The first, the subtraction method, is based on the minimisation of the absolute values, following subtraction, of two consecutive image patterns and the second, the XOR method, relies on maximising the number of zeros obtained in the XOR operation between two image patterns. Displacements were deduced from the position at which the minimum and maximum occurred in the two cases respectively.

Conventional PIV, based on cross-correlation, assumes the velocity to be uniform within a small area. Distortion in the interrogation area occurring between the consecutive image patterns is accommodated by accepting correlation coefficients less than one, by the choice of a suitable threshold setting. This can lead to errors in regions where the velocity gradient is large. In an endeavour to improve the accuracy of velocity extraction, an iterative estimating procedure for velocity gradients has been introduced into the algorithm. Results presented show the effect of the procedure on the velocities obtained in regions where the velocity gradient is large.

2. EXPERIMENTAL APPARATUS AND IMAGE SYSTEM

Figure 1 shows the small perspex water tank that was used for the heat convection experiments. A stainless steel tube, through which water at a constant selected temperature was circulated, passes through the centre of the tank. The water temperatures are adjustable. The water in the tank was seeded with particles of mean diameter 100 μm at a concentration of 0.01 per cent. A thin sheet of white light was projected through the tank and photographs, or video recording, of resolved particles subject to the natural convection from the heated cylinder were made at 90° to the illuminated plane. In the full developed flow field, particles moved along the central line from the hot steel tube to the water surface and then diverted into two rings.

A schematic diagram of the image processing facility used for velocity information is provided in figure 2. A monochrome CCD camera (0.5 Lux sensitivity) was used with a Sony U-matic video recorder to record the image. The monochrome image processing system employs a 386SX personal computer with Data Translation® on board arithmetic frame grabber. Sixteen images of 512x512 pixel × 8-bit resolution can be stored thus allowing the analysis of time dependent flows. A high resolution image monitor is used to view the particle images. A sequence of images were acquired by the frame grabber of the computer. The area of interest within the recorded image is selected and the raw data collected for analysis. The time interval between frames can be controlled but the smallest achievable is determined by the video rate of 25 frames per second which yields intervals of 40 ms.

3. ANALYSIS OF ALGORITHMS

The cross-correlation method is one of the well known effective techniques of calculating two-dimensional flow fields, in which spatial cross-correlations between two consecutive images of the particle image field are calculated for a range of spatial separation of the two images. Suppose two images - A and B - of a flow seeded with particles are captured, and the time interval between them is t. The particle distributions inside the light sheet plane of the flow field are represented by the variation of grey levels of pixels in the images. A square matrix, Mp, centred at point p(i,j) and of size 2m+1 by 2m+1 pixels can be identified in image A. Because of flow motion, the particle pattern inside the square moves to a similar particle pattern in the next image B. This displaced particle pattern will be centred at an unknown position s(i-x,j-y) and represented as matrix Ms. In order to identify the point s(i-x,j-y), the spatial cross-correlation coefficients between two particle patterns; Mp centred at point p(i,j) and Mq centred at point q(i-k,j-l); are calculated as below,

$$R(k,l)=\frac{\sum_{i=-m}^{m}\sum_{j=-m}^{m}M_p(i,j)M_q(i-k,j-l)}{\sqrt{\sum_{i=-m}^{m}\sum_{j=-m}^{m}M_p^2(i,j)\sum_{i=-m}^{m}\sum_{j=-m}^{m}M_q^2(i-k,j-l)}} \qquad (1)$$

where Mp(i,j) and Mq(i,j) are grey levels of the pixels inside the matrices Mp and Mq respectively. k,l = -n, -n+1, ..., n-1, n. Here n is an interrogation radius, which depends on maximum velocity of the flow analyzed and the time interval. Conventional PIV assumes that the velocity distributions are uniform in a small area, and expects that when and only when the centre of the matrix Mq moves to the point s(i-x,j-y) at which the matrix Ms is centred (Mq = Ms) will the cross-correlation coefficient R(k,l) reach a maximum value R(x,y). Here x, y are the displacement components from which the displacement vector and hence the velocity vector can be obtained. Ideally R(x,y) will be equal to 1 if the two particle patterns, Mp and Ms, are exactly the same. The analysis is performed at each of a number of points over the image. In the case reported here a regular measurement array of spacing 11 pixels was used. Figure 4 shows the raw velocity vectors for the heat convection flow. Some erroneous data can be seen in an area where continuous vectors (as marked a and b in figure 4(a)) were expected.

In this paper a subtraction method and a XOR method are presented. The subtraction method determines the position where the sum of the absolute value of Mp(i,j)-Mq(i-k,j-l) is a minimum,

$$r(k,l)=\sum_{i=-m}^{m}\sum_{j=-m}^{m}|M_p(i,j)-M_q(i-k,j-l)| \tag{2}$$

We expect that only when the centre of the matrix Mq is moved to q(i-x,j-y), will r(k,l) reach a minimum value r(x,y). The operation time for equation (2) is less than that for equation (1). Figure 4(b) displays the raw results of the subtraction method. The XOR method determines the position where there are the greatest number of zero value pixels left after the operation of XOR {Mp, Mq}. The XOR operation is a logic operation between two particle patterns, so it is even quicker than the operation of equation (2). The raw results are displayed in Figure 4(c).

4. THE EFFECT OF VELOCITY GRADIENTS

As mentioned above, conventional PIV assumes the velocity to be uniform in a small area. The assumption is invalid in regions where the velocity varies significantly. In such regions, the particle pattern in image A will be distorted in image B. This results in a low value of the cross-correlation coefficient between matrix Mp and matrix Ms. The maximum value of R(k,l) may be found at a point where x and y do not represent the correct displacement components. Under similar circumstances the subtraction and the XOR method will not find the point s(i-x,j-y) accurately. In order to minimise this effect, the particle pattern in image A can be reconstructed to allow for the velocity gradient.

Having obtained estimates of the velocity vectors at the centres of each matrix for the entire image A, the velocity gradient for any matrix Mp can be estimated using its velocity vector and those of its adjacent matrices.

The reconstruction procedure involves three steps. The first includes deformation of the particle image by introducing velocity gradients.

$$x_g=i+\int_0^i\frac{\partial U}{\partial x}dx+\int_0^j\frac{\partial U}{\partial y}dy \tag{3}$$

$$y_g=j+\int_0^i\frac{\partial V}{\partial x}dx+\int_0^j\frac{\partial V}{\partial y}dy \tag{4}$$

where i and j are the coordinates of the central pixel in matrix Mp, x_g and y_g are the coordinates of a corresponding point in a deformed version of matrix Mp, Mp'. This matrix includes the effects of the velocity gradients. The grey level of the pixel (i,j) in matrix Mp will transfer the position (x_g, y_g) in matrix Mp'.

In general x_g and y_g will not be integers and will therefore not correspond exactly to the pixel coordinates in image A. The second step is the estimation of sub-pixel grey level distribution in the deformed matrix.

If the deformed pixel area is centred at (x_g, y_g) as shown in figure 3 then the proportion of the area of the deformed pixel shared with the four overlapping pixels are a, b, c and d. If G is the grey level of the deformed pixel then the grey levels of the four pixels are a×G, b×G, c×G and d×G. Grey levels distributed to the same pixel will be added together, and a new distorted image pattern will be reconstructed.

The final step in the reconstruction involves sampling of new matrix Mp'. The new matrix Mp' is centred at a point in the distorted image pattern corresponding to the point p in image A.

The correction procedure is iterative because of the initially unknown velocity distributions. So the whole procedure is,

1) Obtain initial velocity vectors using cross-correlation, subtraction or XOR methods.
2) Choose an iterative limit according to the results following the cross-correlation, the subtraction or the XOR methods. In this paper the cross-correlation coefficient R(x,y), subtraction result r(x,y) or the XOR result was chosen.
3) Count the number of measurement points which have a cross-correlation coefficient or XOR result below a selected limit, or the subtraction result is above a selected limit. This provides a measure of the success of the correction procedure.
4) Calculation of the deformed matrix Mp' as described above.
5) Apply the cross-correlation, subtraction or XOR operation to obtain new velocity vectors using the new matrix Mp' and matrix Mq but with a reduced interrogation radius.

The procedure is repeated from step (3) until the number of points falling outside the selected limit is found to remain constant.

5. RESULTS AND DISCUSSION

5.1 Extraction time and accuracy

The time for extraction of velocity vectors depends on the operation time of equation (1) or (2) or XOR; the size of the interrogation matrix and the interrogation radius. The operation time for equation (1) is less than that of equation (2) and the XOR operation is even quicker than the operation of equation (2). The three methods employ different algorithms but share image grabbing and image pattern sampling procedures. The calculation time was determined for simple velocity vector extraction for a matrix size of 21×21 pixels and an interrogation radius of 6 pixels. Both new methods - subtraction method and XOR method - are quicker than the conventional cross-correlation method for the case considered but at the cost of accuracy. For each vector, extraction using only the cross-correlation method takes 12.99 seconds, the subtraction method takes 9.12 seconds and the XOR method takes 7.53 seconds.

With reference to the results of the cross-correlation method, errors for the subtraction method (mean error 0.30 pixel) are shown in Figure 5(a) and for the XOR method (mean error 0.72 pixel) in Figure 5(b). The data of errors were calculated by subtracting the corresponding velocity vectors extracted by the cross-correlation methods (maximum displacement 9.01 pixels) from those for each of the other methods. The error distributions show that the subtraction method gives results which agrees more closely with the cross-correlation results than do those from the XOR method. It will be noted that XOR method is effectively the same as the subtraction method in the case of binary image patterns.

5.2 Erroneous velocity vectors and velocity gradients

There are several sources causing erroneous velocity extraction other than the effect of velocity gradients, for example out of plane motion of particles, the thickness of the light sheet and electronic noise. Velocity gradient is one of the important sources, decreasing the correlation rate of the corresponding pattern in image A and image B. The same effects apply to the subtraction and XOR methods. For the cross-correlation technique 10.38 per cent of vectors had the lowest coefficients. After the correction procedure, this decreased to 4.74 per cent. For the XOR method 10.9 per cent decreased to 8.72 per cent and for the highest subtraction results 10.0 per cent decreased to 5.77 per cent (shown in table 1). Figure 6 shows the results corrected by introducing velocity gradients. Comparing with results of the cross-correlation method after correction, the mean errors for the subtraction and XOR methods are 0.35 pixels and 0.74 pixels respectively. Error vectors are shown in figure 7.

6. CONCLUSIONS

Two methods of extracting velocity vectors from particle image patterns have been described; the subtraction and XOR methods. Preliminary results for the case of natural convection from a horizontal cylinder have been presented. Comparison of results with those obtained using the established cross-correlation technique has shown a considerable improvement in computer processing time but at the expense of accuracy. The results presented show the effect of the gradient operator on the velocities obtained in regions where the velocity gradient is large. Further work will be to try to combine the cross-correlation method with the subtraction or the XOR method to gain speed as well as accuracy.

7. ACKNOWLEDGEMENTS

Thanks are due to the Polytechnic and Colleges Funding Council (PCFC) for the financial support given to the work reported here.

8. REFERENCES

1. Kinoshita, R. 1967: "An analysis of the movement of flood waters by aerial photography, concerning characteristics of turbulence and surface flow," Photographic Surveying 6, pp 1-17.
2. Adrian, R J. 1989: " Engineering Application of Particle Image velocimeters," Optical Methods in Flow and Particle Diagnostics, *ICALEO'89* pp 56-71, Oct 15-20, 1989 Orlando, Florida.
3. Utami, T and Blackwelder, R F. 1991: "A cross-correlation technique for velocity field extraction from particle visualization," *Experiments in Fluids* 10, pp 213-223.
4. Cenedese, A and Paglialunga, A. 1990: "Digital direct analysis of a multiexposed photograph in PIV," *Experiments in Fluids* 8, pp 273-280.
5. Adrian, R J. 1986 "Image shifting technique to resolve directional ambiguity in double-pulsed velocimetry," Vol. 25, No.21, 1 Nov. *Applied Optics.*
6. Grant, I. Smith, G H. Liu, A. Owens, E H. and Yan, Y Y. 1989: "Measuring Turbulence in Reversing Flows by Particle Image Velocimeter," Optical Methods in Flow and Particle Diagnostics, *ICALEO'89* pp 56-71, Oct 15-20, 1989 Orlando, Florida.
7. Goss. L P. Post, M E. Trump, D D. and Sarka, B. 1989: "Two-Color Particle Velocimetry," Optical Methods in Flow and Particle Diagnostics, *ICALEO'89* pp 56-71, Oct 15-20, 1989 Orlando, Florida.
8. Kimura, I and Takamori, T. 1986: "Image Processing of Flow around A Circular Cylinder by Using Correlation Technique," *Flow Visualization IV* (ed. Veret, C), pp 221-226, Washington: Hemisphere.
9. Kimura, I. Kimura H and Takamori, T. 1988: "Image Processing of Flow Velocity Vector Distributions," *Second International Symposium of Fluid Control, Measurement, Mechanical and Flow Visualisation.* 5-9 September. Sheffield University, England.
10. Hassan, Y A. and Canaan, R E. 1991: "Full-field bubbly flow velocity measurements using a multiframe particle tracking technique," *Experiments in Fluids* 12, pp 49-60.
11. Wernet, M P. and Pline A D. 1991: "Particle Image Velocimetry for the Surface Tension Driven Convection Experiment Using A Particle Displacement Tracking Technique," *Laser Anemometry*, Volume 1, ASME.
12. Yano, M. 1983: " Velocity measurement using correlation concerning with digital tracer image, flow visualisation. *Flow Visualisation Soc. of Japan* 3, pp 189-192

Table 1 Comparison of the three PIV algorithms

	Calculation time for each velocity vector /s	Number of points outside selected limit / per cent		Mean error / pixels	
		Before correction	After correction	Before correction	After correction
Cross-correlation	12.99	10.38 below	4.74 below	—	—
Subtraction	9.12	10.0 above	5.77 above	0.30	0.35
XOR	7.53	10.90 below	8.72 below	0.72	0.74

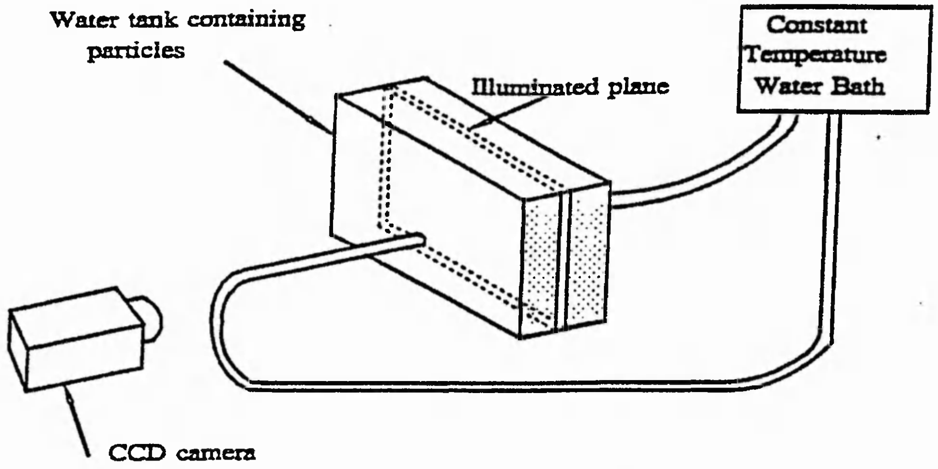

Figure 1. Schematic diagram of experimental arrangement

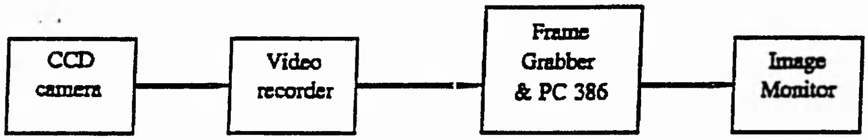

Figure 2. Schematic diagram of the image processing facility.

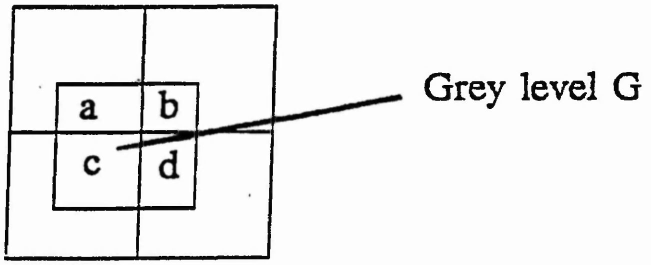

Figure 3. Grey level distribution to the overlapping pixels.

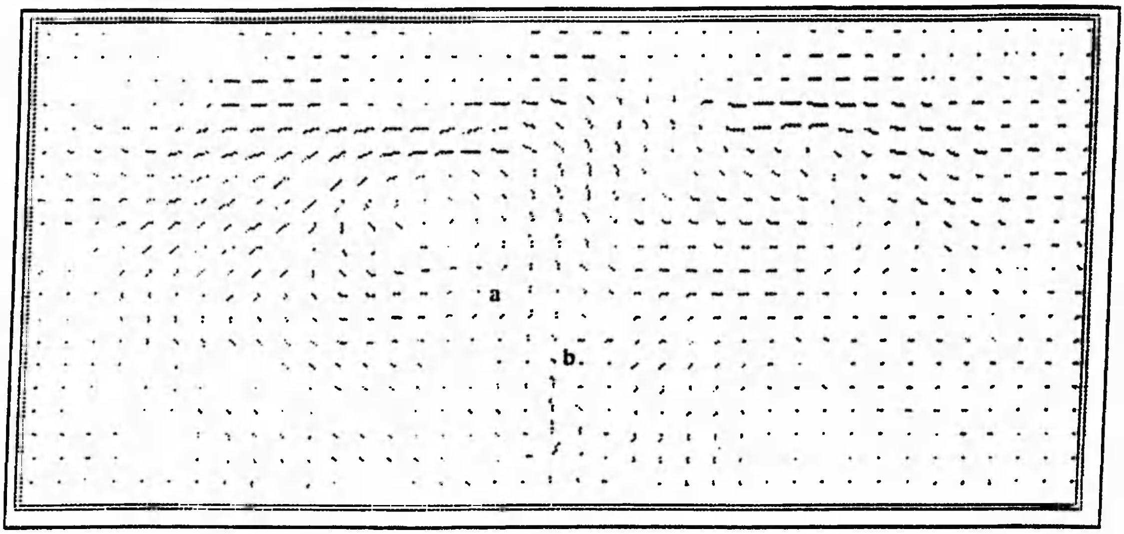

Figure 4. Row velocity vectors for the heat convection.
(a) Cross-correlation.

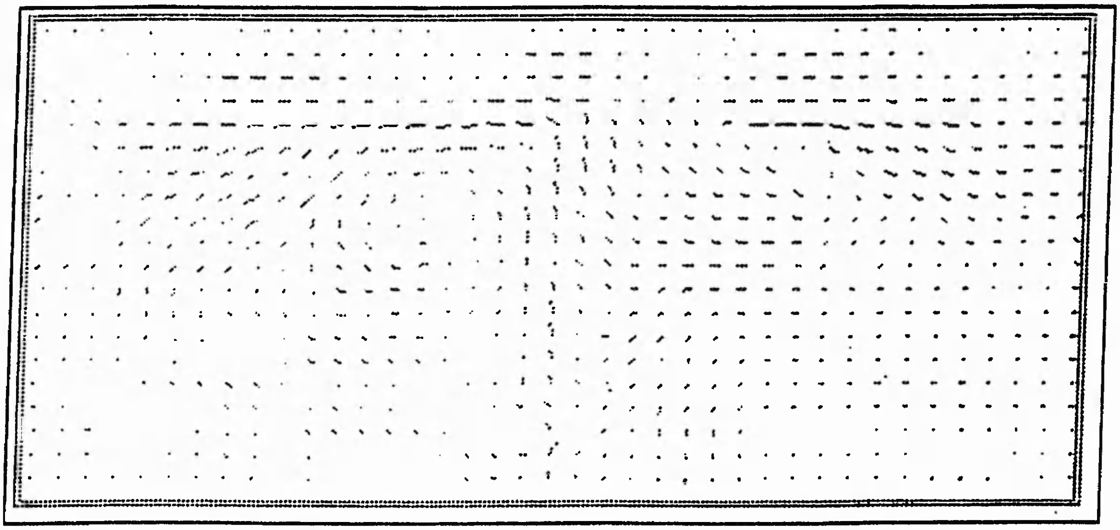

Figure 4. Row velocity vectors for the heat convection.
(b) Subtraction.

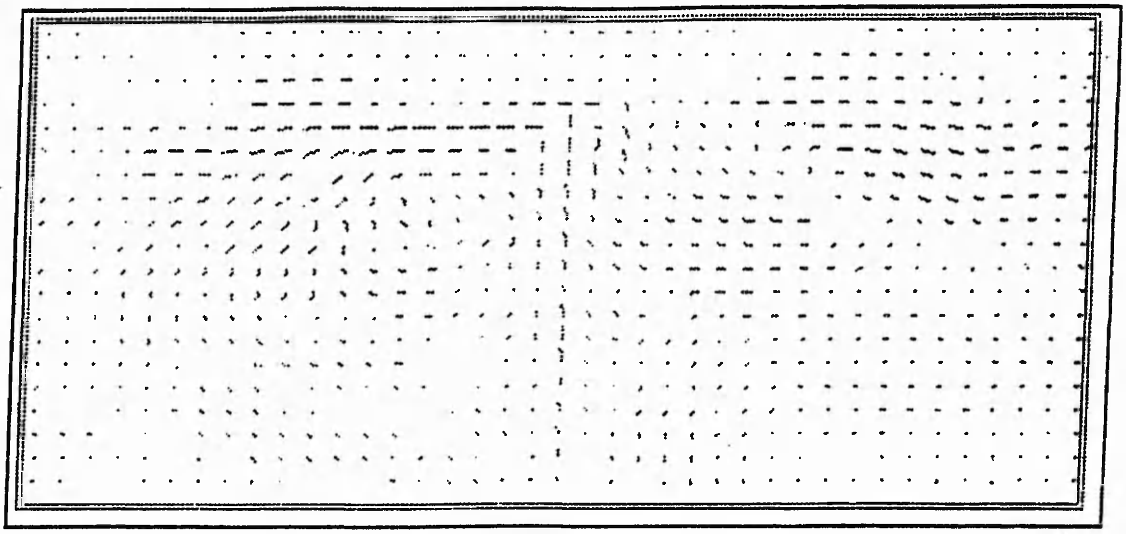

Figure 4. Row velocity vectors for the heat convection.
(c) XOR.

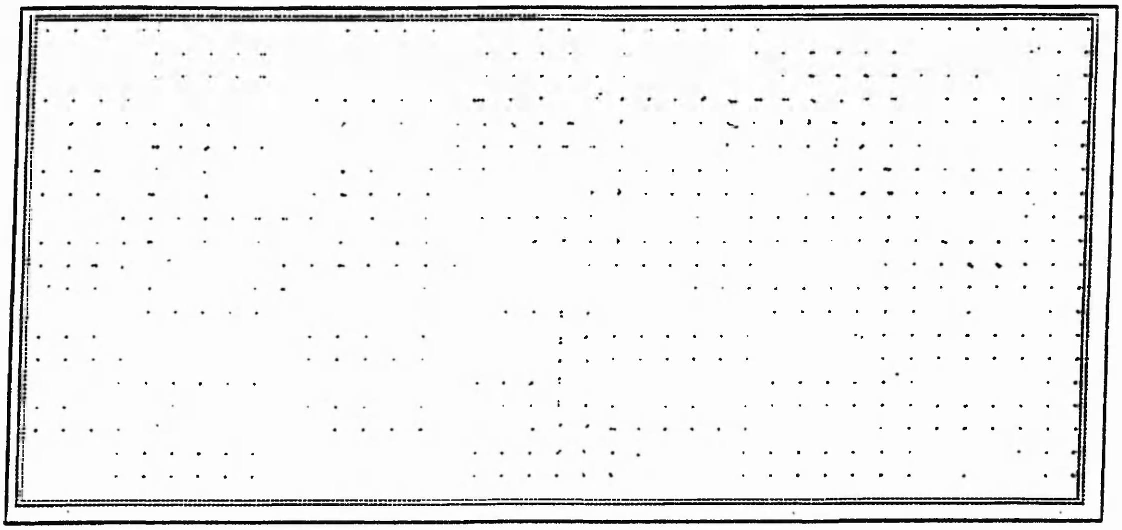

Figure 5. Error distribution. (a) Subtraction.

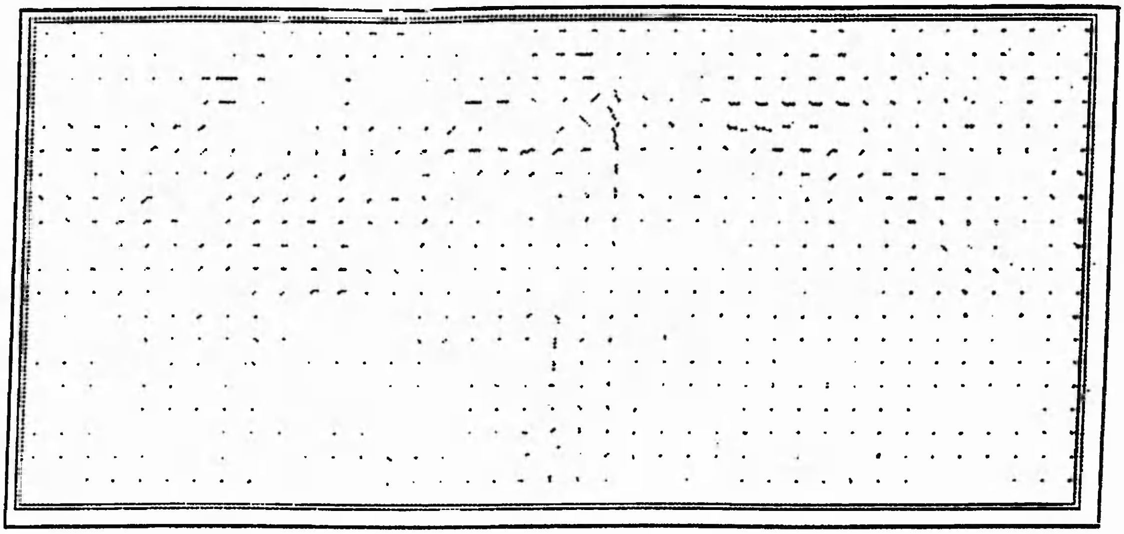

Figure 5. Error distribution. (b) XOR.

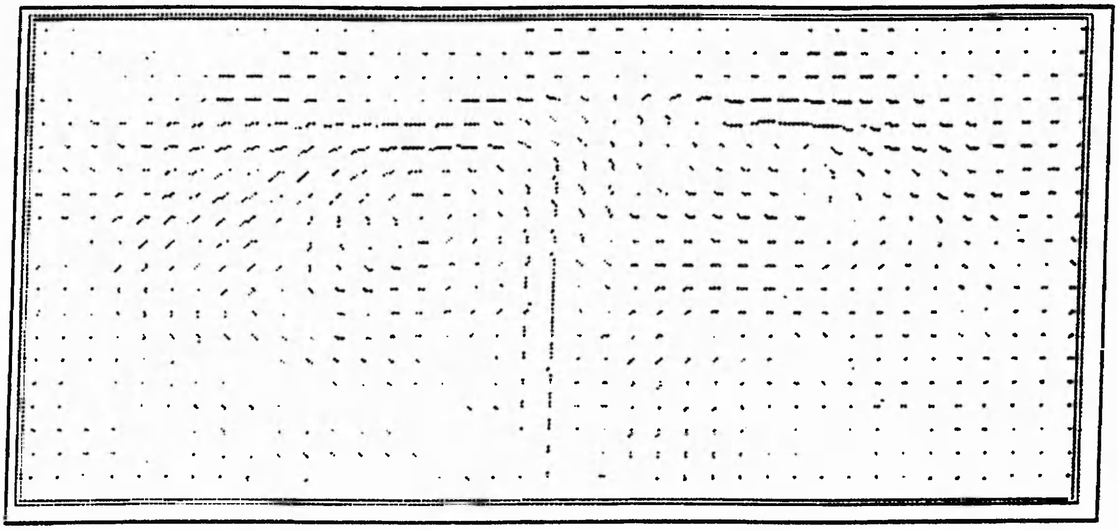

Figure 6. Results corrected by introducing velocity gradients.
(a) Cross-correlation results after correction.

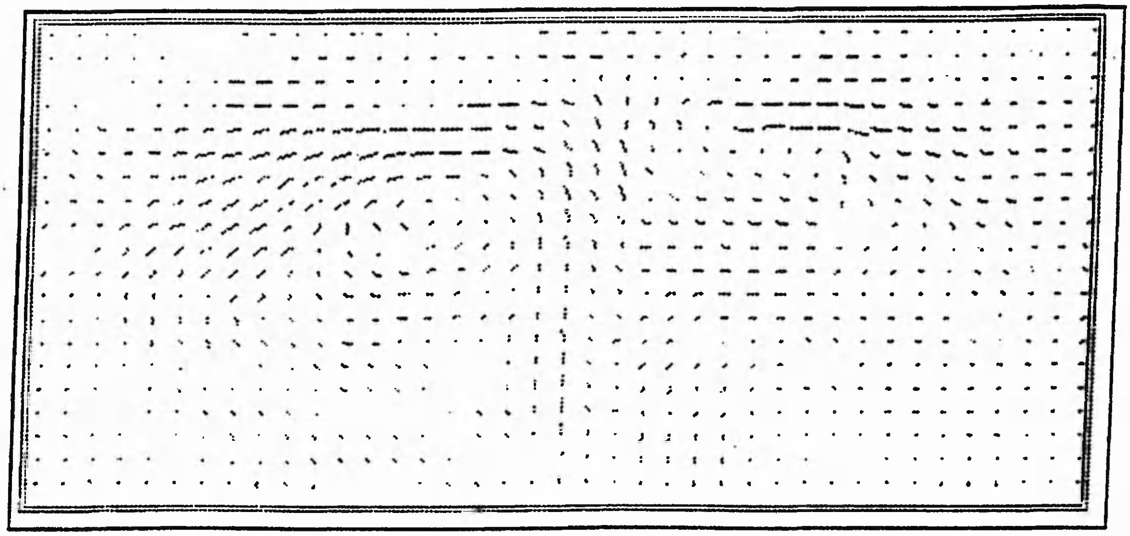

Figure 6. Results corrected by introducing velocity gradients.
(b) Subtraction results after correction.

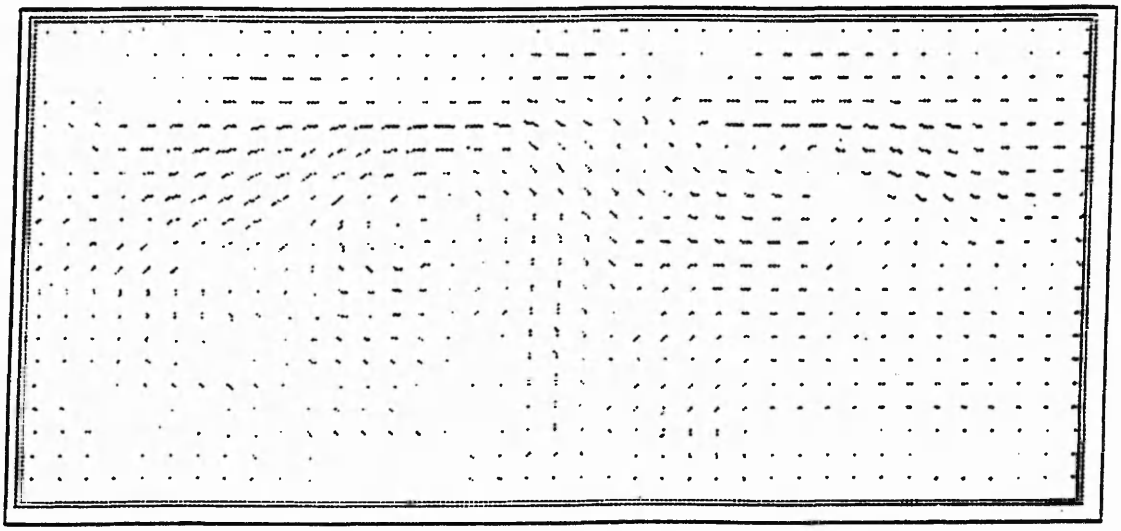

Figure 6. Results corrected by introducing velocity gradients.
(c) XOR results after correction.

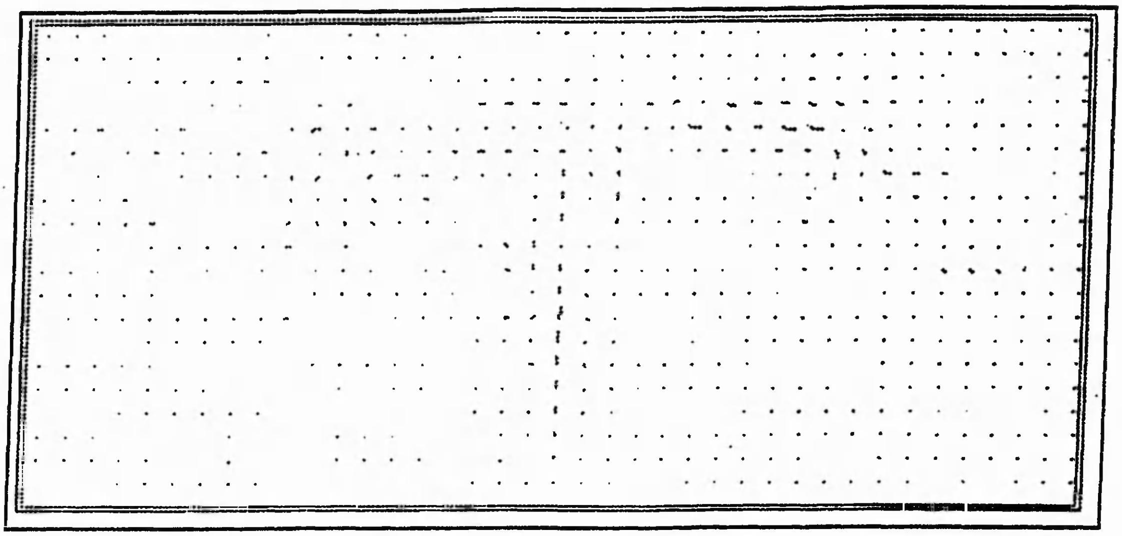

Figure 7. Error distribution after correction.
(a) Errors for subtraction after correction

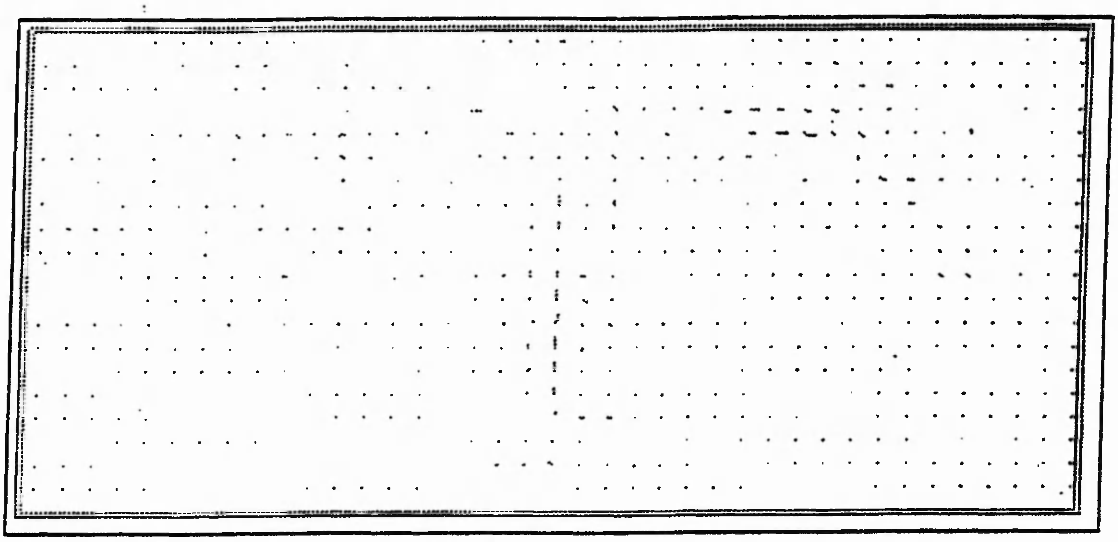

Figure 7. Error distribution after correction.
(b) Errors for XOR after correction

Meas. Sci. Technol. 6 (1995) 507–514. Printed in the UK

An improved cross correlation technique for particle image velocimetry

K Jambunathan, X Y Ju, B N Dobbins and S Ashforth-Frost

Department of Mechanical Engineering, The Nottingham Trent University, Nottingham NG1 4BU, UK

Received 6 December 1994, accepted for publication 6 February 1995

Abstract. The standard cross correlation technique frequently used in particle image velocimetry to extract velocity vectors necessitates the assumption that the velocity gradients inside the interrogation area are negligible. However, the procedure is generally video-based, so such an assumption may no longer be valid. This is particularly so in re-circulation zones, in which the distortion between images can be dramatic. A new iterative procedure for re-building the second image, based on velocity gradients of particles due to displacement, rotation and shear, has been proposed. This improved cross correlation algorithm has been shown to be considerably more accurate for simulated uniform, re-circulating and bi-axial shearing flows, and has been applied to the case of natural convection due to a heated horizontal cylinder.

1. Introduction

Particle image velocimetry (PIV) is a non-intrusive measurement technique, which can be used to measure full field velocity data within a two-dimensional plane of a particle-seeded flow field. That the technique has developed rapidly over the last two decades is indicated by the large amount of published work, which has been reviewed by Adrian (1986, 1991) and Kabayashi (1988). Generally, all PIV methods can be divided into two steps: firstly, recording the images of a particle seeded flow; and secondly, extracting velocity vectors from the recorded images. The PIV techniques are often categorized according to the recording media used (Willert and Gharib 1991). In photographic PIV double/multi-exposure images of a flow field are recorded on film and then various techniques are used to extract the velocity data. Backer and Fourney (1977) used Young's fringes methods, Adrian (1989) used the auto-correlation method and Cenedese and Paglialunga (1990) used the tracking method. In video PIV single-exposure images of a flow are recorded onto video tape or directly into computer memory. Extraction of full-field velocity data can then be achieved by analysis of sequential images using either the cross correlation method (Utami and Blackwelder 1991) or the tracking method (Hassan and Canaan 1991).

The tracking technique measures the velocity based on particle pairs but difficulties arise when the spatial density of particles is high. Young's fringes, auto-correlation and cross correlation methods are frequently applied. All of these techniques assume that velocity gradients are negligible in the interrogation area in the determination of the mean velocity. Usually the interrogation area of photographic PIV is small (around 1 mm^2) and the assumption is thus sustained. However, for the video cross correlation method, the interrogation area is not small enough to be negligible and the non-uniformity in the velocity distribution cannot be ignored. Reconstruction of the interrogation area by considering the velocity gradient has been suggested by Ashforth-Frost *et al* (1993) and Huang *et al* (1993a, 1993b). In this paper, a new method is proposed by which to re-build the second image instead of building each single interrogation area, paying particular attention to the extraction of velocity vectors taking into consideration the effects of three flow movement components, namely spatial uniform transfer, rotation and bi-axial shearing.

2. The conventional cross correlation method and its drawbacks

2.1. The conventional cross correlation technique

After having acquired two sequential images of the flow, we employed cross correlation to extract the velocity vectors from the images via an $N \times N$ pixel interrogation window, which is shown schematically in figure 1. The area of interest in the first frame is A and outside of this window is labelled A_0. Their counterparts in the second frame are B and B_0 respectively. An interrogation window $f(i, j)$ centred at a particular position (x, y) is sampled within A. Its counterpart is $g(i, j)$ within B. The cross correlation coefficient $R_{fg}(k, l)$ is calculated

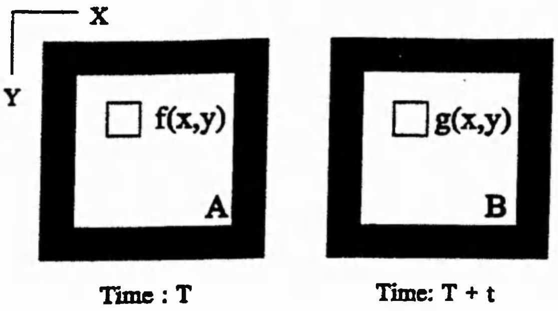

Figure 1. Images *A* and *B*.

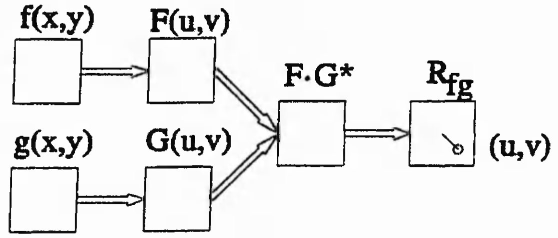

Figure 2. The FFT procedure.

between the patterns $f(i,j)$ and $g(i,j)$ (Kimura and Takamori 1986) using

$$R_{fg}(k,l) = \left(\sum_{i=-\infty}^{\infty}\sum_{j=-\infty}^{\infty} f(i,j)g(i-k,j-l)\right) \times \left(\sum_{i=-\infty}^{\infty}\sum_{j=-\infty}^{\infty} f^2(i,j)\sum_{i=-\infty}^{\infty}\sum_{j=-\infty}^{\infty} g^2(i-k,j-l)\right)^{-1/2}. \tag{1}$$

According to the convolution theory, the correlation operation in the space domain becomes multiplication in the frequency domain (Gonzalez and Wintz 1987):

$$f \circ g \Leftrightarrow FG^* \tag{2}$$

where $\circ$ denotes correlation, F and G are the Fourier transforms of f and g and G^* is the conjugate of G. A fast Fourier transform (FFT) is employed to simplify and significantly speed-up the cross correlation process. The procedure is shown schematically in figure 2. The FFT requires that the number of rows and columns of the input and output must have an exponent of 2; the size of the interrogation window must therefore have corresponding dimensions. A high cross correlation value near unity is observed when many particle images in the first image match their corresponding spatially shifted partners in the second image. Small cross correlation peaks may be observed when individual particle images match with other particle images. The highest correlation peak is considered to represent the best match of particle images between the windows $f(i,j)$ and $g(i,j)$. The offsets $(\Delta x, \Delta y)$ of the peak, which are measured from the origin of the cross correlation coefficient map, represent the average spatial shift of particles from image A to image B at position (x,y).

2.2. The effects of flow movement

Considering $f(i,j)$ to be the input image and $g(i,j)$ the output image, the relation between $f(i,j)$ and $g(i,j)$ will be

$$g(i,j) \approx f(i,j) \star s(i,j) \tag{3}$$

$\star$ denotes the convolution of the two functions $f(i,j)$ and $s(i,j)$ neglecting noise and $s(i,j)$ is an image transfer function. The cross correlation of $f(i,j)$ and $g(i,j)$ can be written as

$$\begin{aligned} R_{fg} &= f(i,j) \circ g(i,j) = f(i,j) \circ f(i,j) \star s(i,j) \\ &= R_{ff} \star s(i,j). \end{aligned} \tag{4}$$

The location of the individual particles is a stationary random process such that the input function $f(i,j)$ correlates with itself only at the origin. The convolution with the image transfer function moves the correlation peak away from the origin.

Considering a flow element of a general two-dimensional flow, Helmholtz velocity theory divides a movement of a flow element into three subsidiary terms (Wu 1982):

$$V = V_0 + \tfrac{1}{2}\Delta V \delta r + \nabla\phi \tag{5}$$

where V represents the velocity in the fluid element and V_0 represents the velocity of the spatial transfer of the fluid element. The three terms on the right-hand side of equation (5) are translation, rotation and element bi-axial shear respectively. Westerweel (1993) pointed out that, if the interrogation window is considered as a flow element, then the rigid shift results in only parts of the $f(i,j)$ and $g(i,j)$ contributing to R_{fg}. The peak is shifted away from the origin and the rotation and deformation terms lead to broadening of the peak (Willert and Gharib 1991). Huang *et al* (1993a) analysed the limitations of conventional PIV due to velocity gradients and out-of-pattern motion. An artificial distortion method was proposed by Ashforth-Frost *et al* (1993) and Huang *et al* (1993b), but only the linear velocity gradients were considered. For the FFT cross correlation method, all of the flow parts affect the coefficients of correlation and influence the peak position.

3. The improved cross correlation method

A method is now proposed that reconstructs a second image by considering the effects of the three terms in a two-dimensional flow. This second image was used to correct the velocity obtained from the conventional cross correlation method. The technique of reconstruction of the second image and the whole procedure of the improved method will be introduced. Three peak location methods were investigated.

3.1. Reconstruction of the second image

If whole field displacement vectors $(\Delta x, \Delta y)$ are known between images A and B, and the flow is two-dimensional, then the second image pattern can be rebuilt to be similar to the first image. The whole field displacement vectors are constituted by

$$x_B = x_A + \Delta x \tag{6}$$

$$y_B = y_A + \Delta y \tag{7}$$

where (x_A, y_A) is the position of a particle in image A at time T and (x_B, y_B) is the position of the same particle in image B at time $T + t$. A digitized particle image is represented by the pixel's grey distribution. This means that the grey $I(x_B, y_B, T + t)$ in image B is equal to $I(x_A, y_A, T)$ in image A.

A new image B' can be reconstructed from image B. The grey $I(x_{B'}, y_{B'}, T)$ in B' is the grey $I(x_B, y_B, T+t)$ in B, where $(x_{B'}, y_{B'})$ is identical to (x_A, y_A). By noting that x_A and y_A must be integers and the displacements $(\Delta x, \Delta y)$ are usually non-integers, the pixel intensity of position (x_B, y_B) is obtained using bilinear interpolation:

$$I(x_B, y_B) = \sum_{i=0}^{3} N_i I_i \tag{8}$$

where

$$i_B = \text{integer}(x_B) \qquad \varepsilon_i = x_B - i_B$$
$$j_B = \text{integer}(y_B) \qquad \varepsilon_j = y_B - j_B$$
$$I_0 = I(i_B, j_B) \qquad I_1 = I(i_B, j_B + 1)$$
$$I_2 = I(i_B + 1, j_B) \qquad I_3 = I(i_B + 1, j_B + 1)$$
$$N_0 = (1 - \varepsilon_i)(1 - \varepsilon_j) \qquad N_1 = (1 - \varepsilon_i)\varepsilon_j$$
$$N_2 = \varepsilon_i(1 - \varepsilon_j) \qquad N_3 = \varepsilon_i \varepsilon_j.$$

$I(x_B, y_B)$ is set at position $(x_{B'}, y_{B'})$ in B'. After the pixels' grey levels have been calculated, B' is constructed. The image B' is sampled by a window $g'(x, y)$ centred at position (x, y). If the displacement data are accurate and the particle flow is two-dimensional, then, neglecting electronic noise and the averaging effect of bilinear interpolation, the highest cross correlation coefficient of $f(x, y)$ and $g'(x, y)$ will be unity.

The whole field displacement is currently unknown. The displacement data $(\Delta x, \Delta y)$ at each point can be calculated using the conventional cross correlation method. Supposing that the actual displacement is $(\Delta x + \delta x, \Delta y + \delta y)$, where $(\delta x, \delta y)$ is a measure of the non-uniformity of the displacement around the point, then if the second image B' were built based on $(\Delta x, \Delta y)$ and the window $g'(x, y)$ were sampled, the peak position of the cross correlation between $f(x, y)$ and $g'(x, y)$ would be offset from the origin by $(\delta' x, \delta' y)$. $(\delta' x, \delta' y)$ is an average over the interrogation $N \times N$ window and is normally small compared with $(\Delta x, \Delta y)$ so that the effects of non-uniformity are reduced. A new displacement vector $(\Delta x + \delta' x, \Delta y + \delta' y)$ is found, which is more accurate.

3.2. The procedure

Before the new procedure is introduced, the assumption is made that, the higher the correlation coefficient, the higher will be the accuracy of the velocity data.

Since the initial velocity data are unknown, it is necessary to use an iterative procedure, which includes six major steps.

(i) Use the conventional cross correlation velocity method to extract initial full field displacement vectors. Eliminate error vectors using a filtering subroutine such as that proposed by Kimura *et al* (1988).

(ii) Bilinear interpolation of the displacement at every pixel inside the first image A using the extracted velocity. Find the grey level of every pixel of the new second image B', which the procedure in the previous section introduced.

(iii) Copy A_0 as the outside image of B' for velocity extraction at the points around its boundary, in case parts of $f(x, y)$ and $g'(x, y)$ have been sampled from the outside images A and B.

(iv) Set a correction count to record the correction time and set it to zero.

(v) Calculate the cross correlation of $f(x, y)$ and $g'(x, y)$. Find the peak position of the coefficient map. If the highest coefficient is larger than the recorded coefficient of position (x, y), add the offset to the recorded displacement at position (x, y) and add 1 to the correction count. Otherwise, omit this position and continue at the next position.

(vi) Continue until all full field velocity vectors have been corrected and check the correction number, if it is not zero, return to step 3; if it is zero exit from the procedure.

4. Validation of the improved method

Synthetic flow images were generated for simulating uniform, re-circulating and bi-axial shearing flows for validation of the improved cross correlation method. The first record image was obtained using a black board with randomly distributed white dots. The second image was generated by translating, rotating or bi-axially shearing the first image to simulate uniform, re-circulating and bi-axial shearing fluid flows using imaging techniques. Typical images are shown in figures 3(*a*)–(*d*). The second image of the synthetic uniform flow was generated by shifting the first image in the X direction by a known distance. Distances of 2, 4, 6, 8 and 10 pixels were applied and the resulting second images were saved separately for velocity extraction. The second images of simulated re-circulating flow were obtained by rotating the first image by angles of 0.035, 0.07, 0.105 and 0.14 rad around the centre of the first image. Shearing flow was simulated by shearing the first image with shear strains of 0.05, 0.1, 0.15, 0.2, 0.25 and 0.3. After the images were generated, the conventional method and the improved method were applied to

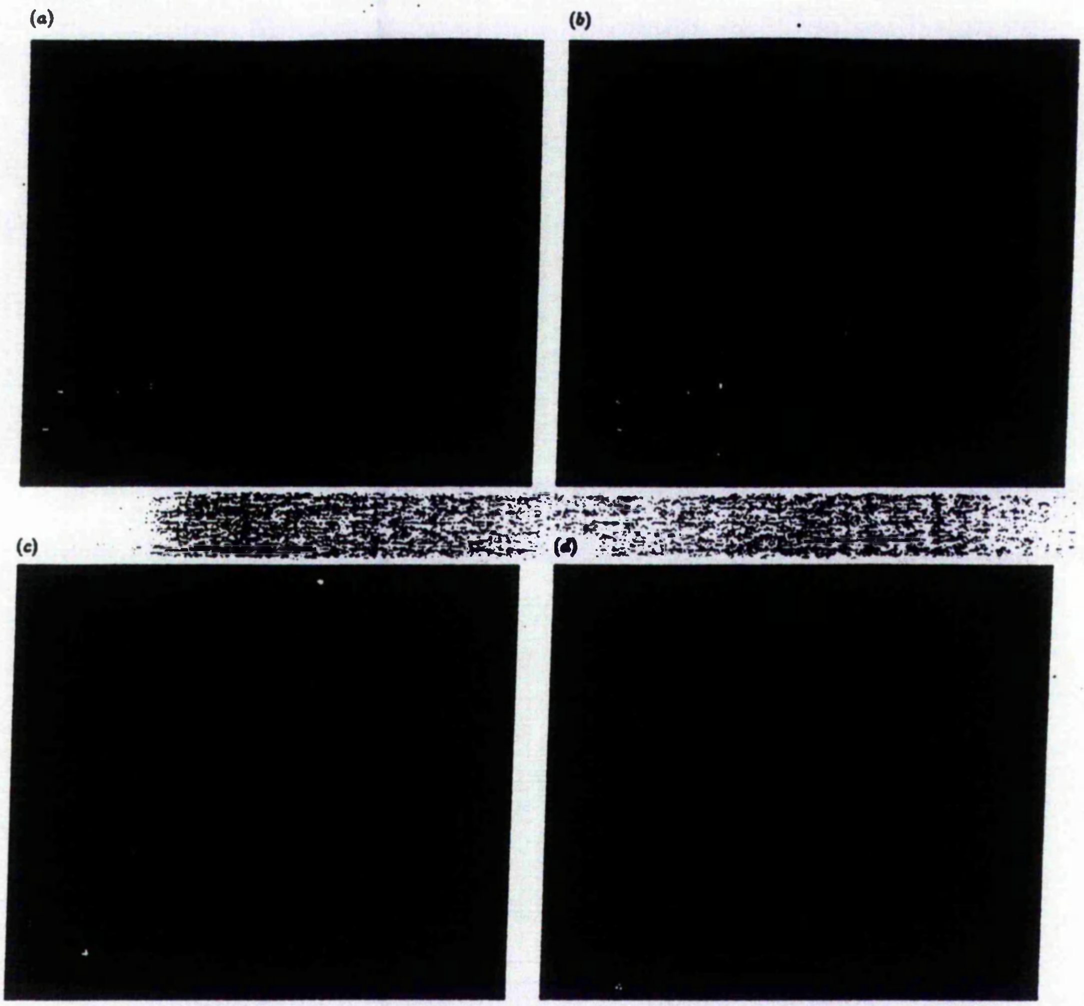

Figure 3. (*a*) The original image. (*b*) The translated image. (*c*) The rotated image. (*d*) The sheared image.

extract the velocity data, which were compared with the expected data.

In step (v) of section 3.2, procedures for locating the peak position were presented. The maximum of the $R_{fg}(i, j)$ yields only a rough estimate of the displacement (with a resolution of one pixel). Sub-pixel results for the peak position can be obtained by three different methods. Willert and Gharib (1991) used a three-point curve fit to find the sub-pixel position. Prasad *et al* (1992) demonstrated that parabolic and Gaussian curve fits yielded RMS errors that were about half those from the centre of mass technique (Willert and Gharib 1991). They also argued that this trend was true only for flows whose velocity gradient is negligible and, consequently, they selected the centre of mass method. In this paper, the centre of mass method, parabolic and Gaussian curve fits are compared. Figure 4 shows that there is little difference in the accuracy of the three methods; full lines represent the results of the improved method and broken lines represent those of the conventional method. A maximum difference of 0.05 pixels occurs for the case of shift (figure 4(*a*)) indicated by different broken lines. However, the parabolic fit has been selected due to its superior accuracy and simplicity.

That the average absolute errors of the improved method are lower than those of the conventional method is illustrated in figure 4(*a*)–(*c*). For translational movements, relative errors were decreased from about 5% with the conventional method to about 1% with the improved one for pure shift measurements. In the case of rotation, relative errors decreased from about 7% to about 3%. The results of shearing showed that relative errors decreased from about 10% to about 5%.

Specifically, for the results of the translational movements, if shift distances in the x and y directions are larger than ten pixels, then the errors in the computed vectors increase rapidly. Willert and Gharib (1991) argued that the maximum measurable displacement is

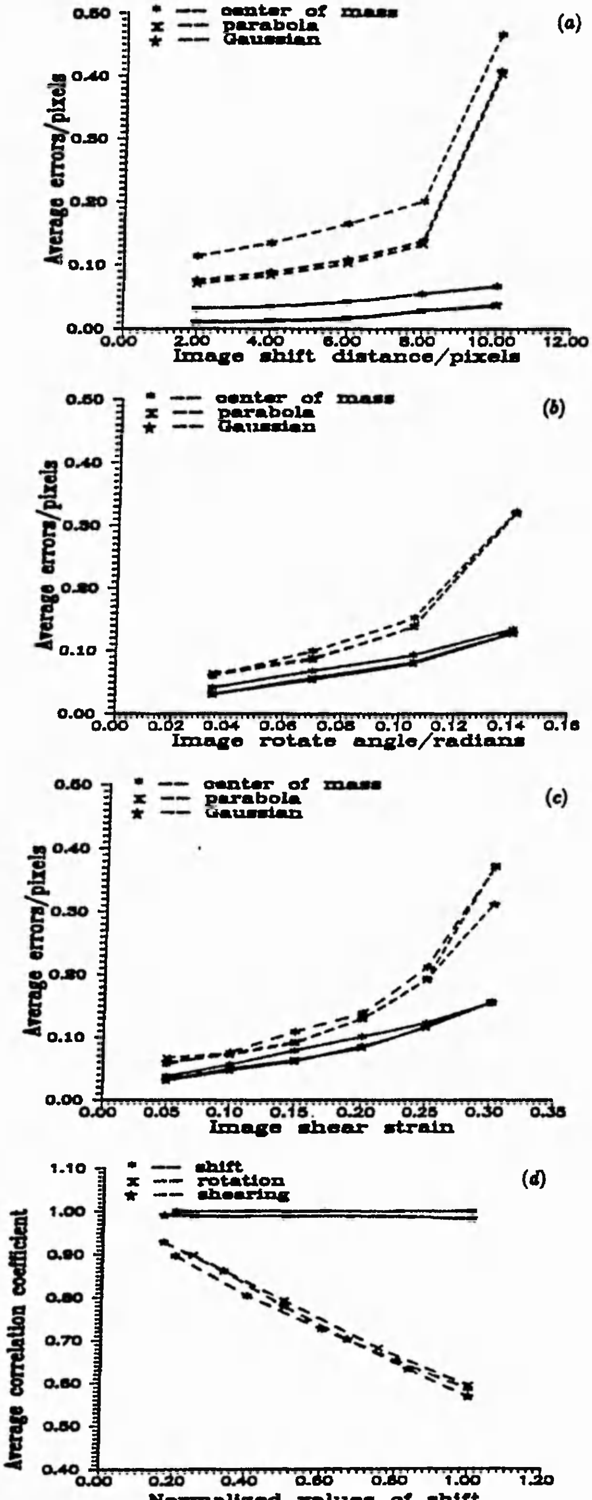

Figure 4. (*a*) Shift, (*b*) rotation, (*c*) shear and (*d*) a comparison of the mean correlation coefficients. Broken lines are results from the conventional method and full lines are results from the improved method.

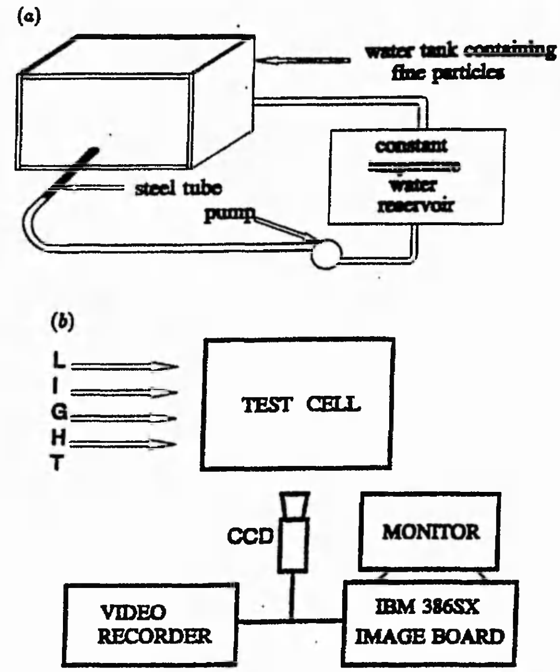

Figure 5. (*a*) A schematic diagram of the experimental rig. (*b*) A schematic diagram of the image acquisition arrangement.

a third of the interrogation window size.

Figure 4(*d*) shows a comparison of the mean value of the maximum correlation coefficients of points inside the area of interest obtained from the conventional method and the improved method using the parabolic curve fitting procedure. The horizontal axis represents normalized values of shift distances, angles of rotation and shear strains, which have been normalized with respect to ten pixels, 0.14 rad and 0.30 respectively. The broken and full lines represent the results of the conventional and improved methods respectively. The mean coefficients of the results of the conventional method decrease as the values of the shift, rotation and shear strain increase. The mean coefficients of the results of the improved method have higher values and are less sensitive to shift, rotation and shear strain. Comparison of figures 4(*a*)–(*c*) with figure 4(*d*) shows that higher accuracy is obtained with a high correlation coefficient since the displacement errors are smaller for higher coefficients.

5. Experimental results

To assess the performance of the proposed technique, it was applied to the analysis of recorded images of natural convection from a heated horizontal cylinder. The experimental arrangement is shown in figure 5(*a*). The test cell consisted of a transparent perspex tank (150 mm × 186 mm × 100 mm) containing water at 25 °C. A thin seamless stainless steel tube (diameter

(*a*)

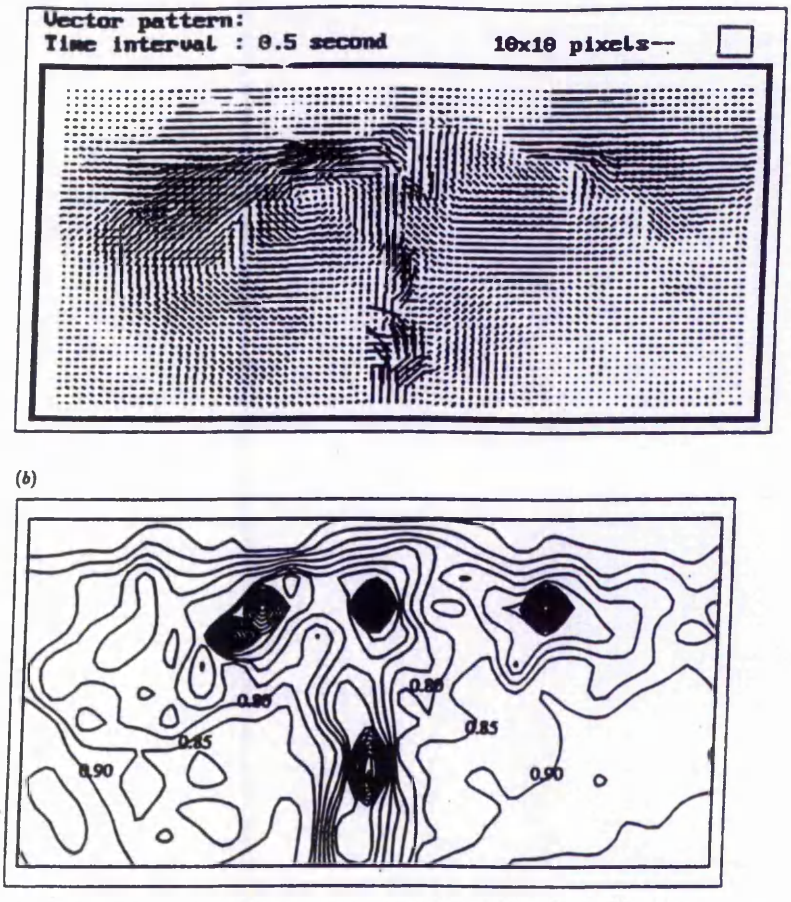

(*b*)

Figure 6. (*a*) Velocity data extracted by the conventional cross correlation method. (*b*) Distribution of correlation coefficient of the conventional correlation method.

13 mm) represented the heated cylinder. Warm water at about 50 °C from a constant-temperature water bath was circulated through the tube. The flow was artificially seeded with 0.01% micro-encapsulated liquid crystal particles of 100 μm mean diameter. A thin plane of the flow domain was illuminated using white light and images were recorded at right angles to this plane using a Pulnix TLC-X CCD camera. The reason for using liquid crystals as the seeding particles is that the current work is aimed at developing a comprehensive system for measuring velocity and temperature simultaneously. This is also the justification for using white light rather than laser light as the source of illumination.

A Data Translation DT2871 image board installed in an IBM PC/SX was used to acquire a sequence of 512 $\times$ 512 pixels $\times$8 bit resolution frames, either directly from the CCD camera or from a Sony U-Matic VO-5800PS video recorder. A high-resolution image monitor was used to view the particle images and select an area of interest before collecting the raw data for analysis. Frames can be analysed at intervals of 40 ms, determined by the video rate (25 frames per second). The image acquisition arrangements are shown in figure 5(*b*).

Figures 6(*a*) and 7(*a*) show the flow patterns in a region 2–8 diameters above the cylindrical tube. Prior to the cylindrical tube being heated, no convective motion was evident within the test section. On supplying heat to the cylinder, the upward convected heat transfer was immediately apparent in a central core directly above the cylinder, shown in figures 6(*a*) and 7(*a*). As the flow reached the free surface of the water, two counter-rotating re-circulation regions were formed, but the flow was not entirely symmetric. The initially isothermal and stationary flow developed into a stratified thermal field. Having allowed a velocity field to develop, two sequential images were acquired with a 0.5 s interval. Figure 6(*a*) shows the resulting velocity field, extracted using the conventional cross correlation method. The calculated correlation coefficients were in the range 0.05–0.95, and are shown in figure 6(*b*) with contour increments of 0.05. The lowest values occurred in the

(a)

(b)

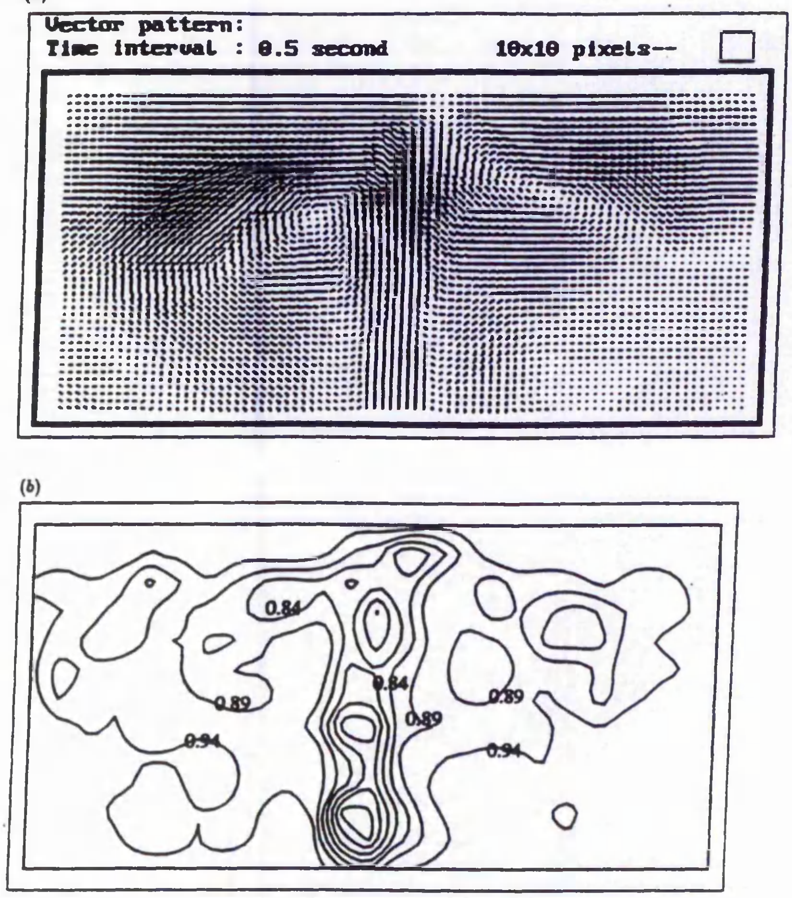

Figure 7. (a) Velocity data extracted by the improved cross correlation method. (b) Distribution of correlation coefficients of the improved method.

shear layer and re-circulation regions. The maximum velocities recorded were of the order of 0.1 m s^{-1}. The proposed improved method was used to correct this velocity data and 42 iterations were necessary to achieve convergence. The results, plotted in figure 7(*a*), show a marked improvement when compared to the recorded images. Corresponding correlation coefficients plotted in figure 7(*b*) show a significant increase in the shear layer and re-circulation regions; from 0.05 to 0.65. The highest correlation coefficients were also marginally improved; from 0.95 to 0.98.

For this particular example, using the improved technique, the overall CPU time increased from 14 min for 3696 vectors to 2 h, which is acceptable considering the improvement in accuracy. However, for economy, it is not always necessary to execute the iterative correction procedure when high correlation coefficients prevail in the previous iteration.

Finally, it is worth noting that the results of the improved technique are dependent on the initial results obtained using the conventional cross correlation method. In the extreme case, if the conventional method yields very poor results, then use of the improved technique may be ineffective.

6. Conclusion

An improved cross correlation technique has been proposed to overcome errors in the analysis of video images for PIV due to appreciable velocity gradients. The technique has been investigated for natural convection from a heated horizontal cylinder. Improvements in accuracy have been observed, indicated by the increase in correlation coefficients. For translational movements, relative errors were decreased from about 5% with the conventional method to about 1% with the improved one for pure shift measurements. In the case of rotation, relative errors decreased from about 7% to about 3%. The results of shearing showed that relative errors decreased from about 10% to about 5%. This has been facilitated by subjecting images to various magnitudes of displacement, rotation and shear strain. The most significant improvements were obtained in the shear layer and re-circulation regions of the flow field in which the highest velocity gradients prevail. The increase in CPU time using the proposed technique is considered acceptable in return for the improvement in accuracy.

Acknowledgment

Thanks are due to The Nottingham Trent University and the UK Higher Education Funding Council (HEFC) for the financial support provided.

References

Adrian R J 1986 Multi-point optical measurements of simultaneous vectors in unsteady flow—a review *Int. J. Heat Fluid Flow* 7 127–45

—— 1989 Engineering applications of particle image velocimeters *ICALEO '89 Optical Methods in Flow and Particle Diagnostics* pp 56–71

—— 1991 Particle-imaging techniques for experimental fluid mechanics *Ann. Rev. Fluid Mech.* 23 261–304

Ashforth-Frost S, Dobbins B N, Jambunathan K, Wu X P and Ju X Y 1993 A comparison of interrogation methods for particle image velocimetry *Proc. SPIE* 2005 478–89

Backer D B and Fourney M E 1977 Measuring fluid velocities with speckle patterns *Opt. Lett.* 1 135–7

Cenedese A and Paglialunga A 1990 Digital direct analysis of a multiexposed photograph in PIV *Exp. Fluids* 8 273–80

Gonzalez R C and Wintz P A 1987 *Digital Image Processing* (Reading, MA: Addison-Wesley)

Hassan Y A and Canaan R E 1991 Full-field bubbly flow velocity measurements using a multiframe particle tracking technique *Exp. Fluids* 12 49–60

Huang H T, Fiedler H E and Wang J J 1993a Limitation and improvement of PIV. Part I: limitation of conventional techniques due to deformation of particle image patterns *Exp. Fluids* 15 168–74

—— 1993b Limitation and improvement of PIV. Part II: particle image distortion, a novel technique *Exp. Fluids* 15 263–73

Kabayashi T 1988 Flow visualization image analysis review *2nd Int. Symp. on Fluid-Control, Measurement, Mechanics and Flow Visualisation* pp 545–56

Kimura I, Kimura H and Takamori T 1988 Image processing of flow velocity vector distributions *2nd Int. Symp. on Fluid-Control, Measurement, Mechanics and Flow Visualisation* pp 189–93

Kimura I and Takamori T 1986 Image processing of flow around a circular cylinder by using correlation technique *Flow Visualization IV* (Washington: Hemisphere) pp 221–6

Prasad A K, Adrian R J, Landreth C C and Offutt P W 1992 Effect of resolution on the speed and accuracy of particle image velocimetry interrogation *Exp. Fluids* 13 105–16

Utami T and Blackwelder R F 1991 A cross-correlation technique for velocity field extraction from particle visualization *Exp. Fluids* 10 213–23

Westerweel J 1993 Analysis of PIV interrogation with low pixel resolution *Proc. SPIE* 2005 624–35

Willert C E and Gharib M 1991 Digital particle image velocimetry *Exp. Fluids* 10 181–93

Wu W Y 1982 *Fluid Mechanics* (Beijing: Beijing University Press) (in Chinese)

Application of liquid crystals to particle image velocimetry

S ASHFORTH-FROST BEng, PhD, AIMechE, **X Y JU**, and **K JAMBUNATHAN** BSc, PhD, FIMechE
Department of Mechanical Engineering, The Nottingham Trent University, UK
X WU
Department of Modern Mechanics, University of Science and Technology of China,
People's Republic of China

ABSTRACT

Particle Image Velocimetry (PIV) is a well established non-intrusive technique for full field flow measurements. The display of colour distribution from thermochromic liquid crystals (TLC) due to changes in temperature has been frequently exploited in the measurement of temperature on solid surfaces. Cholesteric liquid crystals in micro-encapsulated form can conveniently be used as artificial seeding particles enabling velocity and temperature to be visualised and measured simultaneously. The combination of PIV with TLC can provide a powerful approach for obtaining full field information in thermally driven fluid flow during transient and steady states.

NOTATION

C	Mean number of particles per unit volume
g	Locations of the particles
I_0	Intensity of light sheet
I	Transmitted intensities of the image
M	Magnification of the image
N	Number of particles
R	Correlation coefficient
s	Shift of the image
t	Time
u	True velocity vector
u'	Calculated velocity vector
w	Interrogation window function
x	Coordinates of the plane of the light sheet
X	Coordinates of the plane of the image
τ	Intensity transmissivity of the photograph
δ	Dirac function
HSI	Hue, Saturation and Intensity
RGB	Red, Green and Blue

Subscripts:
- 1, 2 — First and second exposure
- i — Individual particles in the image

1. INTRODUCTION

Knowledge of instantaneous temperature and velocity fields in steady and transient heat transfer processes are often required to enable a basic understanding of the heat transfer or convection phenomena. Most techniques used for measurement of velocity and temperature become less effective in transient situations. Thermocouples have been used conventionally for temperature measurements. However, to obtain full field information, extensive thermocoupling is necessary which is expensive and the test fields are invariably intruded. Data collection can also be cumbersome, especially in transient applications. Researchers thus resort to techniques such as schlieren, Mach-Zehnder and holographic interferometry, to visualise temperature fields. However, these cannot be used for direct temperature measurement of aqueous solutions, because the refractive index distributions to be measured vary with both temperature and concentration. Micro-encapsulated liquid crystal particles have been adopted to indicate temperature variations in various systems, particularly involving thermal convection. Liquid crystals change colour according to the environment temperature, the change being reversible and repeatable as long as the crystals are not physically damaged. During the past 20 years, liquid crystals have emerged as reliable temperature sensors, and have been applied in a number of situations to visualise the temperature distribution within complex flow fields. During this same period, the application of computer processing to the liquid crystal technique has enabled the latter to become a powerful new approach: digital processing of liquid crystal images to yield full-field measurements of temperature distributions. The development of liquid crystal techniques for temperature measurement in the past, coupled with image processing, has opened some new avenues for heat transfer research and may lead to important changes in the way research is conducted during the next decade (1).

Laser-Doppler anemometry (LDA) as well as hot-wire anemometry (HWA) have been used in the past to study detailed fluid dynamic characteristics. In HWA, only scalar quantities are measured and the direction of flow is not known. Furthermore, it is sometimes difficult to use HWA to measure profiles near the wall due to physical access. LDA enables components of velocity to be measured to high accuracy and resolution at a single point in a flow. Spatial velocity information therefore requires scanning a single probe throughout the volume of interest which, in an unsteady flow, temporally smooths out the instantaneous nature. Many point measurements must therefore be made to derive a velocity profile or field. If these measurements are not performed simultaneously, any information on coherent structures in the flow cannot be easily determined. The most advanced and widely used full field technique is particle image velocimetry (PIV) which utilises a light sheet to illuminate a plane within the flow of interest. The light scattered from neutrally buoyant seeding particles within the flow, imaged onto a recording medium, gives a random distribution of point particle images. Extraction of particle displacement data from PIV pictures is routine and most commonly achieved by local interrogation of double or multiple exposure images over a regular grid using two dimensional correlation functions (2).

The PIV technique is often categorized into photographic PIV or video PIV depending on the recording media used (3). Video PIV suffers from low resolution of the digital image and low frame rate. The interrogation area is usually not small enough to neglect the non-uniformity of the velocity distribution. A method was proposed previously to compensate the effects of the non-uniformities (4).

In this paper, liquid crystal particles are used to measure the full field velocity and temperature distribution. Liquid crystals in micro-encapsulated form can not only act as particles for establishing the velocity field but, due to their responsiveness to temperature, also enable the temperature field to be measured.

2. EXPERIMENTAL ARRANGEMENT AND IMAGE PROCESSING

To demonstrate the performance of the proposed technique (4), it was applied to the analysis of recorded images of natural convection from a heated horizontal cylinder. The experimental arrangement is described in detail in (5). The test cell consisted of a transparent Perspex tank (150 × 186 × 100 mm) containing water at 25°C heated by a thin seamless stainless steel tube (diameter 13 mm) through which warm water at ~50°C from a constant temperature water bath was circulated. The flow was artificially seeded with 0.01% micro-encapsulated liquid crystal particles of 100μm mean diameter (5). A thin plane of the flow domain was illuminated using white light and images were recorded at right angles to this plane using a Pulnix TLC-X colour CCD camera.

A Data Translation® DT2871 colour image board installed in a IBM 386 PC/SX was used to acquire a sequence of 512 × 512 pixels × 8 bit resolution colour pictures, either directly from the colour CCD camera or, from a Sony U-Matic VO-5800PS video recorder via a RGB decoder. Signals representing the colour picture were digitized into RGB and restored in three buffers or converted to HSI. The DT2871 performs the RGB-to-HSI (and vice versa) colour space conversion using specialized hardware in real time. A high resolution image monitor was used to view the particle images and select an area of interest before collecting the raw data for analysis. Frames can be analyzed at intervals of 40 ms, determined by the video rate (25 frames/s).

3. VELOCITY DERIVATION USING AN IMPROVED CROSS-CORRELATION TECHNIQUE

Usually, film photography or a CCD sensor is used for recording images of flow seeded with fine particles. Since the optical density of a film, or the electric charge collected by a CCD sensor, is proportional to the image intensity field the image intensity can be directly used for particle image analysis. The transmissivity of the photograph is given by superposition of the transmissivity of all the individual particles within the light sheet of intensity $I_0(x)$ when the particle source density is low (2). Thus

$$\tau(X)=\sum_{i=0}^{N} I_0(x_i)\tau_0(X - Mx_i) \tag{1}$$

where $\tau_0(X-Mx_i)$ represents the transmissivity of an individual particle image per unit of illuminating intensity in the light sheet. The locations of particles in the interrogation spot at time t are defined as

$$g(x, t) = \sum_{i=1}^{N} \delta(x - x_i(t)) \tag{2}$$

where N is the total number of particles within the interrogation volume. Alternatively, the intensity transmissivity of the photograph may be written as

$$\tau(X) = \int I_0(x)g(x,\ t)\tau_0(X - Mx)\mathrm{d}x \tag{3}$$

When the flow field images are recorded in separate frames, the transmissivity of a photographic recording of the first single exposure of the flow field, illuminated by a light sheet of intensity $I_0(x)$, and sampled at time t is

$$\tau_1(X) = \int I_0(x)g(x,\ t)\tau_0(X - Mx(t)) \tag{4}$$

Similarly, for a second recording of the flow field sampled at time $t + \Delta t$,

$$\tau_2(X) = \int I_0(x')g(x',t+\Delta t)\tau_0(X - Mx'(t+\Delta t)) \tag{5}$$

When the first and the second frame images are sampled with a window function, $w(X-X_I)$, centred at X_I, the transmitted intensities are

$$I_1(X) = w(X-X_I)\tau_1(X) \tag{6}$$

$$I_2(X) = w(X-X_I)\tau_2(X) \tag{7}$$

respectively. The spatial cross-correlation of I_1 and I_2 with separation vectors s is given by

$$\begin{aligned} R(s) &= \int I_1(X)I_2(X + s)\mathrm{d}X \\ &= \int w(X - X_I)w(X - X_I + s)[\tau_1(X)\tau_2(X + s)]\mathrm{d}X \end{aligned} \tag{8}$$

and is used to determine the image displacement by locating the peak position of the cross-correlation. The statistical properties of the cross-correlation function are determined by an ensemble average of $R(s)$ for the random process. Noting that all of the randomness is contained in $g(x,t)$, then

$$\begin{aligned} g(x,t) &= C(x) + \Delta g(x,t) \\ \langle g(x,t)g(x',t+\Delta t)\rangle &= C(x,\ t)^2 + C(x,\ t)\delta(x' - x - u(x,t)) \end{aligned} \tag{9}$$

where $C(x)$ is the mean number of particles per unit volume and is assumed to be time independent and $\langle\Delta g\rangle = 0$ (6). Combining equations (4) to (9) leads to the ensemble average of the cross-correlation:

$$
\begin{aligned}
<R(s)> = & \int (w(X-X_I)w(X-X_I+s) \int\int C(x,t)^2 I_0(x) I_0(x') \tau_0(X-Mx) \\
& \times \tau_0(X-Mx'+s) \mathrm{d}x \mathrm{d}x') \mathrm{d}X + \int (w(X-X_I)w(X-X_I+s) \\
& \times \int C(x,t) I_0(x) I_0(x+u\Delta t) \tau_0(X-Mx) \tau_0(X-Mx+s-Mu\Delta t) \mathrm{d}x) \mathrm{d}X
\end{aligned} \tag{10}
$$

The first term of equation (10) is the cross-correlation of the mean intensities. The second term is the cross-correlation of the intensity fluctuations corresponding to the mean velocity in the interrogation spot. Usually the fast Fourier transform (FFT) algorithm is used for the correlation calculation. In this case, the uniform transfer of the image pattern causes de-correlation represented by $w(X\text{-}X_I)w(X\text{-}X_I+s)$ and the non-uniformity of the velocity u causes a broadening of the correlation peak. By comparison, the interrogation area of photographic PIV is small (around 1 mm^2) and these effects can be neglected. The interrogation area of video PIV is not small enough for these effects to be ignored. A method proposed previously (4) to compensate these effects reconstructed the second image utilizing the velocity data u' calculated from equation (10). By calculating the cross-correlation of the first image and the reconstructed second image, the velocity compensation can be found:

$$
\begin{aligned}
<R(s')> = & \int (w(X-X_I)w(X-X_I+s') \int\int C(x,t)^2 I_0(x) I_0(x') \tau_0(X-Mx) \\
& \times \tau_0(X-Mx'+s') \mathrm{d}x \mathrm{d}x') \mathrm{d}X + \int (w(X-X_I)w(X-X_I+s') \int C(x,t) \\
& \times I_0(x) I_0(x+(u-u')\Delta t) \tau_0(X-Mx) \tau_0(X-Mx+s'-M(u-u')\Delta t) \mathrm{d}x) \mathrm{d}X
\end{aligned} \tag{11}
$$

The compensation procedure is iterated until $<R(s)>$ reaches its maximum value.

4. TEMPERATURE MEASUREMENT USING THERMOCHROMIC LIQUID CRYSTALS

Liquid crystals display different colours at different temperatures. The temperature can be established by interpreting the colour reflected by liquid crystals when illuminated by white light. A frequently used method of chromatic interpretation relates temperature to hue usually by using RGB decomposition. Even though the liquid crystal spectral display may change with viewing and illumination angles, and the brightness of illumination, according to (6) the objective colour that the liquid crystals display, the true hue, remains unchanged so long as the temperature remains unchanged. Details of using true-colour image processing to calibrate the temperature versus hue relationship can be found in (7-10). This approach is more advantageous than the mono-chromatic approach (eg. 11) in terms of speed, image resolution and suitability for investigating transient phenomena. In the present study, the HSI mode of the DT-Translation® DT2871 colour image board has been employed.

The hue-temperature calibration was performed in the test cell by means of a calibrated mercury-in-glass thermometer (0.1°C resolution) with the water temperature inside the cell maintained constant. Illumination was provided by a thin sheet of white light and images were recorded using the colour CCD camera. An average value of hue obtained in very close proximity to the thermometer was recorded.

5. RESULTS AND DISCUSSION

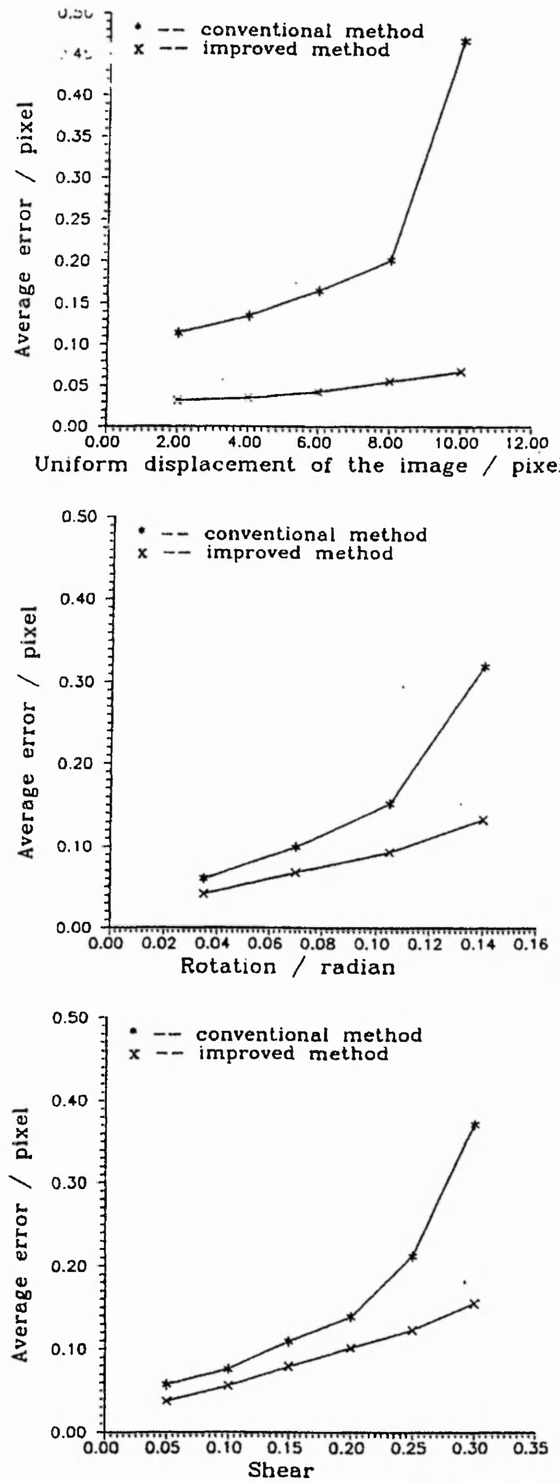

Figure 1. Comparison of conventional PIV and improved PIV for uniform, re-circulating and shear flow.

Simulations were carried out to investigate the effects of uniform, re-circulating and shear flow occurring within the interrogation spot. In Figure 1 it can be seen that when using conventional PIV analysis the errors increase rapidly when the uniform displacement, rotation and shear become large. However, the improved cross-correlation method, described earlier, compensates for these effects and significantly reduces the errors.

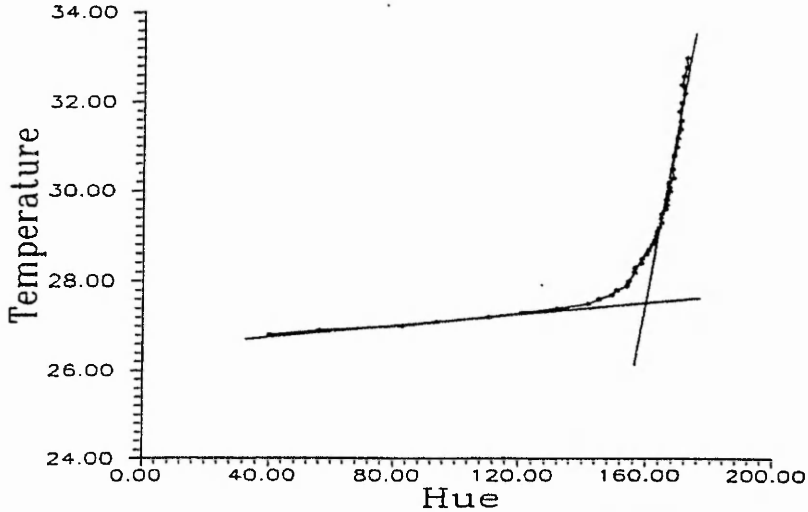

Figure 2. Temperature-hue relationship for the micro-encapsulated liquid crystals.

In Figure 2 linear regression was applied for the two linear parts of the temperature-hue relationship and a simple polynomial fit was applied for the part between them. The sensitivity of the liquid crystal particles was 0.008°C per unit hue in the range 26.8°C to 27.6°C (part 1) and 0.358°C per unit hue in the range 28.8°C to 33.0°C (part 2), and between these two linear parts the sensitivity varied between 0.007 and 0.461. The standard deviation of the errors of regression were 0.06°C and 0.253°C for part 1 and part 2 respectively. Using this calibrated temperature-hue relationship, temperature information was inferred from hue values of the first colour image.

Prior to the cylindrical tube being heated, no convective motion was present within the test section. On opening the hot water supply to the cylinder, the upward convected flow was immediately visible in a central core directly above the cylinder. As the flow reached the free surface of water, two counter-rotating recirculation regions were formed, but the flow was not entirely symmetric. Having allowed a velocity field to develop, two sequential colour images were acquired at a 0.5 second interval using the HSI mode of the colour image grabber. Figure 3 shows the resulting velocity field. The maximum velocities recorded were of the order of 0.1 m/s. The proposed improvement to the algorithm was used to correct this velocity data.

Figure 4 shows the temperature distribution in the test cell where the range of the liquid crystal temperature varied from 27°C to 33°C. The white and black patches indicate the range from low to high values respectively. The grey vertical lines in the centre of Figure 4 show the path of the rising hot stream directly above the heated cylinder.

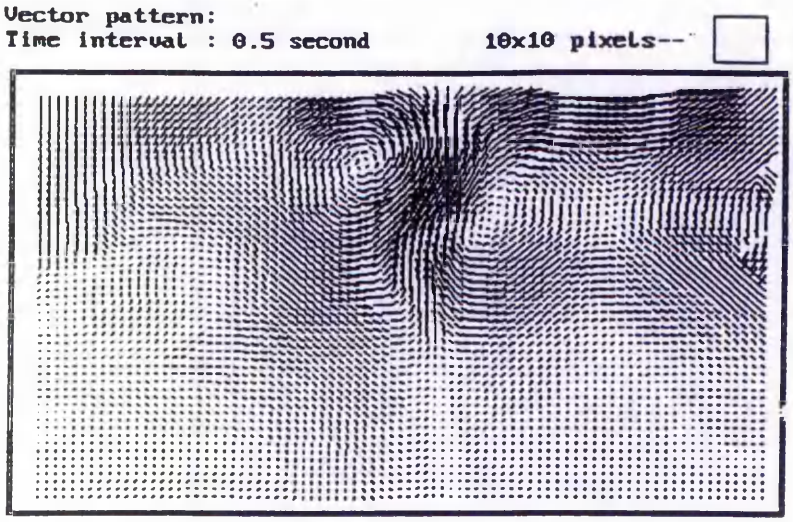

Figure 3. Velocity vectors.

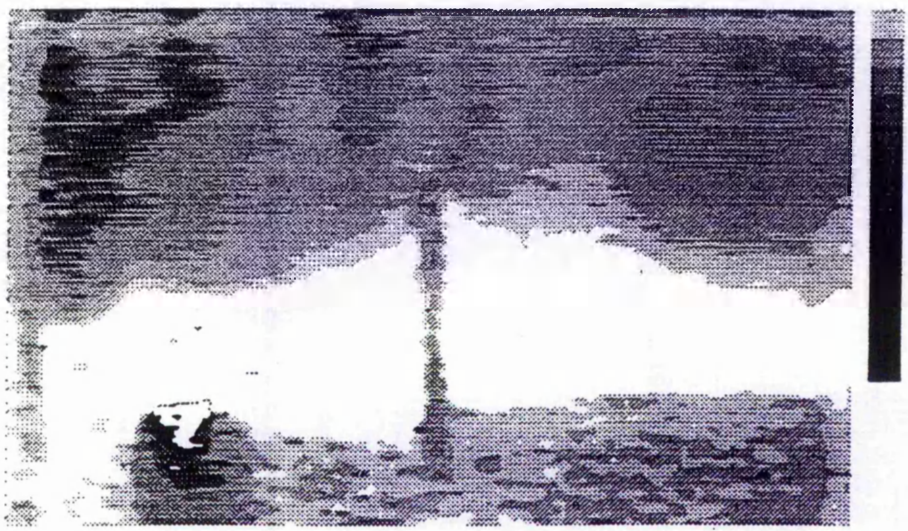

Figure 4. Temperature distribution.

6. CONCLUSION

A method of quantifying velocity and temperature simultaneously in a natural convection water flow has been presented. An improved cross-correlation method was applied to extract the velocity data whilst at the same time the colours displayed by thermochromic liquid crystals were used to extract the temperature field. The work not only demonstrated the feasibility of using liquid crystals to simultaneously measure velocity and temperature, but also provided a useful tool to test the newly developed algorithm for processing of the data.

ACKNOWLEDGEMENTS

Thanks are due to The Nottingham Trent University and the Higher Education Funding Council (HEFCE) for the financial support provided, and to Hallcrest Ltd. (Poole, UK) for providing the liquid crystal materials.

REFERENCES

1. MOFFAT, R. J. Experimental Heat Transfer. Proceedings of 9th Int Heat Transfer Conference. 1991, **1**, 187-209.

2. ADRIAN, R. T. Particle Imaging Techniques for Experimental Fluid Mechanics. Ann. Rev. Fluid Mech. 1991, **23**, 261-304.

3. WILLERT, C. E. AND GHARIB, M. Digital particle image velocimetry. Experiments in Fluids. **10**, 1991, 181-93.

4. JAMBUNATHAN, K., JU, X. Y., DOBBINS, B. N. and ASHFORTH-FROST, S. An Improved Cross-Correlation Technique for Particle Image Velocimetry. Meas. Sci & Tech. **6**, 1995, 507-14.

5. ASHFORTH-FROST, S. and JAMBUNATHAN, K. Flow visualisation using liquid crystals, SPIE Ann. Int. Symp. on Optics, Imaging and Instrumentation: Optical Diagnostics in Fluid and Thermal Flow, San Diego, USA, 1993, 237-45.

6. KEANE, R. D. AND ADRIAN, R. J. Theory of cross-correlation analysis of PIV images. Applied Scientific Research. 1991, **49**, 191-215.

7. BRAUN, M. J., DZODZO, M. AND LATTIME, S. B. Automatic Computer Based Non-Intrusive Temperature Measurements In Laminar Natural Convection Using TLC in Enclosures With Variable Aspect Ratio. Experimental and Numerical Flow Visualization. 1993, ASME FED **172**, 111-79.

8. CHAN, T. L., JAMBUNATHAN, K. LEUNG, T. P. and ASHFORTH-FROST, S. A Surface Temperature Calibration Method for Thermochromic Liquid Crystals using True-Colour Image Processing. In Proc. of The Tenth Int. Heat Transfer Conf., 1994, 2, 201-6 (IMechE).

9. DARIBI, D. AND GHARIB, M. Digital Particle Image Thermometry: Method and Implementation. Experiments in Fluids, **11**, 1991, 77-86.

10. HOLLINGSWORTH, D. K., BOEHMAN, A. L., SMITH, E. G. AND MOFFAT, R. J. Measurement of Temperature And Heat Transfer Coefficient Distributions In A Complex Flow Using Liquid Crystal Thermography And True-Colour Image Processing. Heat Transfer 1989. HTD **123**, 35-42 (ASME).

11. AKINO, N., KUNUGI, T. ICHIMYIA, K., MITSUSHIRO, K. AND UEDA, M. Improved Liquid Crystal Thermometer Excluding Human Colour Sensation. J. Heat Transfer, 1989, **111**, 558-65.